## *Shear banding in polymeric fluids under large amplitude oscillatory shear flow*

CARTER, KATHERINE,ANNE

# Shear banding in polymeric fluids under large amplitude oscillatory shear flow

**Katherine Anne Carter**

A Thesis presented for the degree of
Doctor of Philosophy


Supervised by Prof. Suzanne Fielding
Department of Physics
Durham University
UK

April 2016

## Abstract

In this thesis, I theoretically explore shear banding of entangled linear polymer solutions and melts in large amplitude oscillatory shear strain (LAOStrain) and stress (LAOStress) protocols. This work moves beyond that of Moorcroft and Fielding [32,135,136] who showed time-dependent shear banding in shear startup and step stress protocols. These protocols are only transiently time-dependent. LAOStrain and LAOStress have a sustained time-dependence. I consider the criteria derived in [135] to predict the onset of shear banding in the transient material response for shear startup and step stress, relative to the triggers of shear banding in LAOStrain and LAOStress. I find that stability to the formation of shear banded flow in the LAOS protocols can be understood - to a good approximation - by the known triggers of shear banding in these simpler transiently time-dependent protocols.

I employ the Rolie-Poly (RP) model [110] to investigate the existence of shear banding in LAOStrain and LAOStress over a wide range of imposed amplitudes and frequencies. I find shear banding to occur in the alternance state (where time-translational invariance is achieved), even in materials that are known to remain homogeneous at the steady state.

For each protocol I consider the relative influence of the constraint-release stress relaxation RP parameter $\beta$ and entanglement number $Z$ on the intensity of shear banding across the phase space. I find significant shear banding to occur in both LAOStrain and LAOStress for experimentally-realistic values of $Z$, both in materials that shear band to steady state, and those that don't. The main results of these investigations are submitted for publication in the Journal of Rheology [24].

Finally, I consider the shortcomings of using a single-mode RP model when characterising the full chain dynamics of entangled linear polymers in flow. I employ a multimode approach and fit a power-law spectrum to experimental linear rheology data and investigate time-dependent shear banding in the presence of higher-order relaxation dynamics. For this, I use the simpler shear startup protocol and investigate the limits under which significant shear banding exists for well-entangled polymers and discuss the possible importance of considering edge fracture as a mechanism for shear banding.

# Declaration

The work in this thesis is based on research carried out under the supervision of Prof. Suzanne Fielding, in the Department of Physics, Durham University, UK. No part of this thesis has been submitted elsewhere for any other degree or qualification and it is all my own work unless referenced to the contrary in the text.

# Acknowledgements

I would like to thank Suzanne Fielding for her supervision over the course of my Ph.D. I have learnt a great deal from her about the subject of my Ph.D and research methodology. I would also like to thank my second supervisor John Girkin who played an active part in my supervision, particularly during the second half of my Ph.D and whose wisdom and patience I admire, and am truly grateful for. I would also like to thank Beth Bromley for her kind ear, sensitivity, understanding, and sense of reality that helped me achieve my final goals within my Ph.D and several steps beyond, into my future career.

Thanks are given to Dietmar Auhl for supplying polyisoprene data from the MuPP2 project and to David Hoyle for his expertise with the REPTATE software for fitting the data. I would also like to thank Richard Graham and Halim Kusumaatmaja for agreeing to be my external and internal examiners.

Within my office, I would firstly like to thank Robyn Cooke, who's Ph.D instigated the studies I present in this thesis. She has been a wonderful friend and inspiration to me. I cannot thank her enough for the time she has given me throughout my degree. Thanks are also due to my colleagues and friends, Robert Williams, with whom I started my Ph.D process and who has always been supportive, and Ewan Hemingway, whose expansive knowledge of computational numerics and wonderful patience have been a huge help for me during the on-going learning experience that has been my Ph.D. Finally, David Hoyle, who has been a great friend and aide to my sanity through the years we've spent in the 'green corner', honouring our Leeds roots. I am fortunate to have been partially supervised by David towards the

end of my Ph.D, and I wish him all the best with his career and am certain that his future students will enjoy working with him as much as I have.

I also thank my family. My parents and brothers are a huge part of my life and have supported me, throughout everything, towards this degree. I am very fortunate to consider my immediate family to be my closest friends.

Finally, I would like to thank my husband, Dr Gregory Louis Carter, who has truly kept me going through these last few years. It is through him that I have found my confidence and my passion for what I hope to achieve in my career, of which, I hope this thesis is only the foundation.

# Contents

# List of Figures

# List of Tables

# 1

# Introduction

The term 'rheology' originates from the Greek word 'rheos' meaning 'flow'. It is the study of flow and deformations in matter. Whilst flow is a concept typically associated in the study of fluid dynamics with simple liquids, rheology extends to materials of more complex microstructure and more solid-like properties, encompassing 'complex fluids' or 'soft materials' materials such as polymers, emulsions, foams and liquid crystals, amongst many others. These have mesoscopic substructures (such as entangled polymeric molecules or emulsion droplets, for example) that dominate their rheological response to deformation in different flow protocols [104]. Viscoelastic materials exhibit both liquid-like viscous properties and solid-like elastic properties. At short times, a viscoelastic material will respond elastically to an applied strain, storing energy and recovering its original form from any imposed deformation. On longer timescales the material will dissipate energy and relax its internal microstructure.

Many members of this class of Non-Newtonian fluids have been shown to be unstable to the formation of *shear banded* flow at high enough flow rates. *Shear banding* is a regime where two (or sometimes more [25]) co-existing macroscopic banded regions of high and low shear rates form within the gradient direction of the flow [14,26,45,61,63,119,139,140,165]. This *gradient banding* phenomenon resembles a phase transition, as separate structures form in the flow following an onset to instability. The instability to the formation of these banded macroscopic regions of flow at the steady state occurs when the underlying constitutive curve of the material is non-monotonic. This signature of the constitutive curve, where stress decreases over a range of applied shear rates, was shown to be mechanically unstable to the formation of shear bands in viscoelastic fluids [185]. However, the findings from these two theoretical studies were not confirmed immediately in experiment. It was not until the mid-90's that shear banding was first visualised in NMR experiments of a wormlike micellar solution under steady shear [22, 116–118] and until 2006 for entangled polymeric fluids in step shear [181].

In the studies presented within this thesis, it is only this gradient-direction banding that is considered. The possibility of *vorticity banding* - in an orthogonal direction - is discussed in [73, 139]. Shear bands form in a material in which a state of initially homogeneous shear flow becomes unstable to the growth of heterogeneous perturbations in the flow-gradient direction. They may be seen in a steady flowing state or only during the initial startup of deformation [2, 134–136].

The occurrence of steady state shear banding has been well studied in a wide range of complex materials. Theoretical calculations have largely been able to capture the dynamics of shear banding transitions in materials where steady state shear banding has been seen in experiment. For example in wormlike micelles [16, 22, 77, 87, 104, 116–118, 160], carbopol gels [44, 46], emulsions [33], foams [154], lamellar surfactant phases [161], triblock copolymers [15, 120], star polymers [158] and, though subject to ongoing controversy, entangled linear polymer solutions and melts [107,108,152,152,172,173,179,180]. Molecular dynamic simulations have also shown steady state banding in long-chain polymers [23].

In more recent years, shear banding has also been seen to occur transiently during

time-dependent flows. This occurs for materials with a monotonic underlying constitutive curve and thus preclude shear banding at the steady state. This *transient shear banding* has been experimentally seen in shear startup for entangled linear polymers [19, 28, 88, 107, 152, 179, 180], star polymers [158], wormlike micelles [16], carbopol microgels [44, 46], clays [125], emulsions [33] and foams [154]; in step strain of entangled linear polymers [7, 16, 17, 57, 181], and in step stress of entangled linear polymers [18, 19, 85, 88, 173], wormlike micelle surfactants [16, 86, 87, 167], carbon black suspensions [72] and carbopol microgels [43].

Whilst steady state shear banding has long been associated with the overshoot in stress with strain rate in the underlying constitutive curve of the material [185], it has more recently been suggested that transient shear banding occurs in the shear startup protocol due to the stress overshoot in time (or strain, for fixed-rate protocols) [2, 65, 92, 121, 123, 134–136]. This has been experimentally confirmed for polymeric fluids [19, 88, 151, 152], carbopol gels [44, 46] and laponite clay [125]. Reference [135] defined a fluid- and model-independent set of criteria for the onset of shear banding in time dependent flows such as strain-controlled shear startup and stress-controlled step stress protocols. In the step stress protocol, the corresponding signature to the stress overshoot in strain for the onset to shear band formation in strain-controlled protocols is the increasing, upward-curving shear-rate response to imposed fixed stress amplitude. This has been seen in experiments for entangled linear polymers [16, 19, 85, 88, 151, 173], colloidal gels [72], carbopol microgel [43] and wormlike micelle surfactants [86, 87].

Recent studies have also considered edge fracture to be the trigger to these instabilities in flow [85, 107, 108, 164, 171, 179] and the discussion remains controversial. It was suggested by Hu [85] that edge fracture - often considered to originate from the imbalance between the second normal stress and surface tension of a given sample - acted as a stress perturbation to the fluid surface, leading to shear band formation across the sample. Indeed, ref. [85] contains a good overview of existing papers that consider the influence of edge fracture on the presence of shear banding in entangled polymeric fluids.

Li and McKenna [108] outline some of these outstanding issues within the shear

banding community. They provide an overview of experimental and modelling papers that, for linear polymer solutions with similar entanglement numbers, shear banding under constant controlled shear does not always exist. Indeed, they presented experimental evidence of the absence of shear banding during startup shear in highly entangled ($Z = 61$) polymer solutions that had previously been reported to do so elsewhere (ref. [152], $Z = 27 - 40$). Moreover, the only banding seen for $Z = 61$ was for the highest imposed shear rate and only transient, despite the assertion in [152] that transient shear banding occurred in insufficiently well entangled systems.

Li et al. [107] found that, for a well entangled polymer solution, shear bands were only seen for experiments where edge fracture effected the measurements. Moreover, in ref. [108], it was suggested that it is in highly entangled polymeric solutions, with strong elasticity and thus a relatively flat modulus plateau, that edge effects become problematic and shear banding is prominent. It could therefore be suggested that it is edge fracture that drives a shear banding instability during rheological experimentation, though further investigations are still required in this area.

Although the inclusion of these effects would be an interesting study, the results shown in this thesis are achieved through one-dimensional modelling techniques where there are no free surfaces available for edge effects to be addresses. I therefore cannot numerically consider edge effects in the polymer systems. However, in chapter 6, I revisit this on-going discussion on the origin of shear banding seen in polymeric systems. Fitting a multimode version of the RP model to real polymer data, I allow for heterogeneity and do not find any shear banding for the parameters set directly by the data-fitting process. This could be argued to indicate the need for further dynamics to be considered in the current modelling techniques used here to capture existing experimental results.

It has more recently been suggested that long-lived transient shear bands have been mistaken for steady state shear banding in soft glassy materials due to their slower relaxation dynamics [63, 134]. It has also been shown that steady state shear banding can exist for materials with a monotonic constitutive curve provided there is strong concentration coupling [34, 35, 67], though this dynamic is not considered

in this thesis and is left for future studies. Other instabilities in the flow of complex fluids have been suggested other than shear banding [58], including instability of the interface between the shear banded regions [60, 138] or in the high shear band itself [62], though these are not included in the focus of the studies presented here.

Whilst it has been shown that shear bands may develop transiently in time-dependent flows, protocols such as shear startup, step strain and step stress have only a *transient* time-dependence. In recent years there has been growing interest in the rheological community for oscillatory shear protocols, in particular Large Amplitude Oscillatory Shear Strain (LAOStrain) and Stress (LAOStress), where the nonlinear materials effects in the flow of complex materials can be probed over a wide range of imposed frequencies and amplitudes [39,51–55,89,90,106,137,155–157,172,187,189]. The notation here (where the second 'S' is dropped for clarity) is adopted from [42] following convention in the communtiy. These oscillatory techniques have an advantage over the simple protocols due to their time-dependent deformation: a range of shear rates and stresses can be imposed gradually, using strain-controlled or stress-controlled rheometers [12,130] rather than as a step signal [137]. A recent review of complex materials in LAOS can be found in [90].

Oscillatory protocols have an inherit time-dependence that is *sustained* throughout experimental measurement. It therefore follows from the evidence of shear banding in time-dependent flows that shear banding might be expected to manifest in time-dependent protocols where the flow is continuously changing with time. Otherwise transient short-lived shear bands (in shear startup) may be captured by the oscillatory flow, resulting in a persistent banded state throughout repeated oscillations. However, this inherently time-dependent protocol has rarely been studied from the viewpoint that heterogeneity may arise during deformation and thus allow for the existence of shear banding to occur in the flow [90]. Early exceptions are shown in [58,187,188] for a wormlike micelle surfactant model with a non-monotonic constitutive curve. A study by Adams and Olmsted [4] considered this heterogeneous flow regime for an underlying monotonic constitutive. They found - through numerical study - shear banding in LAOStrain.

Indeed, shear banding in LAOS has since been experimentally observed in polymer solutions [28,150,172] , dense colloids [30] and wormlike micelle surfactants [41, 77, 78, 187, 188] that are known to shear band in steady state. In chapters 4 and 5 I consider the strain-controlled and stress-controlled LAOS protocols and allow for the possibility of shear banding. I find shear banding to be a prevalent feature for both protocols, over a range of imposed amplitudes and frequencies, for materials with non-monotonic *and* monotonic underlying constitutive curves.

Previous theoretical studies of the LAOS protocols have used a number of methods to interpret and quantify the nonlinear response data. Unlike in the small amplitude regime (SAOS) where response signals are sinusoidal and decomposable into their viscous and elastic contribution functions ($G'$ and $G''$, defined in chapter 2), LAOS response signals are distorted, non-sinusoidal and thus more difficult to decompose into simple basis functions. In recent years, studies have focussed primarily on strain-controlled LAOS when attempting to address this issue of interpretation. These include quantifying the signal via whole waveform analysis, in the form of Fourier transformations [182, 183], identifying measures for quantifying the elastic representation (in strain) or viscous representation (in strain-rate) of the material response [176], a decomposition of the signal into characteristic sine, square and triangular wave prototypical response functions [94, 95], generalised stress decomposition using symmetry arguments into elastic and viscous contributions [29] and calculating Chebeyshev coefficients of these elastic and viscous contributions [52,53]. In many cases, this representation of data is a useful tool and enables sufficient interpretation of the material response. Indeed, these mathematically-focused interpretations are attractive to theoretical studies [137], particularly FT-Rheology, as it is widely used by experimentalists. However a drawback of Fourier transform rheology and other orthogonal basis functions is that the coefficients and higher harmonics lack any physical meaning [38, 101].

It was recently discussed in a series of papers by Rogers et al. (2011-2012) [155–157], that these numerical interpretations of the physical material response do not give a complete illustration and rather only provide the reader with a set of numbers

in which to draw their conclusions and record information from. Moreover, it was suggested that these 'linear algebraic periodic techniques' implicitly assume the permanent existence of basis states (an infinite set of sinusoidal waves, of which, higher 'harmonics' have not been given a physical interpretation) in the stress response signal waveform. It is thus suggested that these numerical techniques are more suited to the linear, sinusoidal responses, for which they were originally designed, and function well. Rogers et al. suggested instead that LAOS stress responses could be interpreted as a 'sequence of physical processes' [155–157]. In this approach, sections of the waveform signal are taken separately. By doing this, the elastic and viscous contributions can be considered almost independently. One complete stress response cycle can be built up of regions of linear elastic solid-like behaviour, flowing viscous behaviour, and nonlinear viscoelasticity. Connecting these signatures of known material responses allows a natural illustration to the reader of the real physical material response to deformation. It is this physical approach to interpreting LAOS response data that I adopt throughout this thesis.

In the studies presented within this thesis, I apply known results of time-dependent shear banding in the flow of complex materials [135, 136] to the LAOStrain and LAOStress protocols.

I find that in LAOStrain, low- and high-frequency regimes correspond to the viscous- and elastically-dominated regimes of viscoelastic flow. Moreover, I find that the criterion for instability to the formation of shear bands under shear startup [135] applies - to a good approximation - in its viscous limit (where stability of the stress response depends only on the rate of deformation) and in its elastic limit (where stability is governed by material response to strain). Furthermore, I find that in the material response to LAOStress, there exists a regime where the step stress criterion [135] applies - again, to a good approximation - for predicting the onset of shear banding in the flow. It is via these known criteria, and the 'sequence of physical processes' interpretation of LAOS response data that I explore the existence of shear banding in the oscillatory shearing of entangled polymeric solutions and melts.

## 1.1 Layout of thesis

In the following chapter I define the theoretical rheology that underlies all linear viscoelastic constitutive models used in the current literature. I describe the origins of the viscoelastic stress contribution in polymeric fluids and the tube model for the dynamics of Rouse linear entangled polymers [47, 127]. I then introduce the constitutive model I use throughout the studies in this thesis: the Rolie-Poly model [110], the single-mode approximation to the full microscopic theory of entangled linear polymers [75]. I introduce the mathematical and numerical techniques I employ throughout my simulations and discuss the influence of cell geometry in the rheometer during measurement. Finally, in chapter 3 I complete the introductory sections of my thesis by reproducing results for the existence of time-dependent shear banding in the shear startup and step stress of polymeric flows. I then take the first steps to understand the more complicated protocol of LAOS by using this earlier work. I introduce a LAOS caricature of repeating, forward and backward constant shearing to provide an initial insight into the prevalence of heterogeneous flow in the inherently time-dependent full LAOStrain protocol.

Chapters 4 and 5 present my findings for shear banding in LAOStrain and LAOStress flows, respectively. In each protocol, a combination of time-integrated heterogenous perturbations to linearised equations and full nonlinear spatiotemporal dynamics are used to explore the existence and time-dependent nature of any resultant shear banded flow. For the LAOStrain and LAOStress protocol I have produced a phase diagram for the intensity of shear banding as a function of the number of entanglements per polymer chain and convective constraint release mechanisms in the flow. I find that shear banding exists in both the LAOStrain and LAOStress protocols for sufficiently entangled polymers (within the experimentally-achievable range of entanglements) in both materials with a non-monotonic and monotonic underlying constitutive curve.

The main results of chapters 4 and 5 are accepted for publication to the Journal of Rheology's special edition on shear banding [24].

In chapter 6 I extend the previous studies showing the theoretical existence for steady state and transient shear band formation in the shear startup of polymeric fluid and wormlike micellar flows [2, 4, 135, 136]. I use a form of the Rolie-Poly model that is generalised to include a spectrum of relaxation times for the polymer chain. This multimode approach attempts to capture the higher-order relaxation dynamics of the full polymer chain [11, 13, 82, 147, 166, 169]. I fit experimental data for polyisoprene [10] to form a power law spectrum of $\tau_{d_n}$ and $G_n$ and discuss the influence of the separation of the relaxation timescales on the prevalence of shear banded flow during startup briefly considering the possible impact the inclusion of edge fracture may have on the interpretation of results. As in the oscillatory protocols, I build a phase diagram in entanglement number and the degree of convective constraint release for the intensity of shear banded flow during shear startup.

Finally, in chapter 7 I conclude my findings and discuss the studies that would further the research presented in this thesis. In all chapters, results are presented through Grace [177] and gnuplot [184] plotting softwares.

# 2

# Numerical procedures, rheological set-up and the Rolie-Poly model

In this chapter I introduce the constitutive models that are used to describe the rheology of entangled linear polymers. In particular, I introduce the Rolie-Poly model [110]. This model is the coarse-grained approximation to the full GLaMM [75] model, a tube-based [47, 48, 127] constitutive model shown to capture the linear and nonlinear rheology of entangled linear polymer solutions and melts [31, 79, 113].

I then consider the numerical tools required to undertake the theoretical studies presented throughout this thesis. I describe linear stability analysis as a tool to interpret the susceptibility of a given fluid to the formation of shear bands under imposed deformation in any given flow regime. This process involves adding small heterogeneous perturbations to an initially homogeneous base state and linearising the resultant constitutive equations to form a set of linear equations governed by a

time-dependent stability matrix.

Finally, I will discuss the effect of different commonly-used geometries of a rheometer cell. Specifically, I introduce a toy method to approximate a weakly curved geometry such as that found in a rheometer cell of concentric cylinders with a narrow gap between them [69]. I discuss the effects of the resultant stress gradients within the flow as a trigger to the onset of shear band formation. I also consider the addition of random noise as an alternative seed to trigger shear banding. This serves as an approximation to the resultant heterogeneous perturbations arising in the material, e.g. during experimental sample preparation or due to mechanical noise in feedback-controlled flow protocols.

## 2.1 Rheology: the relationship between stress and strain

Rheometers are widely used to characterise the deformation and flow properties of materials [12, 50, 56, 59, 102, 130, 176]. For example, by applying a deformation across a sample of material, the rheometer can measure the viscosity and the complex modulus of the material (defined below), amongst other relevant properties. Before I describe the geometry in which the polymeric fluids are modelled in the theoretical studies of this thesis, I first explore the origin of stress in an entangled polymeric fluid and discuss the underlying ideas underpinning the rheological constitutive models used in the literature [98, 99].

### 2.1.1 Viscoelasticity and Linear Rheology

Polymeric fluids are a subset of a wider class of complex viscoelastic materials. These materials have a time-dependent response to deformation: at short times, they show elastic-like behaviour, approximately obeying Hooke's law for linear elastic solids. At long times, their response to deformation is viscous-like, and they flow as a Newtonian fluid of viscosity $\eta$. These behaviours differ fundamentally as elastic responses are reversible: the energy expended during deformation is stored, and can

be regained by reversing the deformation. Conversely, viscous responses dissipate energy during deformation and material distortions are permanent. A viscoelastic material, such as a polymeric fluid, exhibits a time-dependent response to deformation that spans both of these respective limiting behaviours at short and long timescales with a continuous crossover in-between.

In the limit of small deformations, a viscoelastic fluid has a linear relationship between its deformation history and its current shear stress:

$$\sigma(t) = \int_{-\infty}^{t} G(t-t')\dot{\gamma}(t')\mathrm{d}t, \tag{2.1}$$

where $\dot{\gamma}(t)$ is the rate at which deformation is applied and $G(t)$ is the relaxation modulus of the material. Using small amplitude oscillatory shear (SAOS) rheology techniques (where $\dot{\gamma}(t)$ is a small amplitude sinusoidal wave) the underlying linear rheology of the material can be assessed. For imposed SAOS with frequency $\omega$, equation 2.1 leads to the definition of the complex modulus (via a change of integration variable):

$$\begin{aligned} G^*(\omega) &= i\omega \int_0^{\infty} e^{-i\omega t} G(t)\mathrm{d}t & (2.2)\\ &= G'(\omega) + G''(\omega), & (2.3) \end{aligned}$$

which, for viscoelastic materials, is a function of $\omega$. $G'(\omega)$ and $G''(\omega)$ are known as the *storage* (or elastic) and *loss* (or dissipative) moduli respectively. It follows that $G'(\omega)$ dominates when the material responds elastically to deformations (associated with short relaxation timescales the in viscoelastic fluid compared with the timescale $2\pi/\omega$ of deforamtion) and $G''(\omega)$ dominates for viscous (long-time) fluid-like behaviours. $G'(\omega)$ and $G''(\omega)$ for the Maxwell model (a simple viscoelastic model with associated relaxation modulus $G$ and timescale $\tau$) are plotted in figure 2.1. For a Maxwell model with relaxation modulus $G$ any shear stress will relax as

$$G(t) = Ge^{-t/\tau} \tag{2.4}$$

The crossover point at $G'(\omega) = G''(\omega)$ defines the characteristic relaxation time

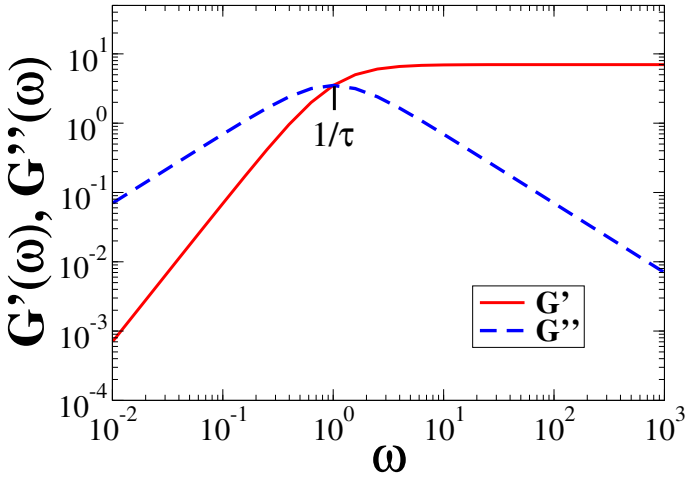


Figure 2.1: Linear rheology, crossover at characteristic relaxation time, and intrinsic timescale to the polymer $\omega = 1/\tau$, $G = \tau = 1$.

of the material, $\tau$. This is an intrinsic timescale to the material response to any imposed deformation. Indeed, it follows from equation 2.2 that $G'(\omega)$ and $G''(\omega)$ satisfy:

$$G'(\omega) = G\frac{\omega^2\tau^2}{1+\omega^2\tau^2}, \tag{2.5}$$

$$G''(\omega) = G\frac{\omega\tau}{1+\omega^2\tau^2}, \tag{2.6}$$

and $G'(\omega) = G''(\omega)$ occurs at $\omega = 1/\tau$.

In entangled polymeric fluids, the entanglement points formed around a single chain by surrounding polymers may be modelled as a smooth continuous tube of confinement. $\tau = \tau_d$ is defined on the microscopic scale as the time required for an entangled polymer to relax all its initial stresses and orientational constraints via longitudinal movement along its own length, called 'reptation' [36]. This assumes that interactions between polymer chains become dominant for chains that are sufficiently long and entangled and forms part of the *tube model* [36, 47, 48], defined in greater detail in section 2.6.

Throughout this thesis I primarily use a single-mode constitutive model with one characteristic timescale for the polymer $\tau_d$ (and corresponding modulus $G$). To non-dimensionalise calculations, I chose time and modulus units $\tau_d$ and $G$ such that $\tau_d = G = 1$, unless stated otherwise. However, in chapter 6 I use a multimode approach.

This uses a combination of characteristic timescales to capture the higher order dynamics of the polymer chain and is required to fully characterise a material [75]. A *relaxation spectrum* of $\tau_{d_n}$ and $G_n$ for each $n^{\text{th}}$ mode of a total of $N$ modes is formed. Equation 2.4 therefore becomes a summation of $N$ modes each contributing to the relaxation spectrum in linear rheology:

$$G(t) = \sum_{n}^{N} G_n e^{-t/\tau_{d_n}}. \tag{2.7}$$

Details of how a relaxation spectrum is defined relative to experimental SAOS data using the linear theory of polymer dynamics [75, 111] are described in chapter 6.

## 2.2 Molecular modelling of polymer dynamics

A linear polymer chain consisting of $N$ monomers can be coarse-grained and modelled by subchains of $N_R+1$ spherical beads joined by $N_R$ springs. This is the Rouse model and describes the rheology of isolated, unentangled linear polymer chains and is defined in full in reference [47]. It provides the underlying relaxation time used in the Doi-Edwards (DE) [47] tube model for entangled polymers. It is this class of polymeric material, where the entanglement (due to the overlapping of chains) dominates the material response in flow that is studied in this thesis. In particular, I focus on the constitutive model based on the DE model: the Rolie-Poly model [110], a single-mode approximation of the GLaMM model [75] which includes the multiple relaxation time dynamics of the entangled network of polymer chains. This is defined in section 2.6.

### 2.2.1 Force balance and fluid incompressibility

In general, the stress in any complex fluid can be decomposed into viscoelastic and Newtonian solvent contributions, plus an isotropic pressure. This takes the general form, for the viscoelastic conformation tensor $\underline{\underline{\sigma}}$ of:

$$\underline{\underline{\Sigma}} = G(\underline{\underline{\sigma}} - \underline{\underline{I}}) + 2\eta\underline{\underline{D}} - p\underline{\underline{I}}. \tag{2.8}$$

Here $p$ quantifies the pressure, determined from the condition that the flow is incompressible, *i.e.* $\underline{\nabla} \cdot \underline{v} = 0$. $\underline{\underline{D}} = \frac{1}{2}(\underline{\underline{K}} + \underline{\underline{K}}^T)$ where $K_{\alpha\beta} = \partial_\alpha v_\beta$, the velocity gradient tensor. $G$ is the elastic modulus for the viscoelastic structure. This is a material property found from linear rheology on the material and, as noted above, is set to $G = 1$ (unless stated otherwise) throughout this thesis. The expression $G(\underline{\underline{\sigma}} - \underline{\underline{I}})$ defines the viscoelastic stress contribution from the material substructure, defined to relax to $\underline{\underline{I}}$ at rest. $\eta$ defines the Newtonian solvent viscosity.

**Polymeric stress** For polymers, this viscoelastic contribution to the stress is denoted here as $\sigma^p$. For a cube element of side-length $L$, the polymeric stress component originates from polymeric chains within the cube: for a surface of the cube element, with normal $\underline{\hat{a}}$ and area $L^2$, a section of polymer chain cutting through that surface carries a force ($F$) across it. This is calculated relative to the number of polymer chains in the cube and the probability ($r/L$) that one chain section will cross the surface in question and summed over all the modes in the chain. This gives rise to an associated (polymer) stress such that

$$\sigma_{\alpha a} = \frac{1}{L^3} \sum_{chains,n} \langle r_{n\alpha} F_{n\alpha} \rangle \,. \tag{2.9}$$

$F_n$ is a function of local chain configuration and is defined by the force-extension law of a Gaussian chain [127]. In the continuous limit, where the polymer chain is integrated along the contour variable $s$, the viscoelastic stress becomes:

$$\sigma_{\alpha\beta} = \frac{c}{N} \frac{3k_B T}{b^2} \int_0^N \left\langle \frac{\partial R_\alpha}{\partial s} \frac{\partial R_\beta}{\partial s} \right\rangle \mathrm{d}s \tag{2.10}$$

where $c/N$ is the polymer concentration and the polymer chain contour variable varies from 0 to $N$ [133].

**Solvent contribution** The origin of $\eta$ may indeed be a solvent present in the material solution or used to encompass all the fast dynamics of the polymer chains (or

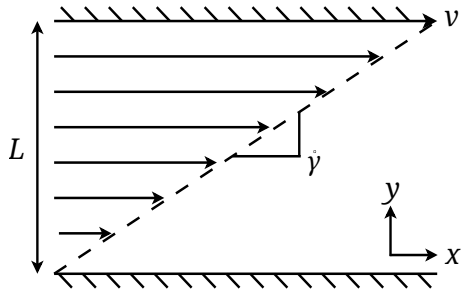


Figure 2.2: The shear stress response to applied strain: constant velocity $v$ is applied in the $\underline{\hat{x}}$ direction, resulting in a shear rate $\dot{\gamma}$ across the cell in the flow-gradient $\underline{\hat{y}}$ direction. The plates are positioned at $y = 0, L$. This is the 'shearing cell' referred to throughout this thesis. Reprinted with permission of R.L.Cooke [32].

other complex structures in other materials) by assuming they relax on an infinitely fast timescale. Based on a survey of the experimental data, a range of $10^{-7}$ to $10^{-3}$ for $\eta$ (in units such that $G = \tau_d = 1$) is suggested [74]. Reference [6] suggests that values of $\eta < 10^{-5}$ are unfeasible to explore numerically due to a resulting large separation of timescales between $\tau_d$ and $\eta/G$. In the studies presented in this thesis, I use $\eta$ ranging between $10^{-4}$ and $10^{-5}$ as used in references [5,135,135] that preceded this work on shear banding in the RP model.

In the experimental regimes studied within this thesis, the viscous and viscoelastic forces in the flow are usually far greater than the inertial forces, This results in a very small Reynolds number: $R_e$ = inertial forces/viscous forces $\ll 1$. It follows that the creeping flow limit ($R_e \to 0$) is used throughout my work. Moreover, this limit leads to the following force balance equation:

$$\underline{\nabla} \cdot \underline{\underline{\Sigma}} = \underline{\nabla} \cdot \left[ G(\underline{\underline{\sigma}} - \underline{\underline{I}}) + 2\eta \underline{\underline{D}} - p\underline{\underline{I}} \right] = 0 \tag{2.11}$$

### 2.2.2 The Rheometer cell

The rheological properties of materials can be measured experimentally using a rheometer [176]. Typically, a sample of material is sandwiched between two plates of some geometry and strain is applied by moving the plates relative to each other. Common geometries include the cylindrical Couette cell with a narrow gap and the cone and plate with a narrow angle. These are all discussed in greater detail

later within this chapter in section 2.5. Here I describe the idealised geometry of two infinitely long parallel plates separated by some finite distance, $L$. The material sample within the cell is assumed not to experience edge effects. I define the $\underline{\hat{x}}$, $\underline{\hat{y}}$ and $\underline{\hat{z}}$ as the velocity, flow-gradient and vorticity directions respectively (shown in figure 2.2). It is assumed throughout the calculations in the studies presented within this thesis that spatial structures (due to shear banding instabilities) only form in the flow gradient direction; translation invariance is imposed in the velocity and vorticity directions. During a protocol, the bottom plate at $y = 0$ remains stationary whilst the top plate at $y = L$ moves with some velocity, $V\underline{\hat{x}}$. This imposes a shear rate across the cell which is defined for $y \in \{0, L\}$ as:

$$\dot{\gamma} = \frac{V}{L}. \tag{2.12}$$

and the velocity gradient tensor $\underline{\underline{K}}_{ij} = \frac{\partial u_i}{\partial x_j}$. For shear flow:

$$\underline{\underline{\mathbf{K}}} = \begin{pmatrix} 0 & 0 & 0 \\ \dot{\gamma} & 0 & 0 \\ 0 & 0 & 0 \end{pmatrix}. \tag{2.13}$$

It thus follows that for the shear component of the stress, equation 2.8 becomes

$$\Sigma_{xy} = G\sigma_{xy} + \eta\dot{\gamma} \tag{2.14}$$

Moreover, it follows from the condition in equation 2.11 that

$$\partial_y \Sigma_{xy} = 0. \tag{2.15}$$

## 2.3 Nonlinear Rheology

In section 2.1.1 above, I have only considered linear rheology which holds for only relatively small deformation rates. Once the rate of deformation increases beyond the linear regime, that is, at rates faster than the intrinsic characteristic relaxation timescale of the material, nonlinear material behaviours dominate and the response

to deformation is no longer independent of the rate at which it is applied. It is within this *nonlinear regime* that forms the focus of the studies within this thesis.

The nonlinear regime of a viscoelastic material's response to deformation is dependent on the rate of deformation, the history of the material behaviour (for example, to previous deformation) and the geometry under which the deformation is applied. Material behaviour to nonlinear deformation rates is often very different than in the linear regime and thus nonlinear rheology has the ability to explore further behaviours and dynamics of complex materials. For shear rates larger than the inverse characteristic relaxation time of the material, the nonlinear shear stress response with increasing shear rate no longer maintains a constant gradient (as in Newtonian flow). Non-Newtonian fluids may (for example) have decreased viscosity when deformed (shear *thinning* fluid), increase their viscosity with increased deformation rate (shear *thickening* fluid) or require a finite yield stress to be attained before beginning to flow (*yield stress* fluid).

### 2.3.1 The underlying constitutive curve and flow curve

The underlying *constitutive curve* of a material is one way to view the material linear and nonlinear behaviours over a wide range of imposed shear rates. In a theoretical study, a constitutive curve is built up through recording the steady state shear stress of the material in a system that is constrained to be spatially homogeneous. The experimental counterpart of the constitutive curve is the material *flow curve*, again formed by the steady state stress recorded at the terminal time of a series of startup experiments. The difference in these curves was markedly different in the original Doi-Edwards theory as the constitutive curve showed a (physically impossible) non-monotonic relationship in $\Sigma(\dot{\gamma})$. It was predicted that homogeneous flow was unstable in the negatively-sloping regime of the underlying constitutive curve [185]. This instability formed two co-existing localised macroscopic regions of flow with different shear rates, separated by an interface region [168]. These are known as "shear bands". Figure 2.3(a) shows a schematic of this response. The corresponding non-monotonic constitutive curve can be seen in figure 2.3(b). Later additions to the DE model such as chain stretch and convective constraint release

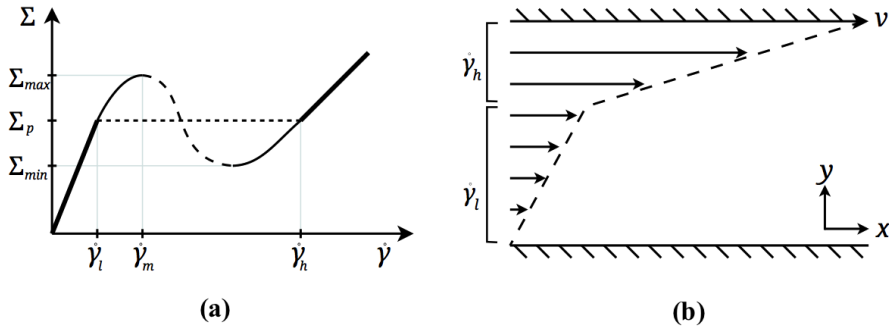


Figure 2.3: **Left:**The homogeneously-constrained constitutive curve of the material (the 's' shape), combined with the heterogeneous flow curve (made up of the thick lines on the stable lower and upper branches of the constitutive curve and the dashed plateau bridging the two). The values of the coexisting shear rates in the shear banded region $(\dot{\gamma}_l, \dot{\gamma}_h)$ are marked, as well as the stress maximum, minimum and plateau values. **Right:** The corresponding shear banded flow profile within the shearing cell as defined in figure 2.2. Spatial invariance is assumed in the $\underline{\hat{x}}$ and $\underline{\hat{z}}$ directions. Heterogeneity is allowed in the flow-gradient $\underline{\hat{y}}$ direction such that $\dot{\gamma} = \dot{\gamma}(y,t) = \frac{\partial v}{\partial y}$. Shear bands form with two coexisting shear rates $\dot{\gamma}_l$ and $\dot{\gamma}_h$ which spatially average to the 'global' shear rate $\bar{\dot{\gamma}} = \frac{1}{L}\int_0^L \dot{\gamma}(y,t)\mathrm{d}y$. Images reprinted with permission of R.L.Cooke [32].

(defined later) removed the unstable non-monotonic region of the constitutive curve and thus precluded the possibility of shear banding at the steady state.

The thick black lines of figure 2.3 mark the high and low viscosity branches of the constitutive curve. Here, the material is experiencing deformation rates within the linear regime ($\dot{\gamma} \to /\tau_d$, rates approaching the intrinsic relaxation time of the material) or is comparable to the solvent viscosity ($\dot{\gamma} \gg 1/\eta$). Within these regimes, the material is stable to the formation of shear bands.

The non-monotonic region of the constitutive curve (where stress is decreasing with increasing shear rate) is marked in figure 2.3(a) by the long-dashed black line. Within this region a state of initially homogeneous flow is linearly unstable to the formation of shear banded flow in the steady state. The short-dashed line marks the plateau-region of the curve formed when spatial heterogeneity is accounted for and shear banded flow is measured at the steady state. This plateau region is the material response seen in practice in the steady state, unlike the non-monotonic nature of the underlying constitutive curve. The resultant monotonic curve (formed by joining the plateau region to the high and low viscosity branches of the linear

regimes) can be recorded in experiment and constitutes the aforementioned *flow* curve of the material at the steady state. The points at which the plateau region (defined for $\Sigma = \Sigma_p$) cross the constitutive curve mark the high and low shear rates that pertain in the co-existing shear bands in the steady state flow, $\dot{\gamma}_h$ and $\dot{\gamma}_l$ as shown in figure 2.3(b). Within this plateau, an imposed $\bar{\dot{\gamma}}$ such that $\dot{\gamma}_l < \bar{\dot{\gamma}} < \dot{\gamma}_h$ leads to shear banded flow, where the proportions of the flow with $\dot{\gamma}_h$ and $\dot{\gamma}_l$ follow the lever rule: $\bar{\dot{\gamma}} = \alpha\dot{\gamma}_l + (1-\alpha)\dot{\gamma}_h$, where $\alpha$ is the fraction of the cell dominated by the low shear rate band and the $\bar{\dot{\gamma}}$ recorded on the $\Sigma(\bar{\dot{\gamma}})$ flow curve is the spatially-average 'global' shear rate $\bar{\dot{\gamma}} = \frac{1}{L}\int_0^L \dot{\gamma}(y,t)dy$.

Finally, the thin-solid black lines of the constitutive curve in figure 2.3(a) indicate the regions of metastability to shear banding. These regions fall between the onset (and exit) of the plateau region of the constitutive curve and the local stress maximum ($\Sigma_{\max}$) and minimum ($\Sigma_{\min}$) that bound the negatively-sloping region of the curve. Consider instead the transit of the $\Sigma(\dot{\gamma})$ curve by a slow upward $\dot{\gamma}$ sweep. On the approach to $\Sigma_{\max}$ for increasing $\dot{\gamma}$, the material does not experience linear instability to the formation of shear bands until the negatively-sloping region of the constitutive curve is reached, *i.e.* once the curve satisfies $\partial\Sigma/\partial\dot{\gamma} < 0$. The shear stress response to an upward $\dot{\gamma}$ sweep would follow the solid lines of the constitutive curve until the material becomes unstable to the formation of shear bands and the stress response drops down to the plateau with $\Sigma = \Sigma_p$. The stress remains at $\Sigma_p$ as $\dot{\gamma}$ continues to increase until the low-viscosity branch of the curve is met. However, if the sweeping were reversed and the curve was now traversed by a downward $\dot{\gamma}$ sweep, the same path would not be traced back [76]. Once already in the shear banded form (within the plateau region where $\Sigma = \Sigma_p$) the material does not increase its stress (to $\sim \Sigma_{\max}$) as $\dot{\gamma}_m$ is approached (from the right, in figure 2.3). The plateau extends to the linear high-viscosity branch at low $\dot{\gamma}$. This difference in $\Sigma(\dot{\gamma})$ pathway for upward and downward $\dot{\gamma}$ sweeps creates a hysteresis loop in the combined - increasing and decreasing - stress response. This hysteresis behaviour is not unique to the direction and would indeed be seen if the $\dot{\gamma}$ sweep directions were reversed, starting with an initial downward sweep from large $\dot{\gamma}$ and $\Sigma$. Experiments have visualised this hysteresis in shear-rate sweep tests [76, 105].

## Numerically allowing for heterogeneous flow

When shear banded flow forms due to spatial heterogeneity, the viscoelastic (or polymer) shear stress $\sigma$ ($= \sigma_{xy}$, where the subscript is dropped from here for clarity) and the shear rate $\dot{\gamma}$ may vary with space ($y$). However, the total shear stress $\Sigma$ ($= \Sigma_{xy}$) remains constant. It is this force balance equation that is employed during numerical simulations to calculate the spatially-dependent quantities as the governing constitutive equations are evolved during an applied protocol.

In the original constitutive models based on the tube theory, only local terms were included. These evolved the equations to describe the material dynamics with respect to time, but did not account for any non-local diffusive behaviour. Without these additional terms, shear banding is an unphysical concept. The existence of two banded regions of flow, shearing at different rates whilst at a common, uniform stress, leads to a strongly inhomogeneous interface between the bands [115]. Constitutive models were therefore amended to include non-local diffusive terms to allow for this transition to a heterogeneous flow profile. This was first attempted in models for wormlike-micelles, where shear banding was first seen in experiment [22]. Reference [168] used numerical methods to compute the formation, width and interface position across cell for two co-existing shear bands when the constitutive equations allowed for inhomogeneity in the material. References [114, 148, 186] added a diffusion term to the Johnson-Segalman model (forming the dJS model) to study shear banding. The interface between the co-existing shear bands was given a finite width set much smaller than the cell width ($L$). This finite width in the flow of polymeric fluids is defined in one example to originate from Brownian dynamics of the polymer chains within the flow, moving back and forth across the interface region [148].

For a general constitutive model, viscoelastic dynamical variables can be defined by a vector $\underline{s} = (\sigma,\ \sigma_{xx},\ \sigma_{yy},\ \ldots)^T$. For a projection vector $\underline{p} = (1,\ 0,\ 0,\ \ldots)$, the total shear stress defined in equation 2.14 can instead be written $\Sigma_{xy} = G\underline{p}\cdot\underline{s}(y,t) + \eta\dot{\gamma}(y,t)$. Moreover, when modelling the dynamics of a complex material, a general

governing constitutive equation can be defined:

$$\partial_t \underline{s} = \underline{Q}(\underline{s}, \dot{\gamma}), \tag{2.16}$$

where $\underline{Q}$ is a function specific to the constitutive model. A general diffusive term can then be added to this equation:

$$\partial_t \underline{s} = \underline{Q}(\underline{s}, \dot{\gamma}) + D\nabla^2 \underline{s}. \tag{2.17}$$

where $D = l^2\tau_0$ is a diffusion constant, defined for a microscopic timescale $\tau_0$ and where $l \ll L$ defines the width of the interface.

This is included in the studies presented in this thesis for the RP model as the mechanism for the emergence of shear banded flow. To numerically perform these simulations on entangled polymer solutions I employ computational numerical methods. In Appendix 2.7, I outline these in detail, though they originate from Ref. [146] and [145].

## Aside: calculation of $Z$

I present a short aside here on a potential confusion in the literature about the calculation of the entanglement number $Z$ between theoretical and experimental studies. The original tube theory from which most constitutive models are derived, defines [47]:

$$\tau_d = 3Z\tau_R = 3Z^3\tau_e,$$

$$\tau_R = Z^2\tau_e.$$

However, this is a approximation from the linear theory. The full version, as derived by Likhtman and McLeish in ref. [111] is defined by the two functions:

$$\tau_{\mathrm{d}f}(Z)/\tau_{\mathrm{d}}^{(0)}(Z) = 1 - \frac{2C_1}{\sqrt{Z}} + \frac{C_2}{Z} + \frac{C_3}{Z^{3/2}},$$

$$\tilde{G}_f(Z) = 1 - \frac{C_1}{\sqrt{Z}} + \frac{C_4}{Z} + \frac{C_5}{Z^{3/2}}$$

where $\tau_{\mathrm{d}}^{(0)}(Z)$ is the reptation or disentanglement time as denoted by $\tau_d$ throughout this thesis and $\tau_{\mathrm{d}f}(Z)$ and $\tilde{G}_f(Z)$ are renormalisations of a dimensionless plateau modulus and reptation time due to contour length fluctuations. Constants $C_1$ to $C_5$ are found via data fitting over a wide range of $Z$ values.

It therefore follows from these higher order correction terms to the calculation of $\tau_d$, that the separation between $\tau_d$ and $\tau_R$ as defined in the RP model (and the tube theory more generally) is reduced. However, as $Z$ becomes large, these correction terms become less important. Table 2.1 gives an illustrative example of this.

| $Z_{\mathbf{experiment}}$ | **Ratio** $\tau_d/\tau_R\vert_{\mathbf{linear\ theory}}$ | **Ratio** $\tau_d/\tau_R\vert_{\mathbf{thesis}}$ |
|---|---|---|
| 6 | 3.77 | 18.0 |
| 48 | 85.59 | 144.0 |
| 96 | 200.68 | 288.0 |
| 144 | 322.44 | 432.0 |
| 192 | 447.67 | 576.0 |
| 240 | 575.12 | 720.0 |

Table 2.1: The difference between the calculated versions of $\tau_d$ and $\tau_R$ showing the decreased influence of the corrective terms as $Z$ is increased.

It was also discussed in [100] that $\tau_e$ was defined in [47] as the Rouse relaxation time of a chain of length equal to one tube segment. In [132], however, $\tau_e$ is defined as the Rouse time of one entanglement segment (with molecular weight $M_e$) giving

$$\tau_R = \left(\frac{4}{5}\right)^2 Z^2 \tau_e.$$

Moreover, for both these definitions, the entanglement number $Z \neq M/M_e$, rather $Z = \frac{5}{4}\frac{M}{M_e}$. It is in reference [59] that indeed $Z = \frac{M}{M_e}$ as used throughout this thesis and in references [27, 165]. In reference [59] the entanglement molecular weight is scaled by $\frac{4}{5}$ to account for reduced stress in the tube model due to the 'sliding of chains'. This dynamic is restricted for a cross-linked classical rubber on which the other definitions of $M_e$ are derived from [100]. Reference [111] deduced that the $\frac{1}{5}$-difference in the values was accounted for in the Doi-Edwards theory by the stress stored in the tubes of confinement after deformation is relaxed along its length.

However, it is possible that this difference of 20% in the value of $Z$ may account for differences in the values of $Z$ for which shear banding is seen experimentally (where $Z$ is a material property defined by measured $M$ and $M_e$) and for what is predicted theoretically (where $Z$ is a ratio of relaxation times $\tau_d$ and $\tau_R$). An example of such differences in opinion between experimental data and theoretical prediction over polymer entanglement in reference [3], though this dispute goes beyond the slight scaling issue in defining $Z$ discussed here.

This discrepancy is not discussed further in this thesis, but is perhaps of interest when comparing further theoretical and experimental data for entangled polymeric fluids.

## 2.4 Linear stability analysis

A linear stability analysis of a constitutive model assesses the response of a particular initial flow state of the fluid to an externally imposed infinitesimally small perturbation [60]. These perturbations may arise from thermal or mechanical noise during an experiment or from cell curvature and are added numerically to the theoretical studies presented here. As the dynamical quantity is evolved through the constitutive equations, the added perturbations to the system will either die away, or grow, exponentially, with time while in the linear regime. The former indicates a stable state of the system, whilst exponential growth in perturbations reveals instability of the initial flow state.

Following the introduction of a generalised governing constitutive equation defined in eq. 2.16, I define the homogeneous base state $\underline{\hat{s}}(t)$ of the material such that homogeneity is artificially enforced in the flow

$$\hat{\Sigma}(t) = G\underline{p} \cdot \underline{\hat{s}}(t) + \eta\hat{\dot{\gamma}}, \tag{2.18}$$

$$\partial_t \underline{\hat{s}} = \underline{Q}(\underline{\hat{s}}, \hat{\dot{\gamma}}) + D\nabla^2\underline{\hat{s}}, \tag{2.19}$$

where $\underline{\hat{s}}$ is a vector containing the dynamical variables from the model-specific constitutive equations. The diffusive term $D\nabla^2\underline{\hat{s}}$ is neglected in the following calculations as the wavelength of perturbations of interest here are $\gg l$. Indeed, the contribution of the diffusive term to the resultant linear perturbation equations is weakly negative, thus a suppressant force on perturbation growth. Linear instability to heterogeneous perturbation growth is therefore not masked by neglecting this diffusive term.

Infinitesimally-small perturbations $(\delta\underline{s}_n, \delta\dot{\gamma}_n)$, decomposed into Fourier modes, are added to a stable (well relaxed and at rest) base state $(\underline{\hat{s}}(y,t), \dot{\gamma}(y,t))$:

$$\hat{\Sigma}(y,t) = \hat{\Sigma}(t), \tag{2.20}$$

$$\underline{\hat{s}}(y,t) = \underline{\hat{s}}(t) + \sum_{n=1}^{\infty} \delta\underline{s}_n(t)\cos(\frac{n\pi y}{L}), \tag{2.21}$$

$$\dot{\gamma}(y,t) = \hat{\dot{\gamma}}(t) + \sum_{n=1}^{\infty} \delta\dot{\gamma}_n(t)\cos(\frac{n\pi y}{L}). \tag{2.22}$$

Note here that no perturbation is added to the total stress ($\delta\hat{\Sigma} = 0$) as the shear stress is uniform across the flow cell.

Expanding in terms of the small heterogeneous perturbations to the homogeneous base state:

$$\begin{aligned} \partial_t(\underline{s} + \delta\underline{s}]) &= \underline{Q}(\hat{\underline{s}} + \delta\underline{s}, \hat{\dot{\gamma}} + \delta\dot{\gamma}) && (2.23) \\ &= \underline{Q}(\hat{\underline{s}}, \hat{\dot{\gamma}}) + \partial_{\underline{s}}\underline{Q}(\hat{\underline{s}}, \hat{\dot{\gamma}})\delta\underline{s} + \partial_{\dot{\gamma}}\underline{Q}(\hat{\underline{s}}, \hat{\dot{\gamma}})\delta\dot{\gamma} + \mathcal{O}(\delta^2) && (2.24) \end{aligned}$$

then neglect terms that are higher than the first order and subtract the base state:

$$\partial_t\delta\hat{\underline{s}} = \partial_{\underline{s}}\underline{Q}(\hat{\underline{s}}, \hat{\dot{\gamma}})\delta\underline{s} + \partial_{\dot{\gamma}}\underline{Q}(\hat{\underline{s}}, \hat{\dot{\gamma}})\delta\dot{\gamma}. \quad (2.25)$$

Adding perturbations to equation 2.19:

$$\hat{\Sigma}(t) + 0 = G\underline{p} \cdot (\hat{\underline{s}} + \delta\underline{s}) + \eta(\hat{\dot{\gamma}} + \delta\dot{\gamma}), \quad (2.26)$$

linearising and subtracting the base state leaves:

$$\begin{aligned} 0 &= G\underline{p} \cdot \delta\underline{s} + \eta\delta\dot{\gamma} && (2.27) \\ \delta\dot{\gamma} &= -\frac{G}{\eta}\underline{p} \cdot \delta\underline{s} && (2.28) \end{aligned}$$

This leaves linearised equations to enable the prediction of the onset of instability to the formation of shear banded flow in a polymeric material. Combining equations 2.25 and 2.28 gives

$$\partial_t\delta\underline{s} = \left(\underline{\underline{M}}(t) - \frac{G}{\eta}\underline{qp}\right) \cdot \delta\underline{s}, \quad (2.29)$$

where $\underline{\underline{M}}(t) = \partial_{\underline{s}}\underline{Q}|_{\hat{\underline{s}},\hat{\dot{\gamma}}}$, and $\underline{q} = \partial_{\dot{\gamma}}\underline{Q}|_{\hat{\mathbf{s}},\hat{\dot{\gamma}}}$. $\underline{\underline{P}}(t)$ is defined as the time-dependent stability matrix:

$$\underline{\underline{P}}(t) = \left(\underline{\underline{M}}(t) - \frac{G}{\eta}\underline{qp}\right). \quad (2.30)$$

The solution of equation 2.29 necessitates finding the eigenvalue of the stability matrix $\underline{\underline{P}}(t)$ on the right-hand side of the equation: for the eigenvalue solution $\lambda$,

heterogeneous perturbations will grow - and thus lead instability and growth of shear banded flow - when $\lambda > 0$. Positive eigenvalues found from linear stability analysis indicate the onset of instability in the material and to the formation of shear banded flow.

There are a number of eigenvalues of the stability matrix. It follows from equation 2.29 that just one positive eigenvalue ($\lambda_n > 0$) facilitates exponential perturbation growth and material instability to shear banding, however, it is required that all $\lambda_n < 0$ for stability in the material flow. This was stated (and shown) in Ref. [32].

**Time-dependent stability** In classical stability theory, the use of linear stability analysis to predict the onset of unstable dynamics depends upon a time-independent base state [170]. This is not the case for the constitutive models used in the studies presented here. Moreover, the stability matrix within the dynamical equation is itself time-dependent. Thus material stability due to the positivity of the eigenvalue and the subsequent growth of the heterogeneous perturbations within the linearised system are only considered at any one precise instant in time. Taking the most positive eigenvalue for each numerical timestep gives a good indication of whether the material is stable, or unstable, at that instant to the growth of heterogeneous perturbations. A negative eigenvalue only predicts the decay of perturbations when the respective eigenvectors of the stability matrix are orthogonal [141]. When considering a time-dependent system this may not be the case and I therefore check these during simulations by numerically integrating the time-dependent perturbations to the linearised system. Whilst a positive eigenvalue is sufficient for perturbation growth, a negative eigenvalue does not guarantee stability. The system may experience transient or non-normal growth in the perturbations, however, I follow the work of reference [32] and neglect the possibility of any significant heterogeneous behaviour due to these undesired perturbations.

**Breakdown of the linear limit** The linear stability analysis of the governing constitutive dynamical equations described here can only accurately predict the growth of heterogeneity (in a full nonlinear system where full spatial-temporal dynamics are employed) when the growth of perturbations is small. At larger material

heterogeneity, the higher order terms (that were dismissed upon linearisation of the homogeneous equations) would become important; it is therefore here that this approximation breaks down.

## 2.5 Geometries

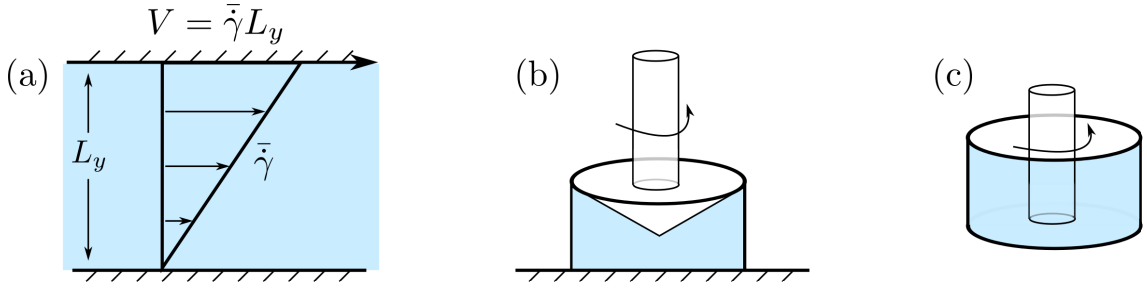


Figure 2.4: Parallel plate, cone-and-plate and Couette rheometer geometries. Reprinted with permission of E. J. Hemingway [80].

In section 2.2.2 I defined the parallel plate cell geometry. This is shown in diagram (a) of figure 2.4. Rheological experiments are also performed in other geometries such as cone-and-plate (diagram (b)) and Couette - or concentric cylinder - flow (diagram (c)), amongst others. In any of these geometries, the material sample is placed between two plates and deformation is applied across the sample. Typically one plate is held stationary while the other moves with some imposed velocity (or rate of rotation).

Rheometers impose deformation to the sample within the geometry via a *strain-controlled* (where stress response is measured) or *stress-controlled* (where strain response is measured) protocol. A comparison of these protocols and the two types of rheometers for large amplitude oscillatory shear (LAOS) is discussed in references [12, 130].

In this section I introduce the addition of *toy* curvature stress gradients to a simple parallel plate geometry to capture the curvature imposed on a flow within a Couette device. Whilst it is possible to perform numerical calculations for a curved geometry, this simple approximation to the geometry could, and indeed has been, used to describe the physical effects of the curved geometries whilst remaining simple to implement in numerical practice [69]. In the majority of the work in this thesis I use this *toy*-approximation to curvature.

This *toy* curvature approximation is defined as follows:
Considering a Couette flow between two concentric cylinders of radii $R_1$ and $R_2$,

the curvature between the cylinders can be parameterised by $q = \ln \frac{R_2}{R_1}$ [5]. That is, for smaller $q$, the geometry is less curved (or equivalently, larger $q$ results in a larger cell curvature). The choice of values for $q$ in this thesis are an approximate value based on the arguments used in reference [5]: in the paper, values of $2 \times 10^{-3}$ and $2 \times 10^{-4}$ are used and noted to be consistent with reported stress gradients in experimental literature.

To approximate the effect of this curvature in a simple, planar cell, a biasing stress gradient is added in the $y$-direction, modifying the force balance equation. This bias is added alongside the addition of heterogeneous perturbations $(\delta\underline{s}_n, \delta\dot{\gamma}_n)$ in linear stability analysis, as described in section 2.4. Equation 2.26 becomes:

$$\hat{\Sigma}(t)(1 + qh(y)) = G\underline{p} \cdot (\hat{\underline{s}} + \delta\underline{s}) + \eta(\hat{\dot{\gamma}} + \delta\dot{\gamma}), \tag{2.31}$$

where $h(y) = \sum_k h_k \cos(ky)$. It is assumed here that $h_k \neq 0$ only for $k = \frac{\pi}{L}$ (*i.e.* curvature only effects the lowest mode across the cell). This adds a curvature term to the right-hand side of equation 2.29, which becomes:

$$\partial_t \delta\underline{s} \;=\; \left(\underline{\underline{M}}(t) - \frac{G}{\eta}\underline{qp}\right) \cdot \delta\underline{s} + \frac{qh_k\Sigma(t)}{\eta}\underline{q}. \tag{2.32}$$

where, as before, $\underline{\underline{M}}(t) = \partial_{\underline{s}}\underline{Q}|_{\hat{\underline{s}},\hat{\dot{\gamma}}}$, $\underline{q} = \partial_{\dot{\gamma}}\underline{Q}|_{\hat{\underline{s}},\hat{\dot{\gamma}}}$ and the scalar $q$ defines the magnitude of *toy* curvature added as a stress gradient to the planar cell. Note that the scalar $q$ (for curvature) and vector $\underline{q}$ are distinct quantities.

*Toy* curvature adds spatial variation to the material stress within the flow cell, enabling the assessment of the emergence of any shear band formation during measurement. It is a constant stress gradient (in time) and does not account for any mechanical noise (caused during initialisation, or imperfections in the measurement environment in the duration of the protocol) that may add random (Brownian-like) heterogeneous kicks to the material and also play a role in triggering shear banding instabilities [76]. This is perhaps a shortcoming of solely using toy curvature as a seed for heterogeneity in the constitutive model, however I found that adding noise or imposing *toy* curvature had qualitatively the same effects. I found the addition of random perturbations in the LAOS protocol resulted in a noisy oscillatory sig-

nal. I therefore favour the *toy* curvature approach throughout the LAOS studies in this thesis. In chapter 6 I revisit the shear startup protocol and employ noise (in the form of continuous random perturbations) in order to compare my results with previous simulations [32]. I therefore define random noise as a seed to heterogeneity in the same form as in reference [32]:

**Random initial condition** A random number from distribution between $-0.5$ and 0.5 is drawn each time the addition of noise is added to the numerical system. In the case of the addition of noise solely upon initialisation:

$$\underline{s}(y, t = 0) = q\underline{X}\cos(\pi y/L). \tag{2.33}$$

An infinitesimally small kick $\underline{\delta s}_k = q\underline{X}$ where $q$ here is the magnitude of the imposed noise and $\underline{X}$ is the distribution of random numbers between $-0.5$ and $+0.5$. This seeds an initial spatial heterogeneity in the material sample and is left to evolve (leading to growth or decay) as governed by the constitutive equations.

**Continuous random noise** Alternatively, randomly noise may be added every numerical timestep. Here,

$$\underline{s}(y, t + dt) = \underline{s}(y, t) + q\sqrt{dt}\underline{X}\cos(\pi y/L), \tag{2.34}$$

where again $q$ defines the noise magnitude, $\underline{X}$ is the distribution of random numbers between $-0.5$ and $+0.5$. It is this approximation of mechanical noise that is employed in the numerics of chapter 6.

## Aside: mistaken shear banding for strong stress gradients

The imposition of a stress gradient onto the flow may cause smooth, bowed velocity profile signatures. Indeed, for a high stress gradient, these have been mistaken for shear banded profiles [4, 152].This confusion of these smooth bowed profiles is born of the wider range of shear rates available to the material with the imposed stress gradient and does not correspond to the formation of distinct regions of shear

banded flow [4]. Larger curvature in the rheometer cell affects the plateau-like region of the material flow-curve: otherwise weakly-increasing slopes (within the plateau-like region) of the monotonic flow curve may become steeper with an increased stress gradient across the cell [4]. Steady state stress values for imposed shear rates within the weakly increasing plateau-like region of the flow curve may be slightly higher or lower than expected from a flat cell. It is here that the steady state velocity profiles are bowed due to curvature-imposed stress gradients, not shear banded.

Throughout the studies carried out within this thesis I found the imposition of toy cell curvature to the nonlinear flows required an additional caveat to account for the effect of curvature when assessing the significance of heterogeneity that formed in the resultant flow. As a precaution to this, I accounted for the influence of cell curvature by defining regions of significant shear banding in the flow to also satisfy $\delta\sigma/G > q$, *i.e.* the growth in heterogeneous perturbations to the polymer shear stress component of the linearised equations must exceed the curvature ratio of the cell.

## 2.6 Rolie-Poly model

In section 2.2 the Rouse model for studying the dynamics of a polymer chain was briefly introduced. In this section I describe a constitutive model based on the *tube theory* [36, 48, 127] where a polymer - a chain of repeating monomer units - is described by its *primitive path*. This describes the shortest path from the end-to-end of the polymer chain with the same topology of the tube. The original chain may therefore be much longer than the primitive path if it were to be pulled out to its full extension. For entangled polymeric fluids, each polymer chain forms part of entangled network where each chain restricts the free movement and orientation of its neighbours. Any individual polymer can freely move along its own length (or *reptate* [36], so called due to its 'snake-like' motion), but is constrained in perpendicular directions by a *tube* of entanglement-point confinements. This forms the basis for the *tube theory* [36, 48, 127]. A schematic of the tube of confinements surrounding a polymer chain in figure 2.5(a), blue dots represent the entanglement points of surrounding chains in the entanglement network. In figure 2.5(b) the polymer chain is described instead by its primitive path.

The extent of entanglement within a polymeric fluid is quantified by the entanglement number $Z$. This is an experimentally measurable quantity that depends on the molecular weight and entanglement weight of the material. The molecular weight $M_w$ is determined during polymerisation but the entanglement weight $M_e$ is an intrinsic material property. $Z$ is defined such that $Z = M_w/M_e$ and the tube surrounding the polymer chain consists of $Z$ segments spanned by $s \in (0, Z)$. Note here $s$ is used as a parametric counting parameter along the length of the polymer chain, not the general vector $\underline{s}$ used in earlier sections. In the constitutive model described here, based on tube theory, the position vector of tube segment $s$ at time $t$ is described by $\underline{R}(s,t)$ and the material relaxation times are related to $Z$ such that:

$$\tau_d = 3Z\tau_R = 3Z^3\tau_e,$$

$$\tau_R = Z^2\tau_e$$

where $\tau_e$ is defined in the tube theory by the Rouse time of a chain of length equal to one entanglement. $\tau_d$ is the full chain relaxation timescale and $\tau_R$ is the Rouse time, on which chain stretch relaxes. Sufficiently well entangled polymers have well separated relaxation timescales such that $\tau_d \gg \tau_R \gg \tau_e$.

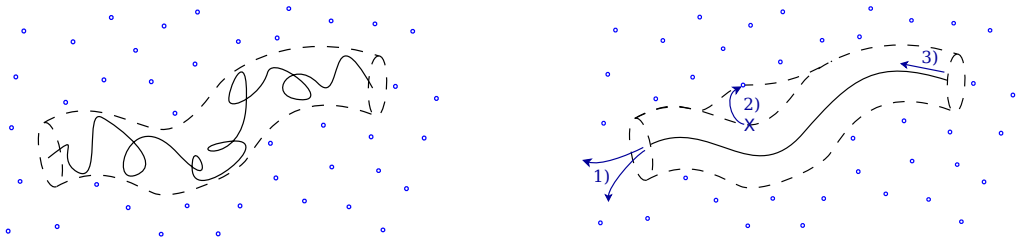


(a) (b)

Figure 2.5: A schematic diagram of the polymer dynamics captured by the Rolie-Poly model: (1) reptation, (2) convective constraint release and (3) chain retraction. Reprinted with permission of R. L. Cooke [32].

The numbered processes in figure 2.5(b) describe the relaxation mechanisms of the polymer chain as described by the GLaMM model for linear entangled polymers [75]. The GLaMM model derived a stochastic constitutive model for the microscopic dynamics of linear entangled polymers with position vector $\mathbf{R}(s,t)$. In full, the equation is:

$$\mathbf{R}(s,t+\Delta t) = \mathbf{R}(s,t) + \Delta\xi(t)\frac{Z}{Z^*(t)}\frac{\partial \mathbf{R}}{\partial s} + \frac{\Delta\xi(t)^2}{2}\frac{Z^2}{Z^*(t)^2}\frac{\partial^2 \mathbf{R}}{\partial s^2} \tag{2.35}$$

$$+\Delta t\Big[\mathbf{K}\cdot\mathbf{R} + \frac{3\nu}{2}\frac{a}{|\mathbf{R}\prime(s)|}\mathbf{R}''(s) + \tilde{g}(s,t) + \frac{1}{2\pi^2\tau_e}\left(\mathbf{R}'\frac{\partial}{\partial s}l(\mathbf{R}'\cdot\mathbf{R}')\right)\Big], \tag{2.36}$$

where $Z^*(t)$ is the instantaneous number of entanglements. The second and third terms on the right-hand side describe *reptation*: the curvilinear diffusion of the entire chain along its own contour (motion (1) in figure 2.5(b)) where $\Delta\xi(t)$ describes the displacement of the chain along the tube due to Brownian motion (reptation). The polymer reptates out of the original tube on a timescale $\tau_d$. The fourth term describes the effect of convection in the flow. The fifth and sixth terms correspond to the constraint release mechanisms due to convection, modelled as a series of Rouse

tube hops assumed to occur at an equal rate at all points along the chain, and to random events, respectively. This mechanism is described in figure 2.5(b) by motion (2). The seventh term describes chain retraction arising from Rouse motion of the chain inside the tube (shown by motion (3)). Retraction thus does not depend on tube constraints themselves and occurs on the timescale of the Rouse time ($\tau_R$).

Each of these time-dependent mechanisms relax the polymer stress. Polymer chains that reptate out of the tube constraints are then free to choose their own isotropic distribution (and thus chain orientation relaxes on the timescale of reptation, $\tau_d$). Within the linear regime, it is the reptation events of surrounding polymer chains that causes the tube constraint release. The constraint release mechanism includes the possibility that whenever a chain-end segment passes through a tube segment, the constraint that is then lost from the tube (once the polymer chain no longer occupies that tube segment) may in turn release an entanglement point on a neighbouring chain. That is, the neighbouring chain is free to explore a wider region in space via its own lateral reptation motion.

Constraint release events occur within the linear and nonlinear regime. It was predicted in the original Doi-Edwards model that 'reptative' or 'thermal' constraint release within the linear regime occurs on a relatively negligible lengthscale and thus negligible timescale when compared with the relaxation of whole chain dynamics. However, constraint release from contour length fluctuations (due to the end-chain segments undergoing faster relaxation than mid-chain segments) can be a significant for moderately entangled polymers even in linear flow. Once in the nonlinear flow regime ($\dot{\gamma} > 1/\tau_d$), constraint release becomes an increasingly significant relaxation mechanism through retraction [122] and the convective flow. In the nonlinear regime, this mechanism is thus known as Convective Constraint Release (CCR). Recall that it is within this regime that the original DE-theory begins to fail and thus more complex dynamics are assumed to be occurring within the flow. Indeed, CCR is the dominant relaxation mechanism in the regime of $1/\tau_d \ll \dot{\gamma} \ll 1/\tau_R$.

In previous studies [91, 129] constraint release events in the nonlinear regime have been assumed to be of microscopic origin, where the relaxation time depends on the molecular-level response to imposed deformation. In the GLaMM model

is was suggested that this method of inclusion of the relaxation mechanism does not hold with the assumption that constraint release itself acts in a global manner thus neglecting any detail smaller than the lengthscale of the whole polymer chain. Instead, the GLaMM model followed the previous work of Likhtman et al. [109] and Milner et al. [133], conceptualising the constraint release mechanism as a behaviour of the tube itself, treating constraint release as a localised Rouse-like tube-hopping motion. Moreover it was speculated the constraint release events are dependent upon chain retraction. A number of retraction events are required before one tube hop of the magnitude of one tube diameter is achieved and there is thus an effective efficiency of CCR built into the final version of the model.

The relaxation mechanism via convective constraint release (*i.e.* constraint release in the nonlinear regime) can also relax chain stretch: the Rouse-like tube hops within the chain length are influenced by the existence of chain stretch. Chain stretch occurs when the length of occupied tube exceeds its equilibrium value. It relaxes on the timescale of Rouse time, $\tau_R$. The inclusion of chain stretch into the tube model enabled the short-time transient behaviour of polymers during startup to be better captured. If the stretch is caused by the local entrapment of the polymer chain by a neighbouring chain, it is energetically favourable to release the entanglement point via constraint release. It thus follows that in the constitutive model, the convective constraint release mechanism will have some dependence on the local potential (due to stretch) of the polymer chain. Chain stretch also has an effect on reptation: stretch increases the monomer-to-monomer length within the chain and thus effectively accelerates the reptation of the chain along the tube.

The GLaMM model takes into account the full relaxation dynamics of a spectrum of timescales (and indeed lengthscales) of the polymer chain. This model is complex and computationally expensive, therefore, in reference [110] a one-mode approximation to equation 2.35 was derived. The so-called ROuse LInear Entangled POLYmers (or Rolie-Poly) model described the microscopic dynamics of linear polymers for one fixed relaxation time and modulus $\tau = \tau_d$ (the longest timescale of polymer relaxation) and $G$. It was developed as a simplified version of the GLaMM model to describe spatially inhomogeneous flows and flows in more complex rheome-

ter geometries. In the generalised constitutive model defined in equation 2.16, $\underline{s} = (\sigma_{xy}, \sigma_{yy}, \dots)^T$ and the model-specific governing equation $\partial_t \underline{s} = \underline{Q}(\underline{s}, \dot{\gamma})$ is defined below.

In its full tensorial form, the governing equation for the RP model (in homogeneous flow) is:

$$\partial_t \underline{\underline{\sigma}} = \underline{\underline{K}} \cdot \underline{\underline{\sigma}} + \underline{\underline{\sigma}} \cdot \underline{\underline{K}}^T - \frac{1}{\tau_d}(\underline{\underline{\sigma}} - \underline{\underline{I}}) - \frac{2(1-A)}{\tau_R}[\underline{\underline{\sigma}} + \beta A^{-2\delta}(\underline{\underline{\sigma}} - \underline{\underline{I}})], \tag{2.37}$$

where $A \equiv \sqrt{\frac{3}{T}}$, $T \equiv \mathrm{tr}\underline{\underline{\sigma}}$ is the chain stretch in system. $\underline{\underline{K}}$ is the deformation rate tensor. The four expressions correspond to advection, reptation, chain retraction, and CCR, respectively. Timescales $\tau_d$ and $\tau_R$ are related by the number of entanglements on a chain, $Z = \frac{\tau_d}{3\tau_R}$. $\delta$ is related to the convective constraint release (CCR), following reference [110] I set $\delta = -\frac{1}{2}$ throughout this thesis. $\beta$ is a parameter that describes the efficiency of CCR in the system such that $0 \leq \beta \leq 1$. When considering the full nonlinear dynamics of spatially heterogeneous flows, the diffusive term, defined in equation 2.17 is added to the right-hand side of equation 2.37.

Equation 2.37 can be simplified further in the limit that chain stretch occurs infinitely quickly. In this limit, $T \to 3$ and equation (2.37) reduces to:

$$\partial_t \underline{\underline{\sigma}} = \underline{\underline{K}} \cdot \underline{\underline{\sigma}} - \frac{1}{\tau_d}(\underline{\underline{\sigma}} - \underline{\underline{I}}) - \frac{2}{3}\mathrm{tr}(\underline{\underline{K}} \cdot \underline{\underline{\sigma}})[\underline{\underline{\sigma}} + \beta(\underline{\underline{\sigma}} - \underline{\underline{I}})], \tag{2.38}$$

For the case of imposed simple shear flow, the tensorial equations (2.37) and (2.38) can alternatively be written in component form, where $\underline{\underline{\sigma}} = \{\sigma_{xy}, T, \sigma_{yy}\}$, the full stretching Rolie-Poly model (sRP) becomes:

$$\begin{aligned}
\partial_t T = &\quad 2\dot{\gamma}\sigma &&- \frac{1}{\tau_d}(T-3) &&- \frac{2(1-A)}{\tau_R}[T + \beta A(T-3)], \\
\partial_t \sigma = &\quad \dot{\gamma}\sigma_{yy} &&- \frac{1}{\tau_d}\sigma &&- \frac{2(1-A)}{\tau_R}(1+\beta A)\sigma, \\
\partial_t \sigma_{yy} = &\quad &&- \frac{1}{\tau_d}(\sigma_{yy}-1) &&- \frac{2(1-A)}{\tau_R}[\sigma_{yy} + \beta A(\sigma_{yy}-1)],
\end{aligned} \tag{2.39}$$

and the non-stretching case (nRP):

$$\begin{aligned} \partial_t \sigma = &\quad \dot{\gamma}[\sigma_{yy} - \frac{2}{3}(1+\beta)\sigma^2)] - \frac{1}{\tau_d}\sigma, \\ \partial_t \sigma_{yy} = &\quad \frac{2}{3}\dot{\gamma}[\beta\sigma - (1+\beta)\sigma_{yy}\sigma] - \frac{1}{\tau_d}(\sigma_{yy} - 1), \end{aligned} \tag{2.40}$$

where now only two dynamical variables are required. Again, note here that these equations apply for homogeneous shear flow.

It is these component-forms of the RP model that I apply in the results presented within this thesis. I consider both the stretching and non-stretching limit and employ the numerical techniques to evolve the constitutive equations that are outlined in Appendix I (section 2.7).

## 2.7 Appendix I: Numerical methods

This section outlines the numerical methods used to solve the constitutive equations detailed in this thesis [146]. Note in all cases the material sample within the shearing cell is constrained to be homogeneous in the $x$ and $z$ directions. In this section I first consider the case where a sample is constrained to remain homogeneous in the flow gradient direction. There is no spatial variation and hence the system will only evolve in time. Here I discard tensorial notation for the constitutive equations and focus on a scalar model example, with a single dynamical variable $\phi$ . It is assumed that all the spatial components will start from some initial state $\phi(t = 0) = 0$ and evolve from this state. Numerically, this is studied using simple Euler time-stepping to integrate the constitutive equations in time. This is illustrated here for a single degree of freedom $\phi(t)$, where $\partial_t\phi(t) = \psi(\phi(t))$ for some dynamical variable $\psi(\phi(t))$, but the method easily generalises for many coupled ordinary differential equations. Using the fundamental theorem of calculus we have:

$$\frac{\phi(t + dt) - \phi(t)}{dt} = \psi(t). \tag{2.41}$$

Discretising time into $n$ timesteps of size $dt$, such that $t = ndt$ for $n = 0, 1, 2, ...$, (2.41) can be written as:

$$\frac{\phi^{n+1} - \phi^n}{dt} = \psi^n. \tag{2.42}$$

This is the 'Explicit Euler' method [146], where the next timestep at $n + 1$ is completely determined by the state of the system at timestep $n$.

Allowing for the possibility of shear banding in the flow requires spatial dependence to be introduced throughout the governing equations. Thus, the equation becomes $\partial_t\phi(t) = \psi(\phi(t), \dot{\gamma}) + D\partial^2\phi(t)$. Whilst the explicit Euler method could be applied again to solve this, a more numerically stable method to employ is the Crank-Nicholson algorithm [146]: Consider the discretisation of $y$: $j$ spatial steps of size $dy$, such that, for cell size $L$, $y = jdy$ for $j = 1, 2, ..., J$. Then, taking steps

either size of $y$ in the function $\phi$ and performing a Taylor expansion, we have:

$$\phi(y+dy) = \phi(y) + \phi'(y)dy + \frac{1}{2}\phi''(y)(dy)^2 + O(dy)^3, \tag{2.43}$$

$$\phi(y-dy) = \phi(y) - \phi'(y)dy + \frac{1}{2}\phi''(y)(dy)^2 + O(dy)^3, \tag{2.44}$$

gives

$$\phi''(y) = \frac{1}{(dy)^2}\left(\phi(y+dy) - 2\phi(y) + \phi(y-dy)\right). \tag{2.45}$$

For the diffusive part (ie. $\partial_t\phi(t) = D\partial^2\phi(t)$), we again discretise $t$ with $n$ timesteps of size $dt$ ($n = 0, 1, 2...$) and the Crank-Nicholson algorithm averages over all neighbouring spatial steps to point $y$, for the current and following timesteps ($t$ and $t + dt$):

$$\frac{\phi_j^{n+1} - \phi_j^n}{dt} = \frac{D}{2(dy)^2}\left[(\phi_{j+1}^{n+1} - 2\phi_j^{n+1} + \phi_{j-1}^{n+1}) + (\phi_{j+1}^n - 2\phi_j^n + \phi_{j-1}^n)\right]. \tag{2.46}$$

The 'shearing cell', defined for $y\epsilon\{0, L\}$, $j = 1...J$, thus requires the points $j = 0$ and $j = J + 1$ to describe $y = 0, L$ respectively in (2.46) which do not exist. Prescribing the boundary condition $\partial_y\phi = 0$ resolves this problem; these 'phantom' points are defined as those mirrored just inside the boundary at $j = 2, J - 1$. Therefore (2.46) may be re-written in vector form (where $\underline{\phi}$ denotes $\phi\forall j\epsilon\{1, J\}$) as follows:

$$\underline{\phi}^{n+1} - \underline{\phi}^n = \frac{Ddt}{2(dy)^2}\underline{\underline{C}}\left(\underline{(\phi)}^{n+1} - \underline{\phi}^n\right), \tag{2.47}$$

or, more instructively:

$$\underline{\phi}^{n+1} = \left[\underline{\underline{I}} - \frac{Ddt}{2(dy)^2}\underline{\underline{C}}\right]^{-1}\left[\underline{\underline{I}} + \frac{Ddt}{2(dy)^2}\underline{\underline{C}}\right]\underline{\phi}^n, \tag{2.48}$$

where

$$\underline{\underline{C}} = \begin{pmatrix} -2 & 2 & 0 & 0 & & & \dots & 0 \\ 1 & -2 & 1 & 0 & 0 & & \dots & 0 \\ & & & \ddots & \ddots & \ddots & & \\ & & & & & 1 & -2 & 1 \\ 0 & & & & 0 & 0 & 2 & -2 \end{pmatrix} \tag{2.49}$$

and the matrix on the left hand side of (2.47) is inverted using the Thomas algorithm for tridiagonal matrices [145].

Evolving $\psi$, the system is determined at each timestep by first locally updating the reaction terms at each point using explicit Euler, then the diffusive terms using Crank Nicholson. Finally, to describe the state of the system, force balance ($\partial_y \Sigma = 0$) must be enforced. Here the local shear rate, $\dot{\gamma}(y,t)$, is updated at each timestep, thus allowing for the possibility for shear banding across the cell. Equating the terms, force balance is numerically implemented at each spatial step as:

$$\dot{\gamma}_j = \bar{\dot{\gamma}} - \frac{G}{\eta}(\bar{\sigma} - \sigma_j), \tag{2.50}$$

where the over-bars indicate spatially-averaged values. It is important to note here the following inequality relations:

$$\sqrt{2Ddt} < dy \ll l \ll L, \tag{2.51}$$

where $l = \sqrt{D\tau_0}$ defines the interface width between the shear bands in the shearing cell (for the microscopic relaxation time of the system, $\tau_0$). This interface width must be sufficiently narrow compared to the width of the cell itself, and large enough compared to the spatial stepsize that it is effectively resolved numerically. These relations are described in the second two inequalities in (2.51). The first of these inequalities is required to ensure the stability of the Crank-Nicholson algorithm used in the above numerical formulation.

Further to these numerical iterations, the results must be checked for convergence in both time and space. In other words, the results must be independent of the stepsizes used, $dt$ and $dy$ [32]. For time, this is confirmed by halving the timestep and comparing the results; for space, the time convergence must be performed at both $dy$ and $\frac{dy}{2}$, then compared to ensure successful convergence. If unsuccessful, the spacestep is decreased and the convergence checks repeated.

# 3

# Existing studies on time-dependent protocols: shear startup and step stress

In this chapter I give a detailed review of the existing literature concerning shear banding in time-dependent flows of entangled polymeric solutions and melts. A succinct review of this, as well as the results from the studies here in chapters 4 and 5 is given in a short précis by Prof. Suzanne Fielding, submitted for review as part of a special edition of the Journal of Rheology, focussing on the shear banding phenomenon [64].

Although LAOS protocols have attracted a lot of interest in recent years, the existence of shear banded flow within the material response to the LAOStrain or LAOStress protocol has rarely been considered, though exceptions can be found in [4, 187, 188]. In this chapter I reproduce results from previous studies on shear banding in time-dependent flows. These flows are simpler than LAOS to introduce

the concepts of the formation of shear bands that will be built on in subsequent results chapters. I discuss two forms of shear banding: transient shear banded flow which regains homogeneity at steady state and persistent, steady state shear banding. The study of these time-dependent heterogeneous behaviours will then underpin the understanding of the emergence of shear banding in the LAOS protocols: these more complex protocols have a sustained time-dependence and thus a 'steady state' is not met and rather continually time-dependent material responses are observed.

Starting with the shear startup protocol, I reproduce the results of Moorcroft and Fielding [135, 136]. These confirm the existence of time-dependent shear banding even in materials that have a monotonic constitutive curve and thus do not exhibit heterogeneity at the steady state. I also confirm the criteria derived in [135] to predict the onset of instability to the formation of shear bands during the time-dependent protocol. Following this, I consider a simplified caricature of LAOStrain using a series of fixed end-strain shear startup protocols to approximate an oscillatory protocol. This provides an insight into the time-dependent material susceptibility to form shear banded flow in the LAOStrain protocol.

I then look at the step stress protocol. Again, I reproduce the results of Moorcroft and Fielding [135, 136] and find transient shear banding within the time-dependent material response on the approach to the steady state. The criterion for the onset of shear banded flow (derived in [135]) is indeed coincident with the regions of shear banded flow within this time-dependent material flow.

Both of these time-dependent simple protocols are modelled here using the non-stretching limit of the Rolie-Poly (RP) model for entangled linear polymer solutions and melts. In this chapter, material response curves are presented in conjunction with the calculation of the eigenvalue evolution for the linearised system (found from the stability matrix in linear stability analysis, see chapter 2). In calculations that allow for spatial heterogeneity, the magnitudes and spatial profiles of any shear bands that may form during the protocols are also shown. Though chain stretch is not included here, very similar behaviours are seen when the full stretching version of the RP model is instead employed. Indeed, the results shown here hold provided the imposed shear rate $\dot{\gamma} \ll 1/\tau_R$, where $\tau_R$ is the chain stretch relaxation time.

# 3.1 Shear startup

## 3.1.1 The shear startup protocol

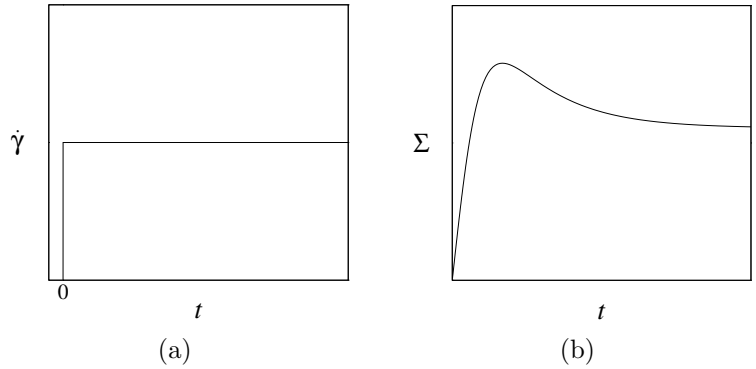


Figure 3.1: The shear startup protocol: in (a), constant shear rate imposed at time $t = 0$. In (b), the shear stress response of a material to the imposed shear rate.

As previously defined in chapter 2, in the shear startup protocol a chosen shear rate ($\dot{\gamma}$) is applied at a time $t = 0$ and held constant for all $t > 0$. The material sample is initially at rest and is well relaxed. The initial response to the imposed deformation is time-dependent; steady state is later reached once the stress is unchanging with increasing time. Simple illustrations of the shear startup protocol and the associated shear stress time-dependent response on the approach to the steady state are shown in figure 3.1.

In figure 3.1(b), there is an overshoot ($\frac{\partial \Sigma}{\partial t} < 0$) in the measured shear stress response, on the approach to the steady state. This is a characteristic feature of a time-dependent stress response during the shear startup protocol due to a competition between early-time elastic response and long-time flowing behaviour. This overshoot in time (or equivalently strain, as $\gamma = \bar{\dot{\gamma}}t$ and $\bar{\dot{\gamma}}$ is fixed) has been shown to be linked to transient shear banding in a number of complex fluids [2,134–136].

## 3.1.2 Steady state constitutive curve

In a theoretical calculation, the underlying constitutive curve of a material can be built up by imposing a fixed shear rate, $\bar{\dot{\gamma}}$, and recording the shear stress value at the

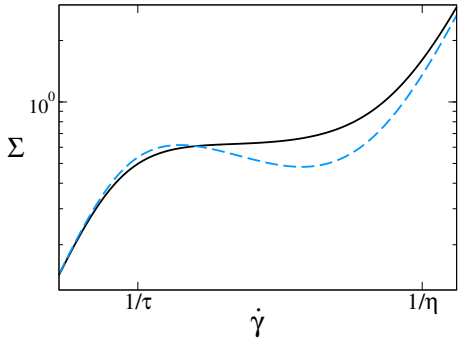


Figure 3.2: Homogeneous steady state constitutive curves, formed from a series of shear start up protocols, using the Rolie-Poly model. Stretching effects are ignored. The blue-dashed line has non-monotonic features (*i.e.* $\partial_{\dot{\gamma}}\Sigma < 0$) over a window of shear rates; the black-solid line is monotonic. Here, the blue line has CCR-parameter $\beta = 0.4$; the black line has $\beta = 1.0$; both curves have solvent viscosity $\eta = 10^{-3}$.

steady state, where the flow is constrained to be homogeneous with an enforced a uniform flow gradient across the rheometer cell. Imposed $\bar{\dot{\gamma}}$ span the full relaxation spectrum of the polymer in question, from $\dot{\gamma} \ll \frac{1}{\tau_d}$ to $\dot{\gamma} \gg \frac{G}{\eta}$, the inverses of the largest and smallest relaxation timescales of the polymeric fluid in this model. Following each imposed $\bar{\dot{\gamma}}$, the material is allowed to fully relax (the system is reinitialised) before subsequent shear rates are applied.

Figure 3.2 shows a non-monotonic (blue-dashed line) and monotonic (black-solid line) underlying constitutive curve for two polymeric fluids as modelled by the non-stretching Rolie-Poly (nRP) model. The decreasing region of stress with shear rate in the non-monotonic constitutive curve has been shown to lead to steady state shear banded flow [185] and has been observed in linear entangled polymers [107, 108, 152, 173, 179, 180], star polymers [158]. tri-block copolymers [15, 120], lamellar sufactant phases [161], foams [154], emulsions [33], microgels [46], carbopol gels [44] and wormlike micelles [16, 77, 87, 104, 160]. However, as introduced briefly above, shear banding may also arise transiently during startup even in materials that do not shear band at the steady state, due to a monotonic underlying constitutive curve, as seen in theoretical [2, 65, 92, 121, 123, 134–136] and experimental studies [17–20, 88, 151, 152, 173].

In the following section, I examine in further detail the time-dependent shear stress response to the shear startup protocol for a fixed $\bar{\dot{\gamma}}$ that lies within the non-monotonic or plateau region of these material constitutive curves. For both a non-

monotonic and monotonic underlying steady state constitutive curve, I consider the evolution of any heterogeneous shear band formation and the analytically-calculated eigenvalue (found from the linear stability analysis; recall chapter 2).

### 3.1.3 Transient and steady state banding in shear startup

Figure 3.3 shows a material response to the shear startup protocol for an imposed shear rate $\bar{\dot{\gamma}} = 30.0$. This reproduces the results of Moorcroft [32] but is my own work and numerically uses a weakly curved cell as a heterogeneous seed to the onset of shear banding, rather than randomly-distributed noise at each timestep. The purpose here in reproducing the results of Moorcroft is twofold: (i) to introduce the concepts of time-dependent shear banding in a simpler flow protocol and (ii) to provide a benchmark to check my own numerical code.

The top row of figure 3.3 shows results for parameters such that the material has a non-monotonic underlying constitutive curve ($\beta = 0.4$). The results in the bottom row have parameters such that the underlying constitutive curve is monotonic ($\beta = 1.0$). (a) and (e) show the shear stress response to the imposed shear rate. The blue-dashed line gives the stress response once heterogeneity is allowed. The black line shows the response for a flow profile that is constrained to be homogeneous. During this time-dependent response to the imposed $\bar{\dot{\gamma}}$, the stress overshoots in strain ($\frac{\partial \Sigma}{\partial \gamma} < 0$). The heterogeneous stress response can be clearly seen to relax at a faster rate than for the homogeneously-constrained system: allowing for heterogeneity enables the stress to relax more quickly after attaining the maximum stress (overshoot). The stress then continues to evolve until it reaches its steady state value. This time-dependent behaviour and overshoot signature occurs for both the non-monotonic and monotonic underlying constitutive curves. This overshoot is due to the short-time elastic effects of the material response to imposed shear. It is independent of any long-time steady state (viscous-dominated) behaviour. It has thus been termed the 'elastic instability' [135] to the formation of shear bands. It can indeed be seen to coincide with the growth of heterogeneity in the flow shown in the other data representations in figure 3.3, as described further here.

Plots (b) and (f) show the evolution of the eigenvalue (found from linear stability

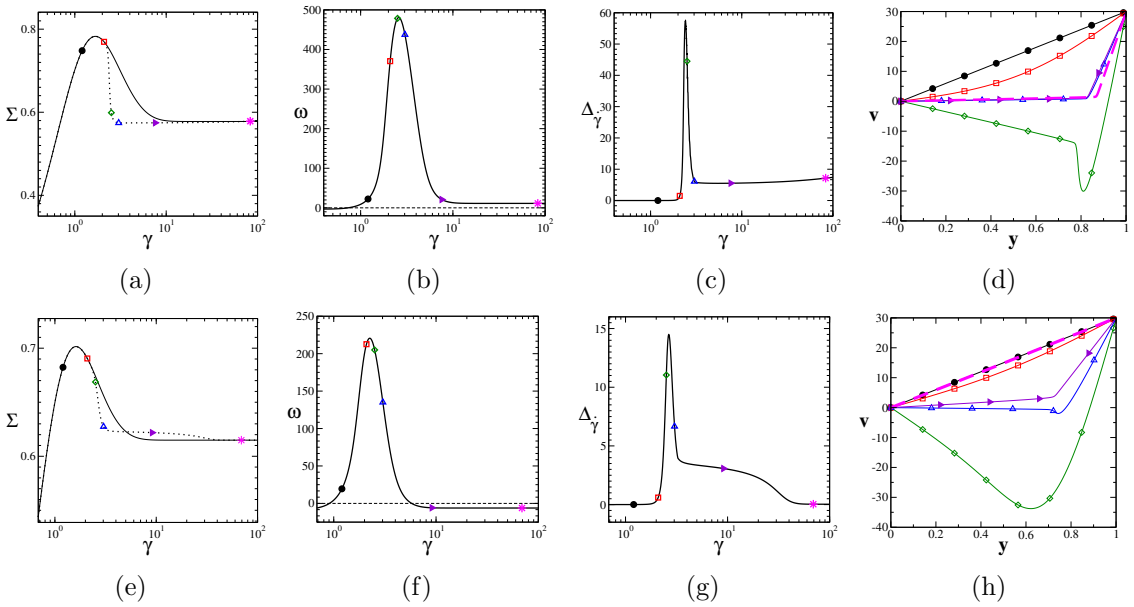


Figure 3.3: Transient stress, eigenvalue, degree of banding and velocity profiles resulting from an imposed shear startup protocol on the non-stretching Rolie-Poly model. A shear rate of $\dot{\gamma} = 30.0$ is applied with equation parameters: $\{\eta, J, l, q\} = \{10^{-4}, 512, 0.02, 10^{-4}\}$. The top row has CCR parameter $\beta = 0.4$ (non-monotonic constitutive curve) and the bottom row has $\beta = 1.0$ (monotonic constitutive curve).

analysis) for a material with a non-monotonic and monotonic constitutive curve respectively. The eigenvalue becomes positive, and strongly so, upon the approach to and after the elastic overshoot. Following the overshoot, the eigenvalue then quickly begins to decrease. Where the underlying constitutive curve is non-monotonic, the eigenvalue remains positive for all further times. In the case of the monotonic constitutive curve, however, the eigenvalue becomes quickly negative following the overshoot region of the stress response curve.

A positive eigenvalue indicates growth in the linear heterogeneous perturbations, thus predicting the onset of banding. If the eigenvalue becomes negative - as in the material with a monotonic constitutive curve here - material stability against shear banding is regained and any shear banded flow decays away. This behaviour is reflected in (c) and (g) where the time-dependent heterogeneity is quantified by the degree of banding. This is defined simply as the difference between the maximum shear rate magnitude and the minimum shear rate magnitude at any location in the

flow cell, normalised by the applied shear-rate, at each point in time:

$$\Delta_{\dot{\gamma}}(t) = \frac{1}{\bar{\dot{\gamma}}}\big[\dot{\gamma}_{MAX}(t) - \dot{\gamma}_{MIN}(t)\big], \tag{3.1}$$

Significant banding (where banding in the material is measurable) is defined as $\Delta_{\dot{\gamma}} > 5\%$. An initial peak in the degree of banding is seen after the overshoot in both cases of a non-monotonic and monotonic underlying constitutive curve. This coincides with the peak in positive eigenvalue. Shear banding can then be seen to decay away for the monotonic constitutive curve material where the eigenvalue is negative. However, for the material with a non-monotonic constitutive curve where the eigenvalue remains positive, appreciable shear banding persists even once a steady state flow is attained.

The coloured symbols in (a)-(c) and (e)-(g) reflect the times at which snapshots of the velocity profiles across the flow cell were taken. These profiles are shown in (d) and (h). The steady state is indicated by the thick magenta dashed line: steady state shear banding is seen in (d) where the underlying constitutive curve is non-monotonic. In (h) the underlying constitutive curve is monotonic and shear banded flow profiles are only seen for times shortly after the elastic overshoot in the startup curve; homogeneous flow is recovered at the steady state.

The results shown in figure 3.3(a)-(h) give a detailed insight into the material response to a constant imposed shear rate starting from an initial rest state. This is, however, only for one shear rate. To provide a comprehensive overview of the behaviour across a wide range of shear rates on the material constitutive curve, Moorcroft and Fielding presented a 'stability profile' [135, 136]. This profile was used to describe what behaviours the sample exhibits at the onset of instability to shear band formation during a shear startup experiment. This is reproduced here, although I replace the initial heterogeneous seeding of noise into the system (as used by Moorcroft) instead with a constant curvature to the cell, in figure 3.4. Each horizontal slice of the plane represents one shear startup experiment. The left-hand side marks the initialised (at rest) system and the steady state is reached at the right-hand side. Each startup experiment is performed for a homogeneously-constrained

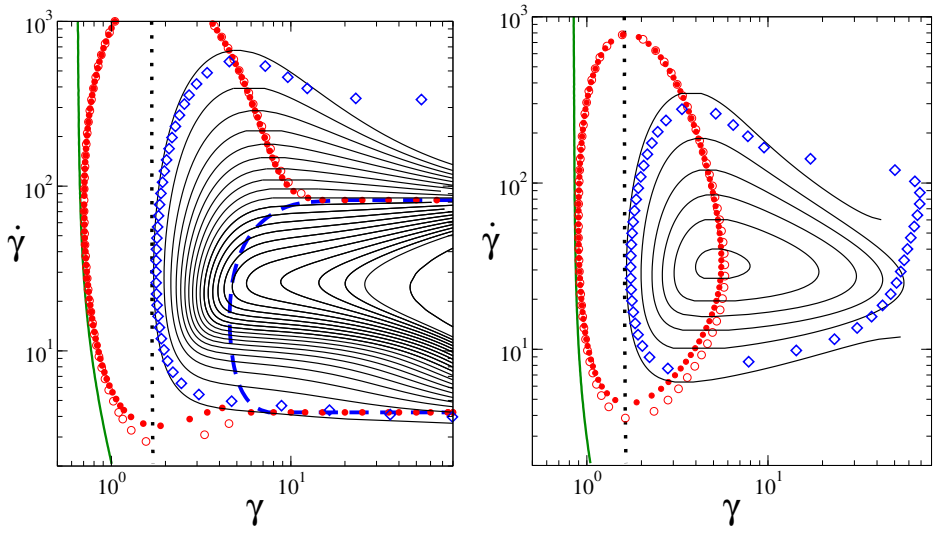


(a) $\beta = 0.4$ (b) $\beta = 1.0$

Figure 3.4: The stability profile for a series of shear startup protocols in the nRP model. Each horizontal slice of the graph represents one shear startup, for fixed $\dot{\gamma}$, plotted against strain $\gamma$. Red, open circles enclose the region of positive eigenvalue, where the 'full criterion' (eq. 3.4) for the onset of instability to the formation of shear bands in shear startup is satisfied; red, filled circles enclose the region where the 'reduced criterion' (eq. 3.8) is satisfied; the black-dotted line shows the time of the stress overshoot ($\partial_\gamma \Sigma < 0$); the green-solid line gives the 'elastic criterion' (eq. 3.5); the red dashed line in (a) indicates where the 'viscous criterion' (eq. 3.7) is satisfied; blue diamonds show where significant shear banding is measured ($\Delta_{\dot{\gamma}} > 5\%$) as measured by full nonlinear simulation, and the thin, black contours show the growth of linear perturbations (where each line marks a growth through $10^M$, $M \epsilon\ \mathbb{Z}; M \geq -2$).

system, where the growth of heterogeneity is measured by the integration of linearised equations (growth in the $\dot{\gamma}$-field) unless stated otherwise. This differs from the results shown in figure 3.3 where the constitutive model was evolved using full heterogeneous nonlinear simulations.

Recall from the linear stability analysis performed in chapter 2 on a general dynamical model with variables defined by the vector $\underline{s} = (\sigma,\ \sigma_{xx},\ \sigma_{yy},\ \ldots)^T$ [1], that infinitesimal heterogeneous perturbations to an initially homogeneous base state

[1] Recall the notation $\sigma = \sigma_{xy}$

obey:

$$\partial_t \delta \underline{s} = \left( \underline{\underline{M}} - \frac{G}{\eta} \underline{q}\underline{p} \right) \cdot \delta \underline{s}, \tag{3.2}$$

$$= \underline{\underline{P}} \cdot \delta \underline{s}, \tag{3.3}$$

where $\underline{\underline{M}} = \partial_{\underline{s}} \underline{Q}|_{\underline{\hat{s}},\hat{\dot{\gamma}}}$, and $\underline{q} = \partial_{\dot{\gamma}} \underline{Q}|_{\underline{\hat{s}},\hat{\dot{\gamma}}}$. Recall for the RP model, $\underline{s} = (\sigma,\ \sigma_{yy},\ T)^T$.

It was shown in [135] that the onset of instability to the formation of shear bands in the shear startup protocol occurs when the following criterion is satisfied:

$$\partial_\gamma \Sigma|_\gamma - \underline{p} \cdot \underline{\underline{M}}^{-1} \cdot \partial_\gamma \underline{s}|_{\dot{\gamma}} + \dot{\gamma} \partial_{\dot{\gamma}} \partial_\gamma \underline{s} < 0. \tag{3.4}$$

The region where this is satisfied for the chosen set of parameters in figure 3.4 is indicated by the open red circles. This region is also satisfied when the eigenvalue (found from the stability matrix) is positive.

At short times, the response of the system is predominantly elastic and therefore is dominated by strain, rather than strain-rate. Taking $\partial_{\dot{\gamma}} \to 0$, equation 3.4 reduces to:

$$-\underline{p} \cdot \underline{\underline{M}}^{-1} \cdot \partial_\gamma \underline{s}|_{\dot{\gamma}} < 0, \tag{3.5}$$

where $\underline{p} = (1, 0, 0)$ is the projection vector and $\underline{s} = (\sigma,\ \sigma_{yy},\ T)^T$, as above. For the non-stretching limit (as used in figure 3.4) where there are only two dynamical variables ($\underline{s} = (\sigma, \sigma_{yy})^T$), this reduces to:

$$-\mathrm{tr}\underline{\underline{M}} \partial_\gamma \Sigma|_{\dot{\gamma}} + \dot{\gamma} \partial_\gamma^2 \Sigma|_{\dot{\gamma}} < 0. \tag{3.6}$$

This is the *elastic* criterion for the onset of instability to the formation of shear banding in time-dependent flows.

The second term here accounts for the negative curvature of the stress as a function of strain as the overshoot (leading to $\partial_\gamma \Sigma < 0$) is approached. The elastic criterion is satisfied in figure 3.4 at the green line where the onset of the elastically-driven instability is captured. As seen in figure 3.4, the negative curvature may be significantly strong to cause linear instability ahead of the overshoot region (indicated by

the black dotted line).

Conversely, at long times it is the viscous behaviour associated with the strain-rate that dominates the flow. Indeed, at steady state the sample's behaviour no longer evolves as a function of time $t$ (or accumulated strain $\gamma$). Taking $\partial_\gamma \to 0$, equation 3.4 becomes

$$\partial_{\dot{\gamma}}\Sigma|_\gamma < 0, \tag{3.7}$$

which is satisfied within the region bounded by the red dashed line in figure 3.4.

Combining these elastic and viscous criteria gives the 'reduced criterion'

$$\partial_{\dot{\gamma}}\Sigma|_\gamma - \underline{p} \cdot \underline{\underline{M}}^{-1} \cdot \partial_\gamma \underline{s}|_{\dot{\gamma}} < 0. \tag{3.8}$$

This combined expression of the elastic and viscous criteria is shown in figure 3.4 by the red filled circles. It can be seen that the reduced criterion captures most of the information of the full criterion, without the more numerically and experimentally difficult cross-term in the equation 3.4.

These criteria and material signatures indicate the time-dependent material response to steadily applied shear. The well known steady state shear banding (viscous) criteria is recovered here for the case of a non-monotonic constitutive curve: the right-hand side of the plane represents the regions of banded and homogeneous flow at the steady state, for intermediate $\dot{\gamma}$ a region of steady-state shear banded flow (bounded by the blue-dashed line where the viscous criteria is also satisfied) is seen where the underlying constitutive curve is known to be non-monotonic. Significant shear banding is also seen for $\dot{\gamma}$ greater than that bounded by the viscous criterion dashed line. This is due to material metastability and is discussed in the following paragraphs. Significant transient heterogeneity is also seen for both the case of a non-monotonic *and* monotonic underlying constitutive curve even when (for the case of the monotonic constitutive curve) there is no shear banding at the steady state. This shows clear time-dependence in the material behaviour to externally imposed deformation in polymeric solutions and melts.

The thin black lines describe the growth of linear perturbations to the $\dot{\gamma}$-field during each startup experiment. As each contour line is crossed (from left to right)

there has been growth through $10^M$, $M\epsilon\ \mathbb{Z}; M \geq -2$. Equivalently, crossing the same contour again indicates a decay through $10^M$, $M\epsilon\ \mathbb{Z}; M \geq -2$. Contours are open-ended in figure 3.4(a) where shear banding persists to the steady state; in figure 3.4(b), contours are closed loops showing the decay to homogeneity at long times. There is, however, a discrepancy between the contour lines and the blue diamonds which calculate the degree of banding using full nonlinear dynamics. This is due to the breakdown of the linear approximation used in the calculation of the contour lines once the degree of shear banding becomes large. Linearised models can only predict the onset of instability to flow heterogeneity; they do not hold for the large amplitude limit.

Moreover there is a further discrepancy between both the contour lines (indicating steady state heterogeneity for the integrated linearised equations), the blue diamonds (signifying steady state shear bands in full nonlinear simulation) and the dashed-blue line which bounds the values of $\dot{\gamma}$ such that the viscous criterion is satisfied. This is due to the metastability of the underlying constitutive curve of the material: for applied $\dot{\gamma}$ within the non-monotonic region of the constitutive curve, the steady state stress achieved will be a stress plateau with $\Sigma = \Sigma_p$ (recall chapter 2). Allowing for heterogeneity in the material causes the material flow curve to exhibit a stress plateau at $\Sigma = \Sigma_p$ between the linearly-increasing high and low viscosity branches of the constitutive curve. This plateau region exists beyond the negatively-sloping region of the constitutive curve, until $\Sigma_p$ coincides with the linear low viscosity branch. This is therefore outside the regime in which the viscous criteria is satisfied. Indeed, for even larger $\dot{\gamma}$, where the corresponding steady state stress lies in the linear low viscosity branch of the constitutive curve, a return to homogeneous flow at the steady state is seen in figure 3.4(a).

In the following section of this chapter, I look to create a caricature of an oscillatory protocol using a series of positively- and negatively-shearing shear startup experiments. This creates a preliminary insight into the behaviour of polymeric solutions and melts in oscillatory flow, building on the intuition just developed for the simpler case of shear startup in this section. This will be studied in full in

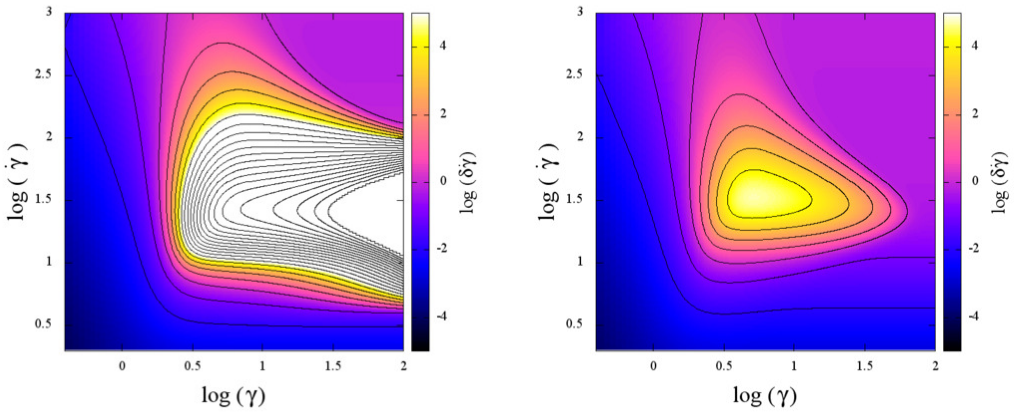


(a) $\beta = 0.4$ (b) $\beta = 1.0$

Figure 3.5: Trajectory colour maps for a material with non-monotonic ($\beta = 0.4$, (a)) and monotonic ($\beta = 1.0$, (b)) constitutive curve. As in figure 3.4, each horizontal slice is formed from one shear startup experiment with fixed $\dot{\gamma} = \dot{\gamma}_0$. The colour indicates the magnitude of heterogeneous perturbation growth to the initially homogeneous flow and is quantified by the scale on the right-hand side. The flow cell is curved with $q = 2 \times 10^{-3}$ and solvent viscosity is $\eta = 10^{-4}$. Note the growth of heterogeneous perturbations, and thus the contours, are cut-off above $10^4$. Contours are automated by gnuplot [184].

chapter 4 with the large amplitude oscillatory shear strain (LAOStrain) protocol. Furthermore, this preliminary study gives insight as to how that more complex protocol can be fundamentally understood through those simpler protocol response signatures.

## 3.2 Trajectory colour maps

In this section, I introduce a new data representation: trajectory colour maps. These maps give a visual description of the regions of instability to heterogeneous perturbations in an initially homogenous system during an experiment. As in figure 3.4, one startup experiment is represented by one horizontal line on the map, running from left to right. The thin black contour lines in figure 3.4 showed the growth of heterogeneous perturbations - as integrated with time from the linearised constitutive equations - across the $\dot{\gamma} - \gamma$-plane. In figure 3.5 this heterogeneous growth is instead represented as a continuous trajectory colour map and quantified by a

logarithmic colour scale shown to the right of each map.

Brighter regions in figure 3.5 indicate where the degree of shear banding, as calculated by integrating linearised equations, is largest. As shown in figure 3.4, this unstable region exists only transiently when the material has a monotonic underlying constitutive curve (in (b)), but persists to the steady state when the constitutive curve is instead non-monotonic (as in (a)).

### 3.2.1 Oscillatory caricature

Oscillatory strain-controlled flow (e.g. LAOStrain) can be crudely approximated by a top-hat function of imposed shear rate. Repeating a series of positively- and negatively-shearing startup protocols (where $\dot{\gamma} = \pm\dot{\gamma}_0$, alternates for fixed strain periods) approximates an oscillatory LAOStrain protocol where there is little time between the peak ($\dot{\gamma}_0$) and trough ($-\dot{\gamma}_0$) in the rate of the input signal. Note, the material is not allowed time to relax its stress between the change in shearing directions.

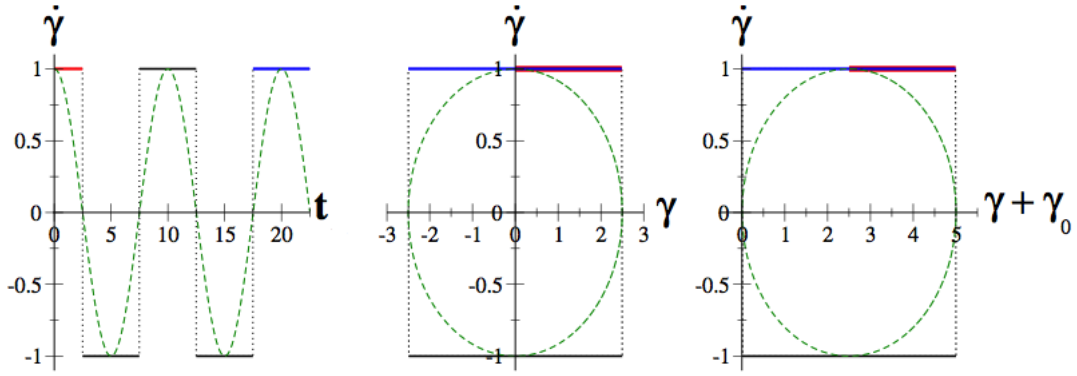


Figure 3.6: The shear startup protocol: $\dot{\gamma}(t) = \dot{\gamma}_0$ is applied until strain $\gamma_0 = 2.5$ is reached. The applied strain-rate is then reversed $\dot{\gamma}(t) = -\dot{\gamma}_0$, until $\gamma(t) = -\gamma_0$. This is repeated with each reversal in strain-rate occurring at $\gamma = |\gamma_0|$. From left to right, $\dot{\gamma}$ is plotted against $t$, $\gamma$ and $\gamma - \gamma_0$. The red and blue lines mark the first quarter- and last half-cycle where $\dot{\gamma}$ is positive, respectively. A series of these are used to form in the colour plots in figure 3.7.

Starting the system from rest (where the material is well relaxed), a constant strain-rate $\dot{\gamma}_0$ is applied for a period of time, $t$, until a desired end-strain, $\gamma_0 = \dot{\gamma}_0 t$,

is reached at time $t = t_{\max}$:

$$\dot{\gamma} = \dot{\gamma}_0, \tag{3.2.9a}$$

$$\gamma = \dot{\gamma}_0 t, \tag{3.2.9b}$$

$$t_{\max} = \frac{\gamma_0}{\dot{\gamma}_0}. \tag{3.2.9c}$$

This initial startup is shown in red in figure 3.6. Once the end strain ($+\gamma_0$) has been attained, the strain-rate is reversed $\dot{\gamma} \to (-\dot{\gamma})$ until the negative end strain ($-\gamma_0$) is reached. This process is repeated for a large number of cycles (where one cycle corresponds to one complete forward shearing and backward shearing motion) until time-translational invariance between two cycles is reached ($t \to t + T_{cycle}$). Figure 3.6 illustrates this oscillatory caricature for just a few cycles, representing the final forward shearing as a blue line.

In figure 3.7 I set the end strain to be $\gamma_0 = 2.5 \sim 10^{0.4}$. In figure 3.5(a) and (b) this end strain lies just within the region of instability to the formation of shear bands where heterogeneous perturbations are significant. It follows that for both the cases of non-monotonic and monotonic constitutive curve, shear bands will exist in the flow at $\gamma(t) = \gamma_0$ for a range of $\dot{\gamma}_0$.

The trajectory colour maps in figure 3.7 shows the magnitude of any growth of heterogeneous perturbations to the otherwise homogeneously-constrained system during the initial (red-line) and final (blue-line) oscillatory caricature as trajectory colour maps. The trajectories here are for positive $\dot{\gamma}$ and thus run from left to right across the plane. Though not shown here, identical information for negative $\dot{\gamma}$ is seen for trajectories running from right to left in the plane; this is due to the symmetry of the protocol within this time-translational invariant state.

The left-hand plots show the perturbation growth from rest during the initial startup (shown in red in figure 3.6). Heterogeneous growth can be seen for both the non-monotonic (a) and monotonic (b) constitutive curve, indicated by the colour transition from the blue to the yellow end of the logarithmic colour scale as the strain approaches the fixed end-strain. Recall $\gamma_0$ indeed lies just within the bright

region of instability to heterogeneous perturbation growth in figure 3.5, hence shear banding is seen for strains near the end-strain in figures 3.7(a) and (b) (left).

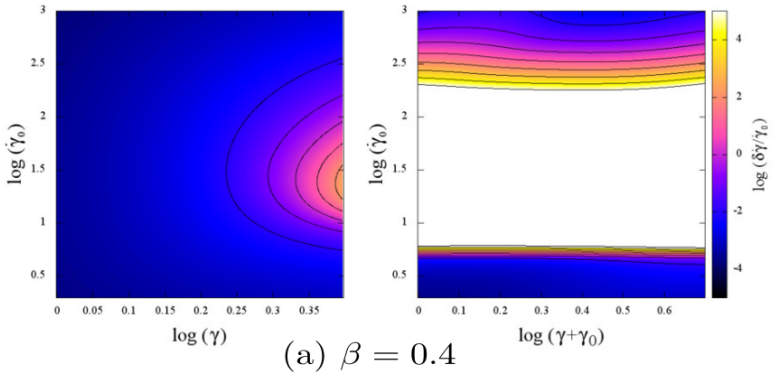


(a) $\beta = 0.4$

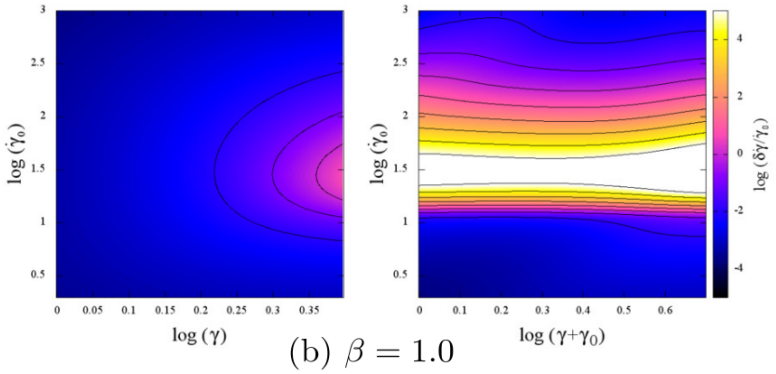


(b) $\beta = 1.0$

Figure 3.7: The linear perturbation growth during a series of shear startups. (a) has a non-monotonic constitutive curve, with $\beta = 0.4$; (b) has a monotonic constitutive curve, with $\beta = 1.0$. All are performed in a theoretical curved cell and have parameters $\{\eta, q\} = \{10^{-4},\ 10^{-4}\}$. The left-hand plots of (a) and (b) are the initial shear startup for each $\dot{\gamma}_0$ (the red line in figure 3.6); the right-hand plots are measured after 10 cycles of imposed $\dot{\gamma}_0$ (the blue line in figure3.6). The colour scale on the right-hand side of the figures indicates the value of $\log(\frac{\delta\dot{\gamma}}{\dot{\gamma}_0})$; with $\frac{\delta\dot{\gamma}}{\dot{\gamma}_0}$ capped at $10^4$.

The right-hand plots show the corresponding results for the final forward-strain cycle shown in blue in figure 3.6. As can be seen, significant heterogeneity for moderate $\dot{\gamma}_0$ persists across the plane. This is seen for both the non-monotonic and monotonic underlying constitutive curves. Reversing the shearing flow whilst still within the region of transient banding (as seen in figure 3.5) therefore causes shear bands to be 'locked' persistently into the flow. This occurs even for materials that have homogeneous flow profiles at the steady state.

It is therefore seen here that the time-dependent nature of the oscillatory car-

icature protocol used here causes shear banding to occur for end-strain value $\gamma_0$ within the transient shear banding region of a corresponding startup protocol. It is important to note that this is irrespective of the monotonicity of the underlying constitutive curve of the material and inherently depends on the time-dependent nature of the material response before the steady state is reached.

It thus follows that shear banding is an important phenomenon to understand in protocols with sustained time-dependence (such as LAOStrain). This is explored in greater detail in chapter 4.

## 3.3 Step stress

### 3.3.1 The step stress protocol

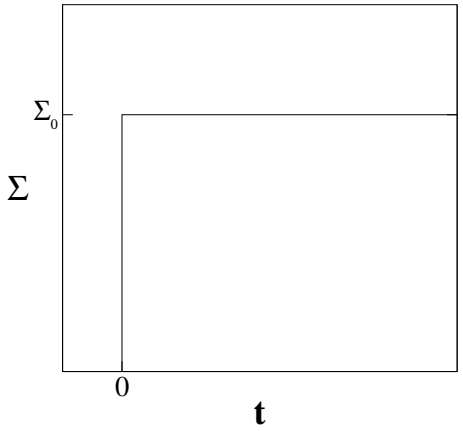


Figure 3.8: The step stress protocol: a constant stress of $\Sigma = \Sigma_0$ is applied for all time $t \geq 0$

The step stress protocol is another well studied simple time-dependent protocol used in the characterisation of materials. In the following section I recap previous results achieved in recent years [135, 136] (though results shown here are again my own work) to form a basis for the concepts introduced in chapter 5 of this thesis where the oscillatory stress-imposed protocol (LAOStress) is introduced.

In the step stress protocol a constant stress amplitude is applied to a material sample. The material is initially at rest, then, at time $t = 0$, the stress ($\Sigma = \Sigma_0$) is applied and held constant for the duration of the experiment. A schematic of this is shown in figure 3.8. The shear rate ($\dot{\gamma}$) response to this imposed deformation is then measured as a function of time.

Figure 3.9 gives an example of the time-dependent shear rate response (in (b)) to a range of stress amplitudes along the material's underlying constitutive curve (in (a)).

The red-dashed regions of the shear rate responses in figure 3.9(b) indicate the region where the criterion for linear instability to the formation of shear bands is satisfied in this step stress protocol. First derived in [135], this criterion predicted the onset of shear banded flow on the approach to steady state for this step stress protocol. Note that this criterion is model and fluid independent and only depends

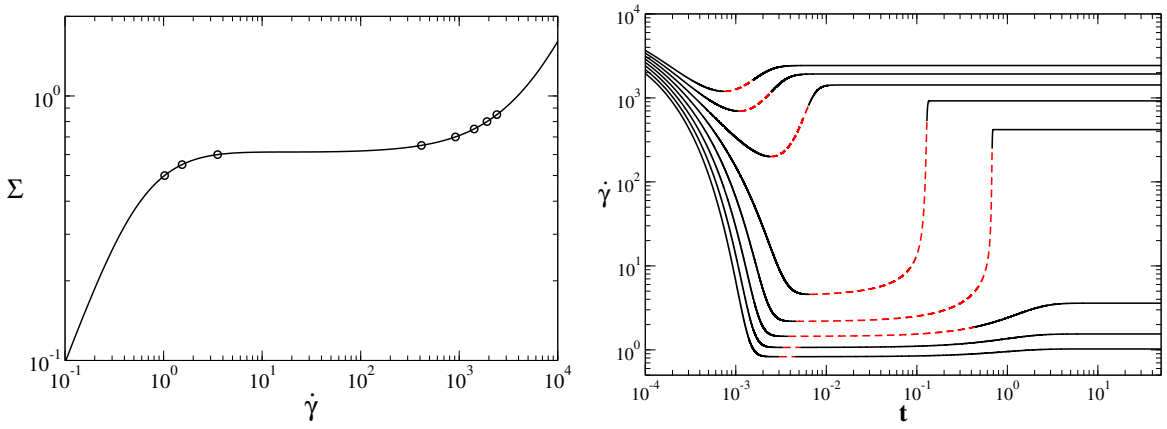


Figure 3.9: Step Stress in the nRP model for $\Sigma_0 = 0.5, 0, 55...0.8$. Circles in (a) show the positions on the constitutive curve these values of $\Sigma_0$ sit; the same values of $\Sigma_0$ are used in (b) to show the time-dependent shear rate response to the step stress protocol on the approach to steady state. Red dashed lines in (b) indicate where the criteria for instability to the onset of shear bands (eq. 3.3.10) is satisfied.

upon the time derivatives of the shear rate itself:

$$\frac{\partial_t^2 \dot{\gamma}}{\partial_t \dot{\gamma}} > 0. \tag{3.3.10}$$

This criterion tells us that the onset of instability to the formation of shear bands in the step stress protocol occurs when the shear rate response is both increasing and curving upwards (for a positive step stress amplitude). In principle, instability is also predicted the for a shear rate signal that decreases and curves downward, though I do not know of any materials that show this in practice.

As seen in figure 3.9, the typical shear rate response to step stress envolves via a fast initial decrease in shear rate, followed by a sharp increase to the final steady state value. This has its most pronounced form for $\Sigma_0$ closest to the weakest slope of the monotonic constitutive curve in (a). Here, the dramatic decrease and increase in $\dot{\gamma}$ spans several decades in magnitude. It is important to note here that whilst the time-dependent shear rate response is dramatic for these values of $\Sigma_0$, the evolution of the signal occurs over a short interval of time. It is unlikely that the initial decay of $\dot{\gamma}(t)$ is experimentally measurable. However, the rise of $\dot{\gamma}$ upon the approach to steady state has indeed been measured [16, 43, 72, 86–88, 173].

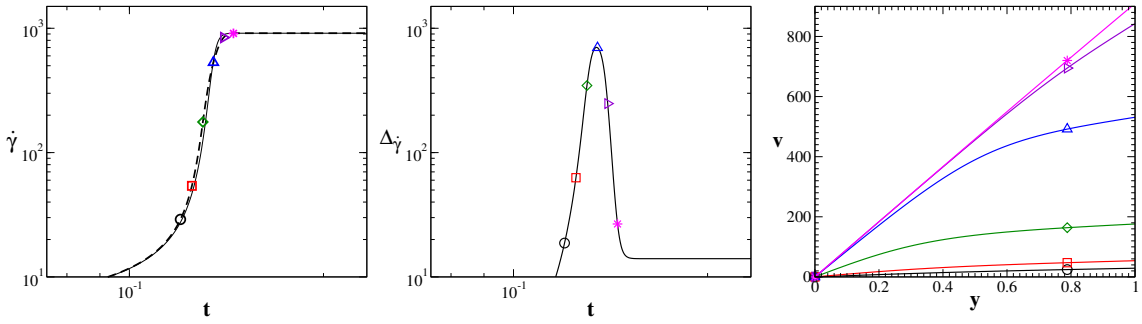


Figure 3.10: Step stress in the nRP model for $\Sigma_0 = 0.7$, $\eta = 10^{-4}$, $q = 10^{-3}$ and $\beta = 0.8$ (which has a monotonic constitutive curve at steady state). **Left:**Shear rate response with time. **Middle:** Degree of banding with time. **Right:** The velocity profiles at snapshots in time (symbols and colours correspond to those in the middle and left graphs).

Indeed, simulations in [135, 136] confirmed the validity of the step stress criteria in equation 3.3.10 to predict the onset of shear banding in step stress. Transient banding was seen on the approach to the steady state for materials with underlying non-monotonic or monotonic constitutive curves. In figure 3.10 I reproduce an example of these findings for an entangled polymeric solution within a curved cell geometry ( [135, 136] used a flat parallel plate cell) with a monotonic constitutive curve.

In figure 3.10 a stress amplitude of $\Sigma_0 = 0.7$ is applied to a sample, with spatial heterogeneity allowed. Any heterogeneity of the shear rate across the cell is quantified by a 'temporarily' localised form of the degree of banding used earlier for the startup protocol. In particular, due to the sometimes dramatic change in $\dot{\gamma}(t)$, the degree of shear banding is normalised by the overall shear rate at each point in time so not to be 'swamped' by the large $\dot{\gamma}_{\text{steady state}}$ value:

$$\Delta_{\dot{\gamma}} = \frac{1}{N} \left[ \dot{\gamma}_{\text{MAX}} - \dot{\gamma}_{\text{MIN}} \right], \tag{3.3.11}$$

where the normalisation factor $N = \dot{\gamma}(t)$, the instantaneous measured shear rate when heterogeneity has been allowed.

The degree of banding plot in figure 3.10 shows a pronounced growth during the regime where the shear rate response is both increasing and curving upwards, thus satisfying the criterion for shear banding instability. Snapshots of the spatial

velocity profiles during this region of transient shear banding are shown (with corresponding symbols) in the right-hand plot. They show a distinct bowed profile between the low and high shear rate regimes (black and magenta lines).

From this discussion, it can be concluded that step stress - a protocol which leads to a time-dependent material response - also exhibits time-dependent transient shear banding on the approach to the steady state. Moreover, shear bands form in materials with a non-monotonic or monotonic constitutive curve. It therefore naturally follows from this to progress onto the Large Amplitude Oscillatory Shear Stress protocol (LAOStress) which, like LAOStrain, has a sustained time-dependence and thus similar shear banding signatures might be expected. In Chapter 5 I call upon the results and criteria from the step stress protocol shown here to form a basis for understanding a material response to the more complex LAOStress protocol.

# 4

# LAOStrain in the Rolie-Poly model

In this chapter, I focus on the nonlinear oscillatory protocol, Large Amplitude Oscillatory Shear Strain (or LAOStrain, where the repeated 'S' is dropped for clarity, as per the convention [42]), calculated within the Rolie-Poly (RP) model for entangled polymer solutions and melts. In this protocol, the stress response of an entangled polymeric fluid to imposed oscillatory shearing is measured. An alternative counterpart protocol to this is Large Amplitude Oscillatory Shear Stress (LAOStress), where stress is instead imposed, and strain-rate response is measured. I consider this later in chapter 5. These protocols have become increasingly popular in studies within the rheological community and provide a complementary approach to shear startup or other large accumulative strain protocols from an experimental perspective: they are easier to perform and the smaller total accumulated strains (than in continuous strain experiments) reduce edge effects during measurement [150].

The RP model itself was introduced in full detail earlier, in chapter 2. For the

majority of this chapter, I focus on the non-stretching limit of the model (nRP) in which polymer chain stretch is assumed to relax infinitely quickly. Chain stretch (sRP) will be incorporated later in section 4.5. Through these versions of the RP model, I interpret the response of polymeric fluids to LAOStrain, after using simplified arguments that recall known triggers of instability to the formation of shear banding in simpler protocols [64, 135] (recall chapter 3). I shall also demonstrate that material response to LAOStrain can be understood and explained on a predominantly physical level, without the use of (for example) more common Fourier Transform methods [182, 183] used in experimental and theoretical studies in the current literature [51, 81, 163].

In chapter 3, I recapped the findings from current literature on shear banding in time-dependent flows. In particular, I recalled the work of Moorcroft and Fielding in deriving a set of model- and fluid-independent criteria to predict the onset of instability to the formation of shear banding in time-dependent protocols [135]. These criteria moved understanding on from the long-standing knowledge that an overshoot in a material's underlying constitutive curve shear stress, leading to a negative slope in $\Sigma(\dot{\gamma})$ indicates that the material exhibits shear banding at the steady state [185].

Moreover, it was shown that transient shear bands may form even when the underlying constitutive curve is monotonic and thus where no shear banding is seen at the steady state. An overshoot in shear stress with increasing strain $\Sigma(\gamma)$ during the startup to steady state is a typical trigger for (and signature of) this short-time short-lived banding in the flow. Whilst the simple criterion $\partial_\gamma \Sigma < 0$ has indeed been shown to hold for soft glassy materials [63], there have been cases reported where this $\partial_\gamma \Sigma < 0$ overshoot does not appear to coincide with observable shear banding [108]. It was derived in [135] that for elastically-dominated flow, the onset to the formation of transient shear bands occurs when the elastic limit (eq. 3.5) of the full criterion (eq. 3.4) is satisfied. This differs from the simple $\partial_\gamma \Sigma < 0$ criterion by the addition of a term that takes into account the curvature of the $\Sigma(\gamma)$ response. Though discussions on the validity of this when capturing elastic behaviour in experiment still continue [108]. At long times, steady state shear banding instead depends on

$\Sigma(\dot{\gamma})$ as described by the monotonicity of the underlying constitutive curve of the material and the viscous limit of the criterion (eq. 3.7).

In section 3.2, I created a caricature of an oscillatory strain-rate-controlled protocol by performing a series of constant shear rate ($\pm\dot{\gamma}$) deformations (from an initial startup experiment) without allowing the polymer time to relax its stress before the deformation direction was reversed. I found that fixing the end-strain (where $\dot{\gamma}$ was reversed) within a region of significant heterogeneity of the initial time-dependent response from startup, resulted in shear banding to persist throughout each reversing shear flow for a wide range of applied $\dot{\gamma}$. That is, at long times (once a time-translationally invariant result was achieved) the oscillatory caricature predicted the prevalence of shear banded flow of entangled polymeric materials under this simple caricature of LAOStrain. Importantly, this occurred both for materials with non-monotonic and monotonic underlying constitutive curves. It is these concepts, together with the use of the viscous and elastic criteria for short- and long-timescale behaviour, I explore further within this chapter with the full LAOStrain protocol.

After first describing the LAOStrain protocol, I will use the numerical methods and linear stability analysis outlined in chapter 2 to explore the underlying material stability of an initially homogeneous flow state to heterogeneous perturbations within the nonlinear regime. Indeed, I find that there exist regimes in the desired parameter space where significant measurable shear banding is found.

## 4.1 LAOStrain protocol

LAOStrain allows oscillatory experiments to probe and measure nonlinear responses of a material to an imposed strain. A recent review [90] gives a general overview of current studies in LAOS. As a protocol, it uniquely allows for amplitude and frequency to be varied independently from one another, enabling the user to assess a wide range of material responses in a methodical fashion [38, 90].

For a fixed frequency, $\omega$, and strain amplitude $\gamma_0$, the imposed strain and strain-

rate in this protocol are defined, respectively, as:

$$\gamma(t) = \gamma_0 \sin \omega t, \tag{4.1.1a}$$

$$\dot{\gamma}(t) = \dot{\gamma}_0 \cos \omega t, \tag{4.1.1b}$$

where $\dot{\gamma}_0 = \omega\gamma_0$.

During measurement, the material sample is sandwiched between two rheometer plates. One plate is held steady whilst an oscillatory deformation is imposed on the other, resulting in a time-dependent velocity to be imposed on the material sample from the moving rheometer plate, $V(t)$. The resultant stress response $\Sigma(t)$ to the time-dependent shear rate across the cell $\dot{\gamma}(t)$ is recorded. This allows the calculation of viscosity and other material characterisation properties. Typical geometries of a rheometer include the parallel plate, cone-and-plate and the Couette cell (of concentric cylinders). In this work, I use a weakly curved geometry formed by imposing a constant (in time) stress gradient across parallel plates. This *toy* curvature approach is discussed fully in chapter 2.

The strain and strain rate signals, defined by equations (4.1.1a) and (4.1.1b), are shown in figure 4.1. Letters A-D are used here, and in further diagrams, as an illustrative tool: at each moment in time where the strain passes through zero, the strain rate is at its maximum, or minimum, value; indicated by A and C respectively. Similarly, B and D refer to the instants in time where strain is at its respective maximum or minimum, and the associated strain rate passes through zero.

These trajectories, in time, of the imposed strain and strain-rate during one cycle of LAOS input could instead be considered in the strain vs. strain-rate plane; in this representation, they form an ellipse (of course, the special case of unitary fixed frequency and amplitude $\gamma_0 = \omega = 1$ gives a circle).For any given protocol, the height and width axes of the ellipse trajectory are defined by the applied strain amplitude ($\gamma_0$) and frequency ($\omega$) (and thus, in turn, the strain-rate amplitude $\dot{\gamma}_0 = \omega\gamma_0$). Figure 4.2 provides an example of the two extremes of these defining parameter choices:

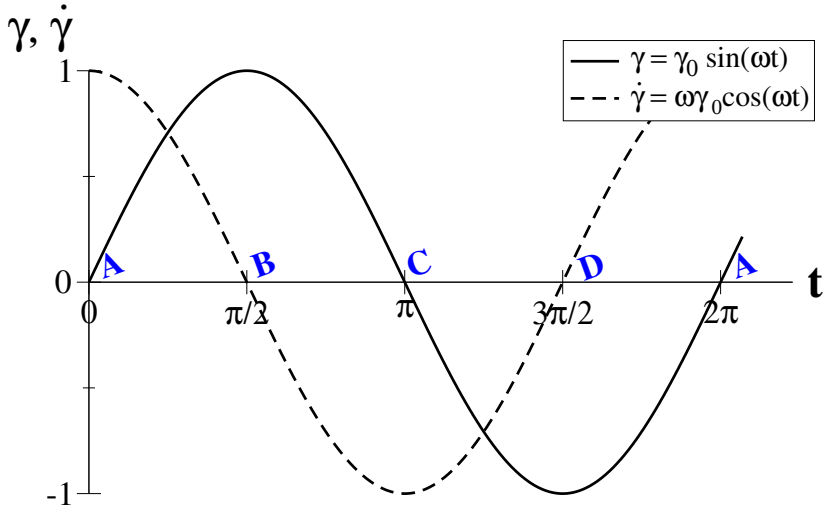


Figure 4.1: One cycle of the LAOS input. Black-solid line: imposed strain; black-dashed line: imposed strain-rate. $\gamma_0 = \dot{\gamma}_0 = \omega = 1$, here.

the ellipses are traversed for a high strain amplitude, low frequency (and therefore low strain-rate amplitude, relative to strain) protocol, in (a), and a low strain, high frequency (therefore, high strain-rate amplitude, relative to strain) protocol, in (b). Each cycle of the applied protocol traverses the space round the ellipse in a clockwise direction, starting at $\{\gamma, \dot{\gamma}\} = \{0, \dot{\gamma}_0\}$. This is illustrated in figure 4.2, where the starting point is indicated by A, as in figure 4.1. The ellipse then follows the lettering indicators: B, C, and D, respectively, as one complete cycle is traversed.

In order to study the effect of LAOStrain on a polymeric material, the time-dependent inputs defined in eq. (4.1.1a) and eq. (4.1.1b) are applied to the Rolie-Poly model described in chapter 2. In the subsequent results presented here, where I focus on the non-stretching limit of the Rolie-Poly model, materials with monotonic constitutive curves have the CCR parameter value $\beta = 1.0$; those with non-monotonic curves have $\beta = 0.4$. This follows on from, and provides natural comparison with, the work of Moorcroft in the shear startup protocol [135,136]. In each case the solvent viscosity $\eta = 10^{-5}$.

**Time to the *alternance state*:** In every LAOS experiment, the protocol is started when the system is initially at rest and any internal stresses are well relaxed. During the first cycle, when the strain is initially increased from $\gamma = 0$, the stress

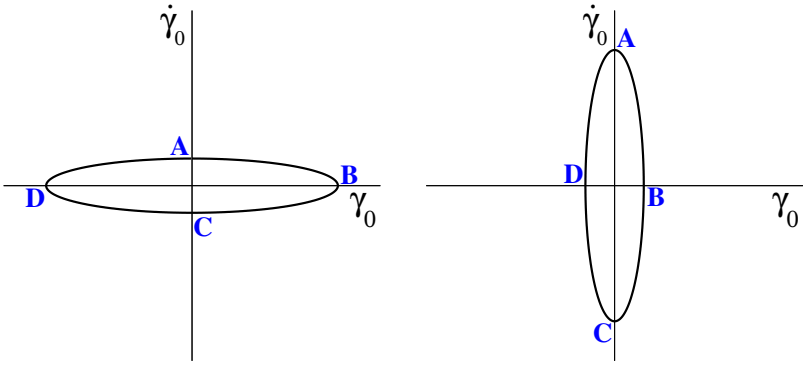


(a) $\omega \ll 1$ (b) $\omega \gg 1$

Figure 4.2: The LAOS protocol for small and large frequency. Since $\dot{\gamma}_0 = \omega\gamma_0$, for fixed $\gamma_0$ on the horizontal axis, the height up the vertical axis is determined by the frequency.

response somewhat resembles a shear startup experiment where transient overshoots in the stress are prominent. However, these overshoots reduce in magnitude in subsequent cycles. In most protocols, the first few cycles do not overlay one another; it takes significant time, where a number of repeated oscillations are performed (typically 20 cycles, for moderate frequency) before the stress response per cycle will begin to retrace itself for every subsequent oscillation. It is this "oscillatory steady state", where the material response is time-translationally invariant from cycle to cycle, $t \to t + 2\pi/\omega$, that is referred to throughout this, and subsequent, chapter(s) as the *alternance state* following the nomenclature of [71]. This state ensures that a repeatable measurement can be made from cycle to cycle. The dependence of the stress response on the cycle number was carefully studied in wormlike micelles in reference [70]. The results presented here are taken once the material has reached the alternance state, unless otherwise stated.

## 4.2 Lissajous-Bowditch curves

The most commonly reported representation of the material response to an imposed LAOStrain protocol is by a Lissajous-Bowditch curve [21,112,143]. This is a parameterised curve of the oscillating stress vs. either strain, or strain rate ($\sigma(t)$ vs. $\gamma(t)$, or $\sigma(t)$ vs. $\dot{\gamma}(t)$). Generally speaking, each parameterised Lissajous-Bowditch curve is a 2D projection of a closed-space curve in the 3D coordinate system of stress,

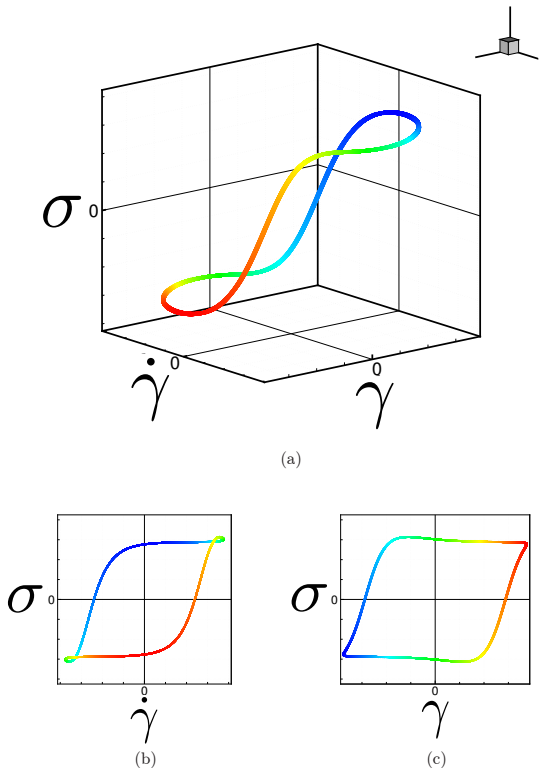


Figure 4.3: Lissajous-Bowditch curves for a material stress response to LAOStrain in the nRP model. (a) gives the full 3D curve, (b) and (c) show 2D projections of the curve onto the $\sigma$ vs. $\dot{\gamma}$- and $\sigma$ vs. $\gamma$-plane respectively. Parameters for the homogeneously-constrained system are:$\{\gamma_0, \omega, \beta, \eta\} = \{3.0,\ 10.0,\ 0.4,\ 10^{-4}\}$.

strain and strain rate, where the three time-dependent quantities form the orthogonal axes. It is by these plane-projections that the material response can be viewed in the *elastic* (stress response with strain), or *viscous* (stress response with strain rate) representation. This follows the vernacular of [52, 90]. The area within an elastic Lissajous-Bowditch curve represents dissipated energy during one LAOStrain response cycle and the area within a viscous Lissajous-Bowditch curve represents stored energy [101]. Elastic Lissajous-Bowdtich ellipses enclose less area and viscous Lissajous-Bowditch curves enclose more area as the frequency of oscillation is increased. Figure 4.3 gives an example of the 3D- and 2D-representations of a closed curve of LAOStrain data, formed using the Rolie-Poly model for a homogeneously-constrained system with a non-monotonic constitutive curve ($\beta = 0.4$).

In figure 4.3 colour is used in the curves as a guide to the reader: for all three representations, the red-to-blue spectrum indicates a positive-to-negative oscillation in the imposed strain ($\gamma$) signal, most easily identified in (c) where $\gamma$ forms the

horizontal axis. This in turn indicates the depth in (a) where otherwise, apparent intersections in the curve may seem physical; the curve in 3D-space is in fact an 'S'-shaped surface that experiences no internal intersection. In a similar vein, the apparent intersections (or, more recently termed 'secondary loops' [55]) in (b) are simply due to the 2D projection to the $\sigma - \dot{\gamma}$-plane, these are generally due to the overshoot in $\sigma(\gamma)$ [55, 77, 78].

As previously stated, the 2D projections of the Lissajous-Bowditch stress response curve, achieve two physically meaningful representations: the *viscous* representation (figure 4.3(b)) and the *elastic* representation (figure 4.3(c)). The reasoning behind these labels becomes clear when considering the limiting cases of a viscoelastic fluid: a viscous fluid, and a linear elastic solid. In the *viscous* representation, where stress is measured against the applied strain-rate, a viscous fluid's stress response would be a straight line; the response of a linear elastic solid, on the other hand, would form a circle. In the *elastic* representation, stress is measured against strain and results in a straight line for a linear elastic solid, and a circle for a viscous fluid. Figure 4.4 shows schematics of these limiting responses.

These linear, limiting stress responses form a starting point from which the more complicated case of a nonlinear viscoelastic response may be interpreted. In LAOS-train, the material response can be thought of as being formed by a combination of elastic and viscous effects, depending on the imposed values of amplitude and frequency in the applied oscillation.

Indeed, between these limiting cases of viscous and elastic behaviour, lies the more complex response of a viscoelastic fluid. For low applied strains this will still form a linear response (an ellipse, when plotted as a Lissajous-Bowditch curve), but for great enough strain amplitude, nonlinear effects come into play and the ellipses become distorted. Figure 4.5(a) shows the viscoelastic elliptical response in the linear regime, and 4.5(b) shows the effect of nonlinearity on the stress response with strain. This nonlinear curve gives an illustration of the direct combination of the viscous and elastic physical processes.

Starting from point 'X' (in a clockwise direction) in figure 4.5(b), where $\dot{\gamma}$ and

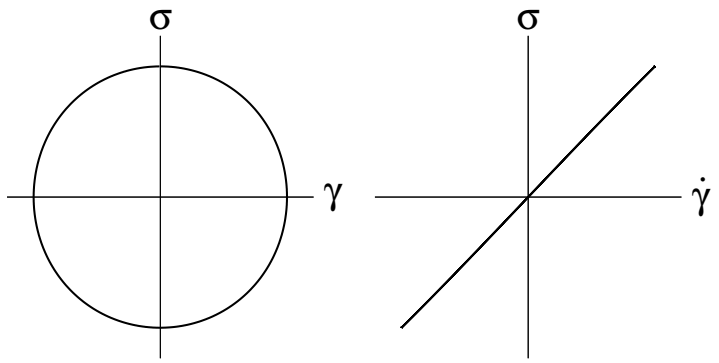


(a) Viscous fluid: $\omega \ll 1$.

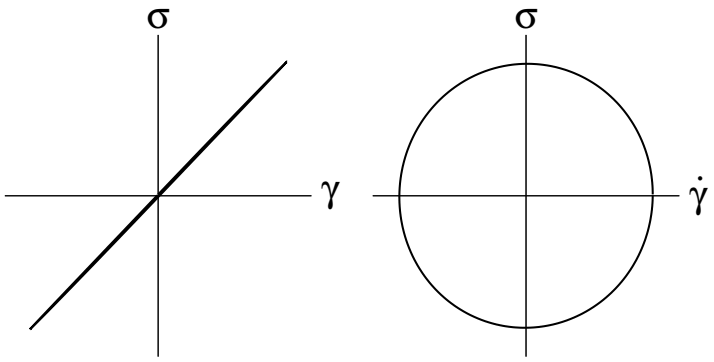


(b) Linear Elastic solid: $\omega \gg 1$

Figure 4.4: In both (a) and (b) the elastic representation ($\sigma$ vs. $\gamma$) is shown on the left-hand side, and the viscous representation ($\sigma$ vs. $\dot{\gamma}$) on the right. Both use the homogeneously-constrained nRP model, $\beta = 1.0, \eta = 10^{-4}$, with (a) ($\omega = 0.001, \gamma_0 = 0.1$) and (b) ($\omega = 100.0,\ \gamma_0 = 0.1$).

$\gamma$ are both positive and increasing, the sequence of material responses (here, in the elastic representation) follow an elastic, linear growth in stress with strain, before an overshoot is reached in the stress, ahead of the maximum strain rate $\dot{\gamma}_0$ at A. The material then continues to flow. The stress decreases slowly with decreasing strain-rate, until the strain-rate reverses direction (at 'B'). This strain-rate reversal coincides with the instant when the maximum strain amplitude ($\gamma_0$) is reached. Now experiencing a negative strain-rate, the material stress quickly responds, approaching zero as the strain approaches 0 by linearly decreasing its stress, then undergoing a negative-stress overshoot as the strain rate is ramped up to its maximum (negative) value, ($-\dot{\gamma}_0$) (at 'C'). This process is symmetric in the regions of positive ('D' to 'B') and negative ('B' to 'D') strain rate. Clearly, nonlinear LAOStrain stress responses show signatures of elastic and viscous material behaviour. It is thus possible to interpret results to a large extent by breaking down the full nonlinear viscoelastic

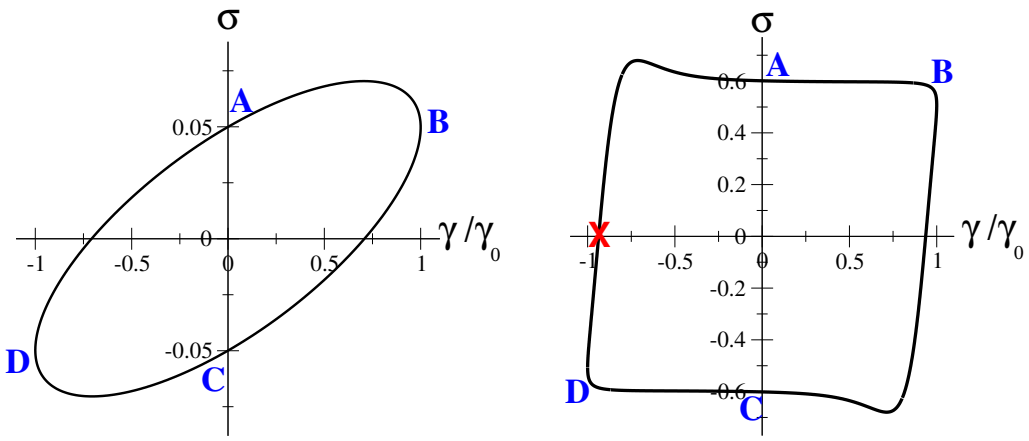


(a) Linear response, $\omega = 1.0, \gamma_0 = 0.1$

(b) Nonlinear response, $\omega = 1.0, \gamma_0 = 10.0$

Figure 4.5: Homogeneously-constrained stress response in the nRP model for ($\beta = 0.4, \eta = 10^{-4}, \omega = 1.0$). In (a), $\gamma_0 = 1.0$, yielding a linear viscoelastic response. In (b), $\gamma_0 = 10.0$, giving a nonlinear viscoelastic response.

regime into separate regimes of elastic and viscous response. This is akin to the method of interpretation of Rogers et al. [155–157] in their series of papers on the concept of stress responses to LAOStrain as a 'sequence of physical processes'. It is this approach to the interpretation of the data that I mainly adopt throughout the remainder of this chapter.

## 4.3 Pipkin Space

As noted above, oscillatory techniques are particularly useful in rheology as they allow the experimentalist to systematically vary the imposed frequency and amplitude in the protocol, independently from one another [38, 90]. In separate experimental runs, a large range of amplitudes at fixed frequency, and frequencies at fixed amplitude, can be accessed. It is then possible to create a map of material responses to deformation, where strain amplitude and frequency are used as the coordinate axes. This representation of data is known as the Pipkin space [144]; an illustration is shown in figure 4.6(a). This space enables the study of the transition in material behaviour from linear to nonlinear and elastic to viscous as the co-ordinate axes of strain amplitude and frequency are traversed, respectively. A Pipkin *diagram*, built up Lissajous-Bowditch curves of material responses within the Pipkin space has been

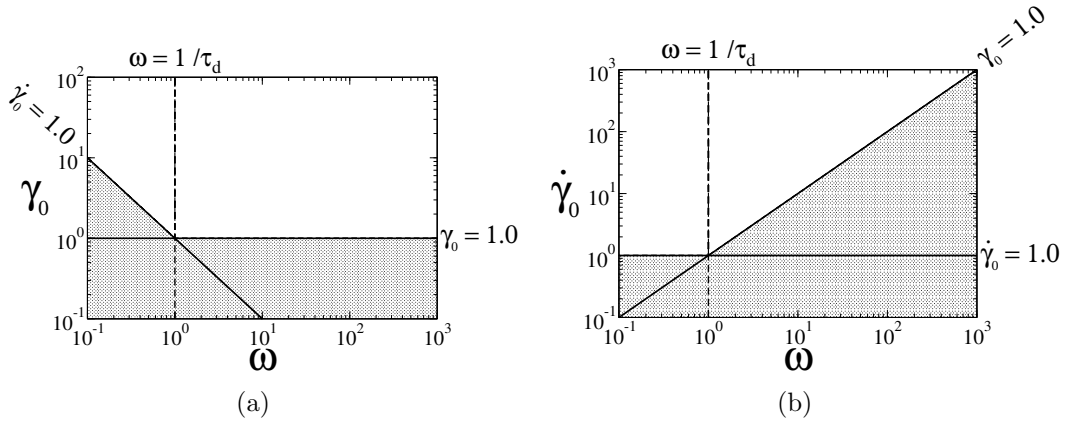


Figure 4.6: The Pipkin space of $\gamma_0$ vs. $\omega$ in (a) and shifted for $\dot{\gamma}_0 (= \omega\gamma_0)$ vs. $\omega$ in (b). Solid lines for $\gamma_0 = 1.0$ and $\dot{\gamma}_0 = 1.0$ are shown in each plot. The linear regime beneath these lines is shaded in grey. A dashed line shows the frequency equal to the inverse intrinsic relaxation time of the polymer $\omega = 1/\tau_d = 1.0$.

termed "the *'rheological fingerprint'* of material behaviour" [52, 53]. In section 4.4 I consider the prevalence of shear banding throughout each LAOStrain response cycle through a series of Lissajous-Bowditch curves forming a Pipkin diagram.

In the studies shown in this thesis, I found that a shifted Pipkin space, where instead the y-axis is for fixed $\dot{\gamma}_0 = \omega\gamma_0$, provided a more useful interpretation. This representation is shown in figure 4.6(b).

Figure 4.6 identifies regimes of material behaviour within the Pipkin space: at low frequencies (that is, $\omega \ll 1/\tau_d$, where $\tau_d$ is the intrinsic relaxation time of the material), the material is dominated by viscous effects. Conversely, in the high frequency regime where $\omega \gg 1/\tau_d$, elastic effects dominate the material behaviour. The line of $\omega = 1/\tau_d$ is shown as a dashed line in figure 4.6(a) and (b).

The linear regime (where there is insufficient imposed strain amplitude for non-linear effects to be important) is highlighted in figure 4.6(a) and (b) by the grey shaded region. This regime has an upper bound of the lines where $\gamma_0 = 1.0$ and $\dot{\gamma}_0 = 1.0$. The lines meet (by definition) at $\omega = 1.0$. This is the inverse characteristic relaxation time of the material and therefore marks a macroscopic timescale above which the flow response begins to be dominated by elastic, rather than viscous, behaviour. Within this linear regime, setting $\omega \ll 1/\tau_d$ leads to a material response of a Newtonian fluid. Instead setting $\omega \gg 1/\tau_d$ allows material behaviour to be accurately described as a linear Hookean elastic solid.

At higher amplitudes, the material response becomes affected by nonlinearity. The material response signatures will also be dependent upon the frequency of oscillation in the nonlinear regime: at low frequency, LAOStrain may effectively sweep the $\Sigma(\dot{\gamma})$ response up and down the underlying constitutive curve of the material (for a homogeneously constrained system). The material stress would have sufficient time to fully relax its stress on the timescale on which the rate the deformation is changed. It would therefore follow that the presence (or absence) of shear banding in this large amplitude, low frequency regime depends upon the non-monotonicity or otherwise of the constitutive curve of the material sample. Conversely, at large frequency and amplitude, it may (loosely and intuitively) be expected that the $\Sigma(\gamma)$ response to LAOStrain traces the short-time shear startup transient curve. If so, shear banding would be expected to emerge around the time of any elastic overshoot in strain (recall that this feature was seen in materials with either a non-monotonic or monotonic constitutive curve in the simpler cases of shear startup [2, 121, 135, 136]). At even larger frequencies, however, any heterogeneous growth in the flow is unexpected to be significant: the fast dynamics will not allow sufficient time for shear bands to develop across the cell [77] regardless of other model parameters determining the monotonicity of the constitutive curve. All of these limiting cases are considered in full detail later in the chapter: see section 4.3.2.

The remaining regime to be discussed here is the mid-frequency range of figure 4.6. Within this regime, the material response is viscoelastic and expected to comprise a complicated combination of the limiting responses just discussed. It is in this region of the Pipkin space that instability to the formation of shear bands is expected to occur for both nonmonotonic *and* monotonic underlying constitutive curves. Indeed, this is shown in section 4.3.2 and discussed further in section 4.4.

In the following section I consider a LAOStrain experiment for two example cases in the shifted Pipkin plane, where predominantly low ('viscous') and high ('elastic') material behaviours are expected. These limiting cases of low and high frequency in LAOStrain have been previously shown in figure 4.2, where the height and width axes of the strain vs. strain-rate plane are emphasised according to the frequency limit.

I adopt the Lissajous-Bowditch representation to consider the stress response to LAOStrain within these viscous and elastic regimes. I will use eigenvalues (attained from linear stability analysis and the stability matrix as outlined in chapter 2) as a numerical aide to identifying the regions of instability during the material response to LAOStrain.

### 4.3.1 Eigenvalues in Lissajous-Bowditch curves

From linear stability analysis (recall chapter 2), it is shown that regions of instability in a simple rheological protocol can be analytically predicted [60]. Through the formation of a stability matrix, an eigenvalue, $\lambda$, is found. This eigenvalue governs the stability of the material at a precise instant in time: if $\lambda > 0$, the material becomes unstable to the formation of shear bands. However, note that the calculation of the eigenvalue presumes a time-independent base state [170] and therefore only provides an indicative guide to predicting the stability of a material to shear band formation in the inherently time-dependent LAOS protocols. Therefore, in the assessment of material instability to form shear banded flow, I supplement my results for the time-dependent eigenvalue by integrating the heterogeneous perturbations to the initially homogeneous base state with time. This method is not flawless, as the linearised equations from which the heterogeneous perturbations are integrated break down in the limit of nonlinear flow. In the unstable regime, the linear calculations predict unbounded exponential growth in time. Because of this, I set a maximum of $10^4$ for the eigenvalue results presented here.

Figure 4.7 and 4.8 show the Lissajous-Bowditch curves' viscous (left) and elastic (right) representations of the material stress response to LAOStrain for a sample with a non-monotonic, and monotonic underlying constitutive curve respectively. In these calculations, the flow is restricted to be homogeneous. The colour scale to the left of each set of graphs and describes the magnitude of the positive eigenvalue growth around the cycle (zero and negative eigenvalues are set to black). In both (a) and (b), the left-hand plot gives an example of the low-frequency regime, with an imposed strain rate in the nonlinear regime $\dot{\gamma}_0 > 1$; the right-hand plot represents the high frequency, high strain regime. These are shown in the viscous

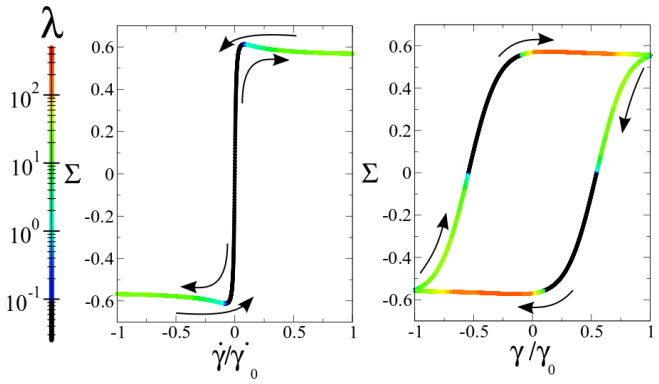


Figure 4.7: LAOStrain in the nRP model where the underlying constitutive curve is non-monotonic ($\beta = 0.4$). Solvent viscosity it taken to be $\eta = 10^{-5}$. **Left:** Viscous Lissajous-Bowditch figure showing stress $\Sigma$ vs. strain rate $\dot{\gamma}$ for an imposed frequency and shear rate $(\omega, \dot{\gamma}_0) = (0.001, 50.0)$, in the low frequency regime. **Right:** Elastic Lissajous-Bowditch figure showing stress $\Sigma$ vs. strain $\gamma$ for imposed frequency and strain rate $(\omega, \dot{\gamma}_0) = (31.6, 200.0)$, in the high frequency regime. Colourscale shows eigenvalue. Note black colour indicates $\lambda \leq 0$.

and elastic representations according to their predominant material effects at play: at low frequency, the LAOStrain signal sweeps slowly up and down the material's underlying steady state constitutive curve. For the value of $\beta$ for which the underlying constitutive curve is non-monotonic there is a clear positive eigenvalue during the non-monotonic region in the $\Sigma(\dot{\gamma})$ response curve shown in the left panel of figure 4.7. This is consistent with the well known criterion for instability to shear banding at the steady state: $\partial_{\dot{\gamma}}\Sigma < 0$ [185]. In the left panel (low frequency run) of figure 4.8, where $\beta$ is such that the constitutive curve is monotonic, the eigenvalue remains negative, or zero, throughout the cycle; this indicates stable, homogeneous flow.

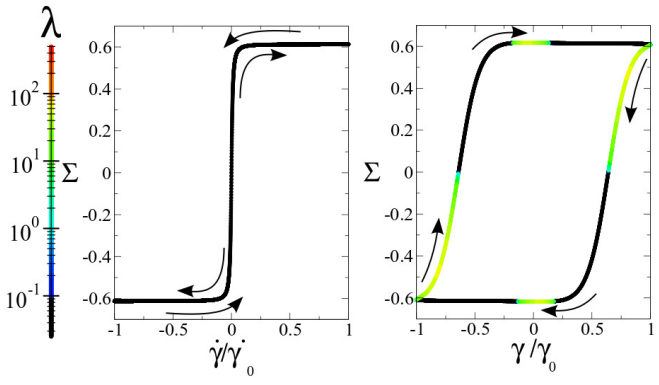


Figure 4.8: As in figure 4.7 for a monotonic underlying constitutive curve ($\beta = 1.0$).

The right-hand plots of figure 4.7 and 4.8 give the material responses to LAOStrain at high-frequency and large amplitude. In this regime, the results are presented in the elastic representation $\Sigma(\gamma)$; coloured regions of positive eigenvalue can clearly be seen following the stress overshoot (or negative overshoot) in increasing (decreasing) strain. This coincides with the elastic criterion found in the shear startup protocol: $-\mathrm{tr}\underline{\underline{M}}\partial_\gamma\Sigma|_{\dot\gamma} + \dot\gamma\partial^2_\gamma\Sigma|_{\dot\gamma} < 0$ ($\mathrm{tr}\underline{\underline{M}} > 0$), which was found to predict transient banding with onset just before the overshoot of stress with strain. These time-dependent shear bands were seen for materials with a non-monotonic or a monotonic constitutive curve. The elastic overshoot at high frequency and high strain amplitude in LAOStrain highlights the elastic material effects within this response regime. It is these effects that are the dominating material behaviour, arising in any protocol with $\gamma_0 > 1$, rather than $\dot\gamma_0 > 1$ as seen in the low frequency regime.

The material responses to LAOStrain within the high frequency, large amplitude regime also show some (weaker) growth in the eigenvalue following the strain-reversal at $\gamma/\gamma_0 = \pm 1$. This additional unstable region in the material elastic response curve can be accounted for by growth in the normal stress component perturbations ($\delta n$) and could be experimentally measured by birefringence [16]. A short study into the growth of $\delta n$ is included in Appendix I, section 4.7, of this chapter. However in this thesis I focus on the heterogeneity in the shear rate profile.

In the following sections I further the ideas developed here. I consider the shifted Pipkin space in two distinct ways: colour maps giving an 'at-a-glance' perspective of the stability of the material to shear banding within a broad spectrum of imposed frequencies and strain amplitudes, and grids of the time-dependence of material responses - Pipkin diagrams - giving detail into single cycles of the LAOStrain response on a grid of particular points within the Pipkin space.

### 4.3.2 Colour Maps

In the following section I look to represent the stability of a polymeric material - as modelled by the nRP model - over a wide range of strain amplitudes and frequencies. This is achieved through pin-point colour maps:

**Pin-point colour maps** provide an 'at-a-glance' perspective of a series of LAOS experiments. Each experiment (where 'experiment' defines a LAOStrain protocol for fixed $\gamma_0$ and $\omega$ and the response once the alternance state is reached) is accounted for by each co-ordinate pair, or pin-point, in the map. Plotting these on a grid where strain amplitude and frequency are the coordinate axes forms a Pipkin space in which we may assess the material behaviour. For example: with 50 fixed strains and 50 fixed frequencies, a map can be created to represent 2500 LAOS experiments. These experiments are performed numerically according to the methods described in chapter 2.

By definition, in these pin-point colour maps, only one value, per experiment with fixed $(\gamma_0, \omega)$, can be represented by each point. In this way, time-resolved information over the cycle is lost. For each co-ordinate pair, the recorded value to indicate the stability of the material to the formation of shear bands under LAOStrain at fixed $\gamma_0$ and $\omega$ is taken to be the maximum degree of heterogeneity during one cycle in the alternance state. While taking the maximum values will not give any indication into how long-lived shear bands may be throughout the cycle, it will clearly indicate the regions within the Pipkin space where instability, and shear banding, are manifest in some form. It is these maximised quantities that I represent on a colour scale in the pin-point maps shown here.

The degree of heterogeneity can be calculated by integrating the heterogeneous perturbations in the $\dot{\gamma}$-field to the linearised equations ($\delta\dot{\gamma}(t)$) or by calculating the degree of banding ($\Delta_{\dot{\gamma}}$) across the flow cell in a full nonlinear simulation. The latter of these is much more time-consuming and computationally expensive than the former. I found that all qualitative features of the material stability to the formation of shear bands in LAOStrain are retained at this zoomed-out, 'at-a-glance' perspective for the linearised equation ($\delta\dot{\gamma}(t)$) calculations as when the full nonlinear ($\Delta_{\dot{\gamma}}(t)$) spatiotemporal dynamics were included. I therefore solely focus on the integrated perturbations $\delta\dot{\gamma}(t)$ in the $\dot{\gamma}$-field for all pin-point colour maps shown in this thesis.

To recap from chapter 2, the following procedure is followed to calculate the linear stability (to shear banding) value presented in the following pin-point colour

maps:

Using the constitutive equations of the Rolie-Poly model, the time-dependent variables are perturbed with a small, heterogeneous value

$$\{\sigma, \sigma_{yy}, \dot{\gamma}\} = \{(\hat{\sigma}(t) + \delta\sigma(t,y), \hat{\sigma}_{yy}(t) + \delta\sigma_{yy}(t,y), \hat{\dot{\gamma}}(t) + \delta\dot{\gamma}(t,y)\},$$

where $\hat{}$ indicates the base state, calculated within the assumption of homogeneous flow and $\sigma = \sigma_{xy}$; the subscript in the shear-component of the stress is dropped for clarity. After expansion, the perturbed constitutive equations are linearised, leaving a differential equation for the evolution of the linearised heterogeneous perturbations to the base state. If $\delta\dot{\gamma}(t)$ experiences growth during LAOStrain, it may be inferred that the material is experiencing instability and is susceptible to forming shear bands. In the following pin-point colour maps this perturbation is scaled by the strain-rate amplitude of the oscillation to give a measure better suited to comparison with experiments: $|\frac{\delta\dot{\gamma}}{\dot{\gamma}_0}|$.

Figure 4.9 shows pin-point colour maps for the stability of a material to the formation of shear bands in the LAOStrain protocol for a wide range of fixed $\dot{\gamma}_0, \omega$ co-ordinate pairs. In (a) the material has an non-monotonic underlying constitutive curve with $\beta = 0.4$; in (b), $\beta = 1.0$ and the underlying constitutive curve is monotonic. Both maps are shown in the strain-rate amplitude-frequency plane, with identical axis-scaling. The plane is a shifted version of the Pipkin space as described earlier in figure 4.6(b), allowing for a wide range of Pipkin space to be explored. Colour, quantified by the logarithmic scales to the right of each plot, indicates the maximised perturbation in the $\dot{\gamma}$-field during one cycle in the alternance state, normalised by $\dot{\gamma}_0$ ($|\frac{\delta\dot{\gamma}}{\dot{\gamma}_0}|$): the brighter the area, the more unstable the material is to shear band formation in any given regime of imposed strain amplitude and frequency. To the left-hand side of the colour maps, the material is subject to low frequency oscillations. In (a), the material with a non-monotonic constitutive curve shows significant $\delta\dot{\gamma}$-magnitude extending to the low frequency limit. However in (b), where the material has a monotonic constitutive curve, there is no

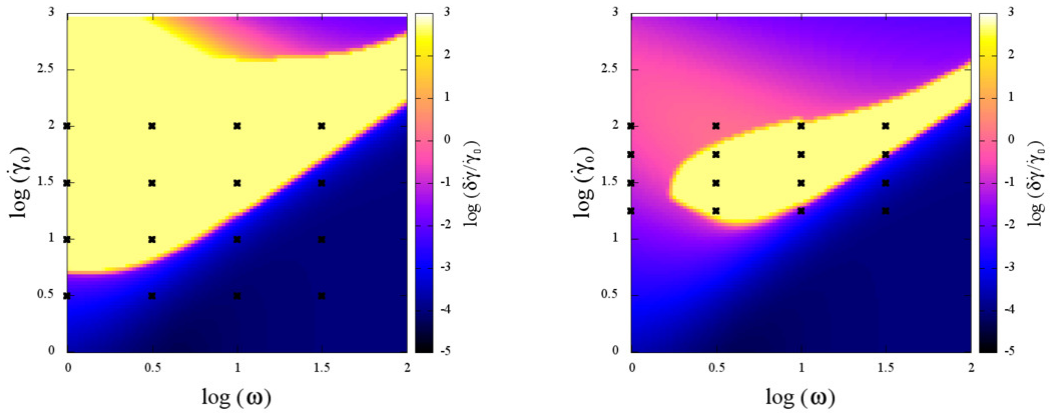


(a) (b)

Figure 4.9: Pin-point colour maps of the maximal growth in the linear perturbations ($|\delta\dot{\gamma}|$) around a LAOS-cycle, measured in the alternance state. The CCR parameter, $\beta$, is taken in (a) as 0.4, and in (b) as 1.0, corresponding to non-monotonic and monotonic underlying steady state constitutive curves respectively. Other parameters taken are: $\{\eta, q\} = \{10^{-5}, 10^{-4}\}$, where q represents the cell curvature ratio. The colour scale for the normalised measure: $\frac{|\delta\dot{\gamma}|}{\dot{\gamma}_0}$, is shown by the colour panel on the right-hand side of each plot. Black crosses indicate the values of $\dot{\gamma}_0$ and $\omega$ used to form the Lissajous-Bowditch curves within the Pipkin figures in 4.15 and 4.16.

significant heterogeneity. This is consistent with expectation as discussed earlier in section 4.3.1: at a frequency sufficiently slower than the intrinsic relaxation time of the polymer ($\omega \ll 1/\tau_d$) the $\Sigma(\dot{\gamma})$-response to LAOStrain traces the underlying constitutive curve of the material. Material stresses have sufficient time to relax on the timescale of deformation [38]. It is only the material with a non-monotonic constitutive curve that exhibits shear bands at the steady state and it thus follows that it is only this material class that exhibits shear banding in the low frequency LAOStrain regime.

Figure 4.10 shows this low frequency LAOStrain response for a range of $\dot{\gamma}_0$ where the flow is constrained to be homogeneous. The data is represented as a viscous Lissajous-Bowditch curve, where only the regime in which both $\Sigma$ and $\dot{\gamma}$ are positive is shown. The underlying constitutive curve of each material is shown by the dashed blue line in (a) and (b).

When $\dot{\gamma}_0 = 1.0$, the $\Sigma(\dot{\gamma})$ response to LAOStrain lies within the low-shear rate

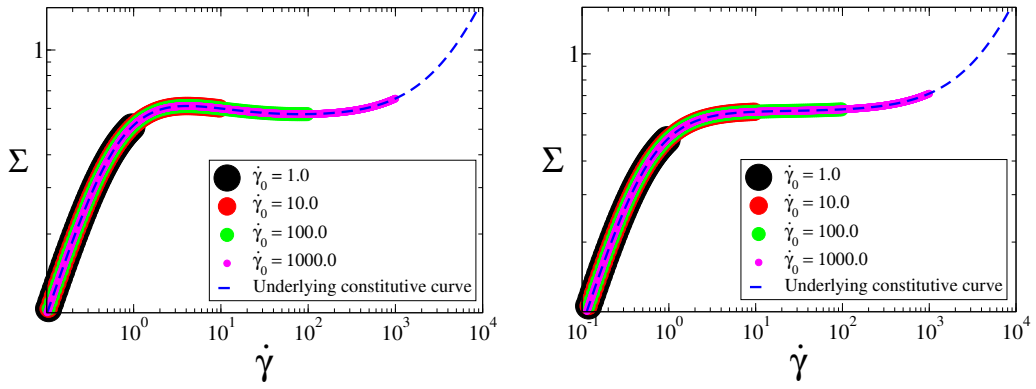


(a) $\beta = 0.4,\ \omega \ll 1/\tau_d$ (b) $\beta = 1.0,\ \omega \ll 1/\tau_d$

Figure 4.10: Low-frequency tracing of the underlying constitutive curve of an entangled polymeric fluid as modelled by the nRP model. The flow that is restricted to be homogeneous (no spatial variation and shear banding are allowed) and results are shown for strictly positive shear rate and stress values. The blue-dashed line shows the underlying constitutive curve for each $\beta = 0.4$ (in (a)) and $\beta = 1.0$ (in (b)). Black, red, green and pink thick lines show the low-frequency LAOStrain response to imposed rates of $\dot{\gamma} = 1.0,\ 10.0,\ 100.0,\ 1000.0$ respectively. Frequency is taken as $\omega = 10^{-4}$; solvent viscosity is $\eta = 10^{-4}$.

(and mostly linear) response regime of the underlying constitutive curve, preceding the overshoot in stress. This is shown by the thick black line in figure 4.10. It is not until $\dot{\gamma}_0$ is sufficiently large (as in the red and green lines, where $\dot{\gamma}_0 = 10.0,\ 100.0$) that the strongly nonlinear regime is reached [34]. This non-linear regime of low-frequency tracing of the underlying constitutive curve is highlighted within the Pipkin space by the red section (A) in figure 4.11. Note that instability to the formation of shear bands only occurs within (A) for an non-monotonic underlying constitutive curve.

For very large $\dot{\gamma}_0$ ($\sim 1/\eta$) the maximum amplitude of the LAOStrain oscillation lies within the high-shear rate linearly increasing branch of the underlying constitutive curve. Shear banding is not expected to occur within this regime (from shear startup) yet bright patches indicating significant heterogeneity in the material sample are seen in the top-left corner of figure 4.9(a). In figure 4.10 it can be seen that for any $\dot{\gamma}_0 = \omega\gamma_0$ in LAOStrain greater than the negatively-sloping region of the constitutive curve, the time-dependent shear rate response $\dot{\gamma}(t)$ must pass through this negatively-sloping region en route to the $\dot{\gamma} = \dot{\gamma}_0$. The material is exposed to shear rates within the regime of instability to the formation of shear bands (albeit

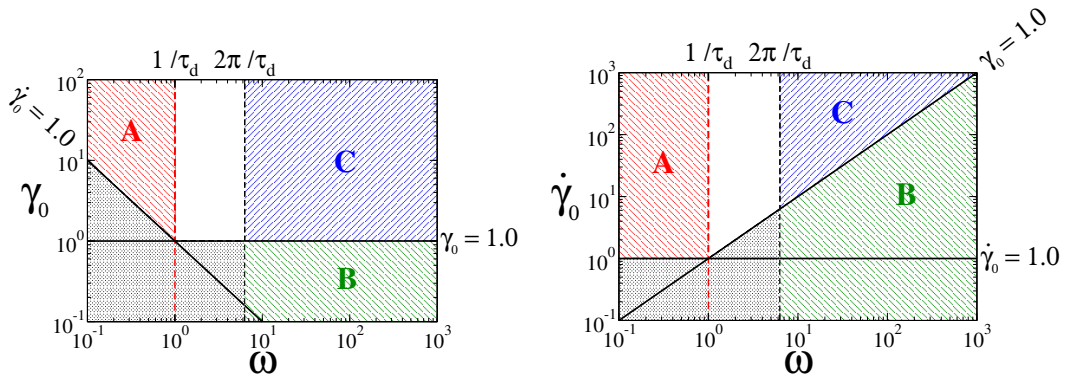


Figure 4.11: The Pipkin space of $\gamma_0$ vs. $\omega$ in (a) and shifted for $\dot{\gamma}_0(=\omega\gamma_0)$ vs. $\omega$ in (b). Solid lines for $\gamma_0 = 1.0$ and $\dot{\gamma}_0 = 1.0$ are shown in each plot. The linear regime beneath these lines is shaded in grey. A dashed line shows the frequency equal to the inverse intrinsic relaxation time of the polymer $\omega = 1/\tau_d = 1.0$. Coloured regions indicate regimes of low-frequency responses (red, A), high-frequency linear elastic responses (green, B) and high-frequency large-amplitude nonlinear responses (blue, C).

transiently) each time the constitutive curve is transited on the approach to (and return from) $+\dot{\gamma}_0$. Therefore significant shear banding is seen in LAOStrain for $\dot{\gamma}_0$ within the high-shear rate linear branch of a non-monotonic constitutive curve. By symmetry, the same behaviour occurs for the negative-shearing region (towards $-\dot{\gamma}_0$) of $\Sigma(\dot{\gamma})$.

The right-hand side of the pin-point colour maps in figures 4.9(a) and (b) shows the material response at large frequency LAOStrain. Here, there is greater similarity in the material stability to shear banding between the material with a non-monotonic underlying constitutive curve (in (a)) and the monotonic underlying constitutive curve (in (b)). At small strains ($\gamma_0 = \dot{\gamma}_0/\omega \ll 1.0$) an initially homogeneous flow is stable against heterogeneous perturbations, illustrated by the dark colouring in the map. Recall in this shifted-Pipkin representation that the line of $\gamma_0 = 1.0$ runs diagonally up the $\dot{\gamma}_0 - \omega$-plane from bottom-left to top-right. This regime is highlighted by the green (B) region in figure 4.11. A detailed elastic Lissajous-Bowditch curve of the material response in this low-strain, high-frequency regime is shown in figure 4.12.

Within this regime, the elastic Lissajous-Bowditch curve for each $\Sigma(\gamma)|_{\gamma_0}$ collapses onto one 'master curve'. The stress responds in this limit as a linear elastic

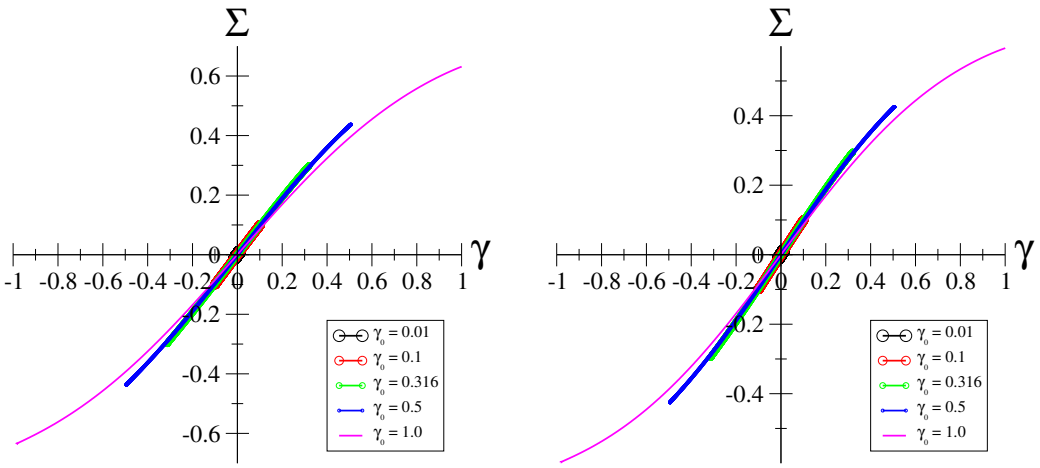


(a) $\beta = 0.4,\ \omega \gg 1/\tau_d,\ \gamma_0 < 1.0$ (b) $\beta = 1.0,\ \omega \gg 1/\tau_d,\ \gamma_0 < 1.0$

Figure 4.12: The low-strain, high-frequency master curve showing the linear elastic solid-like behaviour in this limit of LAOStrain, using the nRP model. Stress responses are shown as elastic Lissajous-Bowditch figures and amplitudes of $\gamma_0 (= \dot{\gamma}_0/\omega) = 0.001,\ 0.1,\ 0.316,\ 0.5,\ 1.0$, where the breakdown of the limit can be seen in the magenta line of $\gamma_0 = 1.0$. Frequency is $\omega = 100.0$; solvent viscosity in $\eta = 10^{-4}$.

solid. However, as the boundary of the regime is approached ($\gamma_0 = 1.0$) the magenta line in figures 4.12(a) and (b) shows the break down of the is linear elastic behaviour. The $\Sigma(\gamma)$ response departs from the master curve as the material behaviour begins to feel the nonlinear effects to the imposed LAOStrain.

Blue region C in figure 4.11 highlights the regime of high-frequency, high-strain LAOStrain where elastic nonlinear effects dominate the material response to the imposed deformation. It may initially be expected that the $\Sigma(\gamma)$ response in this regime of LAOStrain follows the trajectory of a fast shear startup protocol: experiencing a pronounced overshoot in $\Sigma$ with $\gamma$ before a steady state plateau is reached, repeated for positive and negative strain-rate. This, however, is not the case. In shear startup the material begins at a well relaxed rest state before each deformation is applied. Whilst this relates to the first startup transient in LAOStrain, it does not apply for any further: once the shearing direction is reversed in LAOStrain at $\gamma = \pm\gamma_0$ there is little time for the material to relax its stresses accrued during the strain-controlled protocol relative to the intrinsic relaxation time of the polymer. Subsequent positive and negative shearing regimes within this large amplitude, large frequency flow do show stress overshoots, but these are much reduced

compared with the startup case. Moreover, in LAOStrain, $\dot{\gamma}(t)$ requires a finite time to reach $\dot{\gamma}_0$. This differs fundamentally from shear startup where $\dot{\gamma} = \dot{\gamma}_0$ infinitely fast, therefore subjecting the material to greater $\dot{\gamma}$, faster.

There is, however, a second high-frequency master curve for the elastic material response to LAOStrain. At increasingly large strains, the nonlinear $\Sigma(\gamma)$ material response to LAOStrain forms a larger hysteresis area within the elastic Lissajous-Bowditch curves compared with the smaller strain linear profiles (these are shown later, in figures 4.15 and 4.16). However, the fast ramp up (following the reversal at $\pm\gamma_0$) to the stress 'plateau' region at $\pm\Sigma_{\max}$ for positive and negative shearing regions of the curve follows the same trajectory. For fixed high frequency LAOStrain, the transition between the positive and negative 'plateaus' in stress collapse on to one master curve; it is only the length of the 'plateau' that differs, depending upon the magnitude of applied $\gamma_0$ (the end-strain that must be reached before shearing reversal). Figure 4.13 shows the master curve for $\omega = 100.0$, where $\gamma$ is cut off to the right-hand side to focus on this positive shearing transition curve. To form the master curve, each $\Sigma(\gamma)|_{\gamma_0}$ is shifted along the $\gamma$-axis by the value at which $\Sigma(\gamma)$ passes through $\Sigma = 0.0$, for increasing $\Sigma$. $\gamma_{\text{MIN}}$ is defined as this axis-crossing point for each $\Sigma(\gamma)|_{\gamma_0}$ curve. By symmetry, the same master curve signature would be found for the negative shearing transition from $+\gamma_0 \rightarrow -\gamma_0$, though it is not shown here.

In the high-frequency regime, the response of an entangled polymeric solution to imposed LAOStain is dominated by elastic effects. Signatures within the material response only depend on the stress response with strain, rather than the strain rate. Generally, elastically-dominated responses to LAOStrain of frequency $\omega$ require the period of the oscillation to be less than the intrinsic relaxation time of the material:

$$\frac{2\pi}{\omega} \ll \tau. \tag{4.3.2}$$

This line is shown within the Pipkin space in figure 4.11 for $\tau = \tau_d = 1$. A similar conclusion was drawn in reference [38] for thixotropic gels where $\tau$ described the timescale of micro-structure changes in the flow.

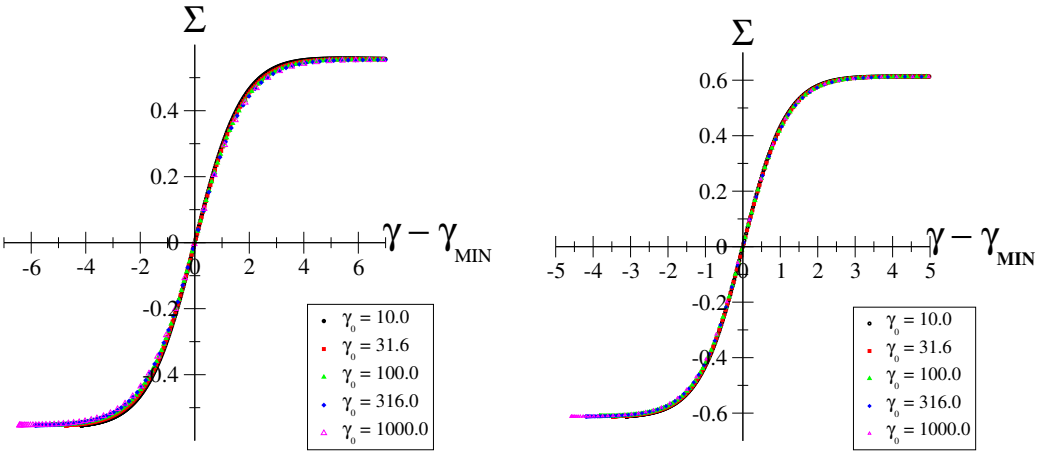


(a) $\beta = 0.4,\ \omega \gg 1/\tau_d,\ \gamma_0 \gg 1.0$ (b) $\beta = 1.0,\ \omega \gg 1/\tau_d,\ \gamma_0 \gg 1.0$

Figure 4.13: The high-strain, high-frequency master curve showing the fast transition between $\pm\Sigma_{\max}$ in the nonlinear stress response to LAOStrain, using the nRP model. Strain amplitudes of $\gamma_0 (= \dot{\gamma}_0/\omega) = 10.0,\ 31.6,\ 100.0,\ 316.0,\ 1000.0$ are applied. Frequency is fixed at $\omega = 100.0$; solvent viscosity is $\eta = 10^4$.

Shear banding is predicted here by the significant growth in heterogeneous perturbations in the $\dot{\gamma}$-field for large strains, $\gamma_0 \gg 1.0$, and large frequencies, $\omega \gg 1/\tau_d$ for both non-monotonic and non-monotonic underlying constitutive curves. I have shown that within this regime the material response is dominated by the elastic behaviours in the polymer and depends on the stress response with strain, rather than strain rate. It therefore follows that the emergence of shear bands here is not dissimilar to the formation of transient shear bands following the overshoot in $\Sigma(\gamma)$ during shear startup. This concept is discussed in more detail in the subsequent section where I focus on individual Lissajous-Bowditch curve of the material responses across the Pipkin space.

To the far right of the Pipkin space shown in figures 4.9(a) and (b), the degree of heterogeneity in $\delta\dot{\gamma}$ can be seen to be tapering off in magnitude. Higher frequencies are not shown here as they are hard to access numerically in the resolution required for the colour map, but it can be inferred that indeed this 'tapering-off' of magnitude in heterogeneity would continue for great $\omega$. At very large frequencies there is insufficient time for any growth in heterogeneity to appreciate to a significant value [58]. The rate of change in the material response does not allow for any shear banding

to form across the cell and thus a homogeneous flow profile persists throughout the response cycle.

The remaining regime in $\gamma_0$ and $\omega$ in the Pipkin space not discussed here is the intermediate region of figure 4.11 (shown in white). Here, significant heterogeneity is seen for both cases of a non-monotonic and monotonic underlying constitutive curve. The material response in this region is a combination of viscous and elastic behaviours and thus cannot be encompassed by any one of the limiting-case behaviours discussed here. At low frequency, banding is seen as $\omega \to 0$, when $\partial_{\dot{\gamma}}\Sigma < 0$; at high frequency, where $\omega\tau_d \gg 1$, banding instead depends upon $\Sigma(\gamma)$. At intermediate frequencies, a smooth crossover between the viscous and elastic material behaviour is expected to be seen. It is this regime of viscoelastic polymer behaviour that the tendency to form bands is most pronounced. Accordingly, I focus on in the following sections.

Though not shown here, the features of the plots in figure 4.9 would remain if the degree of banding around the LAOStrain cycle were measured in a full nonlinear simulation, rather than the linear perturbation growth. The main difference in the results is that the amplitude of the degree of heterogeneity is tempered by nonlinearity.

In the next section, I perform full nonlinear calculations, allowing for heterogeneity in the system, and thus enabling the possibility of shear banded flow to form if the flow experiences instability under the oscillatory deformation. I will first introduce the measurement for shear banding used here (degree of banding), as relevant to the LAOStrain protocol. Then, following some initial, more detailed results, I revisit the Lissajous-Bowditch curves and introduce Pipkin diagrams as a way to represent the heterogeneity of the material across a range of the Pipkin space.

### 4.3.3 Degree of banding

When shear bands form in a deformed material, each band has a different shear rate associated with it. The intrinsic time-dependence of the strain imposed during the

LAOStrain protocol results in the transient evolution of spatial size and shear rate of the bands that may form: if in existence, these bands will change throughout the duration of any given cycle, evolving with the external driving oscillations. By definition, however, the bands will trace their steps exactly from one cycle to another when in the alternance state; moreover, the evolution of their spatial size and shear rate will be symmetric for positive and negative regions of the LAOStrain input signal.

Recall that (as in shear startup) the extent of any shear banding during LAOStrain can be measured during a response cycle as follows: at any given snapshot in time, the faster-flowing shear band can be defined as having shear-rate $\dot{\gamma}_{MAX}$ and the slower as $\dot{\gamma}_{MIN}$. For an imposed strain-rate amplitude of $\dot{\gamma}_0 (= \omega\gamma_0)$, the degree of banding of the material at any instant of time is

$$\Delta_{\dot{\gamma}_0} = \frac{1}{N}[|\dot{\gamma}_{MAX}| - |\dot{\gamma}_{MIN}|], \tag{4.3.3}$$

where $N = \dot{\gamma}_0$. I then define significant banding (where banding in the material is measurable) as $\Delta_{\dot{\gamma}_0} > 5\%$.

Figure 4.14 shows the time-dependent responses of a material with a non-monotonic (top: $\beta = 0.4$) and a monotonic (bottom: $\beta = 1.0$) underlying constitutive curve. These responses are shown during a positive-$\Sigma$ segment of the stress response cycle, measured at the alternance state. Only half a cycle is considered here due to the symmetry of material response to the LAOStrain input; the other (negative-$\Sigma$) portion of the cycle would show the same patterns as seen here, up to the appropriate switching in sign. As in the shear startup case reported in chapter 3, the symbols in (a), (b), (d) and (e) correspond to the velocity profiles shown in (c) and (f), respectively. These symbols, and associated profiles, illustrate the evolution of the shear bands at snapshots in time during a section of one LAOS-response cycle. Comparing the evolution of the velocity profiles with the symbol-markers in graphs (a) and (d), the stress response with time, it can be seen that shear bands form once the stress has gone through the overshoot region. This coincides with the regime of instability to the formation of shear bands predicted by the positive eigenvalue regions of the

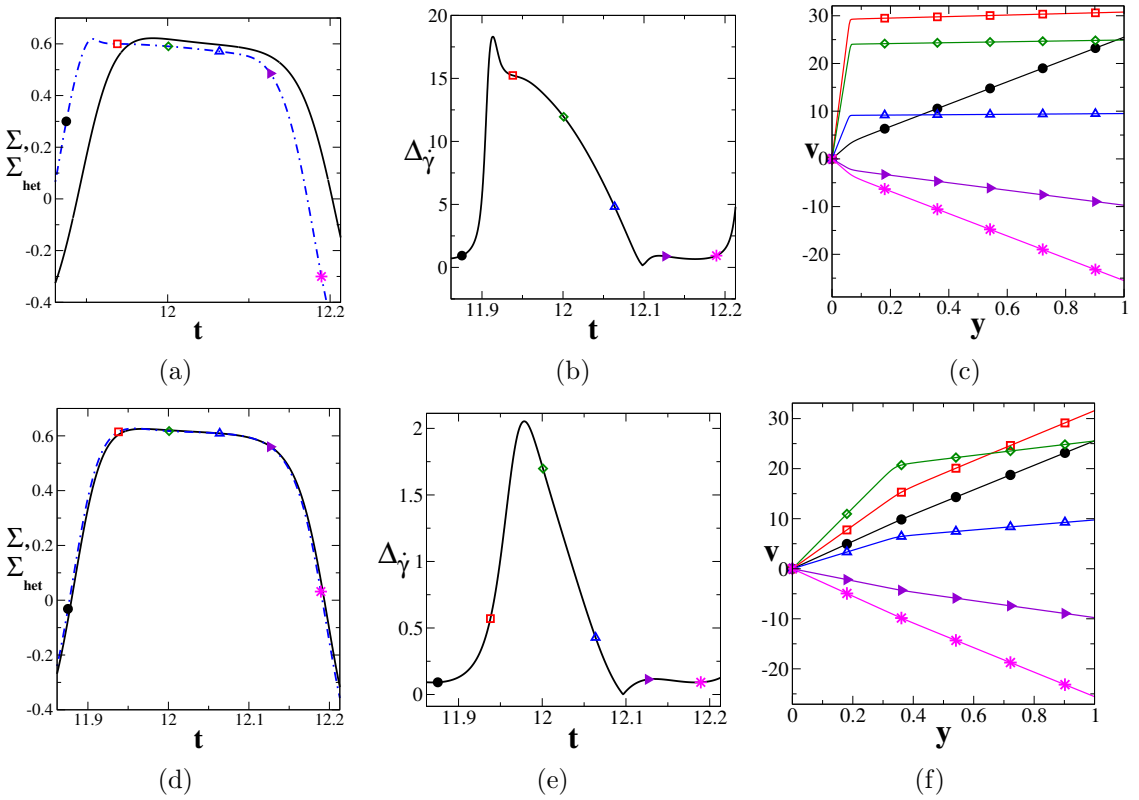


Figure 4.14: Material responses to LAOStrain in the nRP model for $\dot{\gamma}_0 = 31.6$, $\omega = 10.0$. **Top row:** the material has a non-monotonic underlying constitutive curve with $\beta = 0.4$. **Bottom row:** the material has a monotonic underlying constitutive curve with $\beta = 1.0$. (a) and(d) show the homogeneously-constrained (solid black) and heterogeneous (dot-dashed blue) stress response to LAOStrain with time, for positive $\Sigma$ (as the signal is symmetric). (b) and (e) show the corresponding evolution of the degree of banding. (c) and (f) give the velocity profiles across the cell at snapshots in time (indicated by the matching symbols in (a), (b), (d) and (e). The cell is curved with $q = 10^{-4}$; solvent viscosity is $\eta = 10^{-5}$.

elastic Lissajous-Bowditch curves shown in section 4.3.1. Homogeneous flow is not regained until the decreasing region of the stress response. This transient growth and decay of shear bands during the cycle occurs for the non-monotonic *and* monotonic cases, as previously predicted. Note here the similarity with the shear startup transient responses in figure 3.3 in chapter 3, and the significance of the overshoot in the stress to the onset of instability and growth of heterogeneous perturbations.

The leftmost graphs ((a) and (d)) give the homogeneously-constrained stress response to the imposed LAOStrain protocol (solid black lines), together with the stress response once heterogeneity, and thus banding, is allowed (dot-dashed blue lines). For both non-monotonic and monotonic parameter choices (top and bottom

rows of figure 4.14, respectively), the heterogeneous stress can be seen to separate from the homogeneously-constrained stress. This is seen more drastically in the non-monotonic case. The separation occurs due to the faster relaxation of the material stress when shear banding across the cell is permitted. This therefore suggests an note of caution for those in the community who seek to compare experimental results with homogeneously constrained system calculations, in calculating a material's "rheological fingerprint".

### 4.3.4 Shear banding in Lissajous-Bowditch curves

The use of Lissajous-Bowditch curves to represent material responses under LAOStrain has the ability to portray a large amount of detailed information within one curve. It is therefore useful to consider the effect of a large range of fixed frequencies and strain amplitudes in the Pipkin space in this greater level of detail. This is a representation technique used popularly in the LAOS literature. In the following sections I will form Pipkin diagrams: a collection of Lissajous-Bowditch curves, shown in a grid, displaying a range of the Pipkin space [144]. In figure 4.9, 4x4 grids of black crosses were marked; these crosses indicate the regions within the colour map where I have chosen to create Pipkin diagrams. The range of the Pipkin space selected is where the pin-point colour maps have predicted both stable and unstable material responses for a materials with a non-monotonic and monotonic underlying stationary constitutive curve. In the following section, I will apply all the previously described techniques to provide a full picture of the presence, and the persistence, of shear banding in the LAOStrain protocol, for both materials with a non-monotonic *and* monotonic constitutive curve.

#### Colour-coding regions of significant banding

In previous figures, the intensity of shear banding in a material that is allowed to vary spatially has been quantified using the degree of banding, $\Delta_{\dot{\gamma}_0}$. Recall equation 4.3.3. Regions of significant banding (experimentally measurable heterogeneity across a material sample) are defined as having $\Delta_{\dot{\gamma}_0} > 5\%$. The time-dependent degree of

banding during one LAOStrain cycle has previously been presented in this thesis on a time-axis ($\Delta_{\dot{\gamma}_0}$ vs. $t$) in figure 4.14. In the following figures the degree of banding is instead presented as a third dimension to the 2D-projection plots of the closed curve in $\Sigma(t),\ \dot{\gamma}(t),\ \gamma(t)$ space (Lissajous-Bowditch curves) by the addition of a colour gradient. This concise representation illustrates the time-dependent $\Delta_{\dot{\gamma}_0}(t)$ during one cycle of the material response at the alternance state as the system circulates one cycle of its resultant Lissajous-Bowditch curve in either the elastic or viscous representation. The following figures (4.15 and 4.16) use a gradient logarithmic colour scale to represent the magnitude of the degree of banding at any point in time during the cycle.

## 4.4 Pipkin Diagrams

Selecting a wide range of $\dot{\gamma}_0$ and $\omega$ across the Pipkin space enables a diagram to be built up of the material responses to the LAOStrain protocol. These data can be represented as a series of Lissajous-Bowditch curves [21, 112, 143] for each set of fixed $\gamma_0$ and $\omega$, a collection of figures termed a 'Pipkin diagram' [144].

A Pipkin diagram of material responses to an imposed LAOStrain protocol enables a comparison of features in the material behaviour across a range of amplitudes and timescales. Frequency is constant up each column, and strain-rate amplitude (in the shifted Pipkin space representation, consistent with the pin-point colour maps) is constant along each row. This representation of LAOStrain response data enables an effective characterisation of the material throughout the space of the Pipkin diagram. In recent literature, the term has been coined that this representation of material responses 'provides a "rheological fingerprint" of the material behaviour' [52, 53].

In each Lissajous-Bowditch curve within the Pipkin diagrams of figures 4.15 and 4.16, the material stress response to the imposed LAOStrain is plotted against strain (in the elastic representation) in (a) and strain rate (in the viscous representation) in (b) and describes the stress responses for materials with a non-monotonic and a monotonic underlying constitutive curve respectively. The system's full spatio-

temporal state is evolved numerically, encompassing full nonlinear dynamics (described in full in chapter 2) in a system where spatial variation is allowed. Any shear bands that develop over the measured cycle are quantified by the degree of banding and represented on the stress-response curve by the colour gradient. A colour scale is shown to the left of each figure for reference.

At low frequency, banding can be seen to become insignificant for the material with a monotonic underlying constitutive curve. However, as expected from the pin-point colour maps in section 4.3.2, significant shear banding is seen for sufficiently large strain-rate amplitude $\dot{\gamma}_0$ at low frequencies in LAOStrain for the material with a non-monotonic underlying constitutive curve. Moreover, the degree of banding becomes more pronounced after the stress overshoot in strain-rate: $\partial_{\dot{\gamma}}\Sigma < 0$, where the viscous criterion is satisfied [135]. Recall the tracing of the steady state constitutive curve and low-frequency LAOStrain in section 4.3.2.

At more moderate frequencies, shear banding can be seen for both materials with non-monotonic and monotonic underlying constitutive curves, as predicted by the linear stability calculations in the pin-point colour maps (figure 4.9). It is within this region of Pipkin space where the material response behaves as a combination of the viscous and elastic traits of the polymeric solution that shear banding is most evident. Moreover, it is the intrinsic time-dependence of the stress evolution with strain (rather than strain-rate) that appears to dictate the onset of instability and the subsequent formation of bands. This is reminiscent of previous work by Moorcroft and Fielding [135, 136], Adams and Olmsted [4], Adams, Fielding and Olmsted [2], that predicted the occurrence of shear bands in shear startup experiments upon the approach to the steady state when there existed an overshoot in the stress with strain (i.e. $\partial_{\gamma}\Sigma < 0$). These 'transient' bands existed for sufficiently large shear rates, independently of whether the material is known to shear band at steady state (*i.e.* even in materials that have a monotonic underlying constitutive curves [4]). The criterion derived in reference [135] for an elastically-driven instability to shear banded flow in a time dependent protocol included a curvature term as a correction to the overshoot term mentioned here. The inclusion of curvature in the criterion predicts the onset of instability to occur *before* the overshoot in

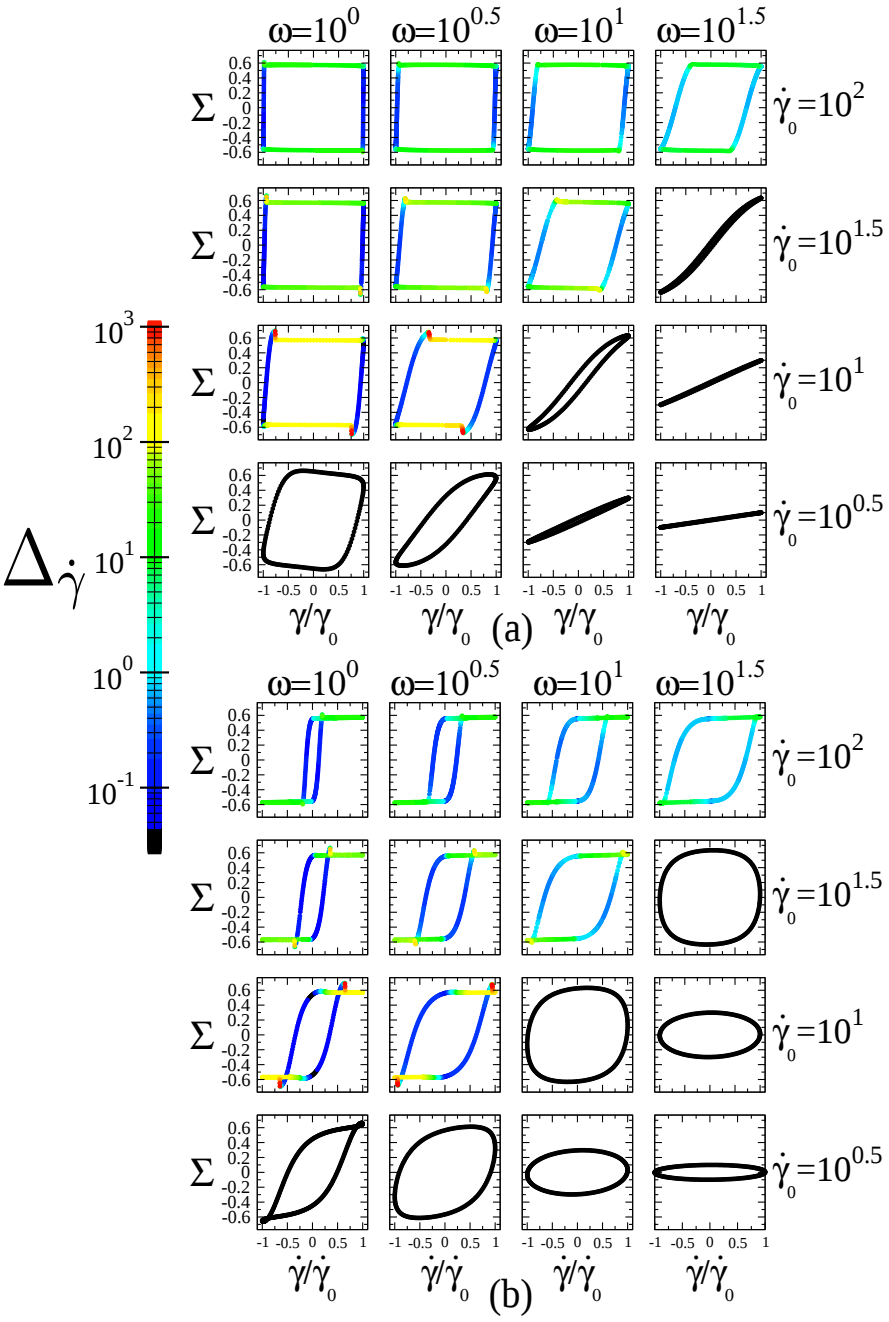


Figure 4.15: A Pipkin diagram of the stress response to imposed LAOStrain in the nRP model for a material with a non-monotonic constitutive curve ($\beta = 0.4$) in the elastic representation, in (a), and the viscous representation, in (b). Strain-rate amplitude $\dot{\gamma}_0$, frequency $\omega$, are employed, these are labelled at the top and right-hand side of each column and row respectively. The solvent viscosity is taken to be $\eta = 10^{-5}$. Allowing for heterogeneity, a curved cell is used, with parameters $q = 1 \times 10^{-4}, J = 512, l = 0.02$. The colours in the Lissajous-Bowditch curves represent the normalised degree of banding, indicated by the coloured log-scale on the left-hand of the grid.

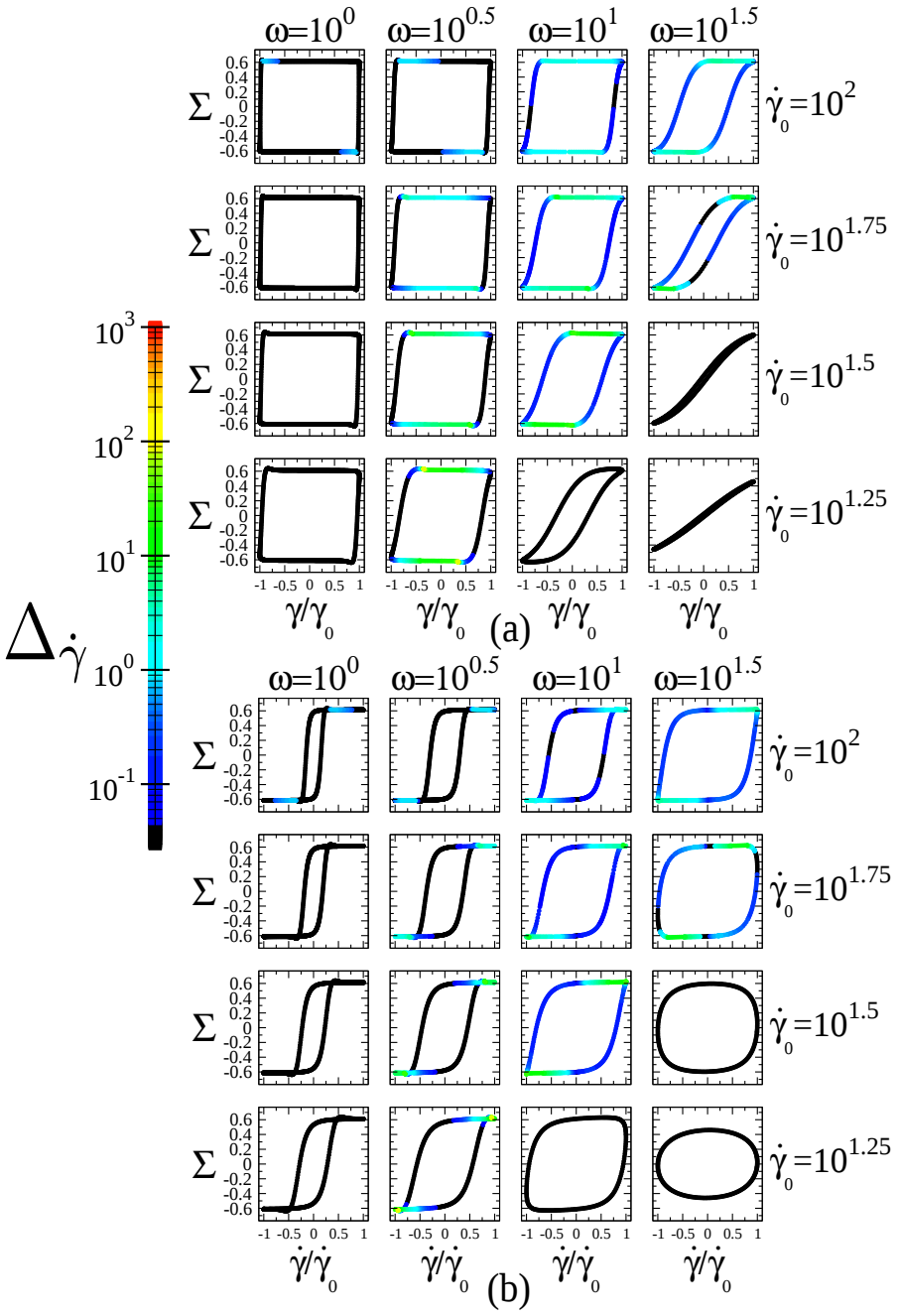


Figure 4.16: As in figure 4.15, for a material with a monotonic constitutive curve ($\beta = 1.0$).

strain for significantly strong negative (positive) curvature when the stress response is increasing (decreasing). Examples of the influence of curvature on the formation of shear-banded flow within the stress response cycle can be seen in figure 4.15 and figure 4.16: for frequency $\omega \geq 10.0$ and strain-rate amplitude $\dot{\gamma}_0 \geq 20.0$ significant shear banding occurs *before* the stress overshoot, with intensity increasing after $\partial_\gamma \Sigma < 0$ is satisfied.

It therefore follows that in the elastic representation of the Pipkin diagram, where stress is plotted against strain, that an overshoot (negative overshoot) in stress with increasing (decreasing) strain predicts an instability in the material flow regardless of the monotonicity of the underlying constitutive curve of the material up to the small curvature correction just discussed. There are, however, two distinct, different types of banding to be seen here: transient banding, and persistent banding. Transient banding is localised after (or around) the stress overshoot and the flow regains homogeneity as the strain is reversed at $\gamma(t) = \gamma_0$, whereas persistent banding *persists* throughout the LAOStrain cycle. There exists a region in the Pipkin space where, given a specific range of parameter values, significant banding exists for the whole of the LAOStrain cycle. This can occur for both non-monotonic and monotonic constitutive curves. Akin to the preliminary study in chapter 3, moderate frequency and strain-amplitude cause any heterogeneity that develops during the initial startup to LAOStrain to be captured by the reversing flow: without sufficient time for polymer stress to relax, shear bands remain in the flow as the deformation oscillates.

An alternative representation for this data is the third projection of the closed loop shown in figure 4.3: plotting strain vs. strain-rate. For fixed frequency (thus traversing up one vertical column in the Pipkin space), increasing strain, or strain-rate, will form a set of concentric circles where the diameter is determined by the imposed amplitude. This representation provides an alternative insight into the time-dependent nature of the LAOStrain protocol and highlights the role of the overshoot (in strain, or strain rate) for the onset of instability during the flow. Indeed, the overshoot in strain (for moderate frequency) or strain rate (for low frequency)

and the maximum degree of banding in the cycle are all located in the symmetric quadrants of this 2D projection where both strain and strain-rate are simultaneously increasing, or decreasing. Plots showing the data in this representation are included in Appendix II in section 4.8.

In the following sections of this chapter I consider effect of chain stretch on the stability to, and the existence of, shear bands within a polymeric material flow under LAOStrain. All figures and results shown in these sections use the full stretching version of the Rolie-Poly model [110], although still include just a single relaxation mode and its associated stretch dynamics. This model includes $Z$, the entanglement number of the material, and the associated chain-stretch relaxation time $\tau_R$. The inclusion of this timescale decreases the extent of monotonicity in the material's constitutive curve and, for monotonic curves, steepens the slope across the plateau-like region. Previously, this monotonicity has been controlled by the CCR-parameter $\beta$ (for sufficiently small $\eta$) which unlike $Z$, is not experimentally measurable and, at present, there exists no consensus to what $\beta$ should be taken as. I therefore include a discussion on the effects of these two parameters, and their impact on material stability to shear banding in LAOStrain. Moreover, it is hoped that these measurements of banding might help with the currently poorly defined $\beta$-value in the model.

## 4.5 Stretch effects

In this section I consider the stress responses, the instability of the initially homogeneous base state and any subsequent susceptibility to shear band, in the full stretching form of the Rolie-Poly model [110]. The inclusion of stretch into this polymeric model affects the relaxation dynamics of the polymer chain. The rate of retraction and convective constraint release (CCR) events in the material depend upon the amount of stretch in the system: large stretch is seen when the rate of externally imposed deformation is faster than the stretch relaxation time. Small stretch is seen along the polymer's chain when the converse is true. Chain stretch can have a stabilising effect on the material and has an associated relaxation time, $\tau_R$. In the Rolie-Poly model, $\tau_R$ is assumed to relate to the 'reptation' time ($\tau_d$) by the number of entanglements in the chain:

$$Z = \frac{\tau_d}{3\tau_R}. \tag{4.5.4}$$

Taking the limit of fast chain stretch relaxation ($\tau_R \to 0$), or, equivalently, an infinite number of chain entanglements ($Z$), the non-stretching limit of the model is recovered. The full constitutive equations of the Rolie-Poly model with chain stretch are defined in chapter 2.

Conceptually, the entanglement number quantifies the number of points along a polymer chain that form entanglements with other chains in the material. These entanglements restrict movement of the polymer and thus affect the relaxation dynamics of a polymer chain. $Z$ is defined by the ratio of the intrinsic material properties: $M_e$, the molecular weight of a segment of polymer chain between entanglements, and the molecular weight of the polymer: $M_w$, such that [127]:

$$Z = \frac{M_w}{M_e}. \tag{4.5.5}$$

In the following section, I consider the effect including chain stretch has on the underlying constitutive curve of a material as calculated by the sRP model. I then further the early, insightful study by Adams and Olmsted [2] into heterogeneous flow

the LAOStrain protocol. As in the non-stretching case, I consider the alternance-state stress response to imposed strain and the polymer's instability to the formation of shear bands in the flow. Results are again presented through pin-point colour maps and Lissajous-Bowditch figures. I also discuss the effect on stability to shear banding within the Pipkin space for the range of values of the CCR-parameter and the number of entanglements. This approach enables a stability phase diagram to be built up for significant shear banding in polymeric materials under the LAOStrain protocol.

### 4.5.1 The interplay of $Z$ and $\beta$ on the monotonicity of the constitutive curve in the sRP model

The convective constraint release (CCR) stress relaxation mechanism has an associated efficiency, described by the parameter $\beta \in \{0, 1\}$. The value of $\beta$ has an effect on the monotonicity of the material constitutive curve, depending also upon the quantity $Z$. Very few entanglements (small $Z$) increases the steepness of the intermediate $\dot{\gamma}$ plateau-like region of the material constitutive curve, regardless of $\beta$, compared with the counterpart curve for a highly entangled material. In terms of the RP-model definition of $Z$, small $Z$ implies a larger Rouse relaxation time $\tau_R$. This reduces the separation between the two timescales used in the sRP model, $\tau_R$ and $\tau_d$ and thus shortens the plateau region of the underlying constitutive curve.

The relationship between the monotonicity of the material constitutive curve and the values of $Z$ and $\beta$ is shown by the red line in figure 4.17 for a particular value of the solvent viscosity $\eta = 10^{-5}$. The red-shaded region indicates where the constitutive curve is non-monotonic for any $Z$ or $\beta$.

A comprehensive study of the tendency to form shear bands as a function of these two parameters was performed as follows:
For each set of values $(\beta,\ Z)$ I constructed a full pin-point colour map $(\dot{\gamma}_0,\ \omega)$. This colour map spanned $\dot{\gamma}_0 \epsilon \{10^{0.5}, 10^3\}$ and $\omega \epsilon \{10^0 - 10^2\}$ for a resolution of $20 \times 20$ co-ordinate pairs. Recall, for the construction of a pin-point colour map, one LAOStrain experiment is performed for each co-ordinate pair $(\dot{\gamma}_0,\ \omega)$. Once the alternance state is reached, the maximum degree of banding (as measured by the heterogeneous

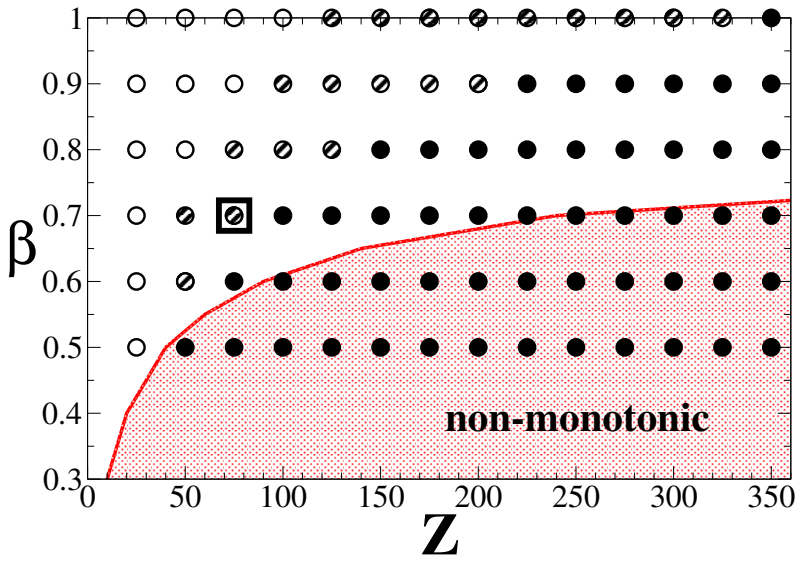


Figure 4.17: Effect of CCR parameter $\beta$ and entanglement number $Z$ (and so of chain stretch relaxation time $\tau_R = \tau_d/3Z$) on shear banding in LAOStrain. (Recall that the non-stretching version of the model has $\tau_R \to 0$and so$Z \to \infty$.) Empty circles: no observable banding. Hatched circles: observable banding, typically $\Delta\dot{\gamma}/\dot{\gamma}_0 \approx 10\% - 100\%$. Filled circles: significant banding $\Delta\dot{\gamma}/\dot{\gamma}_0 \geq 100\%$. For hatched and filled symbols we used the criterion that banding of the typical magnitude stated is apparent in a region spanning at least half a decade by half a decade in the plane of $\dot{\gamma}_0, \omega$, by examining maps as in figure 4.18 in by eye. The square shows the parameter values explored in detail in figure 4.18.

perturbations in the $\dot{\gamma}$-field) over one cycle is recorded, quantified by a logarithmic colour scale. Each pin-point colour map is described by one circle in figure 4.17.

Filled circles indicate that significant shear banding of at least $100\%\dot{\gamma}_0$ is seen in a reasonably large region (at least one half-decade in $\omega$ and one half decade in $\dot{\gamma}_0$) of the $\dot{\gamma}_0 - \omega$ plane. Hatched symbols indicate that less, but still significant ($10\%\dot{\gamma}_0$), shear banding is seen across the $\dot{\gamma}_0 - \omega$ plane (again, for at least one half-decade in $\omega$ and one half decade in $\dot{\gamma}_0$). Open symbols show immeasurable heterogeneity across the $\dot{\gamma}_0 - \omega$ plane. Together with the red line of the relation of $\beta$ and $Z$ to the monotonicity of the underlying constitutive curve of the material, these circles enable a phase diagram to be built up of shear banding intensity in LAOStrain across the parameter space.

This phase plane gives a clear indication of the extent of heterogeneity in the flow, at the alternance state. In particular, it is important to note that there is significantly measurable banding in a large region of this phase plane over which the

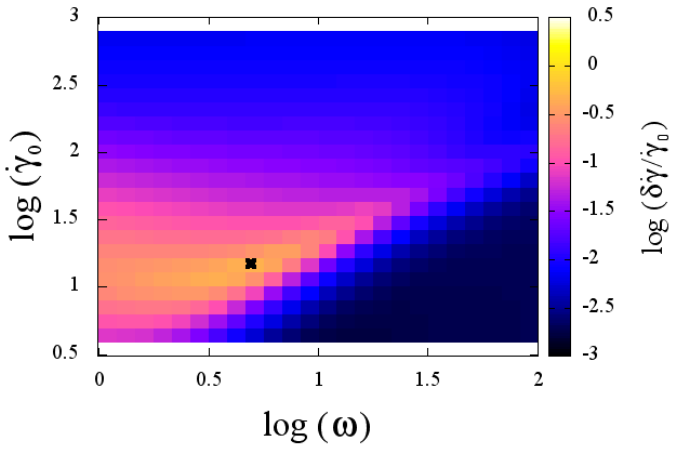


Figure 4.18: Pin-point colour map of the normalised degree of shear banding for the sRP model with a monotonic constitutive curve. Each point in the $\dot{\gamma}_0, \omega$ plane corresponds to one LAOStrain run with strain-rate amplitude $\dot{\gamma}_0$ and frequency $\omega$. For computational efficiency, these calculations are performed by integrating the linearised equations introduced in chapter 2. Reported is the maximum degree of banding at any point in the cycle, after many cycles. Model parameters: $\beta = 0.7, Z = 75$ (and so $\tau_R = 0.0044$), corresponding to the black box in figure 4.18. $\eta = 10^{-5}$ and cell curvature is $q = 2 \times 10^{-3}$. Note the different colour scale from figure 4.9. The model's full nonlinear dynamics for the $(\dot{\gamma}_0, \omega)$ value marked by the cross are explored in figure 4.19.

underlying constitutive curve is monotonic. At $Z = 50$ significant shear banding is seen where $\beta$ is such that there is a underlying monotonic constitutive curve ($\beta = 0.6,\ 0.7$ in figure 4.17). This value of $Z = 50$ is within the region of the value measured in a typical LAOStrain rheology experiment, which commonly range from 20-100 entanglements [10,28,107]. At fixed $\beta$, moving horizontally through the plane where $Z$ is increasing (thus decreasing $\tau_R$), the region of measurable, significant shear banding also increases whilst within the monotonic constitutive curve region of the $\beta - Z$ phase plane. At high $Z$ (towards the right-hand side of the phase plane) significant banding is measured for all values of $\beta$. As $Z$ is increased, the red perimeter line that encases the region of the $\beta Z$ plane where the underlying constitutive curve of the material is non-monotonic begins to reach a plateau in $\beta$. For infinitely large $Z$, the non-stretching limit of the Rolie-Poly constitutive equations is reached, where the monotonicity of the constitutive curve is no longer dependent on $Z$.

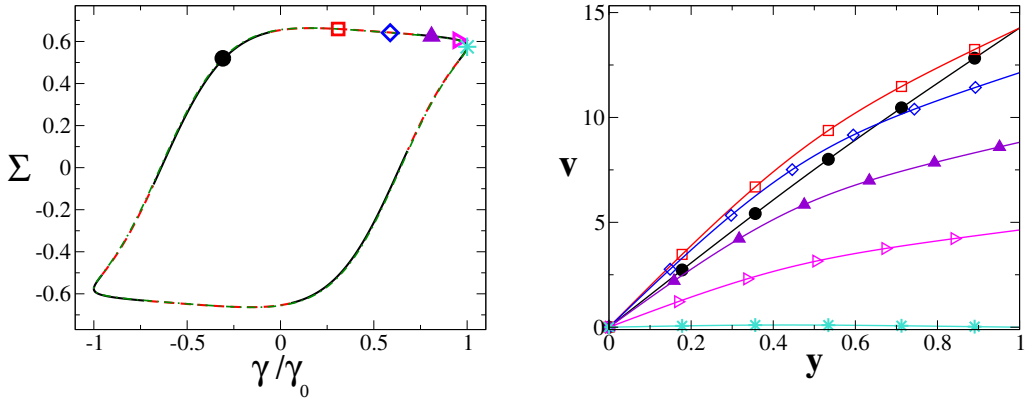


Figure 4.19: sRP model with a monotonic constitutive curve in LAOStrain of strain-rate amplitude $\dot{\gamma}_0 = 20.0$ and frequency $\omega = 8.0$. Model parameters $\beta = 0.7, Z = 75, \eta = 10^5$. Cell curvature $q = 2 \times 10^3$. Number of numerical grid points $J = 512$. **Left:** Stress response in the elastic representation. Solid black and red-dashed line: calculation in which the flow is constrained to be homogeneous. Red-dashed region indicates a positive eigenvalue showing instability to the onset of shear banding. Green dot-dashed line: stress response in a full nonlinear simulation that allows banding (almost indistinguishable from the homogeneous signal in this case). **Right:** Velocity profiles corresponding to stages in the cycle indicated by matching symbols in left panel.

Note here that the values used previously in the initial study by Adams and Olmsted [2] ($Z = 265, \beta = 0.728$) are indeed within the region of the $\beta - Z$ phase plane for which the underlying constitutive curve is monotonic. However, for the range more typically used in nonlinear rheology experiments [10, 28, 107], $Z = 265$ is much larger. In the following figures, I focus on a value of $Z$ within the range of experimentally achievable values, together with a $\beta$-value that lies well within the monotonic constitutive curve region of the phase space. Here, I use $Z = 75, \beta = 0.7$. This is highlighted by the thick black box in figure 4.17 and is shown as a hashed circle, indicating banding within a significantly large region (at least one half-decade in $\omega$ and one half decade in $\dot{\gamma}_0$) of the pin-point colour map that is at least 10% of the imposed strain-rate amplitude, $\dot{\gamma}_0$. The pin-point colour map for these parameters is shown in figure 4.18. The region of significant shear banding is described by the gradient colour scale to the right-hand side of the figure. This represents the degree of banding (normalised by the strain-rate amplitude) as calculated by integrating the linearised perturbation equations with time. Similar features are recovered at the low and high frequency limits as seen previously in the nRP case (figure 4.9).

The cross marked on figure 4.18 indicates the region in the $\dot{\gamma}_0, \omega$-plane where the Lissajous-Bowditch curve shown in figure 4.19 lies. The colour of the pin-point map at this set of parameters indicates the existence of shear banding in the alternance state. Figure 4.19 shows the Lissajous-Bowditch curve in the alternance state for both the case where homogeneity is artificially enforced (black-solid and red-dashed lines) and where heterogeneity is allowed (green dot-dashed line). The red-dashed line highlights the regions of the homogeneously-constrained material response where the eigenvalue (calculated via linear stability analysis and the associated eigenvalue matrix) is positive. The symbols on the Lissajous-Bowditch curve indicate the times at which the velocity profiles across the rheological cell are taken. Clear heterogeneity in the velocity profile (shown by the non-linear, bowing signatures) can be seen once the stress has passed the overshoot $\Sigma(\gamma)$. Before this overshoot (at the filled black circle) the profile is homogeneous. This homogeneity is regained following the strain-reversal point at $\gamma = \gamma_0$. By symmetry, the same pattern (with negative velocities) would be seen on the negative stress and decreasing strain region of the Lissajous-Bowditch curve.

## 4.6 Conclusions from chapter 4

In this first results chapter I have studied the stability of entangled polymeric solutions to the formation of shear bands under large amplitude oscillatory shear strain (LAOStrain). I have achieved this by employing the Rolie-Poly model in both the non-stretching and stretching limits.

Through this work, I have identified regimes of parameter space where shear banding is significant. I have shown that materials that have a monotonic constitutive curve (and therefore do not exhibit shear banding at the steady state but have been shown to form transient shear bands in time-dependent flow [2, 135, 136]) or a non-monotonic constitutive curve show significant shear banding in LAOStrain.

The following points may be concluded from the work presented in this chapter:

- Shear banding in LAOStrain is an intrinsically time-dependent phenomenon. Crucially, the work here reiterates the message from previous studies that shear bands form in entangled polymeric fluids during a protocol with a sufficiently strong time-dependence. Moreover, shear banding is seen in polymers under LAOStrain for non-monotonic *and* monotonic underlying constitutive curves.

- The inherently time-dependent nature of the LAOStrain protocol causes continual elastic shear banding triggers in the flow as the deformation is continually ramped up and down in magnitude. Any transitory elastic and unstable heterogeneous effects are no longer insignificant factors when measuring at the alternance state. Transient shear banding signatures akin to those seen in startup protocols have insufficient time to die out on the timescale of deformation and therefore shear banded flow is captured in the reversing flow.

- At low frequencies ($\omega \ll 1/\tau_d$), the material response to LAOStrain corresponds to a quasi-static strain-rate sweep up and down the steady state flow curve. Shear bands will form if the material's underlying homogeneously-constrained constitutive curve is non-monotonic: *i.e.*:

$$\frac{\partial \Sigma}{\partial \dot{\gamma}}|_{\omega \ll 1/\tau_d} < 0.$$

This corresponds to the *viscous instability* derived in ref. [135] for the simple shear startup case.

- At high frequencies ($\omega \gg 1/\tau_d$), shear banding occurs for a significant region of parameter space for materials with non-monotonic *and* monotonic constitutive curves. Here, it is the overshoot of the stress signal in strain and strong curvature effects that are the important mechanical triggers to instability and heterogeneous growth: *i.e.*:

$$\Big[ -\mathrm{tr}\underline{\underline{M}}\partial_\gamma \Sigma|_{\dot\gamma} + \dot\gamma \partial_\gamma^2 \Sigma|_{\dot\gamma} \Big]_{\omega \gg 1/\tau_d} < 0,$$

where $\mathrm{tr}\underline{\underline{M}} > 0$.

This corresponds to the *elastic instability* derived in ref. [135] for the simple shear startup case for high imposed strain-rates. Moreover, elastically-dominated responses to LAOStrain require the period of the oscillation to be less than the intrinsic relaxation time of the material:

$$\frac{2\pi}{\omega} \ll \tau.$$

- A map of shear banding intensity within the space of the experimentally measurable entanglement number $Z$ and theoretical CCR-parameter $\beta$ is shown, providing a roadmap for further experimental and theoretical studies on this subject. The map shows a significant region of the plane where shear banding is sufficiently intense to be measurable, but the material constitutive curve is monotonic.

In the following chapter I will consider the counterpart protocol to LAOStrain: large amplitude oscillatory shear stress (LAOStress). In a similar vein to the work in this chapter, I will consider the extent to which material response and susceptibility to the formation of shear bands under LAOStress can be understood, and predicted, by existing knowledge of the simpler step stress protocol (recall chapter 3). Refer-

ence [135] derived criteria for the onset of instability in this simple protocol; I employ this as a guide to understand the mechanisms and triggers to shear band formation in LAOStress.

# 4.7 Appendix I

## 4.7.1 Growth in the normal stress component, $\sigma_{yy}$

In section 4.3.1 it was suggested that the region of positive eigenvalue following the reversal in strain rate at $\pm\gamma_0$ could be accounted for by growth in the normal stress component perturbations, $\delta n$. In this appendix I present full nonlinear calculations of the heterogeneous growth of the normal stress component, together with the shear stress component, the degree of banding and the evolution of the viscoelastic stress with time under LAOStrain in the nRP model. The figures shown here are the counterparts to the right-hand panels of figures 4.7 and 4.8 in section 4.3.1 where the flow was constrained to be homogeneous. Regions of positive eigenvalue are shown here by the red-dashed lines within the homogeneously-constrained stress response; recall that these regions were coloured according to magnitude in figures 4.7 and 4.8. Figure 4.20 shows the first of these, for a material with a non-monotonic constitutive curve, $\beta = 0.4$.

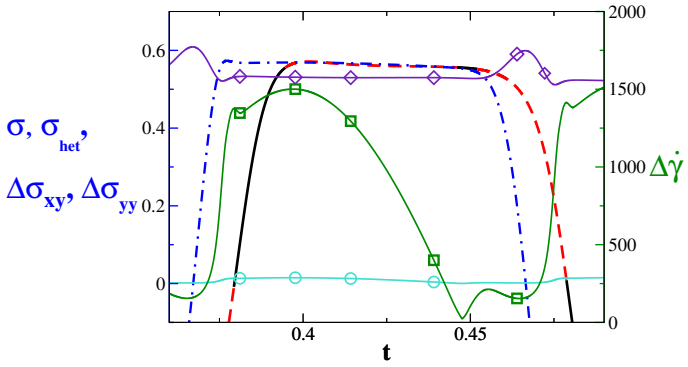


Figure 4.20: Evolution of the shear stress $\Delta\sigma_{xy}$(turquoise) and normal stress $\Delta\sigma_{yy}$(purple) components, the degree of banding $\Delta_{\dot{\gamma}}$(green) and the full viscoelastic contribution to the shear stress with time(black and red-dashed for homogeneous; blue dot-dashed for heterogenenous), to LAOStrain in a system where spatial variation is allowed and the underlying constitutive curve is non-monotonic ($\beta = 0.4$). Modelled by the nRP model, frequency $\omega = 31.6$ strain-rate amplitude $\dot{\gamma}_0 = 200.0$. $\{J, q, \eta\} = \{512, 10^{-4}, 10^{-5}\}$.

Clear growth in the magnitude of heterogeneity in the normal stress component $\Delta\sigma_{yy}$ can be seen in figure 4.20 where the eigenvalue becomes positive around the strain-reversal region of the response to LAOStrain. It is this region of positivity in the eigenvalue that can not be accounted for by the overshoot in stress with strain,

unlike the other region of positive eigenvalue in the material stress response. The spatial profile for this at the snapshots in time defined by the symbols in figure 4.20 can be seen in figure 4.21. Each profile for the shear rate $\dot{\gamma}$(green square), shear stress $\sigma_{xy}$(turquoise circle) and normal stress $\sigma_{yy}$(purple diamond) components have corresponding colour and symbol to the signal plotted against time in figure 4.20.

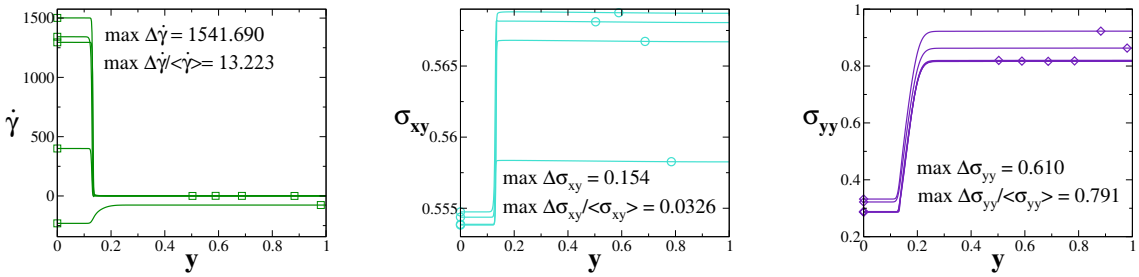


Figure 4.21: Spatial profiles across the rheometer cell for the shear rate $\dot{\gamma}$(green), shear stress $\sigma_{xy}$(turquoise) and normal stress $\sigma_{yy}$(purple) components in LAOStrain for a material in which the underlying constitutive curve is non-monotonic ($\beta = 0.4$). Each time-dependent quantity is normalised by its cycle-averaged value, represented by $< >$. Modelled by the nRP model, frequency $\omega = 31.6$ strain-rate amplitude $\dot{\gamma}_0 = 200.0$. $\{J, q, \eta\} = \{512, 10^{-4}, 10^{-5}\}$.

It is not unexpected that the degree of heterogeneity in the shear stress component is $\eta$-times smaller in magnitude: recall, $\dot{\gamma} \sim \frac{G\sigma}{\eta}$ ($G = 1$). Clear shear banding profiles can be seen in the $\dot{\gamma}$-field, though this is not the focus of this appendix. The spatial profile of $\sigma_{yy}$ vs. $y$ shows significant heterogeneity in the normal stress component. When normalised by the cycle-averaged normal stress, close to 80% banding is seen. Similar results are seen for a material with a monotonic constitutive curve: the counterparts of figures 4.20 and 4.21 are shown in figures 4.22 and 4.23 for $\beta = 1.0$.

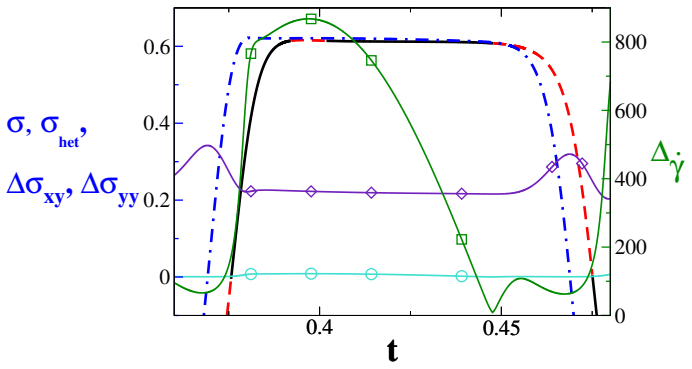


Figure 4.22: As in figure 4.20 for an underlying monotonic constitutive curve.

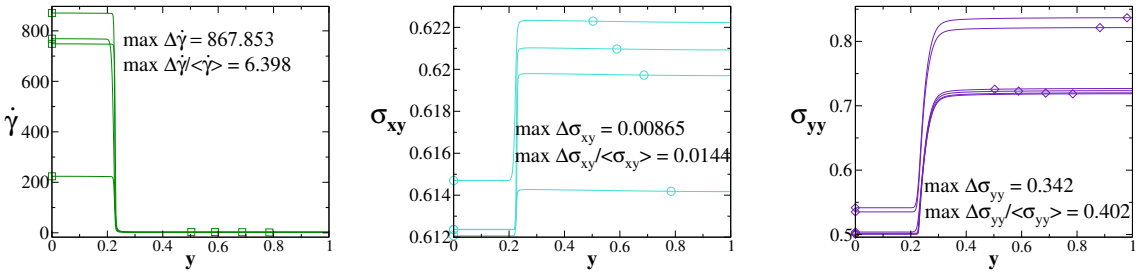


Figure 4.23: As in figure 4.21 for an underlying monotonic constitutive curve.

As before, significant growth in heterogeneity can be seen in the normal stress component when coincident with the positive eigenvalue at the strain reversal. In this case, where the material constitutive curve is monotonic, heterogeneity can be seen to be approximately 40% of the cycle-averaged normal stress component.

Clearly, this short exploratory study into the growth of heterogeneity in the normal stress component of polymeric flow in LAOStrain shows some interesting material properties. This would be worth expanding in further work to gain deeper insight into the unstable flow in material responses to LAOStrain. Recent work on the role of the normal stress component in this protocol has been published for the Giesekus model in reference [93].

# 4.8 Appendix II

## 4.8.1 Strain vs. strain-rate plane: concentric circle plots

Recall from section 4.2 that the elastic and viscous representations of Lissajous-Bowditch curves are 2D projections of a closed 3D curve in stress, strain and strain-rate, where these dynamical quantities form orthogonal axis. In this appendix I consider the 2D projection of strain vs. strain-rate. In this representation, the LAOStrain protocol forms an ellipse. For fixed frequency (thus traversing up one vertical column in the Pipkin space), increasing strain or strain-rate (as $\dot{\gamma}_0 = \omega\gamma_0$) will form a set of concentric circles where the diameter is determined by the imposed amplitude. A schematic of this for just one amplitude is shown in figure 4.24.

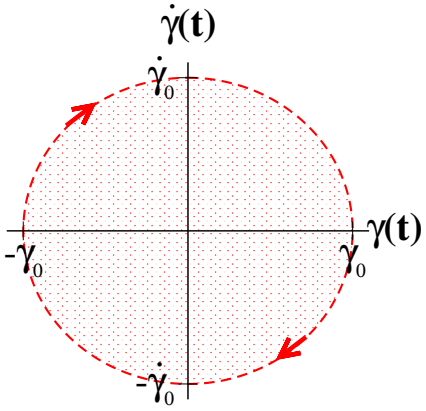


Figure 4.24: Fixed frequency circles: $\dot{\gamma}(t)$ vs. $\gamma(t)$.

Within each of the four quadrants of the plane, strain and strain-rate will either both be increasing or both decreasing, or increasing while the other decreases, and vice-versa. For instance, the top-left quadrant has $\gamma = -\gamma_0 \to 0$ and $\dot{\gamma} = 0 \to \dot{\gamma}_0$ thus both quantities are increasing. By symmetry, the bottom-right quadrant has both of these quantities decreasing.

Figure 4.25 shows four concentric circle plots in the strain vs. strain-rate plane. These plots are each built up for multiple $\dot{\gamma}_0$, measured in the alternance state. In each plot, the frequency is held constant; this is directly comparable to one column in the Pipkin diagrams in section 4.4, or one vertical line of pin-points in the colour maps in section 4.3.2. Strain-rate is increased, resulting in expanding circle diameter. In each plot, $\gamma_0 = 1$ is marked by a white circle as a guide to the eye.

Figures 4.25(a) and (c) have a fixed frequency of $\omega = 1.0$. As $\tau_d = 1$ in the units used here, this frequency of deformation is on the inverse timescale of the intrinsic relaxation time of the polymer, thus the viscous dynamics are expected to largely govern the material behaviour, though frequency is not sufficiently small for

the material response to trace the underlying constitutive curve. Here, the black line indicates the point at which - for each LAOStrain experiment that forms a concentric circle in this plane - there exists an overshoot (negative overshoot) in increasing (decreasing) stress with increasing (decreasing) strain-rate. This *viscous* ($\partial_{\dot{\gamma}}\Sigma < 0$) overshoot only exists for $\gamma_0 > 1$. The black line in figures 4.25(b) and (d), where frequency is fixed at $\omega = 10.0$, shows the point where the material passes instead through an *elastic* ($\partial_{\gamma}\Sigma < 0$) overshoot in stress with increasing strain (or the negatively-shearing alternative). At this faster frequency, material behaviour is described by the elastic, short timescale effects. Again, there is no overshoot in the stress when $\gamma_0 < 1$.

In all cases, whether the material has a non-monotonic or monotonic underlying constitutive curve, it is clear that the overshoot - in either strain, or strain-rate - is a crucial factor in predicting the onset of instability in a material. Following each overshoot the maximum growth in the linear perturbations is attained. Moreover, both these types of overshoot exist within the quadrants where strain and strain-rate are simultaneously increasing, or decreasing. This is unsurprising as for simultaneously increasing (or decreasing) $\gamma(t)$ and $\dot{\gamma}(t)$ $\partial_{\gamma}\Sigma = \partial_{\dot{\gamma}}\Sigma < 0$.

It therefore follows that the pin-point colour plots in figure 4.9 could instead be attained - and look identical - if only this simultaneously increasing (or decreasing) strain and strain-rate quadrant, rather than the complete cycle, was considered. I have indeed checked for this, though the data is not shown here.

In (c) the material has a monotonic underlying constitutive curve; it is thus not expected to see any perturbation growth as the frequency reaches the lower limit ($\omega \ll 1$). However, at $\omega = 1.0$ (as in (c)), this low frequency limit has not yet been reached and small perturbation growth can be seen following the overshoot line. This instability is transient and can be seen to decay away as the cycle is traversed (before the symmetrical negative overshoot is reached). Transient instability can also be seen in (a), (b) and (d) at for large strains. However, in these three cases, significant heterogeneity can be seen at intermediate $\gamma_0$. For $\gamma_0 > 1$, there exists a region where heterogeneity is present throughout the whole of each cycle. Any detail in the colour graduation here is not accessible for this linearised limit: the growth

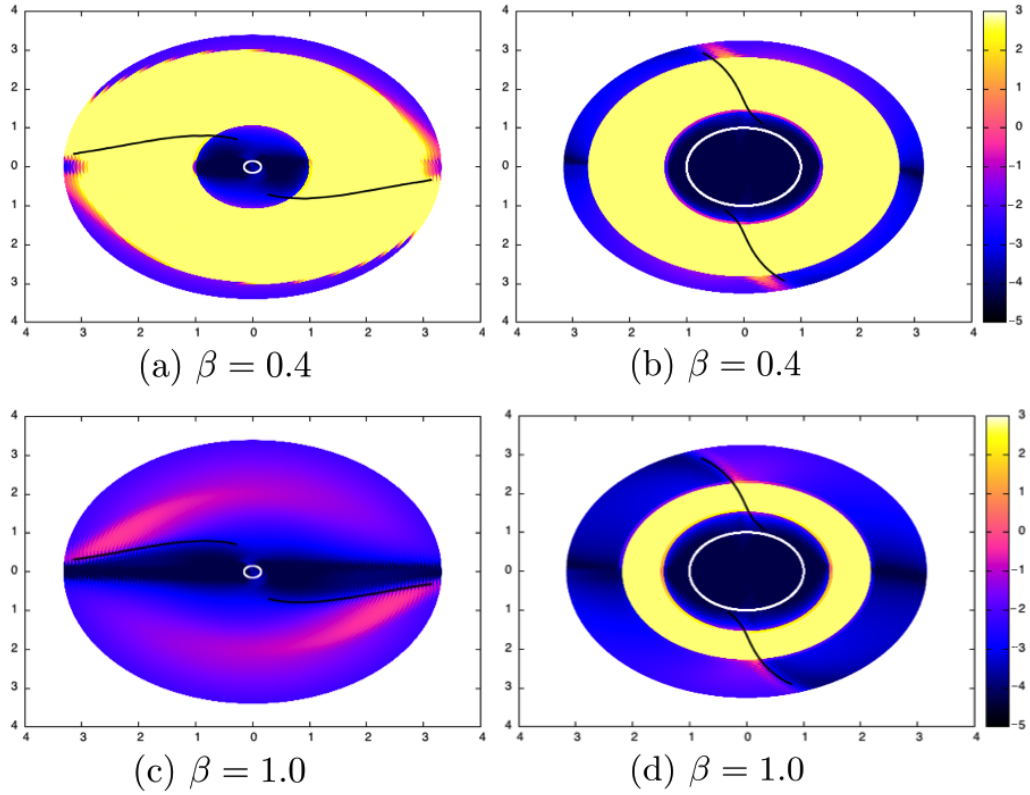


Figure 4.25: Concentric circle plots at fixed frequencies: $\omega = 1.0$ in (a) and (c), $\omega = 10.0$ in (b) and (d). One LAOStrain cycle forms one concentric circle; the circle's radius increases with increasing $\gamma_0$ (or, equivalently, $\dot{\gamma}_0$). A white circle indicates $\gamma_0 = 1.0$. The magnitude of the growth of linear perturbations to the system is shown by the colours; a scale is given as a guide to the right of each plot. All LAOStrain protocols are performed using the non-stretching Rolie-Poly model in a curved (constant imposed stress gradient) rheological cell, with parameters: $\{\eta, q\} = \{10^{-5}, 1 \times 10^{-4}\}$. Materials in (a) and (c) have a nonmonotonic underlying constitutive curve ($\beta = 0.4$); (b) and (d) have a monotonic constitutive curve ($\beta = 1.0$). Black lines in each circle indicate the time of overshoot of the polymer stress with increasing strain or strain-rate, as indicated in the subfigure captions.

of these heterogeneous perturbations to an otherwise homogeneous flow profile can only predict the onset of instability at an instant of time, any time-dependent growth or decay in heterogeneity following this onset can only be fully described through full nonlinear calculations (where heterogeneity in the flow is allowed).

It is this region, where heterogeneity persists throughout the whole cycle, that gives an illustrative example of the transient shear bands captured by LAOStrain seen earlier in the heterogeneous Pipkin diagrams (*i.e.* where significant shear banding persisted throughout the response cycle to LAOStrain). Within this regime of moderate applied strain amplitude and fixed frequency there is insufficient time for

full polymer chain relaxation before further deformation, thus any elastic instability leading to the formation of shear banded flow is captured by the strain reversal at $\gamma = \pm\gamma_0$. This feature occurs for materials with a non-monotonic *and* monotonic underlying constitutive curve.

# 5

# LAOStress in the Rolie-Poly Model

In this chapter I consider the response of an entangled polymeric fluid to an applied Large Amplitude Oscillatory Shear Stress (LAOStress, where the repeated 'S' has been dropped, as per convention [42]) using the Rolie-Poly (RP) model [110]. In chapter 3, I revisited the results found for the step stress protocol in the literature [135, 136]. Here, after a short recap, I consider how these findings, and the derived criteria, may apply to the LAOStress protocol. This nonlinear oscillatory protocol is of similar form to the previously used LAOStrain protocol. However, the oscillatory forcing is provided by controlled stress, rather than controlled strain [42, 101]. In a LAOStress experiment, stress is applied to a material and the corresponding strain-rate response is measured.

The current literature for LAOS protocols primarily focus on the strain-controlled LAOStrain protocol. Any existing literature on the LAOStress protocol has largely focussed on the response of gels and soft solids (that exhibit thixotropic behaviour

and yield-like transitions) such as Carbopol microgels, doughs and Xanthan gum [37, 42, 101, 103]. It was shown in [101] that materials can behave substantially differently in LAOStrain to LAOStress protocols due to their nonlinear response under the different cyclic loading histories. It thus follows that the use of LAOStress as a complementary protocol to LAOStrain may provide insight into additional material responses within the nonlinear regime.

Studies have also considered the inversion properties of measuring a stress response signal to strain-controlled LAOS in strain-controlled and stress-controlled rheometers [12, 101, 130]. Lauger and Stettin [101] also performed direct controlled stress - imposing a sinusoidal stress signal to the material sample - as an independent protocol. Results showed a large jump in strain over a small increase in stress in the crossover region from linear to non-linear behaviour in a gel-like material [101]. A similar feature for entangled polymeric fluids under LAOStress will be seen in the results that follow in this chapter. Moreover, I find that it is within the region of fast-transit in strain rate due to a small increase in stress that shear bands form in the response flow. This shear banding instability lies just inside the nonlinear regime of material behaviour where the non-monotonic, or weakly-sloping monotonic, region of the underlying constitutive is traversed. It is the effect of this short timescale growth in strain rate relative to the slow evolution (long timescale) of the stress, that is the catalyst to heterogenous growth and shear band formation in entangled polymers.

As discussed in chapter 3, the onset of instability to shear band formation in the step stress protocol can be analytically and numerically predicted. For fixed stress amplitude, it was found that the onset to shear banding occurs when the shear-rate response is both increasing and curving upwards:

$$\frac{\partial_t^2 \dot{\gamma}}{\partial_t \dot{\gamma}} > 0. \tag{5.0.1}$$

This is a model- and fluid-independent prediction that applies to all complex materials and depends only on the derivatives of the shear rate response with time.

In this chapter, I show that this criterion for step stress can also be applied to the

LAOStress protocol as a theoretical predictor to the onset of shear banding. I also consider the time-dependent eigenvalue (as found from linear stability analysis) and the evolution of heterogeneous perturbations (to the otherwise linearised system) during LAOStress, to assess the stability of an entangled polymeric fluid to the formation of shear bands. I extend this assessment over a range of imposed stress amplitude and frequency in a Pipkin-like plane [37].

Unlike in the LAOStrain protocol, shear banding in LAOStress is not found to persist throughout the whole response cycle for any regime of fixed amplitude and frequency. This is perhaps not unexpected as shear bands are not seen to persist to the steady state in the step stress protocol (unlike the shear startup protocol) regardless of the monotonicity of the material constitutive curve [16, 19, 43, 72, 85–88, 173]. Shear bands in LAOStress occur when the shear rate magnitude increases sharply over a short, fast increase in stress magnitude, akin to the 'yieldlike' transition described in some experimental literature [173, 174]. Moreover, these shear banded regions are localised to the region in the shear rate response when it is both increasing and curving upwards (for positive stress) or decreasing and curving downwards (for negative stress) in time, thus extending the message from the step stress criterion to the LAOStress protocol [135].

In the calculations that follow, I will consider the time dependent eigenvalue (calculated from the linear stability analysis matrix) and how this compares with the step stress criterion and regions of significant shear banding. Results are represented as responses against time, pin-point colour maps and pipkin diagrams where the Lissajous-Bowditch curves use logarithmic colour-gradients to describe the growth and significance of the emerging shear bands.

In the first part of this chapter, I consider the limiting case of the non-stretching Rolie-Poly (nRP) constitutive model equations. The tensorial and component forms of the constitutive equations for this model are given in chapter 2. Recall that the shear stress component $\sigma_{xy} = \sigma$, where the subscript is dropped for clarity, throughout this chapter (the notation $\sigma_{yy}$ for the normal stress component remains unchanged).

Later, I use the full stretching version of the Rolie-Poly model (sRP) to build up

a phase diagram describing the intensity of shear banding across a range of CCR-parameter ($\beta$) and entanglement number ($Z$) space during LAOStress. This is akin to that shown in chapter 4 for LAOStrain.

## 5.1 The LAOStress protocol

The LAOStress protocol involves an imposed, time-dependent stress onto a sample of material. The imposed stress is sinusoidally varied with time, parameterised by the stress amplitude, $\Sigma_0$, and frequency, $\omega$:

$$\Sigma(t) = \Sigma_0 \sin(\omega t). \tag{5.1.2}$$

Figure 5.1 shows a schematic of this LAOStress protocol. The shear rate response to this stress is then measured.

For large amplitudes and high frequencies, a caricature of the LAOStress could be a square-wave function of positively and negatively imposed stress, with an infinitely fast transition between the opposing regions. Using this caricature, it can be inferred that a way to approximate the time-dependent oscillatory LAOStress protocol is to combine a series of positive and negative simple step stress protocols. It therefore seems intuitive to interpret, at least as an initial guideline, to interpret the material response to LAOStress using the known characteristics and instability signatures of the step stress protocol. I discuss this in greater depth in section 5.3 and focus first

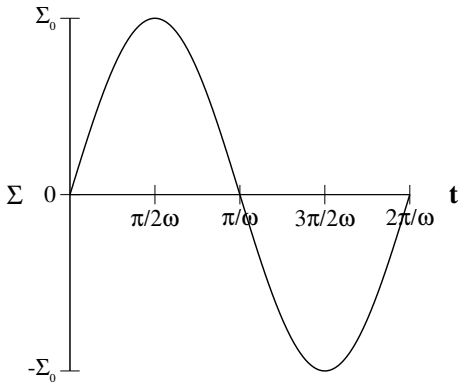


Figure 5.1: The LAOStress protocol: a time-dependent, sinusoidally varying stress is applied. The stress evolves, parameterised by the stress amplitude, $\Sigma_0$, and frequency $\omega$.

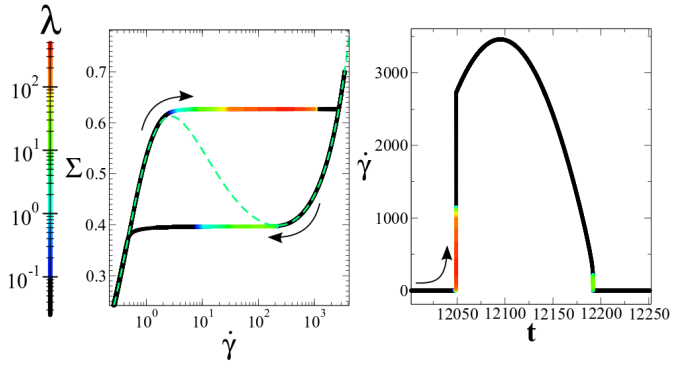


Figure 5.2: LAOStress in the nRP model with a non-monotonic constitutive curve. Model parameters: $\beta = 0.1$, $\eta = 10^{-4}$. Frequency $\omega = 0.01$ and stress amplitude $\Sigma_0 = 0.7$. **Left:** stress versus strain rate (shown on a log scale) in the positive stress part of the cycle. Colour scale shows eigenvalue, with negative values also shown as black. Green dashed line: underlying constitutive curve. **Right:** corresponding stress versus time plot.

here on eigenvalues as a predictor of instability to shear banding in LAOStress.

## Eigenvalues as a predictor of instability

In previous chapters I have considered the role of the time-dependent eigenvalue - found from the linear stability analysis matrix - in predicting the regimes of linear instability to the onset of shear banding during the LAOS protocol. The role of the eigenvalue in the step stress protocol was not explored in the previous work of Moorcroft and Fielding for step stress [135, 136], but I introduce it here for the LAOStress protocol. The process to find this eigenvalue for a general system is described in full detail in chapter 2.

Figures 5.2 and 5.3 show the regions where the eigenvalue is positive around the material response cycle to LAOStress with the amplitude being shown by the colourscale. Recall, a positive eigenvalue indicates a region where any heterogeneous perturbations to an initially homogeneous flow will grow, forming a heterogeneous, shear-bands.

The frequency of LAOStress used in figures 5.2 is low ($\omega \ll 1/\tau_d$), thus the stress amplitude is changing on a timescale lower than the intrinsic relaxation time of the polymer. As a viscous Lissajous-Bowditch curve ($\Sigma$ vs. $\dot{\gamma}$) the LAOStress response traces the linearly (to a good approximation) increasing branches of the material

constitutive curve shown by the green-dashed line. Note the viscous Lissajous-Bowditch curve shown here is in the regime of positive $\Sigma$ and $\dot{\gamma}$. It is logged along the horizontal axis to regain the familiar signature of the underlying constitutive curve and to enable detail to be seen at small and intermediate $\dot{\gamma}$. The right-hand plot shows this same data from the material response cycle as the shear rate evolution with time. Arrows indicating the evolution direction are included in both figure panels as a guide to the eye.

Whilst the high and low viscosity branches of the non-monotonic underlying constitutive curve of the material are traced by the slow sweep of LAOStress at this low frequency, the unphysical non-monotonic stress region is 'jumped' over. Moreover, for increasing stress, the local stress maximum is reached before 'jumping' occurs; for decreasing stress this local stress maximum is not in the same place. This behaviour is due to the metastability of entangled polymeric solutions as discussed in chapter 2 and is not unique to the LAOStress protocol. It is important to also note that the protocol is performed here in a weakly-curved cell and stochastic noise is neglected. This discards the possible effect of thermal nucleation events that in experiment are likely to trigger banding before the onset of linear instability [76]. Known to occur in low frequency experiments in particular, thermal nucleation events seeded (in simulation) through stochastic noise would contribute to shear banding during the 'jumping' mechanism in low-frequency LAOStress.

During the transit of this 'jumping' region, there is considerable growth in the eigenvalue, indicating growth of instability to heterogeneous perturbations and the region in which to expect shear-banded flow. Stability is regained as the strain-rate approaches the linearly increasing low viscosity branch of the constitutive curve at large strain-rate. After reaching the stress maximum ($\Sigma_0$), the stress then begins to decrease and thus, accordingly, so does the strain-rate. In a similar fashion to the increasing stress region, the material response at the low-frequency rate follows the steady state constitutive curve until the stress negative overshoot as stress decreases from $\Sigma(t) = \Sigma_0$ is reached. At this point, 'bottom-jumping' is observed and the response quickly rejoins the linear high viscosity region of the constitutive curve. Again, positive growth in the eigenvalue is seen during this 'jumping' region,

however, the extent of this growth is somewhat less and shorter-lived than in the increasing-stress case. This is due to the requirement on the material to increase its polymer stress compared with being forced to relax over a short period of time. The former leads to a far greater acceleration in the shear rate than required on the downward stress trajectory. *i.e.* 'top-jumping' is more unstable to the formation of shear banding than 'bottom jumping'. In this low-frequency regime, it follows that as the shear rate responds to the sinusoidally varying stress, the material will repeatably be exposed to an instability to the formation of shear bands as the material is passes through this unstable region of the response curve twice in every oscillation.

In the right-hand plot of figure 5.2 the same information is represented as the shear rate response against time. It is clear here that these unstable (positive eigenvalue) 'jumping' regions seen in the left-hand plot where the shear-rate response traverses from the high viscosity to the low viscosity branch of the material constitutive curve, occur during a very short period of time within the response cycle. This timescale is of order $\eta/G$ within this low-frequency regime. The stress evolves on a much longer timescale (for this selected low frequency) of $2\pi/\omega$. This large difference in timescales during the fast strain-rate jumping response leads to a relatively constant applied stress during the transition. It therefore follows that the step stress criterion applies during that transition, certainly to a good approximation. Moreover, it is seen later in this chapter that the criterion is both applicable (to good approximation) and satisfied in this region and significant heterogeneity is measured when the model's full spatiotemporal dynamics are considered.

Figure 5.3 shows the counterpart of figure 5.2 for model parameter values for which the underlying constitutive curve is monotonic. The frequency of oscillation is fixed at $\omega = 1.0$, the inverse relaxation timescale of the polymer. The green dashed curve in the left-hand panel (as in figure 5.2) shows the steady state constitutive curve, where stress is plotted against shear rate. This viscous Lissajous-Bowditch curve representation shows clear hysteresis behaviour in the material response to LAOStress when comparing the increasing- and decreasing-$\Sigma$ portions of the curve. Again, the plot shows the region of the shear rate response to LAOStress when

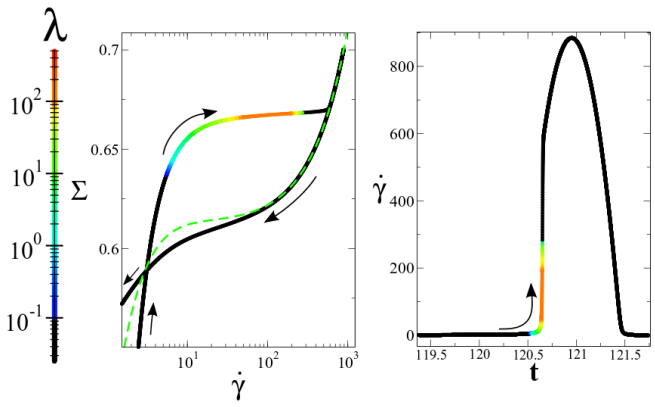


Figure 5.3: As in Fig. 5.2 but at a higher imposed frequency $\omega = 1.0$ and for a value of the CCR $\beta = 0.9$, for which the nRP model has a monotonic underlying constitutive curve. **Right:** corresponding stress versus time plot.

$\dot{\gamma}$ and $\Sigma$ are strictly positive. There is a less full agreement with the underlying constitutive curve of the material at this finite frequency compared with the low frequency results shown in figure 5.2 for a non-monotonic constitutive curve. Later in the chapter LAOStress is performed at low frequency for both non-monotonic and monotonic underlying constitutive curves using full spatial-temporal dynamics and good agreement is found with the steady state constitutive curve.

Positive eigenvalues (indicating regions within the shear rate response curve where the material is unstable to the onset of banding) can be seen to occur during the weakest slope of increasing stress. The right panel ($\dot{\gamma}$ vs. $t$) confirms this region of material instability to the formation of shear banded flow to occur when the shear rate response is both increasing and curving upwards with time, as predicted from the step stress criterion. However, unlike in the non-monotonic, low frequency case of figure 5.2, there is no positivity in the eigenvalue during the decrease of stress ($\Sigma > 0$). This is not unexpected for this higher frequency LAOStress protocol. On the downward stress sweep, shear rate response is more gradual as the stress is allowed to relax slower on the finite frequency timescale of LAOStress evolution.

Clearly, the analytically-found eigenvalue provides an insight into the stability of a material to form shear bands during LAOStress. In the following section, I use linear stability analysis to numerically analyse the growth of any heterogeneous perturbations to the initially homogeneous system. Integrating these perturbations

with time, I build a portrait of stability to shear banding across the plane of stress amplitude and frequency as a guide to the regions of interest (from a shear banding perspective) before further study.

## 5.2 Pin-point colour maps in LAOStress

A pin-point colour map represents the material stability to applied LAOStress over a wide range of frequencies ($\omega$) and amplitudes ($\Sigma_0$). Each coordinate pair (pin-point) on the colour map represents one LAOStress experiment: the sinusoidal stress is applied to the material sample for many (roughly 20) cycles until the strain-rate response has reached the alternance state. This is reached when any two consecutive cycles provide exactly the same response data, *i.e.* the material response is time-translationally invariant under $t \to t + 2\pi/\omega$. Once at the alternance state, reliable, repeatable measurements may be taken. For the pin-point colour maps shown below, each recorded pin-point displays the maximum value of any heterogeneous perturbations in the shear rate field to the linearised homogeneous system around one cycle in the alternance state. This quantity is taken as a magnitude and is normalised by the (effective) magnitude of the instantaneous strain-rate ($\dot{\gamma}(t) + 1.0$). The (+1.0) is added to avoid division by zero when the strain rate crosses zero. This does not significantly affect the results as shear banding tends to occur in the region where $|\dot{\gamma}(t)| \gg 1$. Thus, the degree of banding for LAOStress is defined as:

$$\Delta_{\dot{\gamma}}(t) = \frac{1}{N}\Big[|\dot{\gamma}_{\mathrm{MAX}}(t) - \dot{\gamma}_{\mathrm{MIN}}(t)|\Big], \tag{5.2.3}$$

where $N = |\dot{\gamma}(t)| + 1.0$, and $\dot{\gamma}(t)$ here refers to the instantaneous measured shear rate where heterogeneity has been allowed.

The change in normalisation factor here compared with that used in LAOStrain is due to the quick, localised shear banding events seen in LAOStress. This has already been seen in the short timeframe of eigenvalue positivity in figures 5.2 and 5.3. I found in practice that, setting the normalisation factor to the maximum shear rate during the cycle swamps any localised heterogeneity in the material flow during LAOStress and therefore do not use it here.

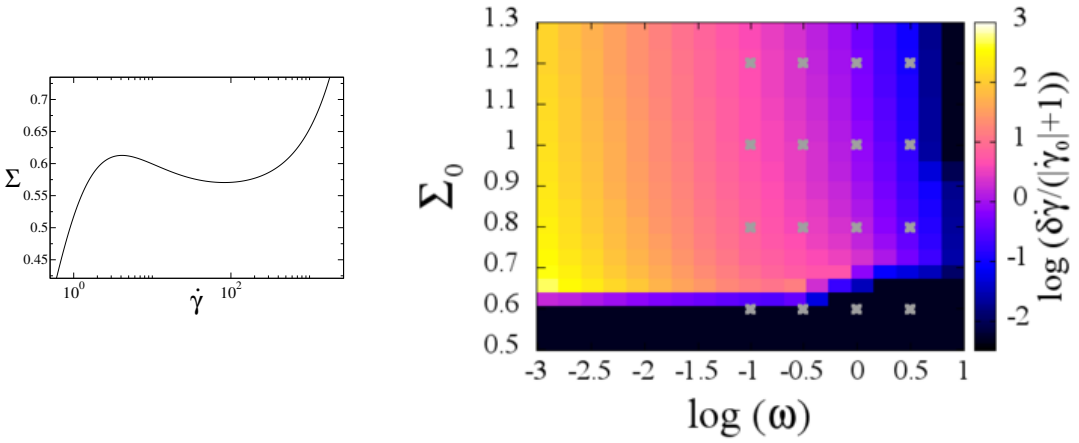


Figure 5.4: Colour map of the normalised degree of shear banding for the nRP model with a non-monotonic constitutive curve. Each coordinate pair in this $\Sigma, \omega$ plane corresponds to a particular LAOStress run with stress amplitude $\Sigma_0$ and frequency $\omega$. For computational efficiency, these calculations are performed by integrating the linearised equations. Reported is the maximum degree of banding that occurs at any point in the cycle, after many cycles. Model parameters: $\beta = 0.4, \eta = 10^{-4}$. Cell curvature $q = 2 \times 10^{-3}$. Crosses indicate the grid of values of $\Sigma_0$ and $\omega$ in figure 5.9.

Figures 5.4 and 5.5 show the LAOStress pin-point colour maps for materials with a non-monotonic and monotonic underlying constitutive curve, respectively. The plots show a grid 20 x 20 experiments, where one measurement (the normalised degree of banding measured from the integrated linearised equations of the nRP model) is presented per grid point. Visually, significant magnitudes of heterogeneity in the $\dot{\gamma}$ field are described in the colour map by brighter patches within the plane. This is quantified by the colour scale to the right of the figure. The underlying constitutive curves for each are shown to the left-hand side of each colour map.

In figure 5.4 the overshoot in $\Sigma(\dot{\gamma})$ of the non-monotonic constitutive curve occurs roughly at $\Sigma = 0.6$. This coincides with the low stress amplitude boundary of the bright region within the pin-point colour map at low frequencies ($\omega < 1/\tau_d$). Moreover, at the lowest frequency shown ($\omega = 10^{-3}/\tau_d$, recall $\tau_d = 1.0$), significant heterogeneity in the $\dot{\gamma}$-field occurs for all $\Sigma_0 > \Sigma_{\text{overshoot}} = 0.6$. At this low frequency,

where $\Sigma$ evolves at a much slower rate than the intrinsic relaxation time of the polymer, the underlying steady state constitutive curve of the material is traced during the LAOStress oscillation. As seen in figure 5.2, at these low frequencies, 'top-jumping' events occur at the top of the region of the negatively-sloping stress in the underlying homogeneously-constrained constitutive curve. It is within this region that growth of heterogeneous perturbations and the onset of shear banding occurs.

Imposing $\Sigma_0$ beyond the non-monotonic region of the constitutive curve (approximately $\Sigma_0 \geq 0.65$ here), where the underlying $\Sigma(\dot{\gamma})$ is monotonically increasing, bright signatures of significant heterogeneity can still be seen in the pin-point colour map. This is due to the nature of LAOStress as opposed to step stress: for the same applied $\Sigma = \Sigma_0$ in this monotonic region of the low-viscosity branch of the constitutive curve, step stress protocols only experience this one imposed stress. In contrast, LAOStress is an oscillatory function, thus requiring stress to be ramped up (and down) to the end amplitudes, $\pm\Sigma_0$, and exposing the material to all stress magnitudes up to this final maximum. LAOStress for large $\Sigma_0$ therefore requires the transition of the material through the non-monotonic region of the constitutive curve, and thus heterogeneity will always ensue in the part of the cycle where the overshoot of the underling $\Sigma(\dot{\gamma})$ is found. It is for this reason that heterogeneity (brightly-coloured section) extends to large $\Sigma_0$ for low frequency in figure 5.4.

As the frequency is increased (moving towards the right-hand side of the $\Sigma_0, \omega$ plane) significant heterogeneity is still only seen for $\Sigma_0 > 0.6$ and frequency $\omega < 1/\tau_d$. As the frequency becomes faster than the intrinsic relaxation time of the polymer ($\omega > 1/\tau_d$), any heterogeneity in the material under LAOStress significantly decreases. Once $\omega \sim 10$ there is no visible heterogeneity: the material remains homogeneous in its response throughout the measured alternance-state cycle. At this fast rate of evolution in $\Sigma$, there is insufficient time for any heterogeneous perturbations during the oscillation to grow large enough to lead to shear banded flow.

Figure 5.5 is the counterpart of figure 5.4 for a material with a monotonic constitutive curve. At high frequency, as before, the flow remains homogeneous as any

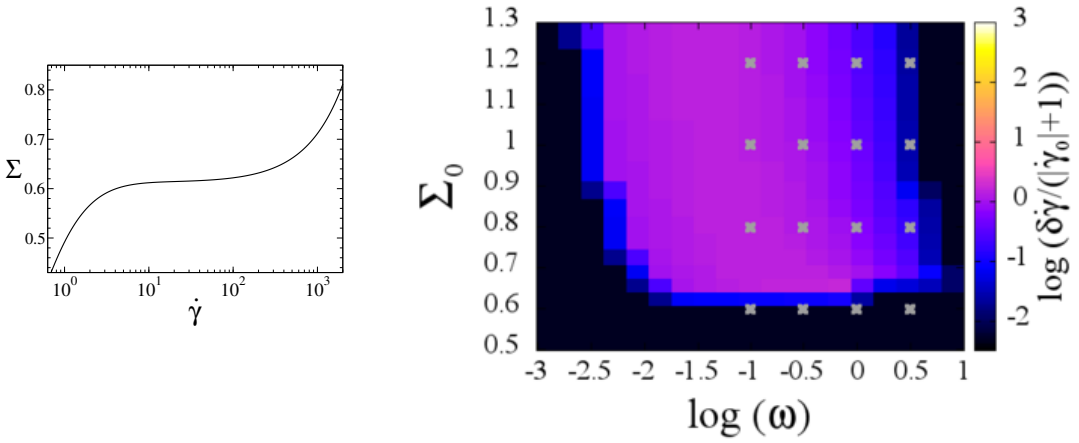


Figure 5.5: As in figure 5.4, but with a CCR parameter $\beta = 0.9$, for which the fluid has a monotonic underlying constitutive curve. Crosses indicate the grid of values of $\Sigma_0$ and $\omega$ used in the Pipkin diagram of figure 5.10.

heterogeneous perturbations to the sample have insufficient time to grow on the timescale of oscillation. At low frequency, where LAOStress traces the underlying constitutive curve of the material, there is no observable heterogeneity for any $\Sigma_0$. Here, the constitutive curve is monotonic, thus there is no strict 'top-jumping' mechanism during the slow LAOStress protocol and thus the resultant flow remains homogeneous throughout the cycle.

There is, however, significant heterogeneity in the $\dot{\gamma}$-field recorded at intermediate frequencies. This instability to the onset of shear banding occurs for $\Sigma_0$ greater than the stress at which the plateau-like region of the underlying monotonic constitutive curve is entered. For the material in figure 5.5 this is approximately $\Sigma_0 = 0.6$. Within this intermediate frequency range, the LAOStress response experiences instability to the onset of shear band formation due to the rapid transit (resembling top-jumping) of $\dot{\gamma}$ from low to high magnitude with time. The criterion (originating from step stress) $\frac{\partial_t^2 \dot{\gamma}}{\partial_t \dot{\gamma}} > 0$ is satisfied. As in the non-monotonic constitutive curve, heterogeneity is seen at each fixed frequency (vertical column) within this region of interest for all $\Sigma_0 > 0.6$ as the time-dependent criterion is satisfied for any sufficiently large $\Sigma_0$.

This significant heterogeneity within the $\Sigma, \omega$ plane is perhaps unexpected a priori for the monotonic constitutive curve material, however, the criterion for the

onset of shear banding is time dependent and irrespective of the monotonicity of the constitutive curve. LAOStress is an inherently time-dependent protocol and thus any time-dependent criteria may indeed apply (to some extent). I observe and discuss this in greater detail later in this chapter.

Note here that in fact for very weak slopes in the plateau region of a monotonic constitutive curve, homogeneity across this region at very low frequencies can not always be achieved: this very weak increasing slope causes the jump in shear rate to occur very quickly over a very small increase in stress, regardless of the fact that the constitutive curve itself is indeed monotonic in this region. It is this timescale with the applied stress in LAOStress that causes this numerical stiffness and difficulty to produce reliable results at this limit of weak slope. I found this to occur for $\beta = 0.7$ and thus choosing the monotonic constitutive curve CCR-parameter here as $\beta = 0.9$ avoided this numerical problem.

## 5.3 LAOStress: similarities to step stress

In the following section I will explore in detail the time-dependent material response to LAOStress, focussing particularly here on any similarities to the strain-rate response to step stress.

The fast transit of $\dot{\gamma}(t)$ over a wide range of $\dot{\gamma}$ amplitudes in response to LAOStress occurs in a time interval over which stress is approximately constant. It is therefore expected that the step stress criterion [135] should apply here, too. Note that in LAOStress, due to symmetry, the same expression for the criterion holds for negative stress and a decreasing, downward curving shear rate response.

I find that this criterion and time-dependent eigenvalue (described earlier) form good approximate predictors of instability to the formation of shear bands in an initially homogeneously flow. Both predictors of instability are used in the following figures. In previous chapters, red-dashed lines on the homogeneously-constrained flow response curves have indicated the regions of positive eigenvalue. In this chapter, however, red-dashed regions identify where the step stress criterion is satisfied,

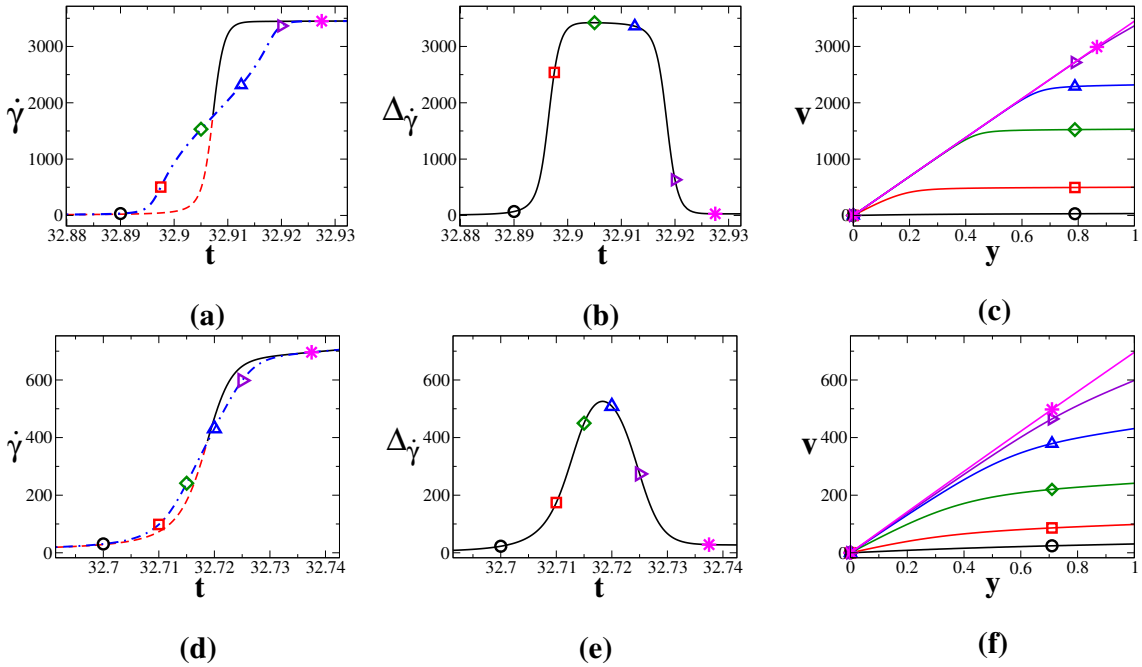


Figure 5.6: The time-dependent material response to LAOStress in the Rolie-Poly model for $\Sigma_0 = 0.7$, and $\omega = 1.0$, for a non-monotonic ((a)-(c), $\beta = 0.1$) and monotonic ((d)-(f), $\beta = 0.8$) underlying constitutive curve. (a) and(d) show the shear rate response with time. (b) and (e) show the evolution of the degree of banding across the cell over the same time-period as in (a) and (c). Coloured symbols in these plots correspond to the snapshots taken of the velocity profile across the cell, these are shown in (c) and (f) . The rheological cell is curved and the parameters $\{\eta, J, q, \tau_R\} = \{10^{-5}, 256, q = 2 \times 10^{-3}, 0\}$ are imposed. Red dashed regions of the leftmost plot indicate where the criterion for instability to the formation of shear bands is satisfied.

unless stated otherwise. Note that I find that the regions where the criterion is satisfied largely coincide with regions of positive eigenvalue in the shear rate response.

In figure 5.6, material responses to imposed LAOStress are shown in the same format as that presented earlier for step stress in figure 3.10 (chapter 3). The parameters and amplitudes are matched to the step stress case and a frequency on the timescale of the material's slowest relaxation time ($\omega = 1/\tau_d = 1.0$) is used. This frequency choice is well within the region of the pin-point colour maps where significant instability to the onset of shear band formation is seen for the material with a non-monotonic and that with a monotonic underlying constitutive curve (see figures 5.4 and 5.5). The portion of the cyclic material response to LOAStress is focused on the region where strain-rate is strictly positive and increasing. This region of the LAOStress shear rate response cycle is coincident with the fast 'top-jumping'

process seen when shown as a viscous Lissajous-Bowditch curve of increasing stress against strain-rate as seen previously in figure 5.2.

Plots (a) and (d) show the shear rate response to imposed LAOStress for a non-monotonic and monotonic constitutive curve respectively. The blue dot-dashed line shows the response when heterogeneity is allowed; the solid black and re-dashed line comprise the homogeneously-constrained response. (b) and (e) show the evolution of the degree of banding across the cell during the same segment of time as the shown shear rate response. (c) and (f) show the velocity profiles across the cell taken at snapshots in time during the protocol; these are indicated by the corresponding coloured symbols in the $\dot{\gamma}(t)$ and $\Delta\dot{\gamma}(t)$ plots.

There are some considerable similarities with the step stress case, as follows. In both (a) and (d), the shear rate response (when heterogeneity is allowed) can be seen to separate from the homogeneously-constrained shear rate during the steep, increasing region as the stress input increases from zero. It is within - and just ahead of - this region of separation in the shear rate, where both the imposed stress and shear rate are increasing, and the shear rate is curving upwards, that the step stress criterion is satisfied (red dashed line). During this region of fast increase in the shear rate magnitude, the degree of banding (in (b) and (e)) increases, then decreases as the flow regains homogeneity. The bowed velocity profiles in (c) and (f) give a visual representation of the transition between homogeneous and heterogeneous flow during this transiently shear-banded response.

Appreciable shear banding is seen here within this region for the case of a non-monotonic and a monotonic underlying constitutive curve. Recall this region of significant shear banding coincides with the fast transit across the $\Sigma(\dot{\gamma})$ curve seen previously for both non-monotonic and monotonic constitutive curves earlier in this chapter.

Note here the experimental impact of this fast transient banding in LAOStress. Within localised regions of the shear rate response there is significant transient band formation within the material flow. However, the maximum shear rate attained dur-

ing the response to LAOStress will be $\sim 1/\eta$ ($= 10^4$ in this case). The relative size of the shear rate when shear banding is expected, combined with the fast transient nature of the bands within the flow, may make this very difficult to experimentally capture. One way to counter this potential problem is to instead perform a LAOStress experiment about the weak slope of the constitutive curve: taking the mid-plateau value of stress as $\Sigma_{\text{plat}}$ and oscillating across a small $\Sigma$-spectrum, $\Sigma(t) = \Sigma_{\text{plat}} + \Delta\Sigma \sin(\omega t)$. This could provide some interesting and useful insight in future studies, but is however beyond the scope of this thesis.

In the following section, I introduce the Lissajous-Bowditch curve representations for reporting LAOStress material responses. I will focus on the full nonlinear dynamical calculations and the magnitude of any shear banding. Later, as in the previous chapter, I consider the material "rheological fingerprint" [52,53] of stability to shear banding under LAOStress by representing the material response to a range of imposed amplitude and frequencies.

## 5.4 Lissajous-Bowditch curves

The dynamical variables $\Sigma$, $\gamma$ and $\dot{\gamma}$ form a 3-D representation of a material response to LAOS protocols. The 2-D projections of this, $\Sigma(\dot{\gamma})$ and $\Sigma(\gamma)$, are called Lissajous-Bowditch curves [21,112] and provide physically intuitive representations of the data [143]. The *viscous* Lissajous-Bowditch curve, $\Sigma(\dot{\gamma})$, and *elastic* Lissajous-Bowditch curve, $\Sigma(\gamma)$, are typically used when the material stress response is dominated by more fluid-like or elastic-like behaviours respectively [52, 90, 101].

Figure 5.7 shows the shear rate response with time (in (a) and (d)) and the elastic ((b) and (e)) and viscous ((c) and (f)) Lissajous-Bowditch curves for the same parameters used in figure 5.6 for one complete cycle at the alternance state in LAOStress. The inset of figures (a) and (d) show the zoomed in region used in figure 5.6 where shear banding is evident. The data shown here are the material response when heterogeneity has been allowed in the material. Colour is used to indicate the emergence of significantly shear banded regions within the material

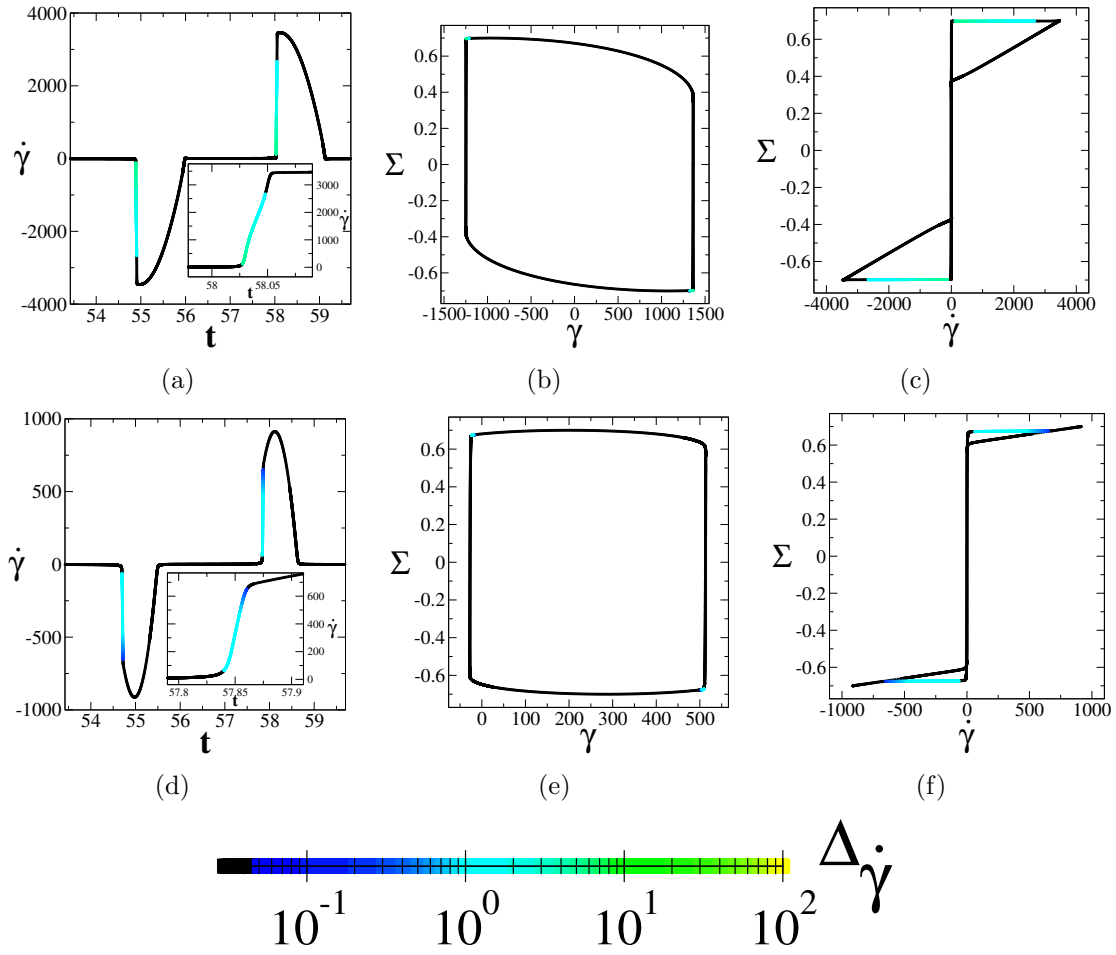


Figure 5.7: Heterogeneous stress responses of the LAOS(stress) protocol for $\Sigma_0 = 0.7$ and $\omega = 1$. The transient degree of banding is indicated by the colour gradients, quantified by the scale at the bottom of the figures . The top row has a non-monotonic constitutive curve (with $\beta = 0.1$); the bottom row has a monotonic constitutive curve (with $\beta = 0.8$). (a) and (d) give the transient shear-rate response to the imposed oscillatory stress, where the inset shows a zoomed in shear-banded region of the cycle. (b) and (e) show the same response for a Lissajous-Bowditch curve in the elastic representation, and (c) and (f) show this for the viscous representation.

response to LAOStress. This is quantified by the logarithmic gradient colour scale shown beneath the figures. Insignificant ($\Delta\dot\gamma < 5\%$) shear banding and homogeneous flow are shown in black.

Clearly, the elastic Lissajous-Bowditch response $\Sigma(\gamma)$ provides little information on the nonlinear flow response and the shear banded region [101]. In this representation, the heterogeneous flow is localised to a very small region of the curve. Therefore, for the remainder of this chapter I will not use this elastic representation

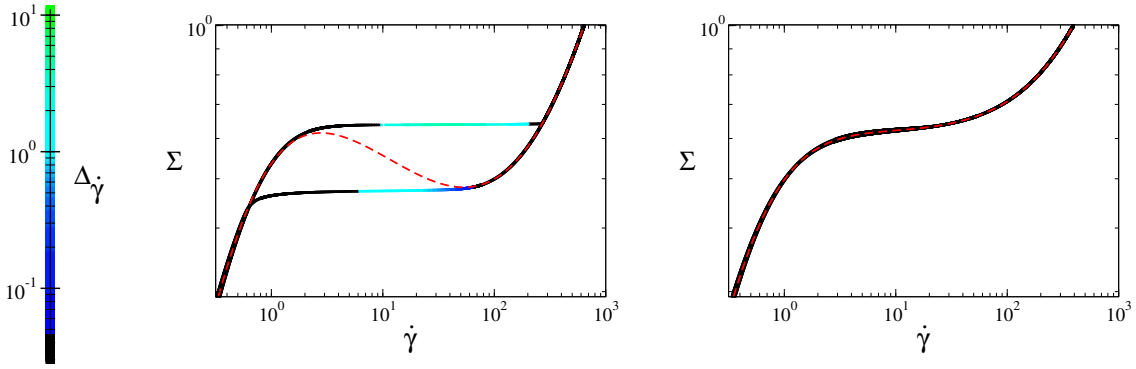


Figure 5.8: Low-frequency limit of LAOStress, with frequency $\omega = 0.01$, and applied stress $\Sigma_0 = 1$. The steady state constitutive curve formed from a series of shear startup experiments is shown in red-dashed lines. The thick, gradient-colour lines use the log-scale code in previous figures for the degree of banding. The cell is curved, and the parameters $\{\beta, \eta, J, q, dt, \tau_R\} = \{0.1, 10^{-3}, 256, 2 \times 10^{-3}, 10^{-6}, 0\}$ are used.

of the data and focus only on the $\dot\gamma(t)$ and viscous $\Sigma(\dot\gamma)$ responses.

Combining the representations of the data in figures 5.6 and 5.7 provides an in-depth overview of the existence of transient shear banding in an entangled polymeric material during LAOStress. Certainly, for $\Sigma,\ \omega = 0.7,\ 1.0$ used here, significant shear banding forms when the shear rate response quickly transits over a large range of $\dot\gamma(t)$ with only a small change in $\Sigma$ and $t$. This occurs when $\dot\gamma(t)$ is increasing (decreasing) and curving upwards (downwards) for positive (negative) $\Sigma(t)$, thus satisfying the criterion for the onset of banding in the flow. Figure 5.7 illustrates that this region of shear banding is indeed coincident with the sharp increase in $\dot\gamma(t)$ and the 'top-jumping'-type behaviour of the viscous $\Sigma(\dot\gamma)$ curve. For this moderate frequency, this behaviour occurs for both a non-monotonic and a monotonic underlying constitutive curve. However, at low frequency ($\omega \ll 1/\tau_d$) it was shown in figure 5.5 that homogeneity is recovered for all imposed $\Sigma_0$ when the constitutive curve is monotonic. Figure 5.8 shows this for a material where spatial heterogeneity has been allowed.

Here, the underlying constitutive curve of the material is shown as a red-dashed line and the stress and shear rate are strictly positive in this region. Significant shear banding is represented, and quantified, by the gradient colour. Top- and bottom-jumping mechanisms are seen on the increase and decrease of LAOStress

respectively. Homogeneous flow is regained as the heterogeneous response traces the underlying homogeneously-constrained constitutive curve in the high- and low-viscosity branches. As the non-monotonic region of the constitutive curve is quickly traversed by the heterogeneous response, there is significant shear banding. Indeed, this was predicted by the positive eigenvalues in figure 5.2. Conversely, there is no shear banding for the material with the monotonic constitutive curve. At this low frequency, the homogeneous flow traces the underlying constitutive curve for all $\Sigma(t)$.

In the following section, I focus on the mid-range frequency region of the (equivalent) Pipkin space (where the vertical amplitude axis is now shear stress amplitude, $\Sigma$) for the LAOStress protocol. I assess the material response and the emergence of any shear banding during the protocol at a range of fixed applied stress amplitudes and frequencies, as described by the crosses on the pin-point colour maps in figures 5.4 and 5.5.

## 5.5 Pipkin diagrams

Figures 5.9 and 5.10 show the Pipkin diagrams for the material responses to imposed LAOStress at a range of fixed frequency and stress amplitudes. In both figures, (a) shows the strain-rate ($\dot{\gamma}(t)$) response with time, and (b) gives the viscous Lissajous-Bowditch representation ($\Sigma(\dot{\gamma})$). Each response is the measurement for one cycle at the fixed parameters, in the alternance state. In figure 5.9, the material has a non-monotonic underlying constitutive curve (with $\beta = 0.4$) and figure 5.10 has a monotonic constitutive curve (with $\beta = 0.9$) with a sufficiently steep plateau-like region to ensure feasible numerical study. Significant shear banding is quantified by the logarithmic colour scale shown to the left of each set of Pipkin diagrams. Homogeneous flow and insignificant shear banding ($\Delta\dot{\gamma} < 5\%$) is shown as black.

As expected from the pin-point colour maps in figures 5.4 and 5.5, there is significant heterogeneity in the material response to LAOStress within this moderate frequency range for sufficiently large $\Sigma_0$. This can be seen in both figure 5.9 and 5.10: for $\Sigma_0 = 0.6$ the material response remains homogeneous throughout the cycle.

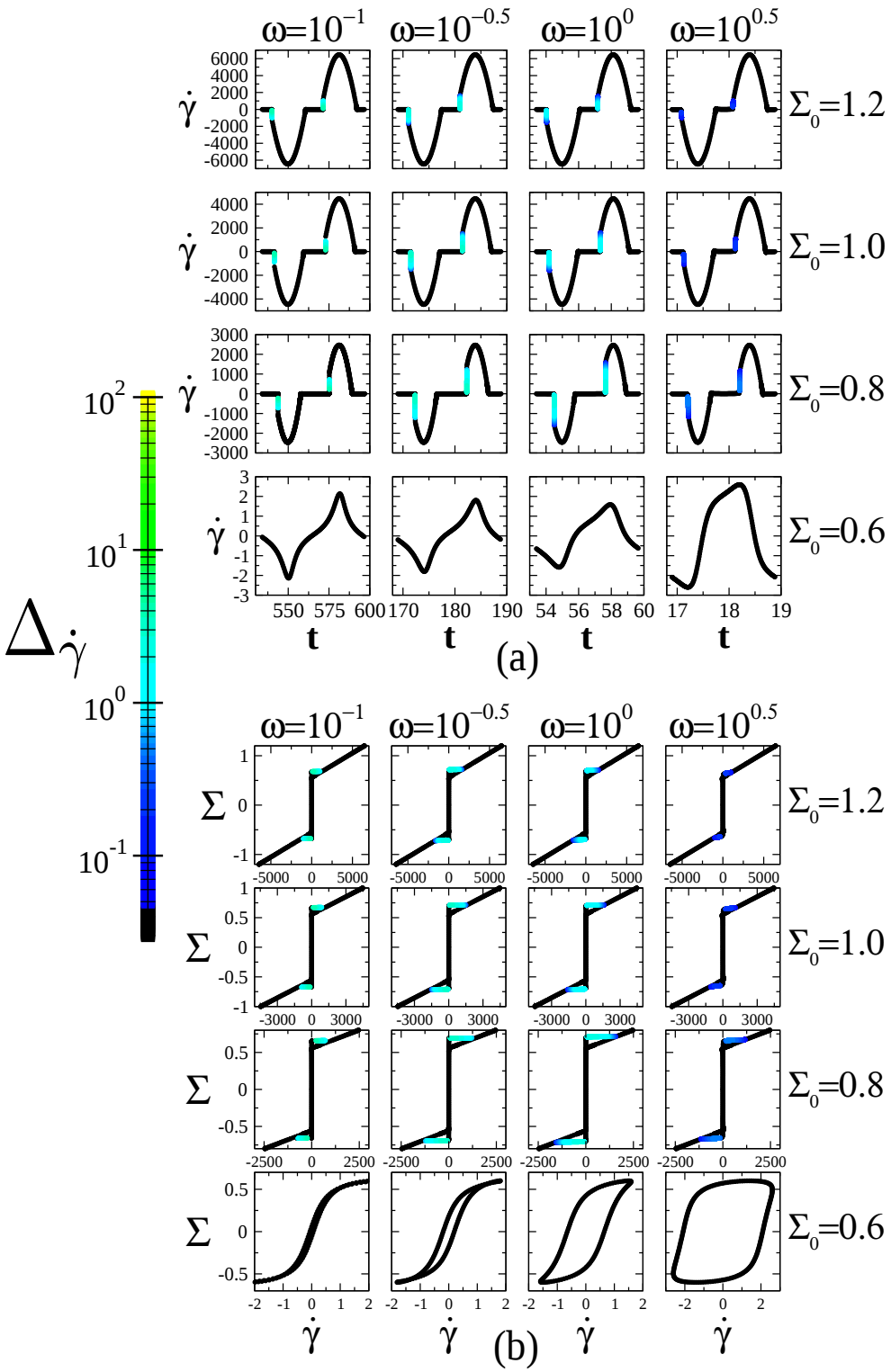


Figure 5.9: Lissajous-Bowditch curves in LAOStress for the nRP model with a non-monotonic constitutive curve. Results are shown as shear-rate vs. time in (a), and in the viscous representation of stress vs. strain rate in (b). Columns of fixed frequency and rows of fixed strain-rate amplitude $\dot{\gamma}_0$ are labeled at the top and right-hand side. The colour scale shows the time-dependent degree of shear banding. Model parameters: $\beta = 0.4, \eta = 10^{-4}, l = 0.02$. Cell curvature: $q = 2 \times 10^{-3}$. Number of numerical grid points $J = 512$..

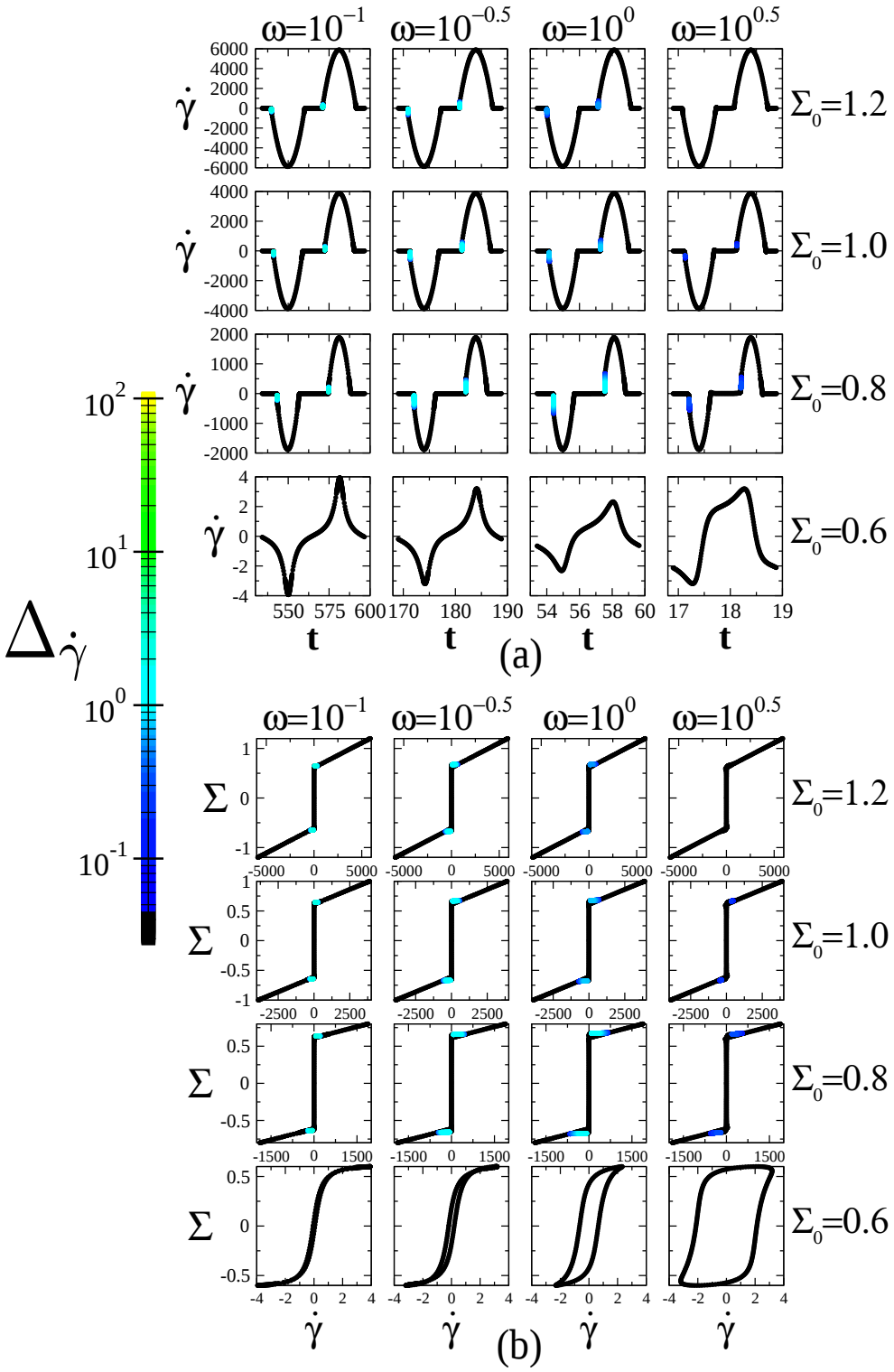


Figure 5.10: As in figure 5.9 but for a value of the CCR parameter $\beta = 0.9$, for which the fluid's underlying constitutive curve is monotonic. Number of numerical grid points $J = 512$.

However, for $\Sigma_0 \geq 0.8$ significant shear banding is seen for both the non-monotonic and monotonic underlying constitutive curves. At the largest frequency shown here, $\omega = 10^{0.5}$, the magnitude of the shear banded regions is smaller. This is not unexpected, as seen in the pin-point colour maps, stability to the formation of shear bands is regained at large frequencies irrespective of the monotonicity of the constitutive curve. This is due to the rate of the LAOStress oscillation: there is insufficient time for any seed of heterogeneity to grow and form a shear band within the flow [77].

In the figures shown throughout this chapter so far, it can be noted that the step stress criterion [135] does indeed predict the onset of instability to shear banding in the material response. It is still the simultaneous increasing magnitude and positive curvature of the shear rate response (here, for LAOStress, coupled with the positive, increasing imposed stress) that satisfy the condition for instability to the formation of shear bands. Again, by the symmetry of the LAOStress protocol, the opposite of these conditions (for negative, decreasing stress and shear rate response) follows for the second half of the cycle (not shown here).

Clearly, it is possible (and indeed helpful) to interpret the material response and any susceptibility to the formation of heterogeneous, shear banded profiles, by the understanding and experience of the simpler, step stress protocol. I have further shown here that measurable, significant shear banding is found over a wide range of the $(\Sigma_0, \omega)$ space for materials with a non-monotonic *and* monotonic underlying constitutive curves.

All of the above results use the non-stretching limit of the Rolie-Poly model. In the following section I introduce polymer chain stretch effects and look to confirm the existence of these shear banded profiles even with these additional physically relevant material properties that tend to stabilise a material against banding. Moreover, I consider a range of values of the experimentally measurable entanglement number $Z$, together with the convective constraint release parameter $\beta$ to form a phase plane of significant shear banding intensity in a polymeric material under the LAOStress protocol. I hope this will prove a useful roadmap for experimentalist and

theoreticians alike.

## 5.6 Stretch effects

The inclusion of polymer chain stretch into the numerical model adds another intrinsic material timescale to be considered when analysing the relaxation dynamics of an entangled polymer solution or melt. Chain stretch tends to stabilise the system against banding. However, as will be seen later, shear banding is still nonetheless predicted in LAOStress even in regimes where non-trivial chain stretch develops.

In contrast to the non-stretching Rolie-Poly (nRP) model used previously in this chapter, the full stretching version of the RP model used here is referred to as the sRP model. This three-dynamical variable model is defined in full in equation 2.39, chapter 2. The addition of chain stretch in the sRP model includes the experimentally measurable entanglement number $Z$ and the related chain-stretch relaxation time $\tau_R$. Defined as [110, 127]:

$$\tau_R = \frac{\tau_d}{3Z}. \tag{5.6.4}$$

thus, $\tau_R$ is a faster relaxation dynamic in the polymer as $\tau_R^{-1} \gg \tau_d^{-1}$ for a sufficiently entangled solution (large $Z$).

It follows that chain stretch only becomes important for large imposed shear rates ($\dot{\gamma} > \tau_R^{-1}$). This corresponds to shear rates approaching the low viscosity branch of the constitutive curve towards the end of the non-monotonic or weakly increasing monotonic region of the constitutive curve. As already shown in this chapter, it is within this region of fast $\dot{\gamma}$ transit over a small increase in $\Sigma$, that shear banding may occur. It is thus found that stretch effects in the polymer are indeed important (to some degree) in determining the extent of any shear banding that may form in the LAOStress protocol.

Figure 5.11 is the counterpart to figure 4.17 in chapter 4. It shows a map of shear banding intensity in a material under the LAOStress protocol, measured over a range of $\Sigma_0$ and $\omega$ for fixed parameters $\beta$ and $Z$. By varying these parameters, a phase plane may be built up to enable insight into the effect on the monotonicity of the material constitutive curve and the intensity of significant, measurable shear band formation in the flow during the experiment (when measured in the alternance

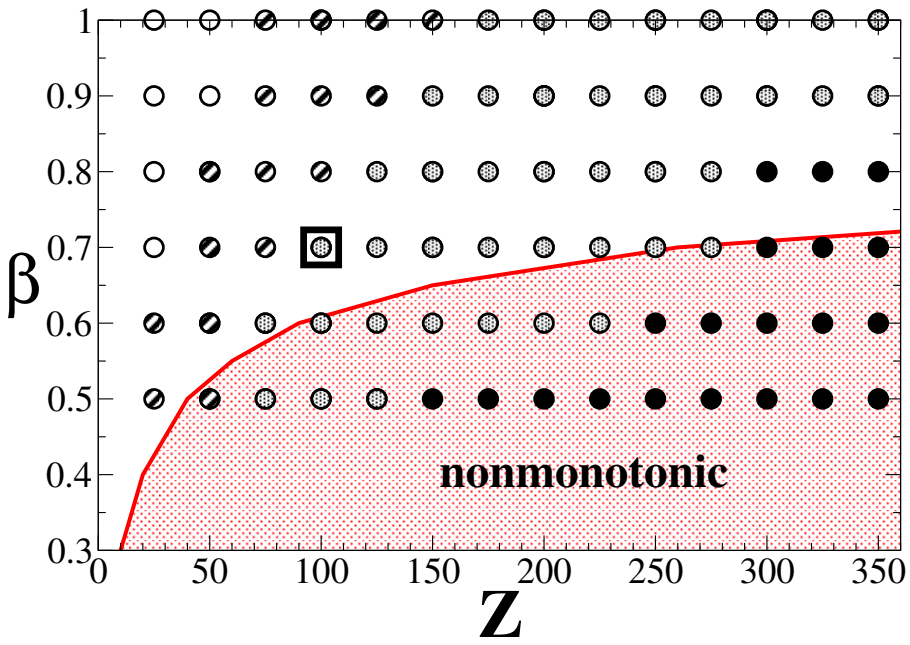


Figure 5.11: Effect of CCR parameter $\beta$ and entanglement number $Z$ (and so of chain stretch relaxation time $\tau_R = \tau_d/3Z$) on shear banding in LAOStress. (Recall that the non-stretching version of the model has $\tau_R \to 0$ and so $Z \to \infty$.) Empty circles: no observable banding. Hatched circles: observable banding, $\Delta_{\dot\gamma}/(1 + |\dot\gamma(t)|) = 10\% - 31.6\%$. Dot-filled circles: significant banding, $\Delta_{\dot\gamma}/(1+|\dot\gamma(t)|) = 31.6\% - 100\%$. Filled circles: strong banding, $\Delta_{\dot\gamma}/(1 + |\dot\gamma(t)|) > 100\%$. For the hatched, dot-filled and filled symbols we used the criterion that banding of the typical magnitude stated is apparent for any of $\omega = 0.1,\ 0.316$ or $1.0$, given a stress amplitude $\Sigma_0$ exceeding the region of weak slope in the constitutive curve. The square shows the parameter values explored in detail in figure 5.12. The solvent viscosity $\eta$ is $3.16 \times 10^5$.

state).

The inclusion of chain stretch into the RP model has an effect on the plateau-like region in the underlying constitutive curve: larger $Z$ (and thus smaller $\tau_R$) extends the breadth of $\dot\gamma$ spanned before the low viscosity branch is reached. Conversely, smaller $Z$ (and thus larger $\tau_R$) shortens and steepens the slope of this intermediate $\dot\gamma$ region and tends to restore monotonicity. This interplay of the CCR parameter $\beta$ and entanglement number $Z$ affect the monotonicity of the constitutive curve. This is shown by the red shaded region in figure 5.11, which indicates all pairs of $\beta, Z$ for which the underlying constitutive curve is non-monotonic. As $Z \to \infty$, the non-stretch limit is reached and the transition between a non-monotonic and monotonic constitutive curve depends only on $\beta$ (for a fixed small $\eta$). The boundary of the red shaded region in figure 5.11 can already be seen to be tapering off to a plateau for

large values of $Z$.

Circles in figure 5.11 show a series of chosen parameter sets $\beta, Z$ across the plane, spanning both regions of the plane where the underlying constitutive curve is non-monotonic or monotonic. At each circle I performed LAOStress simulations for one sweep of the $\Sigma_0, \omega$ plane for values of $\omega = 0.1, 0.316, 1.0$ and $\Sigma_0$ sufficiently large that it exceeds the plateau-like region of weak slope in the material's constitutive curve. (Full pin-point colour maps as used in figure 4.17 are not used here due to numerical expense of performing calculations across the full $\Sigma_0,\ \omega$ plane.) For each of these circles in the $\beta, Z$ plane, open circles indicate insignificant banding in the $\Sigma_0, \omega$ plane. Hatched, dotted and filled circles represent significant banding: hatched, $\Delta_{\dot{\gamma}}/(1 + |\dot{\gamma}(t)|) = 10\% - 31.6\%$, dotted, $\Delta_{\dot{\gamma}}/(1 + |\dot{\gamma}(t)|) = 31.6\% - 100\%$ and filled, $\Delta_{\dot{\gamma}}/(1 + |\dot{\gamma}(t)|) > 100\%$. Together, these circles give an overview of the intensity of shear banded flow in the LAOStress protocol for entangled polymer solutions or melts for a wide range of entanglement number $Z$ and theoretical CCR-parameter $\beta$. Moreover, significant shear banding is seen for materials with a monotonic underlying constitutive curve. It is hoped that this exploration of the $\beta, Z$ plane and the prevalence of shear banding within these materials with monotonically increasing constitutive curves proves useful to both the experimental and theoretical rheological communities.

The thick black box shown around the dot-filled circle in figure 5.11 indicates the $\beta,\ Z$ values used in figure 5.12. This selection of $Z$ is within the typical experimental range of entanglement numbers used [10, 28, 107]. With these fixed parameters, the material has a monotonic underlying constitutive curve and therefore lacks shear banding in steady shear flow. However, in LAOStress it exhibits significant shear banding across the $\Sigma_0,\ \omega$ plane. This can be seen in figure 5.12. The left panel of figure 5.12 shows the shear rate response to imposed LAOStress, zoomed into the region of positively increasing stress and shear rate where the material response transits the fast 'jumping' region from low to fast shear rate. The coloured shapes indicate the snapshots in time that velocity flow profiles are recorded. These are shown in corresponding colours and symbols in the right-hand plot.

The shear rate response once heterogeneity is allowed in the material is shown

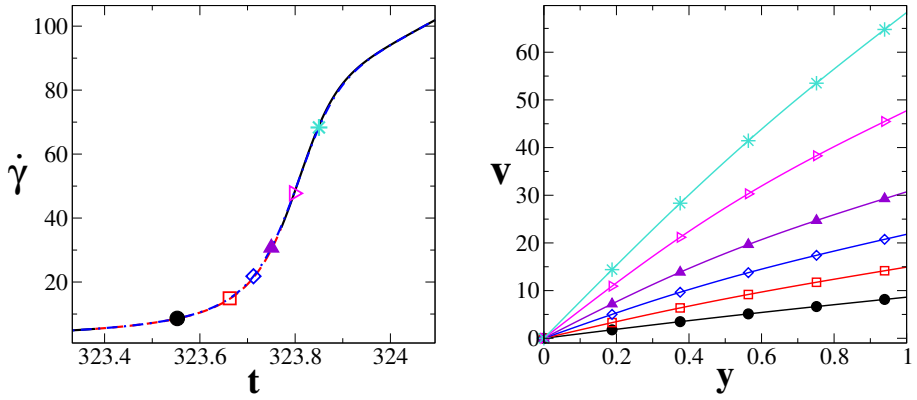


Figure 5.12: sRP model with a monotonic constitutive curve in LAOStress of stress amplitude $\Sigma_0 = 0.8$ and frequency $\omega = 0.1$. Model parameters $\beta = 0.7$, $Z = 100$, $\eta = 3.16 \times 10^5$. Cell curvature $q = 2 \times 10^3$. Number of numerical grid points $J = 512$. **Left:** strain rate signal versus time. Solid black and red-dashed line: calculation in which the flow is constrained to be homogeneous. Red-dashed region indicates when the step stress criteria is satisfied. Green dot-dashed line: stress response in a full nonlinear simulation that allows banding (indistinguishable from homogeneous signal in this case.) Right: Velocity profiles corresponding to stages in the cycle indicated by matching symbols in left panel

as the blue dot-dashed line. Here, this line is almost indistinguishable from the homogeneously-constrained shear rate response (shown here by the combined solid black and red dashed lines). However, during the upward curving, increasing shear rate (with increasing, positive stress) region on the material response, shear banded flow is seen. This is illustrated by the bowed (banded) velocity profiles in the right-hand plot.

In this section, I have shown that shear banding of entangled polymer solutions and melts is seen during the LAOStress protocol, even when chain stretch is significant. This is captured here using the sRP model for linear polymers. Shear banding is seen for a value of $Z$ within the typical experimentally achievable range [10,28,107] and parameter choices $\beta$ and $Z$ such that the material constitutive curve may be either non-monotonic or monotonic.

## 5.7 Conclusions from chapter 5

In this chapter I have explored shear band formation in entangled polymer flow under the LAOStress protocol, modelled by the nRP and sRP model. The crucial point from the previous chapter (where LAOStrain is instead employed) is illustrated and re-confirmed here: shear bands can form in a protocols with sufficiently strong time dependence, even in fluids that do not shear band in steady state. This point follows directly on from the work by Moorcroft and Fielding [134–136] which showed that strong time dependence during the transit to the steady state can lead to the formation of shear banded flow. However, the flows considered by Moorcroft and Fielding were only transiently time-dependent. Here I have considered a flow with a sustained time-dependence.

I have shown here that shear banding can occur in LAOStress for parameters such that the underlying constitutive curve of the material is either non-monotonic, or weakly positively increasing (monotonic) in $\Sigma(\dot{\gamma})$. Shear bands form when the shear rate $\dot{\gamma}$ experiences a large 'jump' in magnitude as the flat region of the constitutive curve is transited following a relatively very small increase in $\Sigma$. This regime of shear band formation during the material response to LAOStress is short-lived in comparison with the rest of the stress cycle. Whilst prominent and significant within the small part of the cycle, the shear banded flow does not dominate the cycle. It may thus be difficult to experimentally capture and localised measurement about the plateau-like region may instead be required.

It is further shown here, as in the previous chapter, that the more complex LAOS protocols can be understood, for the most part, by the already established understanding of the time-dependent material response during the approach to the steady state in simpler time-dependent protocols. Moreover, the set of criteria derived for the simple protocols still hold, to good approximation, for the LAOS protocols. It was shown for the step stress protocol that the onset of shear banding would occur on the approach to steady shear when the shear rate was increasing and has positive curvature as a function of time [135]. This criterion is entirely dependent on the strain rate response to the applied stress as a function of time and it is found to translate directly to the LAOStress protocol when combined with an

increasing and positive stress. The same criterion is satisfied for negative, decreasing stress (and thus with negative, decreasing and downward curving shear rate) in the LAOStress input due to the symmetry of the protocol.

In addition to this understanding of the stability to the formation of shear bands in the LAOStress protocol, I have also provided here the counterpart to the map of shear banding intensity in the space of CCR-parameter $\beta$ and entanglement number $Z$ given in chapter 4 for LAOStrain, here, for LAOStress. As for LAOStrain, a large region in $\beta - Z$ space shows significant shear banding for which the underlying constitutive curve of the material is monotonic.

# 6

# Multimode calculations using the Rolie-Poly model

A number of previous theoretical studies have used the Rolie-Poly (RP) model [110] to describe the dynamics and relaxation mechanisms of linear entangled polymers [2, 4, 136] and wormlike micelles (so-called 'living polymers' [26]) [1]. However, the RP model is a simplified single-mode approximation to the GLaMM model for linear polymers [75]. This sophisticated model extended the Doi-Edwards tube theory [47] by considering the configuration of a polymer chain down to the lengthscale of one entanglement. It includes the strongly nonlinear regime where chain stretch and constraint release are significant relaxation mechanisms and gives good agreement with experimental data [75]. However, the GLaMM model is complex and computationally expensive. The RP model was derived from directly coarse-graining the GLaMM model to capture the fundamental physics of chain reptation, retraction,

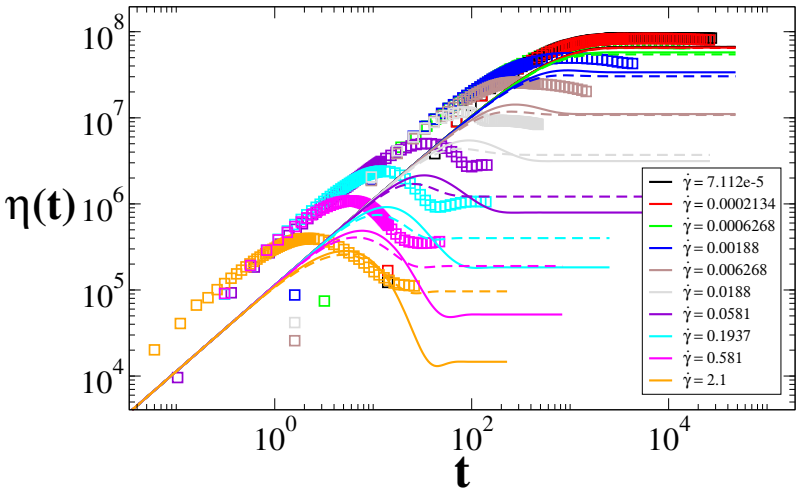


Figure 6.1: Single-mode RP 'fit' using numerical simulations to experimental shear rheology data of monodisperse polyisoprene. Solid lines have CCR parameter $\beta = 0.0$, dashed lines have $\beta = 1.0$. $G = 113420.0$, $\tau_d = 588.84$ and $\tau_R = 8.0$. Both lines show poor fit for single mode and thus multimode modelling is required to fully describe chain dynamics. Temperature $-20°C$. Experimental data from MuPP2, has been previously published in [10, 75].

stretch and convective constraint release (CCR). Thus the RP model provides a set of simple differential equations (2.39, chapter 2) through which complex polymer dynamics could be explained in different flows such as rheometric shear [31] and extensional [8] as well as more complex geometries featuring mixtures of both shear and extension, such as cross-slot experiments [113] (through computation fluid dynamic simulations) [126]. The downside to this single-mode version of the GLaMM model is the loss in detail of the full chain dynamics [74].

Figure 6.1 shows a single mode 'fit' to experimental shear data for entangled monodisperse polyisoprene. The parameters are taken to be the slowest mode in the full multimode fit (shown later, in table 6.1). In reference [10], the GLaMM model [75] showed close agreement with the data. However, by taking just the single mode RP model and numerically solving these dynamics, I find the 'fit' of this model has poor agreement with the rheological data. The RP single-mode fit for each imposed shear rate is shown by the lines [$\beta = 0$ (solid), $\beta = 1.0$ (dashed)] in figure 6.1. Corresponding colours are used for the experimental shear data (shown as squares) measured at the same shear rate. Clearly higher order dynamics are required to correctly describe this data via constitutive modelling (as seen in [10]).

Furthermore, industrial grade polymers are typically polydisperse and thus contain a distribution of polymer chain lengths and molecular weights ($M_w$). A multimode model would therefore be needed to capture the effects of the multiple relaxation timescales associated with this large variation in $M_w$ in a material sample. The poor fit in figure 6.1 shows that even for a monodisperse sample, a single-mode model is insufficient to capture both the transient stress growth and the steady state stress of the polymer. This illustrates the necessity of multiple relaxation times to fully describe the dynamics of long-chain entangled polymers.

In this chapter I use a multimode approach [49] with the RP model. I revisit the shear startup protocol and capture the higher order relaxation dynamics of the full polymer chain. I use a spectrum of relaxation times $\tau_d$ and elastic moduli $G$ together with the RP-parameter for chain-stretch relaxation, $\tau_R$, and employ both the stretching and non-stretching (where stretch is relaxed infinitely fast, *i.e.* $\tau_R \to \infty$) limits of the RP model.

## Summary of multimode modelling

Recall section 2.1.1 of chapter 2. Higher order relaxation dynamics of a polymer chain can be captured in a theoretical fit to experimental data by summing over a total of $N$ *Maxwell modes* (with behaviour governed by a simple Maxwell model, c.f. chapter 2). This forms a *relaxation spectrum* of the characteristic relaxation times $\tau_{d_n}$ and elastic moduli $G_n$ for each of the $n$ modes. Maxwell modes are fitted first to the linear rheology of the material. A schematic of this is shown in figure 6.2 where each Maxwell mode is described by the yellow diamonds. The fit is then checked against the nonlinear rheology of shear and/or extension data where additional model-dependent parameters (e.g. $\tau_R$ in the RP model) may be introduced to capture the transient and steady state behaviours.

The multimode model of Maxwell modes (total $N$) is formed from the sum of the relaxation dynamics of each mode ($n$):

$$G(t) = \sum_{n=1}^{N} g_n e^{-t/\tau_n}, \tag{6.0.1}$$

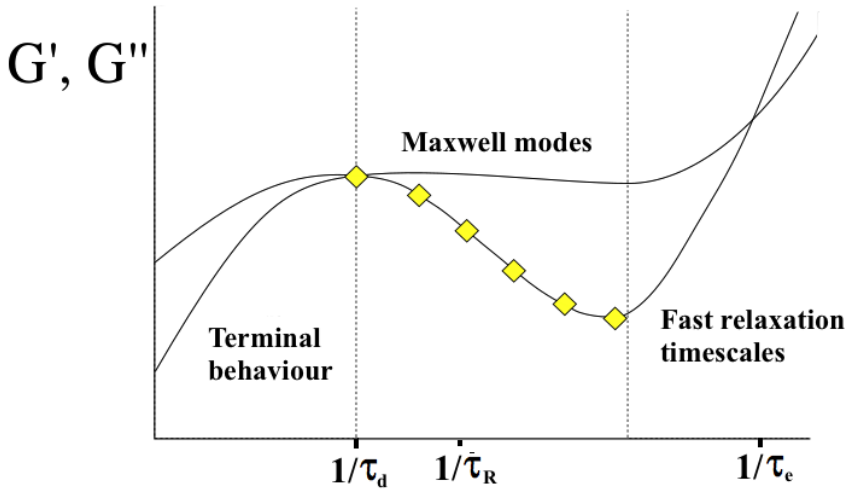


Figure 6.2: A schematic of the storage and loss moduli for an entangled polymeric fluid. Viscous-dominated rheology is recovered in the terminal regime for frequencies less than $1/\tau_d$. Within the region of moderate frequency (between the two dotted vertical lines) where the response is elastically-dominated, Maxwell modes are fitted to the data (each mode symbolised by a yellow diamond) to encapsulate the higher order chain dynamics described by the chain relaxation times $\tau_d$, $\tau_R$ and $\tau_e$.

where the set of moduli and corresponding timescales $\{g_n, \tau_n\}$ form the relaxation spectrum of the polymer.

As described in chapter 2, the longest relaxation time of an entangled polymeric material ($\tau_d$, an intrinsic material property) is defined as the inverse frequency at which the storage and loss moduli ($G'$ and $G''$) intersect in the linear rheology measurement of the material. This intersection can be seen on the left-hand side of figure 6.2, forming the boundary to the terminal relaxation behaviour of the material at low frequency. The upper boundary for the mode-fitting is set at high frequency such that beyond this timescale all chain dynamics are sufficiently fast that they are well described by the solvent contribution. The right-hand intersection of $G'$ and $G''$ at high frequency defines $\tau_e$, the time taken for one single entanglement to relax its constraints [47] beyond which the polymer dynamics are not constrained by entanglements [159].

Recall from chapter 2 that in the RP model these timescales are related by the

experimentally measurable quantity, the entanglement number $Z = \frac{M_w}{M_e}$:

$$\tau_d = 3Z\tau_R = 3Z^3\tau_e,$$

$$\tau_R = Z^2\tau_e,$$

where $\tau_R$ defines the chain-stretch relaxation time in the RP model. Recall that the higher order correction terms from linear theory [111] are omitted. In the multimode RP model $Z$ is fitted relative to the nonlinear shear rheology data rather than defined as $\tau_d/3Z$.

Note here that polymer lengthscales are inherently tied to the relaxation timescales defined here: $\tau_e$ is the fastest dynamic, associated with a single entanglement length in the polymer chain and the slower relaxation timescales $(\tau_d, \tau_R)$ are dependent on this fundamental time.

Multimode approaches have been used to describe linear polymers (via the Giesekus model) [11, 40], branched polymers (via the pom-pom model) [9, 83] and used for experimental comparison in high-density polyethylene [40], polystyrene [153] and gluten-gel [137]. In particular, a multimode version of the RP itself has also been used: References [31] and [113] use the full stretching version of the RP model for the first (slowest mode) and the non-stretching limit for the higher order modes. Collis et al. [31] and Auhl et al. [8] showed good agreement of the multimode RP model with nonlinear shear and extensional data, respectively. Lord et al. [113] showed a good match between simulations of 3D time-dependent solutions of a multimode RP model and experimental data in contraction-expansion slit and cross-slot geometries for pressure drop and principle stress difference profiles. Hassell et al. [79] also illustrated the good predictive ability of the multimode RP model. They considered shear in contraction-expansion slit geometries and found good agreement in the transient evolution of principle stress differences but a failure to accurately capture the pressure drop, highlighting the need for further work.

In the following sections I consider the effect on the time-dependent polymer dy-

namics during shear startup when a multimode RP model is used. I fit experimental linear rheology and shear data for monodisperse polyisoprene [10, 75] and establish a power-law distribution for the relaxation timescales and moduli associated with each Maxwell mode [84, 96, 97]. Indeed, I find good agreement with the data for a theoretical power-law fit. Moreover, I consider the existence of shear banding during the time-dependent shear startup protocol relative to the magnitude of the power-law exponent and the separation of relaxation timescales $\tau_d$ and $\tau_R$. As in the oscillatory protocols in chapters 4 and 5, I build a phase diagram in entanglement number and the convective constraint release parameter for the intensity of shear banded flow during shear startup.

## 6.1 Experimental data fitting: a multimode model for polyisoprene

I have fitted multimode RP parameters to experimental data for a well-entangled monodisperse linear polymer melts (polyisoprene). The data was provided by the MuPP project and thanks are given to Dietmar Ahul for these measurements. Details of experimental procedure are provided in reference [10].

Polyisoprene consists of repeated units of isoprene ($C_5H_8$) monomers. Isoprene has four possible molecular configurations (or *isomers*), each exhibiting different material characteristics. The isoprene samples prepared for this study used *cis*-1, 4 polymer which has elastic properties but becomes isotropically distributed in the absence of imposed deformation. The polyisoprene was prepared using aionic polymerisation, and samples were prepared for a wide range of molecular weights all with a narrow molecular weight distribution, such that the material is almost monodisperse [10].

The dynamic moduli $G'$ and $G''$ over several decades of frequency $\omega$ are measured by imposing small amplitude oscillatory shear (SAOS) to the material sample. The linear and nonlinear startup transient data were plotted at each imposed shear rate and a consistent response shape (linear viscoelastic envelope) was seen for each

sample, ensuring the reliability of measurements.

Entanglement numbers ($Z = M_w/M_e$) ranged from unentangled $Z = 0.5$ and highly entangled $Z = 235$. In this study I consider the two polyisoprene (PI) samples used in [10] with the largest number of entanglements where nonlinear startup data was available. These have molecular weights of 95kg/mol and 226kg/mol, giving the number of entanglements as $Z = 20$ and $Z = 47$, respectively, for $M_e$ measured as 4.82kg/mol. I continue the nomenclature of [10] and refer to the samples as PI90k and PI200k. In [10], these samples were indicated to be experimentally difficult to measure under shear. Moreover the steady-state theory predictions for both the PI90k and PI200k samples were similar and showed a plateau region over a range of shear rates where it was speculated that the uniform shear profile may be unstable to heterogeneous perturbations. These materials were also used by Graham et al. [75] to compare with the GLaMM model in transient shear. This therefore provides an ideal benchmark for investigating shear banding in the coarse-grained RP model.

### 6.1.1 Fitting procedure

I fitted both the linear and nonlinear rheology of the experimental data using REPTATE [1] [149] software. Thanks are given to David Hoyle for tutorials and guidance with REPTATE. Using the parameters given in reference [10] for the molecular characteristics ($M_w,\ M_e,\ \tau_e$) of the samples, the characteristic reptation time and chain-stretch relaxation time are then calculated using the theory of Likhtman and McLeish [111].

For each material I fit the dynamic moduli using the following procedure:

1. Set the terminal relaxation time (slowest mode) to the reptation time predicted by Likhtman-McLeish theory [111].

2. Fit around 7 modes in total at around 2 modes per decade in order to include the chain-stretch regime.

[1] **R**heology for **E**ntangled **P**olymers: **T**oolkit for **A**nalysis of **T**heory and **E**xperiment.

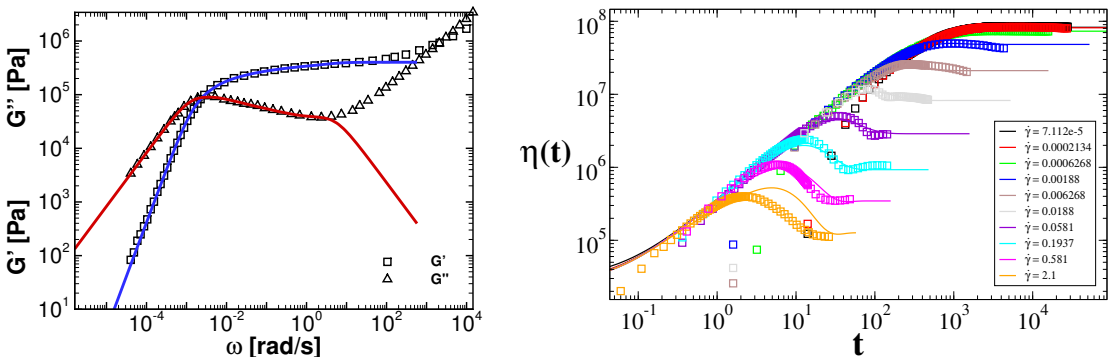


(a) (b)

Figure 6.3: (a) Linear rheology of PI200k at $-20°C$, blue and red lines show the fit from linear theory for $G'$ and $G''$, respectively. (b) shows the nonlinear transient shear rheology for PI200k, solid lines show the multimode RP fit. In both fits I use the REPTATE [149] software.

3. The nonlinear RP [110] parameters are fitted in shear startup experiments using at least 3 stretching modes and then non-stretching modes thereafter. The highest order mode (fastest relaxing) is attributed to the solvent viscosity contribution.

Including the fastest relaxation dynamics of the polymer as a solvent contribution to the constitutive model is based on the assumption that shorter lengthscale dynamics in the polymer chain relax infinitely quickly such that the flow is Newtonian. This is appropriate since the viscous effects of the fluid dominate the fast-relaxing Maxwell-modes at high frequencies [147]. The resultant fit for PI200k using these techniques is shown in figure 6.3(a) and (b). The values of $G_n$, $\tau_{d_n}$ and $\tau_{d_R}$ for each mode are given in table 6.1. Here (following procedure 3) $\eta = \tau_{d_7} G_7$ and RP parameters for convective constraint release (CCR) were fitted to be $\beta = 0.1$ and $\delta = -0.5$.

It is important to note that the multimode fit described here, where the CCR parameter is $\beta = 0.1$, results in a monotonic underlying constitutive curve. This is shown in figure 6.4. The steady state flow profile of the material will therefore be homogeneous. However, the single-mode RP model for $\beta = 0.1$ results in a non-monotonic underlying constitutive curve and thus predicts shear banding at the steady state for shear rates within the negatively-sloping region of the curve [185]. This difference is due to the influence of the higher order dynamics captured by the multiple relaxation times that are not accounted for by the single mode model. In

| Mode ($n$) | $G$ | $\tau_{d_n}$ | $\tau_{R_n}$ |
|---|---|---|---|
| **1** | 113420.0 | 588.84 | 8.0 |
| **2** | 80683.0 | 161.61 | 7.0 |
| **3** | 54268.0 | 44.354 | 5.0 |
| **4** | 44963.0 | 12.173 | 3.0 |
| **5** | 34827.0 | 3.3408 | 0 |
| **6** | 27567.0 | 0.9169 | 0 |
| **7** | 46103.0 | 0.25164 | 0 |

Table 6.1: Values for the multimode RP fit to PI200k data at $-20°C$. The $7^{th}$ mode forms the solvent contribution and encompasses the fast relaxation dynamics of all 6 slower modes.

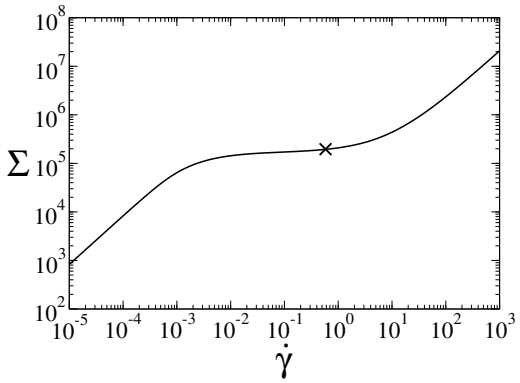


Figure 6.4: Underlying constitutive curve for the multimode RP fit for PI200k as defined in table 6.1 with CCR parameters $\beta = 0.1$ and $\delta = -0.5$.

the following section I consider the possibility of transient shear banding during a shear startup protocol for the multimode RP fit of the experimental data described here. Allowing for heterogeneity in the sample may enable this short-time elastically-driven instability to form shear banded flow where homogeneity is regained at the steady state (as predicted by the monotonic underlying constitutive curve).

## Banding from experimental data

Figure 6.5(a) shows the transient shear response to an imposed shear rate $\dot{\gamma} = 0.581$ as modelled by the theoretical multimode RP fit to experimental data for PI200k. This $\dot{\gamma}$ is shown in figure 6.3 by the magenta squares (data) and line (multimode RP fit). I have also considered the $\dot{\gamma} = 2.1$ and $\dot{\gamma} = 0.1937$ cases and find approximately the same results (data not shown here).

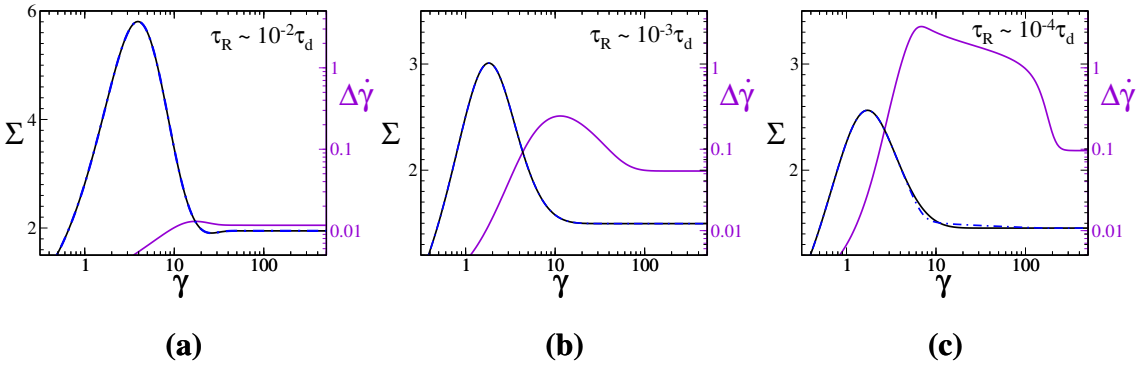


Figure 6.5: Shear startup protocol for $\dot{\gamma} = 0.581$ as modelled by the multimode RP fit for PI200k as defined in table 6.1 with CCR parameters $\beta = 0.1$ and $\delta = -0.5$. Homogeneously-constrained stress response (black line) in (a) corresponds directly to the magenta line in figure 6.3. Blue dot-dashed lines show the heterogeneous stress response and purple lines describe the time-dependent degree of banding $\Delta\dot{\gamma}$. The distance between relaxation times $\tau_d$ and $\tau_R$ is increased by orders of magnitude from $10^{-2}$ to $10^{-4}$ in (a)-(c). A weakly curved cell is used with $q = 10^{-3}$, there are $J = 1024$ spatial grid-points, timestep $dt = 10^{-7}$ and solvent viscosity $\eta = \tau_{d_7} G_7 \sim 10^{-5}$.

The blue dot-dashed line in figure 6.5 shows the stress signal in a calculation once heterogeneity is allowed. The black line shows the stress signal in a calculation where the flow is artificially constrained to be homogeneous (the quantity shown by the solid magenta line in figure 6.3(b)). The purple line is the degree of banding $\Delta\dot{\gamma} = (\dot{\gamma}_{\max}(t) - \dot{\gamma}_{\min}(t))/\dot{\gamma}_{\text{imposed}}$. Insignificant magnitudes of the degree of banding (relative to the cell curvature) are recovered at the steady state where the flow is homogeneous.

There is no significant transient shear banding seen for the multimode RP fit to PI200k data in shear startup (figure 6.5). In figures 6.5(b) and (c) I artificially increase the separation between $\tau_d$ and $\tau_R$ to investigate the influence of the stretch relaxation time on the prevalence of transient shear banding during startup. This effectively increases the region between $\tau_d$ and $\tau_e$ in the linear rheology, or, alternatively, acts to increase the molecular weight of the polymer.

I use the notation $\tau_R \sim 10^m \tau_d$ to represent the difference in magnitude of the two material relaxation times (describing orientation and chain stretch) for the first (slowest) mode. Recall from table 6.1 that for $n = 1$, $\tau_d = 588.84$ and $\tau_R = 8.0$, the ratio of $\tau_R$ to $\tau_d$ is thus of order $10^{-2}$, giving $\simeq -2$. In (b) and (c), $m \simeq -3$ and

$m \simeq -4$, respectively. A decrease in the local stress maximum is seen for larger $m$ where the influence of chain stretch relaxation on the short-time dynamics of the polymer is decreased (note the change n the $\Sigma$-axis required in subfigures (b) and (c)).

There is a clear increase in the magnitude of the degree of banding during startup (compared to that determined by the cell curvature in steady state) for increased separation in the orientation and chain stretch relaxation timescales. Indeed, in figure 6.5(c), significant transient shear banding is seen for $\tau_R \ll \tau_d$, *i.e.* when the effects of stretch on the relaxation dynamics have been reduced. There is, however, even for $\tau_R \sim 10^{-4}\tau_d$, very little separation between the homogeneous and heterogeneous stress responses. Indeed, for $\tau_R \sim 10^{-2}\tau_d$ and $\sim 10^{-3}\tau_d$ the two lines are indistinguishable in the plot. Importantly, no significant shear banding was seen for the experimental fit of PI200k data in figure 6.5(a).

In the following sections I continue to explore the possibility of shear banding in time-dependent flows as modelled by the multimode RP model. I set $N$ Maxwell modes to form a power law spectrum of $\tau_{d_n}$ and $G_n$ [84, 96, 97]. This will allow me to explore the effect of increasing the number of chain entanglements, and hence the separation of the orientation and chain-stretch relaxation times on the existence of shear banding in the flow.

## 6.2 Power-law fit for Linear Rheology

Figure 6.6 shows the linear rheology data for mondisperse polyisoprene for four different samples. The black line describes a material that is only weakly entangled ($Z = 6$). The materials described by the green and blue lines are well entangled ($Z = 20$ and $Z = 47$ respectively). These are the PI90k and PI200k samples I will continue to discuss in this chapter. The material described by the red line is very highly entangled, with $Z = 235$, resulting in it being unmeasurable in shear flow [10]. Note here that increasing molecular weight increases the range of frequencies encapsulated within the intrinsic material relaxation times $\tau_d$ and $\tau_e$, defined at the left- and right-crossover points in the linear rheology data.

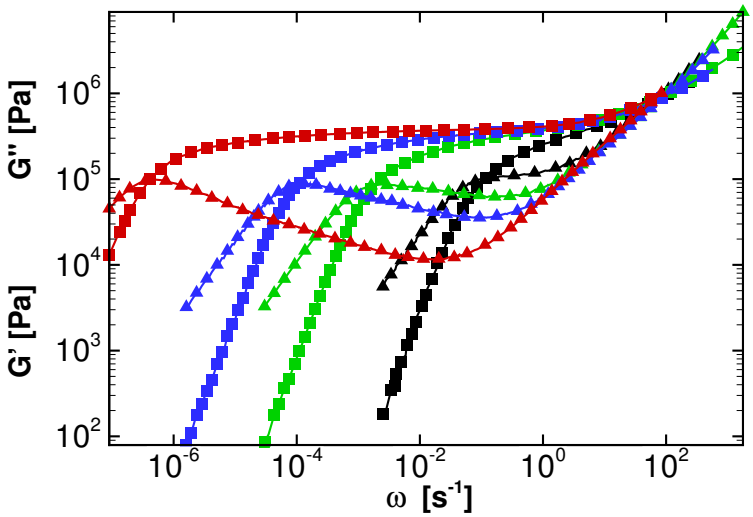


Figure 6.6: Linear rheology for mondisperse polyisoprene (all at $-35°C$) for four different molecular weight (and thus degree of entanglement) samples. Black is weakly entangled ($Z = 6$). Green and blue are well entangled ($Z = 20$ and 47). Red is highly entangled (Z=235) such that the rheology is unmeasurable in shear flow.

Discarding the weakly entangled polymer sample (black symbols), each of the loss moduli (shown by the triangle data lines in figure 6.6) for frequencies beyond the characteristic reptation time approximately follow a decreasing straight line with constant gradient in a log-log representation. In this section I approximate the Maxwell mode spectrum of a material (as described by the yellow diamonds in figure 6.2) by a power-law relationship, motivated by the constant gradient observation in figure 6.6. The resultant power-law distribution of values defines the spectrum of relaxation times and moduli that capture the full chain dynamics of the polymer.

### 6.2.1 Power-law fitting procedure

As motivated by the preceding discussion, here I approximate the broad range of relaxation times ($\omega_n = 1/\tau_{d_n}$) seen in experimental linear rheology using a power law. The relaxation times and moduli are related by:

$$\frac{G_n}{G_1} = \left(\frac{\tau_{d_1}}{\tau_{d_n}}\right)^{-\alpha}, \tag{6.2.2}$$

with an associated stretch relaxation time for each RP mode is given by:

$$\tau_{R_n} = \frac{\tau_{d_n}}{\kappa Z}, \tag{6.2.3}$$

for $n = 1 \dots N$ for a total of $N$ modes. $\alpha$ is the power-law exponent, $\kappa$ is a constant for which the single-mode RP model is set to $\kappa = 3.0$. In the following sections, I will use $\kappa$ as an independent scaling variable to explore the influence of extending the separation of $\tau_d$ and $\tau_R$ stress relaxation timescales. I show that large departures form $\kappa = 3.0$ are needed for the multimode RP model to match shear banding profiles seen in experimental literature. Recall $Z$ is the entanglement number $Z = \frac{M_w}{M_e}$ [110] and it thus follows that $\kappa = \frac{\tau_d}{Z\tau_R} = \frac{\tau_d}{Z^3\tau_e}$. Note for any non-stretching modes $\tau_{R_n} = 0$ and all fast dynamics (assuming infinitely fast chain stretch relaxation) are included in the solvent viscosity where fast relaxation dynamics are described $G_N\tau_N = \eta$. This viscosity encompasses all fast dynamics beyond the regime of viscoelasticity of the Maxwell modes described by the theoretical spectrum in $G$ and $\tau_d$ [147].

This power-law is fit by the following data:

1. Set the terminal relaxation time (slowest mode) to the reptation time predicted by Likhtman-McLeish theory [111].

2. Select $\alpha$ to describe the power-law relationship for increasing frequency.

3. Select $\kappa$ to capture the influence of the stretching modes. $\tau_R$ is then defined according to the RP model relationship $\tau_{R_n} = \tau_{d_n}/\kappa Z$ where for the single-mode RP model $\kappa = 3.0$.

This definition of the power-law relationship between the variables of the relaxation spectrum allows the exploration of parameter space determined by $\alpha$, $\kappa$ and the RP parameter $\beta$ to investigate and quantify where shear banding may occur in flows modelled by the multimode RP model. This is explored in the following sections.

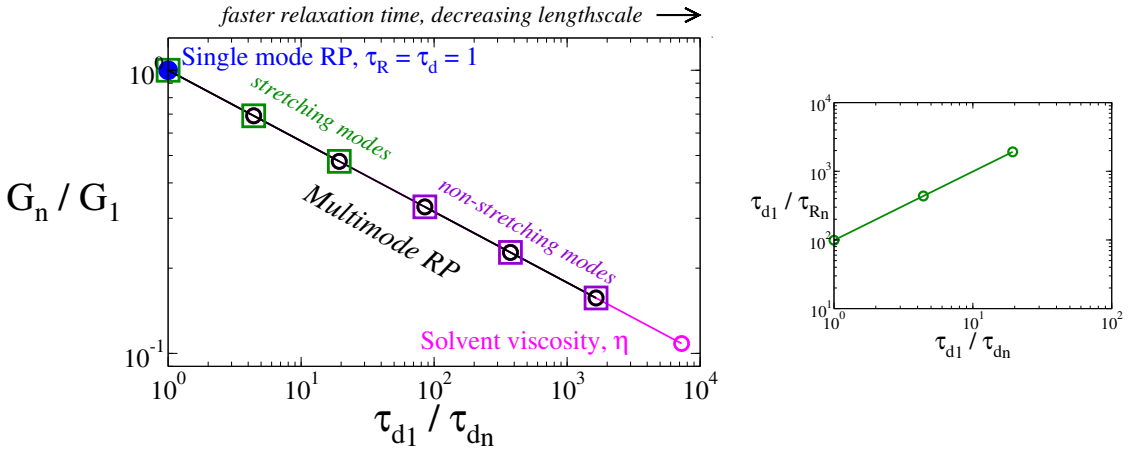


Figure 6.7: A power-law spectrum for a 7-mode Multimode RP model with 3 stretching modes (green), 3 non-stretching modes (purple) and the fastest dynamical mode ($n = 7$) forming the solvent viscosity contribution, $G_7\tau_7 = \eta$, to the entangled polymer solution (magenta). The slowest mode - which would form the single-mode RP model - is shown in blue. The relationship between the RP parameters $\tau_d$ and $\tau_R$ is shown in the right-hand figure. Here, $Z = 33$ and $\kappa = 3.0$ giving $\tau_{R_1} \sim \tau_{d_1} 10^{-2}$.

An example power-law spectrum is shown in figure 6.7. The single mode approximation of the RP model (used previously in this thesis) where $G = \tau_d = 1.0$ is highlighted in blue, for reference. I take the first three slower modes to be stretching modes to encompass the stretching dynamics of the polymer (employing the full RP model with chain stretch). These are indicated in the figure by green boxes. The second (faster) set of three modes are taken to be in the non-stretching limit of infinitely-fast stretch relaxation (employing the non-stretching limit of the RP equation) and are indicated by purple boxes. The fastest mode ($n = N = 7$) is taken to be the solvent viscosity which includes all the fast dynamics of the slower modes not captured by the timescales $\tau_d$ and $\tau_R$. The solvent mode is shown in magenta in figure 6.7.

The relationship between $\tau_d$ and $\tau_R$ for the first three (stretching) modes is shown to the right of figure 6.7. The ratio of the two relaxation times is set at the intersect of the vertical axis: here $\tau_d/\tau_R \sim 10^2$. Increasing the separation of the two relaxation timescales (by decreasing $\tau_R$ through increasing $\kappa$ in equation 6.2.3) shifts the line in the right-hand figure of 6.7 up the vertical axis. Equivalently, $Z$ could instead be varied and $\kappa$ held constant to alter the separation in the $\tau_d$ and $\tau_R$ timescales. However, I have chosen to keep $Z$ constant and within the experimentally-achievable

regime and focus purely on the effect of scaling factor $\kappa$. I relax any physical limits on $\kappa$ to investigate the regime in which shear banding is recovered and consistent with that seen in experiment for the shear startup protocol [19, 28, 88, 107, 152, 179, 180]. Fixing $Z = 33$ takes the average of the two polyisoprene samples I focus on here (with $Z = 20$ and $Z = 47$).

In order to validate the use of this multimode power-law RP model, I approximate the experimental multimode RP fits (using REPATATE [149]) of the experimental data for PI90k and PI200k by the power-law defined in equation 6.2.2. I then further investigate the possibility of shear banded flows in the multimode RP model.

## 6.3 Power-law fit to experimental data

In the left-hand graph of figure 6.8 I have plotted the relaxation spectra for PI90k (shown in green) and PI200k (shown in red) as found via the experimental fitting procedure described in section 6.1.1. The spectrum for the latter is defined in table 6.1. Each quantity is scaled by the lowest order mode: $G_n/G_1$, $\tau_{d_n}/\tau_{d_1}$, such that the crossover in $G_1$ and $\tau_{d_1}$ occurs at $\omega = 1.0$, in the linear rheology. This follows the setting of $G = \tau_d = 1.0$ used throughout this thesis.

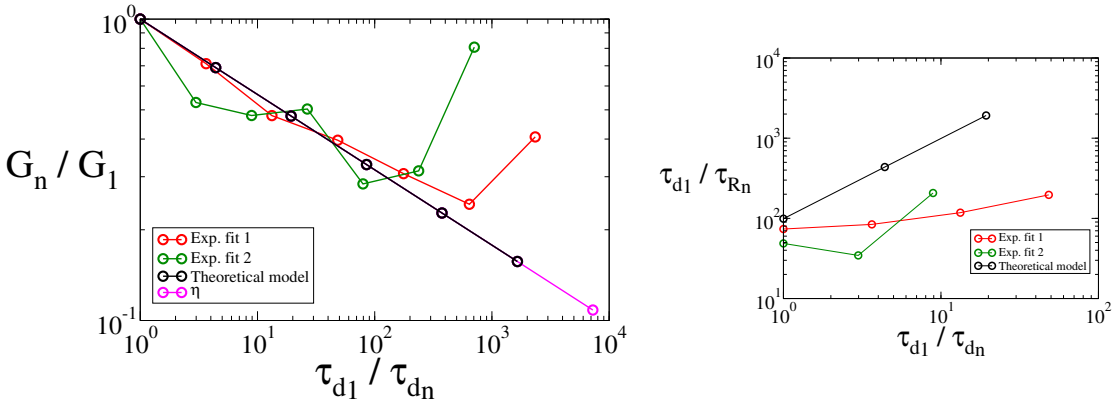


Figure 6.8: Power-law fit with $\alpha = 0.25$ to PI90k (green) and PI200k (red) multimode RP data fits for **left**: $G$ vs. $\tau_d$ and **right**: $\tau_R$ vs. $\tau_d$. Relaxation spectrum values are described in table 6.2, set by the formula outlined in section 6.2. Here $\kappa = 3.0$ and $Z = 33$ giving $\tau_R \sim 10^{-2}\tau_d$. Any change in this relationship represents a shift up (for increased time-separation) or down (for decreased time separation) the vertical axis.

| **Mode** ($n$) | $G$ | $\tau_{d_n}$ | $\tau_{R_n}$ |
|---|---|---|---|
| **1** | 1.0 | 1.0 | 0.0101 |
| **2** | 0.690 | 0.227 | 0.00230 |
| **3** | 0.477 | 0.0517 | 0.000522 |
| **4** | 0.329 | 0.0117 | 0 |
| **5** | 0.227 | 0.00267 | 0 |
| **6** | 0.157 | 0.000606 | 0 |
| **7** | 0.108 | 0.000138 | 0 |

Table 6.2: Relaxation spectrum values for each mode of the pow-law fit shown in figure 6.8. The $7^{th}$ mode forms the solvent contribution $\eta$ and encompasses the fast relaxation dynamics of all 6 slower modes.

Using the power-law relationship in section 6.2 for the relaxation spectrum I found an exponent of $\alpha = 0.25$ best fits the two data sets. The black line in figure 6.8 shows this power-law fit. The spectrum of relaxation times and moduli are prescribed for equally spaced modes along the power-law fit line. These are indicated by the black circles. The first three (slowest) modes are taken to be stretching RP modes (with associated $\tau_R$) and the next three faster modes are taken to be non-stretching RP modes. The fastest ($n = 7$) mode is taken to be the solvent viscosity contribution such that $\eta = \tau_{d_7} G_7$. This is shown in magenta for the power-law fit. The final mode of the experimental fits (red and green) increases due to fitting the upturn in the viscous modulus from its local minimum. However this final mode is attributed to the solvent contribution and it is taken as an arbitrary value when fitting the power law. For consistency I choose to set this solvent contribution to $\eta \simeq 10^{-5}$. Thus neglecting this fastest-relaxation mode, there is good agreement between the power-law fit and both sets of polyisoprene data. Table 6.2 gives the values for data points in the fit shown in figure 6.8.

The relationship between $\tau_d$ and the RP-parameter $\tau_R$ is shown in the right-hand graph of figure 6.8. The black line (as defined by equation 6.2.3) does not fully capture the best fit of the PI90k and PI200k experimental fit values for $\tau_R$. This is due to the fact that $\tau_{R_n}$, when fitting experimental data, are prescribed values to fit the data, rather than using the relation $\tau_R = \tau_d/\kappa Z$ for $\kappa = 3.0$. Here, I have ensured a good fit for the slowest mode, leaving the higher order stretching modes to

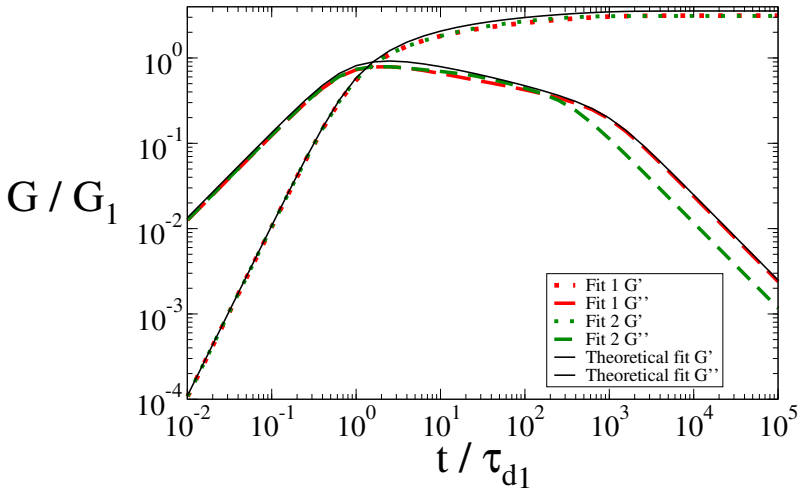


Figure 6.9: Comparison of the linear rheology (loss and storage moduli) for the multimode experimental polyisoprene fits (PI90k and PI200k) and the theoretical fit model.

have $\tau_R$ determined by equation 6.2.3. Moreover, $Z$ is a defined material quantity, not a fit parameter.

Figure 6.9 shows the storage and loss moduli for the experimental data fits by the green (PI90k) and red (PI200k) lines (dotted for $G'$ and dashed for $G''$) normalised by the slowest mode such that $G_1 = \tau_{d_1}$ occurs at $\omega = 1.0$ for both samples. The solid black lines show the moduli for the theoretical power-law fit (shown in figure 6.8) of the experimental fits' relaxation spectrums. The theoretical fit captures the linear rheology of both experimental fits with excellent agreement. There is a slight deviation for the second (green) fit in the high-frequency regime.

## Banding from the power-law fit

Figure 6.10 shows two underlying constitutive curves for the power-law fit to the experimental PI data ($\alpha = 0.25$) outlined in table 6.2. $\kappa$ is artificially increased in subfigure (b) from $\kappa = 3.0$ to 300.0 such that the resulting separation of $\tau_d$ and $\tau_R$ relaxation timescales is increased (and thus so is $M_w$) from $\tau_R \sim 10^{-2}\tau_d$ to $\tau_R \sim 10^{-4}\tau_d$. This large separation in timescales is where transient shear banding features were most prominent in the time-dependent startup flow shown in figure 6.5. By setting the RP CCR-parameter $\beta = 0.0$ and $\beta = 0.2$ the underlying constitutive curves are non-monotonic and monotonic respectively.

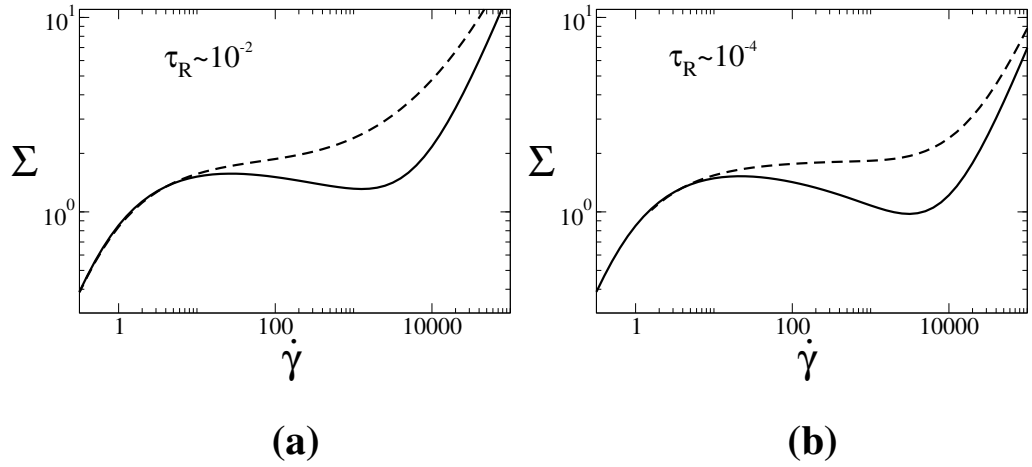


Figure 6.10: Constitutive curves for 6-mode RP model for $\tau_R \sim 10^{-2}\tau_d$ (as defined in table 6.2) and $\tau_R \sim 10^{-4}\tau_d$ (attained by artificially increasing $\kappa = 3.0$ to 300.0). Dashed lines are monotonically increasing and have $\beta = 0.2$, solid lines are non-monotonic and have $\beta = 0.0$. Increasing the ratio of $\tau_d$ and $\tau_R$ lengthens the plateau-like region in the curves. $\alpha = 0.25$ and $Z = 33$.

Figures 6.11(a)-(h) show the time-dependent material responses for the power-law fit material ($\alpha = 0.25$ and varying $\tau_R/\tau_d$ between $10^{-2}$, $10^{-3}$ and $10^{-4}$), with underlying constitutive curves as described in figure 6.10, in the shear startup protocol. These time-separations are increased by setting $\kappa = 3.0,\ 30.0,\ 300.0$ respectively, for fixed $Z = 33$. Velocity profiles are shown for the largest ratio $\tau_R \sim 10^{-4}\tau_d$ in subfigure (d) (where the underlying constitutive curve is non-monotonic) and (h) (where the constitutive curve in monotonic) where shear banding was most significant. The applied shear rate $\dot{\gamma} = 342.12$ (where $\tau_d = 1.0$). This has the same Weissenburg number ($\mathrm{Wi} = \dot{\gamma}\tau_d$) used in figure 6.5; where $\dot{\gamma} = 0.581$ and $\tau_d = 588.84$, giving $\mathrm{Wi} = 342.12$.

Steady state shear banding can be seen for the top row for each value of $\kappa$ where the underlying constitutive curve of the material is non-monotonic. In the bottom row, the material has a monotonic underlying constitutive curve and thus precludes shear banding at the steady state under steadily applied shear (chapter 3). Significant transient shear banding is seen to occur only in the case of artificially-increased values to $\kappa = 30.0$ (subfigure (f)) and particularly $\kappa = 300.0$ (subfigure (g)). Indeed, the shear banded velocity profiles shown in (d) and (h) for $\kappa = 300.0$ are consistent with those seen in experiment for the shear startup protocol [19, 28,

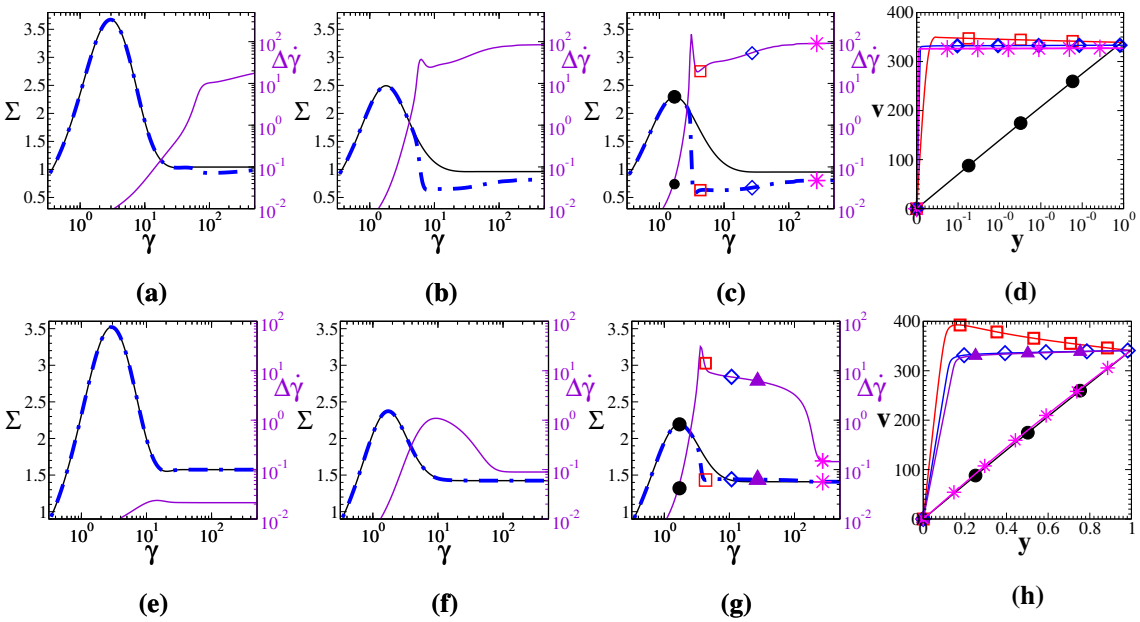


Figure 6.11: Transient shear stress, degree of banding and associated velocity profiles at snapshots in times (indicated by corresponding colours and symbols) under shear startup ($\dot{\gamma} = 342.12$) using the power-law RP multimode model with $\alpha = 0.25$, $Z = 33$. In (a) and (e), $\kappa = 3.0$ ($\tau_R \sim 10^{-2}\tau_d$), (b) and (f) have $\kappa = 30.0$ ($\tau_R \sim 10^{-3}\tau_d$) and (c), (d), (g) and (h) have $\kappa = 300.0$ ($\tau_R \sim 10^{-4}\tau_d$.). 3 stretching modes and 3 non-stretching modes are used. $\eta \simeq 10^{-5}$. **Top row:** $\beta = 0.0$ and the material has an non-monotonic underlying constitutive curve. **Bottom row:** $\beta = 0.2$, and the material has a monotonic underlying constitutive curve. Simulations are performed using full nonlinear spatio-temporal dynamics with a weakly curved cell ($q = 10^{-3}$) and $J = 1024$ spatial gridpoints. $dt = 10^{-7}$.

88,107,152,179,180]. As before, the finite degree of banding seen at long times in (f) and (g)) is insignificant compared with the effects of the weak curvature of the cell: at the steady state a weakly-curved velocity profile may occur for imposed $\dot{\gamma}$ within the weakly-increasing (plateau-like) region of the underlying constitutive curve [4] (recall chapter 2). It can be seen in subfigure (h), however, that the steady state velocity profile (magenta line and stars) is indeed homogeneous to the eye.

The initial pronounced peak in the degree of banding seen for $\kappa = 30.0$ and 300.0 follows the stress overshoot in strain. It is around this time that the heterogeneous stress relaxes at a faster rate than its homogeneously-constrained counterpart. This is seen for both the non-monotonic and monotonic underlying constitutive curves. Moreover, the increased values of $\kappa$ can be seen to decrease the local stress maximum and decrease the strain at which the onset of instability to the formation of shear

banding occurs. The change in stress is not unexpected as the increase of $\kappa$ decreases the influence of chain stretch (with relaxation time $\tau_R = \tau_R(\kappa)$). Recall chain stretch helps capture the short-time dynamics (on the onset to, and at, the local stress maximum). However, the earlier (and indeed increased) instability to shear banding seen for larger $\kappa$ recovers banding profiles seen in experiments [19,28,88,107,152,179,180]. It is thus suggested here that chain stretch in the RP model perhaps overly suppresses shear banding in shear startup.

Recall that when fitting the experimental data, $Z$ and $\tau_{R_n}$ are fixed and thus the relationship defined in equation 6.2.3 for the power-law fit (as based on the RP model) is not required. If, however, $\kappa$ was to be calculated for the first mode of each multimode fit, $\kappa$ is then a function of $Z$. Indeed from Likhtman and McLeish linear theory [111] and confirmed by experimental observations [10], that for PI90k, $\kappa = 1.3$ and for PI200k, $\kappa = 1.6$. Therefore, in the following sections I use the contraction $\kappa_Z = \kappa Z$ without loss of generality. Again I relax the physical constraints on this value to determine the existence of significant shear banding in the multimode model.

In the following sections I compare my findings with two case studies of theoretical papers for the existence of shear banding in startup flows. In these case studies, I confirm the use of the power-law multimode RP model's ability to reproduce previously published -and cited- results. In these studies, $\tau_d/\tau_R(= \kappa_Z)$ ranges from $10^2$ to $10^4$, thus justifying the inflation of $\kappa$ used previously in this chapter to capture the shear banding found in experiment for similarly-entangled linear polymers.

A summary of the parameters I use to consider the case studies (Cooke [32], Adams and Olmsted [4]) is shown in table 6.3. For both case studies, I chose $\alpha = 2.75$ to more closely approximate the single-mode modelling for similar values of $\beta$ used in the references, whilst investigating the higher order relaxation.

| | $\alpha$ | $\beta$ | $\kappa_Z$ |
|---|---|---|---|
| **Case study (a)** | 2.75 | 0.4 | $10^2 - 10^4$ |
| **Case study (b)** | 2.75 | 0.65 & 0.85 | $10^3 - 10^4$ |

Table 6.3: A summary of parameters for the theoretical case studies (a) and (b).

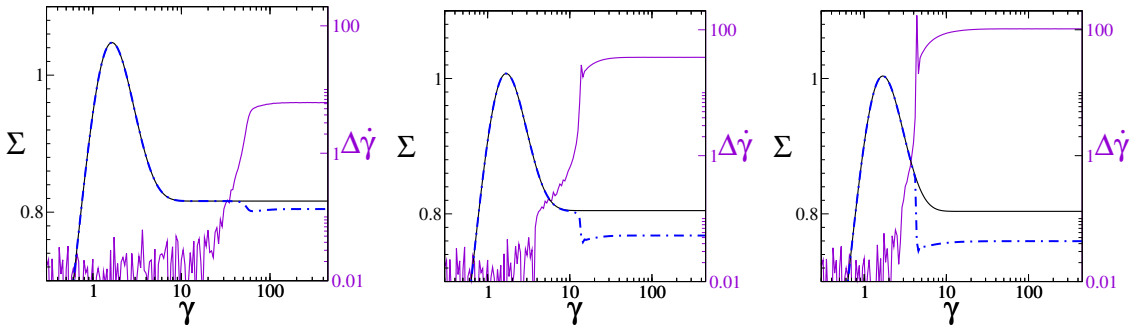


Figure 6.12: Shear startup transient stress and degree of banding as modelled by a power-law multimode RP model ($\alpha = 2.75$, $Z = 61$, $\kappa = 1.6$ initially). $\kappa$ is increased by factors of 10 in (b) and (c) such that: (a) has $\tau_R \sim 10^{-2}\tau_d$, (b) has $\tau_R \sim 10^{-3}\tau_d$ and $\tau_R \sim 10^{-4}\tau_d$. These timescale separations have all been cited in previous theoretical work on shear banding. Underlying constitutive curve for the material is non-monotonic. Heterogeneous seed provided by continuous random noise with amplitude $q = 1e-2$ as in [32]. $\beta = 0.4$, $J = 512$, $dt = 10^{-7}$.

## Theoretical case study (a)

Cooke, in figure 5.4.3 of reference [32] describes the behaviour of an entangled polymeric fluid under the time-dependent material response to shear startup for the single-mode RP model. In [32], significant transient shear banding was seen for $\tau_R \sim 10^{-2}\tau_d$ and $\tau_R \sim 10^{-4}\tau_d$. A pronounced overshoot in the degree of banding $\Delta\dot{\gamma}(t)$ (spatial heterogeneity in the $\dot{\gamma}$-field, measured with time) was seen for $\tau_R \sim 10^{-4}\tau_d$ following the stress overshoot in strain ($\partial_\gamma \Sigma < 0$). Both samples had a non-monotonic underlying constitutive curves and thus exhibited steady state shear banding. In figure 6.12 I reproduce these results for the 6-mode RP model with fit parameters: $\alpha = 2.75$, $\kappa_Z = 10^2$, giving $\tau_R \sim 10^{-2}\tau_d$ and then increase $\kappa_Z$ to give $\tau_R \sim 10^{-4}\tau_d$ (consistent with the two values used in [32]). I include $\tau_R \sim 10^{-3}\tau_d$ in figure 6.12 for comparison. The width of the spectrum in time and moduli is set such that the fastest mode gives $g_N\tau_{d_N} \sim 10^{-5}$. The results shown in figure 6.12 use the addition of random mechanical noise as the numerical seed to growth in heterogeneity (as in [32]), though I found consistent results for a weakly curved cell in the absence of noise.

Between (a)-(c) in figure 6.12, I consider the influence of the $\tau_d/\tau_R$ ratio on the transient 'peak' in the degree of banding by increasing $\kappa$ by factors of 10. It can

be seen in figure 6.12 that $\Delta\dot{\gamma}(t) \sim \tau_d/\tau_R$. The ratio of relaxation times $\tau_d/\tau_R$, acts to lengthen the decreasing (or weakly increasing plateau for monotonic curves) region of the constitutive curve since this is indicative of increasing $M_w$ (and thus an increase in $Z$) and hence the separation between material timescales $\tau_d$ and $\tau_e$. It is as this separation in polymer chain relaxation timescales is increased that a pronounced peak in the degree of banding can be seen following the overshoot in the time-dependent stress response with increasing strain ($\partial_\gamma \Sigma < 0$). This peak is not seen for $\tau_d/\tau_R = 10^2$. It therefore follows that the two relaxation timescales must be sufficiently well separated for this transient shear banding signal to be seen. Moreover, that an increased influence of chain stretch on polymer relaxation suppresses transient shear banding in the material response to shear startup.

## Theoretical case study (b)

Adams and Olmsted, in reference [4] showed results of transient shear banding in shear startup for the absence of a non-monotonic constitutive curve. Two values for $\beta$, the CCR-parameter, were chosen such that the underlying constitutive curve of the material only varied slightly between non-monotonic and monotonic ($\beta = 0.65$ and $\beta = 0.728$ for the single-mode RP model). In figures 6.13 and 6.14 I use correspondingly closely separated values of $\beta$ in the multimode RP model (as defined by the same power-law fit as in comparison (a)). I set $\beta = 0.65$ and $\beta = 0.85$, and choose the power-law exponent to be $\alpha = 2.75$ to closely reproduce the weakly non-monotonic and weakly monotonic underlying constitutive curve seen in [4] respectively. I also use a weakly curved cell formed by imposing a constant stress gradient across an infinitely-long parallel plate geometry with *toy* curvature $q = 10^{-3}$ (as used in [4]). For both cases, I set $\tau_d/\tau_R = 10^3$ (as used in [4]) and $\tau_d/\tau_R = 10^4$, for comparison. Both ratios show transient shear banding during the time-dependent flow, shown by the pronounced magnitude of $\Delta\dot{\gamma}(t)$ following the transient stress overshoot. However, for both $\beta = 0.65$ and $\beta = 0.85$, $\tau_d/\tau_R = 10^4$ resulted in a significantly larger peak in the degree of banding.

Note also that in both comparisons (a) and (b), the increase in the relaxation

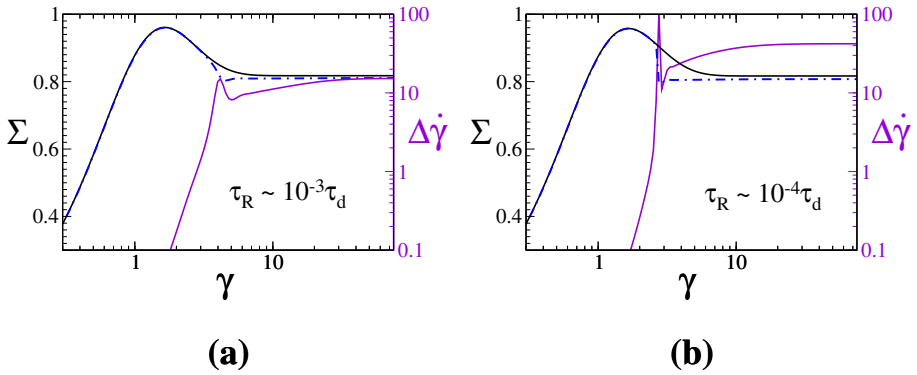


Figure 6.13: Transient stress and degree of banding for a shear startup as modelled by a multimode RP model (power law exponent $\alpha = 2.75$) for a material with a non-monotonic underlying constitutive curve ($\beta = 0.65$). $\kappa = 16.0$ and 160.0 for $Z = 61$ giving $\tau_d/\tau_R = 10^3$ and $10^4$. $J = 512$, $dt = 10^{-7}$. Cell curvature $q = 10^{-3}$.

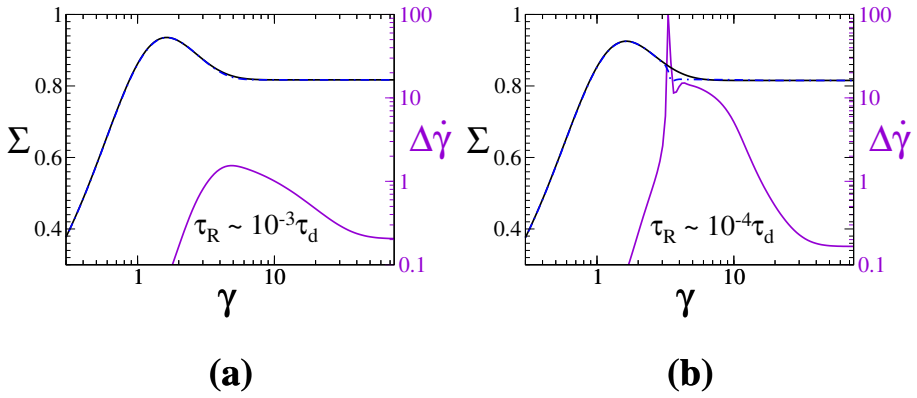


Figure 6.14: As in figure 6.13 for a monotonic underlying constitutive curve ($\beta = 0.85$).

time separation of $\tau_d$ and $\tau_R$ reduces the strain (or equivalently time, for constant $\dot{\gamma}$) at which the onset of shear banding occurs in the transient stress curve. Recall that earlier, in figure 6.12(a), where $\tau_d/\tau_R = 10^2$, significant shear band formation does not occur until far beyond the overshoot region in the stress and rather appears to be a steady state property. Conversely, for $\tau_d/\tau_R = 10^3,\ 10^4$, this onset of shear banding occurs much closer to the overshoot region. It is therefore suggested that increased relative chain stretch relaxation time (smaller $Z$ or $M_w$) dampens the elastically-driven instabilities in the flow during the startup transient. It is the inclusion of stretch effects on the polymer chain that helps capture the short-time transient shear rheology of the polymer. The increased chain stretch here can be seen to act as a stabilising influence against the formation of shear banded flow during shear startup.

In the following section I consider the relative influence of fit parameters $\alpha$ and $\kappa$ on the growth of transient shear banding in flow for a monotonic underlying constitutive curve.

## 6.4 Power-law fit: the influence of $\alpha$ and $\kappa$ fitting parameters

Recall that in the power-law fit of linear rheology, $\alpha$ sets the gradient of the relaxation spectrum. Infinitely large $\alpha$ recovers the single-mode RP model. $\kappa_Z = \kappa Z$ relates the separation of stretch relaxation time $\tau_R$ and tube disentanglement time $\tau_d$, required in the RP constitutive model to describe the dynamics of an entangled polymer chain in nonlinear flow.

Figure 6.15 shows a brief overview of a comparison between $\alpha$ and $\kappa_Z$, resulting from a extensive study where I explored a wide range of $\beta$-values. Here I focus on the case of a monotonic constitutive curve and take $\beta = 0.6$. I varied $\alpha$ and $\kappa_Z$ for $\alpha \in (0.1,\ 5.0)$ and $\kappa_Z \in (10^2,\ 10^4)$; I show here $\alpha = 0.5$ and 2.0, with $\kappa_Z = 10^2$ and $10^4$. The corresponding constitutive curves are shown at the top of figure 6.15. At the bottom of the figure, plots (a), (b) and (c) show the time-dependent material response to shear startup with $\dot{\gamma} = 50.0$. The solid-black constitutive curve corresponds to subfigure (a), the red-dashed constitutive curve corresponds to (b) and the blue dot-dashed curve corresponds to (c). As in section 6.3 this value of $\dot{\gamma}$ lies within the weakly-sloping plateau region of each monotonic underlying constitutive curve.

For both $\alpha$ values, homogeneous flow is recovered at long times, relative to the finite degree of banding due to cell curvature. Larger $\alpha$ decreases the dependence of the multimode model on the higher-order modes. In (b), larger $\alpha$ can be seen to reduce the stress maximum at the overshoot but slightly increases the degree of banding (associated with the elastically-driven flow instabilities). In particular, the reduction in the stress maximum and increased degree of banding is due to the reduced influence of the stretching modes for increased steepness of the power-law

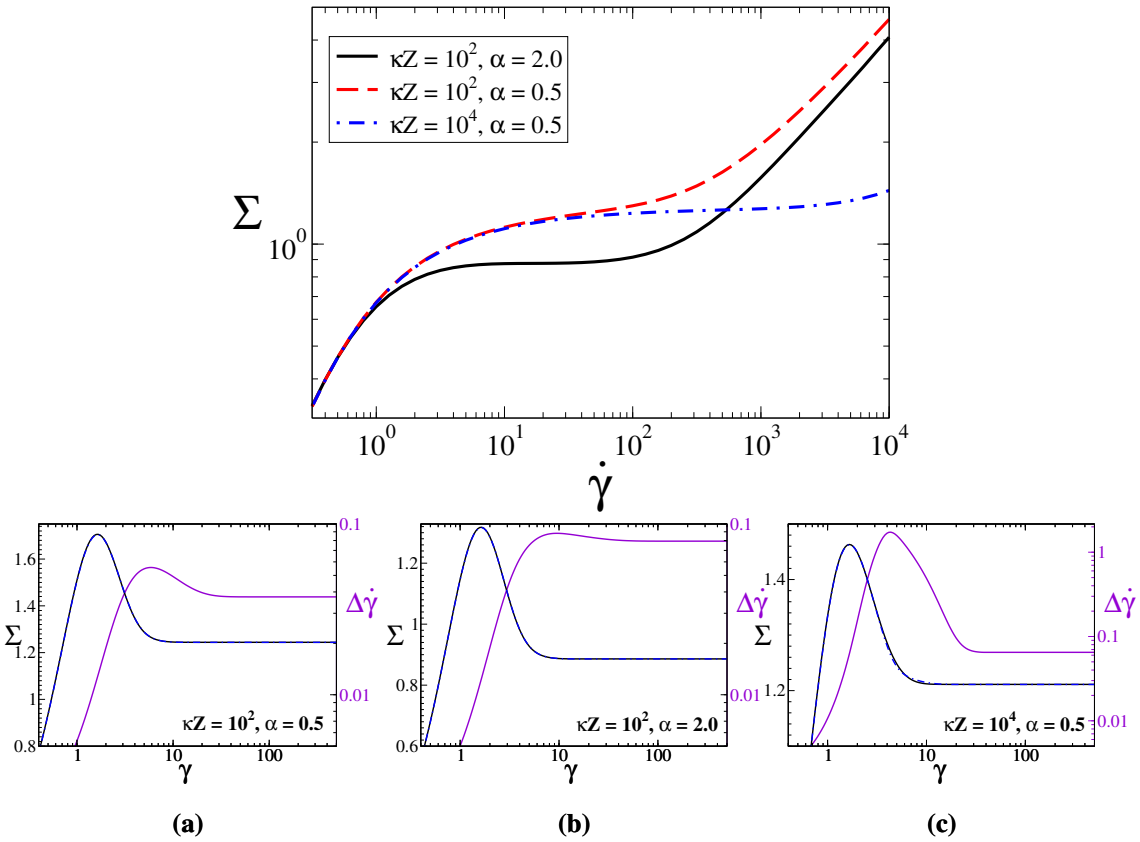


Figure 6.15: Importance of $\alpha$ and $\kappa$ in the emergence of transient shear band formation in shear startup. Multimode model, with 3 stretching, 3 non-stretching modes and the effective solvent viscosity $\eta = 10^{-5}$. Bottom row $\dot{\gamma} = 50$. $\beta = 0.6$.

(larger $\alpha$). The inclusion of chain stretch is known to help capture the short-time dynamics of the transient stress response to shear startup [124, 128, 142]. Moreover, a larger chain-stretch influence suppresses the transient shear banding dynamics.

In (c) $\alpha$ is set to the lower value and $\kappa Z$ is increased by two decades to give $\kappa Z = \tau_d/\tau_R = 10^4$. It is at the large separation in $\tau_d$ and $\tau_R$ that significant transient shear banding was seen in sections 6.1.1 and 6.3. Recall that this corresponds to an increase in the molecular weight of the polymer. Again, as in section 6.2 increasing $M_w$ decreased the stress maximum since all parameter sets have $\tau_d$ set to unity (and thus each plot (a)-(c) is at the same Weissenburg number, $Wi = 50.0$). Moreover, a significant peak in the degree of banding (to $\Delta\dot{\gamma} \sim 100\%\dot{\gamma}$) is seen following the stress overshoot. However, for all plots there is no significant difference between the homogeneous and heterogeneous stress response.

Transient shear banding is a more pronounced feature for well separated timescales

$\tau_d$ and $\tau_R$ (and large $M_w$). It is at this artificially inflated separation (via $\kappa_Z$) in the timescales that shear banding profiles are seen that are consistent with what is seen in experiment [19, 28, 88, 107, 152, 179, 180]. Indeed, it was at large separations ($\tau_d/\tau_R = 10^3$ and $10^4$) that significant transient shear banding was seen in theoretical studies (recall case studies (a) and (b)).

An alternative interpretation of the results shown in this chapter is to consider the possibility that in order to achieve shear banding profiles consistent with that seen in experiment, there may be a significant influencing factor that is not considered here. In each study shown here, there has been no appreciable shear banding for values consistent with the fit found for real polymer data. It is only by artificially increasing molecular weight - or indeed the degree of entanglement - that shear banding profiles are seen. Whilst this is consistent with Wang's group [152] (despite their issues with the tube theory) it has been suggested by groups such as Hu [85] and Li and McKenna [107, 108] that edge fracture is an important influencing factor on the presence of shear banding in flow. It could therefore be argued that the results presented here - where edge effects are neglected and cannot be modelled - present a compelling case for edge fracture as a trigger for shear banding. Further work here is needed to establish if this indeed could be the case.

In the present study, where physicality is relaxed on $\kappa_Z$, as $\kappa_Z$ is increased, the non-stretching limit of the RP model is recovered for each mode since $\tau_R \to 0$. Performing a multimode non-stretch RP model for the experimental fit data shown earlier in figure 6.5 I found very similar results for the transient stress response to shear startup as seen in 6.5(c) where $\tau_d/\tau_R = 10^4$ (data not shown).

This suggests that it is the ratio of $\tau_d/\tau_R$ (or indeed the value of $\kappa_Z$) is an important quantity when studying transient shear banding through the multimode RP model in time-dependent flows. $\alpha$ is certainly important too, though taking $\alpha \to \infty$ (and thus recovering the single-mode RP model) may provide a useful tool in exploring the prevalence of transient shear banding over a wide range of entanglement numbers $Z$ and RP CCR-parameter $\beta$ and thus the dependence of shear banding during startup on the chain stretch relaxation time $\tau_R = \tau_R(Z)$.

In the following section I include a study of shear banding intensity in the limit

of finite (multimode) and infinite (single-mode) $\alpha$ for non-monotonic and monotonic underlying constitutive curves. For finite $\alpha$, I focus on the influence of $\kappa_Z$ which, so far, I have shown that chain stretch in the RP model overly suppresses the levels of shear banding. Recall that varying $\kappa$ or $Z$ is an arbitrary choice and I have chosen to relax physicality on $\kappa$ (and hence the contraction $\kappa_Z$) here for a fixed, experimentally achievable $Z$. Following similar analyses in chapters 4 and 5 for large amplitude oscillatory protocols, I build two maps of shear banding intensity across the $(\beta,\ Z)$ and $(\beta,\ \kappa_Z)$ planes for transiently time-dependent flow within the shear startup protocol. These maps provide the final roadmaps for time-dependent shear banding in the RP model for entangled polymer solutions and melts presented in this thesis.

### 6.4.1 Shear banding intensity in the $(\beta,\ Z)$ and $(\beta,\ \kappa_Z)$ planes

I present two roadmaps for shear-banding intensity across the space defined by the convective constraint parameter $\beta$ and entanglement number $Z$. I consider two key $\alpha$-values: $\alpha \to \infty$, recovering the single-mode RP model, and $\alpha = 0.25$, found to be a good fit to PI90k and PI200k data (section 6.3). For $\alpha = 0.25$ I consider the contraction $\kappa_Z$ rather than $Z$, consistent with the work presented above.

In each case, I define transient shear banding to be significant when $\Delta_{\dot{\gamma}} > 10\%\dot{\gamma}$ during shear startup. Recall that this can decay away to regain a homogeneous flow at the steady state. 10% transient shear banding is shown by dotted circles and hatched circles describe stronger transient shear banding, when $\Delta_{\dot{\gamma}} > 100\%\dot{\gamma}$. Black filled circles indicate significant shear banding at the steady state. In each figure, the red-shaded region indicates where the underlying constitutive curve of the material is non-monotonic.

#### Single-mode approximation: $\alpha \to \infty$

It can clearly be seen from figure 6.16 that shear banding exists in the time-dependent flow of entangled polymers for a wide region of $(\beta,\ Z)$ parameter space.

Despite the value of $\beta$ being a poorly defined material property with respect to theory calculations, transient shear banding is seen for a wide range of $\beta$, for $Z$ well within the regime of experimental measurablability. Transient shear banding arises in shear startup for a wide region of the space where the underlying constitutive curve is monotonic and the steady state flow is homogeneous. Moreover, the intensity of the shear bands is creased as $Z$ is increased. Whilst this directly refers to entanglement number here, it could instead be solely considered as the separation parameter between $\tau_d$ and $\tau_R$, for comparison with the previous discussions in this chapter.

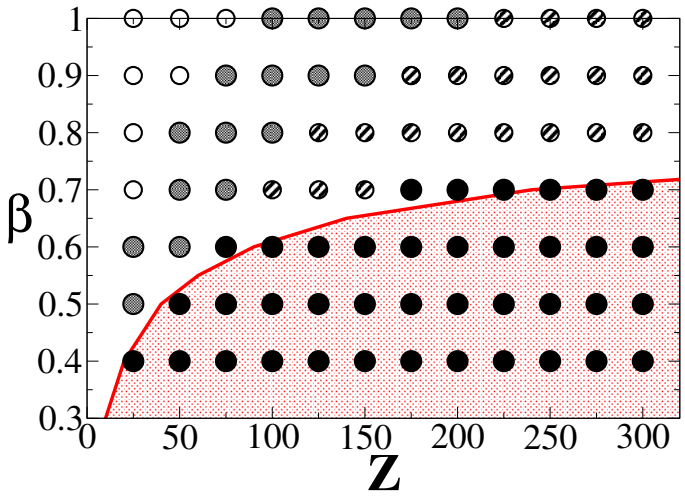


Figure 6.16: $\beta - Z$-plane for the stability to the formation of shear bands during the shear startup protocol. This phase plane is for linear entangled polymers and melts, described by the single-mode stretching Rolie-Poly model. Open circles indicate no measurable banding. Dotted and hatched circles indicate significant transient shear banding: $\Delta_{\dot{\gamma}} > 10\%\dot{\gamma}$, and $\Delta_{\dot{\gamma}} > 100\%\dot{\gamma}$ during shear startup, respectively, such that homogeneity is regained at the steady state. Black filled circles indicate significant shear banding at the steady state. Red-shaded region indicates a non-monotonic underlying constitutive curve.

Note that steady state shear banding appears to occur for a monotonic underlying constitutive curve for ($Z = 75,\ \beta = 0.6$), ($Z = 175,\ \beta = 0.7$) and ($Z = 200,\ \beta = 0.7$). This significant heterogeneity at the steady state is accounted for by the imposed curvature stress gradient on the rheological cell for a weakly-increasing plateau-like region of the underlying constitutive curve [4].

## Multimode RP: $\alpha = 0.25$

In figure 6.17 I show a shear banding intensity map over the ($\beta$, $\kappa_Z$) plane for a finite $\alpha$-value, *i.e.* using the multimode RP model. Indeed, significant transient shear banding is seen for materials with a monotonic underlying constitutive curve for values of $\kappa_Z$ beyond $\tau_d/\tau_R \sim 10^3$. Note here that the red shaded region for which values of $\beta$ and $\kappa_Z$ have non-monotonic underlying constitutive curves is notably smaller in $\beta$ than for the single-mode RP case in figure 6.16.

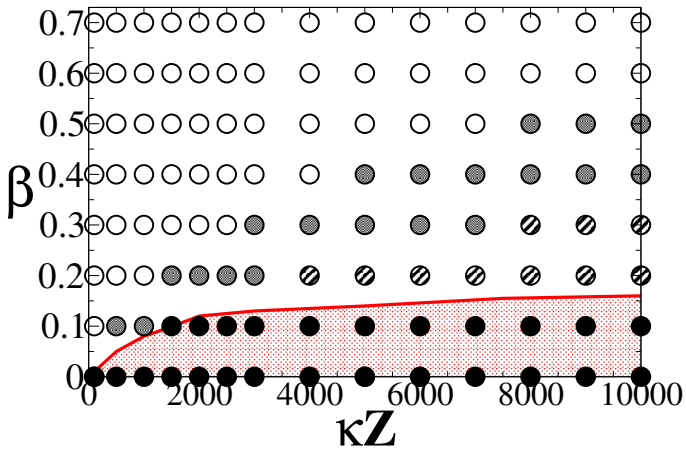


Figure 6.17: ($\beta$, $\kappa_Z$) plane for the stability to the formation of shear bands during the shear startup protocol. This phase plane is for linear entangled polymers and melts, described by the multimode Rolie-Poly model. Open circles indicate no measurable banding. Dotted and hatched circles indicate significant transient shear banding: $\Delta_{\dot\gamma} > 10\%\dot\gamma$, and $\Delta_{\dot\gamma} > 100\%\dot\gamma$ during shear startup, respectively, such that homogeneity is regained at the steady state. Black filled circles indicate significant shear banding at the steady state. Red-shaded region indicates a non-monotonic underlying constitutive curve.

Figure 6.17 shows that a large $\kappa_Z$ value is required to see transient shear banding in the multimode RP model as defined by a power-law relationship fit to experimental PI relaxation spectrum data. It is thus suggested that the way in which chain stretch is incorporated into the RP model, whilst captures the short-time dynamics of the stress response to shear, suppresses shear band formation in the regime of experimentally-achievable entanglement number $Z$. Whilst the single-mode RP model is a a helpful indicative tool when studying the stability of an entangled polymeric fluid to the formation of shear bands in time-dependent flow regimes, it does not capture the full chain dynamics of the polymer. Indeed, the single-mode

RP model requires a much larger $Z$ to capture the shear banding profiles seen in experiment (for smaller $Z$).

## 6.5 Conclusions from chapter 6

In this chapter I have considered a multimode Rolie-Poly (RP) model for linear entangled polymer solutions and melts [110]. Using experimental rheology data for a well entangled monodisperese polyisoprene [10], I have characterised the linear rheology of the dynamic moduli and relaxation time spectrum over a wide range of frequencies in SAOS, and under nonlinear shear.

I then further approximated the relaxation spectrum of the polymer by a power-law distribution of multiple Maxwell modes. The slowest mode was set to the slowest relaxation time (the characteristic reptation time, $\tau_d$) of the polymer and higher-order dynamics were described by faster-relaxing modes across the power-law distribution of increasing frequencies ($\omega_n = 1/\tau_{d_n}$). In each fit (to experimental data, and in the power-law approximation) slower modes were described by the full stretching version of the RP model. Higher order modes used the non-stretching version of the model, taken in the limit where chain stretch relaxes infinitely fast. The fastest mode was taken to be the solvent viscosity contribution, allowing the possibility of shear banding to be calculated during constitutive modelling of the polymer dynamics under the shear startup protocol.

I found the formation of shear bands in the flow for the multimode RP model for imposed $\dot{\gamma}$ within the negatively-decreasing stress region, or weakly increasing plateau-like region of the underlying constitutive curve of the material. As expected, steady state shear banding was only seen in materials that had a non-monotonic underlying constitutive curve. However, the existence of transient shear banding during shear startup was shown to depend upon the separation of relaxation timescales $\tau_d$ and $\tau_R$ - or equivalently, the molecular weight $M_w$ - of the polymer. An increased separation (or $M_w$) resulted in a significantly pronounced peak in the degree of shear banding measured in the flow following the transient overshoot in stress $\Sigma(\gamma)$.

A study of parameter space was carried out to investigate the influence of the exponent $\alpha$ of the negatively-decreasing power-law distribution of relaxation times and moduli, the effective entanglement number $\kappa_Z$ representing the separation between $\tau_d$ and $\tau_R$, and the RP-model CCR parameter $\beta$, on the existence (and intensity) of shear banding in shear startup for the multimode RP model.

Whilst $\alpha$ clearly influenced the material response to shear startup, I focussed on the role of $\kappa_Z$ on the existence and intensity of transient shear banding in the shear startup protocol. Taking the limit $\alpha \to \infty$ (and thus recovering the single-mode RP model) enables a quick exploratory study into the dependence of transient shear band formation on the parameters $\beta$ and $Z$, across the phase space. Indeed, I found significant (transient) shear banding intensity across the $(\beta,\ Z)$ phase space for a wide range of polymers that have a monotonic underlying constitutive curve.

A comparative survey of the $(\beta,\ \kappa_Z)$ phase plane for the multimode RP model was shown for the power-law exponent $\alpha = 0.25$. This value of $\alpha$ approximated the PI90k and PI200k data characterisation. This showed significant measurable transient shear banding for monotonic underlying constitutive curves for sufficiently large $\kappa_Z$. Moreover, the underlying constitutive curve of the material was monotonic for a wider range of $\beta$ values. It was seen that large $\kappa_Z$ (and thus a reduced influence of chain stretch) is required to recover significant shear banding in shear startup.

Clearly, whilst the single-mode RP model provides a computationally inexpensive and fast technique to explore the prevalence of shear banding in the time-dependent flows of polymers, significant dynamics of the polymer chain cannot be captured by this simplified model. The single-mode model does, however, provide a helpful indicative measure for transient shear banding in shear startup.

It is suggested that the need for large $\kappa_Z$ in the multimode RP model (or indeed $Z$ in the single mode model) to achieve the shear banded profiles seen in experiment indicates that the way in which the RP model itself includes chain stretch relaxation, overly suppresses shear banding for experimentally achievable entanglement numbers. Whilst the stress response to shear startup is well captured by the model, the degree of banding only matches that seen in experiment for artificially inflated (large $\kappa$) separations in the relaxation timescales $\tau_d$ and $\tau_R$. An example of this was seen in [178] where Wang et al. commented on a paper [4] using the RP model for $\tau_d/\tau_R \sim 10^3$, giving $Z \sim 333$. Similar banded profiles were seen in the theoretical RP study [4] as in the experimental paper [174, 175], but the experimental paper had $Z = 47$, thus the RP model simulation required an inflation by nearly a decade in the $\tau_d/\tau_R$ ratio ($\kappa$, here) in order to capture the experimental results.

An alternative interpretation of the results seen here is the possibility of edge fracture. Though not included in the calculations performed here, it was discussed that this, rather than any shortcomings of the RP model, may be the trigger for instability in the flow leading to the formation of shear bands. The inclusion of edge fracture in calculations may lead to the initial parameter fits of the multimode RP model, when allowing for heterogeneity, to produce results consistent with that seen in experiment.

In another experimental study by Wang et al. [28] both shear banded and homogeneous flow profiles were measured at the steady state for the strain-controlled deformation of a well entangled polymer. The end state of the flow depended on the slow ramping rate (as opposed to fast shear startup) of the deformation imposed on the polymer. There was no measurable difference in the steady state stress value. This could be considered to coincide with the suggestion here that the RP model captures the stress response of the polymer to imposed shear well, but overly suppresses the otherwise possible shear banding in the flow. Alternatively, it could be suggested that the slow ramping rate used in the experiment by Wang et al. protected the sample from edge effects and thus precluded the possibility of shear banding being triggered in the flow.

Another alternative may be that the suppression of shear banding for experimentally used values of $Z$ could be resolved by coupling the Maxwell modes in the power-law distribution used here. In each mode I have assigned a distinct relaxation time and moduli. There is no interaction between the relaxation dynamics described by the timescale of each mode. This is perhaps undesirable as in the GLaMM and RP models themselves, the relaxation dynamics of the polymer are dependent on one another (e.g. stretch relaxation via convective constraint release). An interaction between the modes may enable any overly suppressed shear banding by chain stretch seen in the results presented here to be alleviated.

Finally, the work here is limited to the *transiently* time-dependent shear startup protocol. An interesting progression of this would be to consider the existence of shear banding in LAOStrain and LAOStress protocols where the flow has a *sustained* time-dependence. This, however, amongst the other suggestions given here, is left

for future study.

# 7

# Conclusions

Throughout this thesis I have presented evidence, through numerical simulations, of shear banding in time-dependent flows. I have predominantly focused on large amplitude oscillatory shear strain and stress (LAOStrain and LAOStress) protocols, using the stretching and non-stretching limits of the Rolie-Poly model. This model is the single-mode approximation to the GLaMM model, which considers a spectrum of relaxation times to capture the full chain dynamics of a polymer. In chapter 6 I considered the influence of higher-order relaxation time dynamics on the existence of shear banding in time-dependent flows for the simpler shear startup protocol. I found numerical evidence for shear banding flows for sufficiently well entangled, high-molecular weight polymers. I also considered the other side of the ongoing discussions over the origins of shear banding by considering the influence edge fracture may have on these results.

**Extension I:** A natural extension to the studies presented here would be to study the multimode Rolie-Poly model (as defined by the power-law distribution in chapter 6) in the LAOStrain and LAOStress protocols. These protocols, unlike shear startup, have a sustained time-dependence and have been shown in chapters 4 and 5 to exhibit short-lived and persistent shear bands in flow. It was shown in chapter 6 that a multimode model is required to fully describe polymer dynamics in flow. It would be interesting to see how the inclusion of higher order relaxation dynamics would affect the results for shear banding shown in chapters 4 and 5.

In chapter 4 I considered strain-controlled oscillatory flow in the nonlinear regime. This so-called LAOStrain protocol has the benefit of the experimentalist being able to independently vary the amplitude and frequency of imposed oscillations to asses a wide range of elastically- and viscously-dominated flow behaviours, and linear and nonlinear flows. In this work I furthered the initial study by Adams and Olmsted [2] that showed the existence of shear banding in entangled polymers under LAOStrain. I referred to the criteria for shear banding in transiently time-dependent flows in [135] and extended the work of Moorcroft and Fielding [32, 135, 136] to consider LAOStrain: a protocol with a sustained time-dependence. Indeed, I found shear banding in sufficiently well entangled polymers under LAOStrain, occurring over a wide range of imposed amplitudes and frequencies.

I discussed the ability to understand - to a good approximation - the onset of instability to the formation of shear bands in LAOStrain by the time-dependent criteria and triggers for the onset of instability defined for the simpler shear startup protocol in [135, 136]. At low-frequencies, such that the deformation to the fluid is imposed at a slower rate than the inverse characteristic relaxation time of the polymer, the material response follows the stationary flow curve of the polymer. Shear bands form in this low-frequency regime due to an overshoot in $\Sigma(\dot{\gamma})$ leading to a negatively-sloping region in the underlying constitutive curve of the material (formed in theoretical simulation for homogeneously-constrained flow).

At finite frequency, elastically-dominated flow responses to LAOStrain were seen if the period of oscillation was much less than the inverse characteristic relaxation

time of the polymer. In this regime, the elastic criterion for shear banding in shear startup gives a good approximation to the onset of shear banding in LAOStrain. This criterion is satisfied when there is an overshoot in the $\Sigma(\gamma)$ response with an added influence from strong curvature in $\Sigma(\gamma)$ (which may result in instability to shear banding *ahead* of the overshoot in strain).

Over a range of amplitude $\dot{\gamma}_0$ and frequencies $\omega$, a combination of these two limiting responses gave rise to significant shear banding across the $(\dot{\gamma}_0,\ \omega)$ plane. This occurred for materials with non-monotonic *and* monotonic underlying constitutive curves. Moreover, once chain stretch was included in the RP model, a phase diagram was built up for a range of convective constraint release parameter $\beta$ and entanglement number $Z$ for the intensity of shear banding in LAOStrain. There was a significant regime of shear banding (seen for a wide range of imposed amplitude and frequency in LAOStrain) recorded for materials that had a monotonic underlying constitutive curve.

**Extension II** : In appendix I (section 4.7) of chapter 4, I briefly discuss the existence of normal stress differences in the flow during LAOStrain. These approached $40 - 70\%$ of the cycle-averaged normal stress value and were significant throughout the cycle. Normal stress differences have been known to couple with the dynamics of concentration coupling in the flow to form shear bands [66–68, 131, 162]. This effect was neglected in the calculations of this thesis but - through the findings within this appendix - would undoubtable prove an interesting area to explore in further studies.

In chapter 5 I consider the stress-controlled oscillatory protocol: LAOStress. In this protocol, imposed stress is the amplitude that is sinusoidally varied for a range of fixed amplitudes and frequencies. Unlike the LAOStrain protocol, I did not find shear banding to be a persistent feature throughout one cycle in the alternance state. Rather, I found shear banding to be a temporally localised instability to a sudden increase in $\dot{\gamma}$ as the $\Sigma(\dot{\gamma})$ curve was transited. In the low-frequency regime, this transit occurred over the region of non-monotonic, or weakly-increasing monotonic, underlying constitutive curve. Linear response regions at the low- and high-

viscosity branches of the non-monotonic constitutive curve were traced by the $\Sigma(\dot{\gamma})$ response to LAOStress, whilst the fast 'top-jumping' (and to a lesser extent 'bottom-jumping') mechanisms over the negatively-sloping stress regime provided the trigger to shear band formation. No shear banding was seen in this low frequency regime for a monotonic underlying constitutive curve, but the same fast-transit trigger to shear banding is seen over the weakly increasing plateau-like region of the homogeneously-constrained $\Sigma(\dot{\gamma})$ response at finite frequency.

It is in these regions of fast $\dot{\gamma}$ transit for a small increase in $\Sigma(t)$ that means the stress is effectively constant and therefore that the step-stress criterion for shear banding applies for LAOStress. Although the step-stress protocol is only transiently time-dependent, the criterion holds - to a good approximation - in the LAOStress protocol which has a sustained time-dependence.

An additional phase plane for the interplay of the convective constraint release parameter $\beta$ and entanglement number $Z$ - for the stretching version of the RP model - on the intensity of shear banding across a wide range of imposed $\Sigma_0$ amplitudes and frequencies is also shown in chapter 5. As for LAOStrain, significant shear banding is seen for the LAOStress protocol for a large region of the $\beta - Z$ phase plane for which the underlying constitutive curve of the material is monotonic.

**Extension III:** An additional study to further the work presented here would be to consider the influence of inertia. At large shear rates the assumption taken here that inertial effects are negligible and thus can be neglected may not always be applicable. In particular, the fast transit of $\dot{\gamma}$ on a timescale of $G/\eta$ seen in LAOStress to trigger a shear banding instability may warrant the inclusion of inertia when small values of $\eta$ (which thus increases the timescale of transition) are used.

Additional studies of shear banding in LAOStrain and LAOStress could be carried out in the regimes that have been neglected here:

**Extension IV:** The studies shown here predominantly use a weakly curved cell as the seed to spatial heterogeneity in the flow. The absence of stochastic noise in the calculations suppresses the possibility of nucleation events in the flow which may

further trigger shear banding instabilities. Whilst the results presented here show consistent behaviour when weak curvature was instead replaced by small stochastic noise, it may be an interesting future study to consider the inclusion of nucleation kinetics in the flow for finite temperature simulations.

**Extension V:** As discussed in chapter 6, recent studies have considered edge fracture to govern elastically-driven instabilities in flows [107,108,164]. The calculations performed here make the assumption that edge effects are negligible and are thus ignored. Including the possibility for these effects in numerical simulations by adding a free surface may aid the understanding of these currently-debated instabilities.

**Extension VI:** The calculations performed in this thesis assumed, form the outset, that spatial variations only occurred in the flow gradient direction. I ignored the possibility of any secondary instabilities [58] of the interface between the shear bands [60, 138], or indeed in the high shear band itself [62]. It is unknown if these instabilities will form, or persist, to the alternance state in any given regime of amplitude and frequency space. Investigations into this are left to further studies.

Through the studies and results presented in this thesis I have shown evidence through numerical simulation of shear banding in rheological protocols with sustained time-dependence. Clearly - as suggested through the proposed extensions here - there is much of the story still to explore to further understand the full dynamics of entangled linear polymers in flow. I am interested to see where the field goes next with these studies.

# Bibliography


[1] J. Adams, S. M. Fielding, and P. D. Olmsted. The interplay between boundary conditions and flow geometries in shear banding: Hysteresis, band configurations, and surface transitions. *Journal of Non-Newtonian Fluid Mechanics*, 151(1-3):101–118, 2008.

[2] J. Adams, S. M. Fielding, and P. D. Olmsted. Transient shear banding in entangled polymers: A study using the Rolie-Poly model. *Journal of Rheology*, 55(5):1007, 2011.

[3] J. Adams and P. D. Olmsted. Adams and Olmsted Reply:. *Phys. Rev. Lett.*, 103(21):219802, 2009.

[4] J. Adams and P. D. Olmsted. Nonmonotonic Models are Not Necessary to Obtain Shear Banding Phenomena in Entangled Polymer Solutions. *Physical Review Letters*, 102(6):067801, 2009.

[5] J. M. Adams and P. D. Olmsted. Nonmonotonic models are not necessary to obtain shear banding phenomena in entangled polymer solutions. *Phys. Rev. Lett.*, 102:067801, 2009.

[6] O. S. Agimelen and P. D. Olmsted. Apparent Fracture in Polymeric Fluids under Step Shear. *Physical Review Letters*, 110(20):204503, 2013.

[7] L. A. Archer, Y. L. Chen, and R. G. Larson. Delayed slip after step strains in highly entangled polystyrene solutions. *Journal of Rheology*, 39(3):519, 1995.

[8] D. Auhl, P. Chambon, T. C. B. McLeish, and D. J. Read. Elongational flow of blends of long and short polymers: effective stretch relaxation time. *Physical review letters*, 103(13):136001, 2009.

[9] D. Auhl, D. M. Hoyle, D. Hassell, T. D. Lord, O. G. Harlen, M. R. Mackley, and T. C. B. McLeish. Cross-slot extensional rheometry and the steady-state extensional response of long chain branched polymer melts. *Journal of Rheology*, 55(4):875, 2011.

[10] D. Auhl, J. Ramirez, A. E. Likhtman, P. Chambon, and C. Fernyhough. Linear and nonlinear shear flow behavior of monodisperse polyisoprene melts with a large range of molecular weights. *Journal of Rheology*, 52(3):801, 2008.

[11] J.-E. Bae and K. S. Cho. Semianalytical methods for the determination of the nonlinear parameter of nonlinear viscoelastic constitutive equations from LAOS data. *Journal of Rheology*, 59(2):525–555, 2015.

[12] J.-E. Bae, M. Lee, K. S. Cho, K. H. Seo, and D.-G. Kang. Comparison of stress-controlled and strain-controlled rheometers for large amplitude oscillatory shear. *Rheologica Acta*, 52(10-12):841–857, 2013.

[13] M. Baumgaertel and H. H. Winter. Determination of discrete relaxation and retardation time spectra from dynamic mechanical data. *Rheologica Acta*, 28(6):511–519, 1989.

[14] J.-F. Berret. Rheology of Wormlike Micelles: Equilibrium Properties and Shear Banding Transitions. In R. Weiss and P. Terech, editors, *Molecular Gels*, chapter 19, pages 667–720. Springer, Dordrecht, 2005.

[15] J.-F. Berret and Y. Séréro. Evidence of shear-induced fluid fracture in telechelic polymer networks. *Phys. Rev. Lett.*, 87:048303, 2001.

[16] P. E. Boukany and S.-Q. Wang. Use of Particle-Tracking Velocimetry and Flow Birefringence To Study Nonlinear Flow Behavior of Entangled Wormlike Micellar Solution: From Wall Slip, Bulk Disentanglement to Chain Scission. *Macromolecules*, 41(4):1455–1464, 2008.

[17] P. E. Boukany and S.-Q. Wang. Exploring Origins of Interfacial Yielding and Wall Slip in Entangled Linear Melts during Shear or after Shear Cessation. *Macromolecules*, 42(6):2222–2228, 2009.

[18] P. E. Boukany and S.-Q. Wang. Exploring the transition from wall slip to bulk shearing banding in well-entangled DNA solutions. *Soft Matter*, 5(4):780, 2009.

[19] P. E. Boukany and S.-Q. Wang. Shear banding or not in entangled {DNA} solutions depending on the level of entanglement. *Journal of Rheology*, 53(1):73–83, 2009.

[20] P. E. Boukany, S.-Q. Wang, and X. Wang. Step Shear of Entangled Linear Polymer Melts: New Experimental Evidence for Elastic Yielding. *Macromolecules*, 42(16):6261–6269, 2009.

[21] N. Bowditch. *On the motion of a pendulum suspended from two points.* 1815.

[22] M. M. Britton and P. T. Callaghan. Two-Phase Shear Band Structures at Uniform Stress. *Physical Review Letters*, 78(26):4930–4933, 1997.

[23] J. Cao and A. E. Likhtman. Shear Banding in Molecular Dynamics of Polymer Melts. *Phys. Rev. Lett.*, 108(2):28302, 2012.

[24] K. A. Carter, J. M. Girkin, and S. M. Fielding. Shear banding in large amplitude oscillatory shear (LAOStrain and LAOStress) of polymers and wormlike micelles, `http://arxiv.org/abs/1510.00191`. 2015.

[25] L. Casanellas, C. J. Dimitriou, T. J. Ober, and G. H. McKinley. Spatiotemporal dynamics of multiple shear-banding events for viscoelastic micellar fluids in cone-plate shearing flows. *Journal of Non-Newtonian Fluid Mechanics*, 2014.

[26] M. E. Cates and S. M. Fielding. Theoretical Rheology of Giant Micelles. In R. Zana and E. Kaler, editors, *Giant Micelles*, chapter 4, pages 109–161. Taylor and Francis, London, 2007.

[27] M. E. Cates, T. C. B. McLeish, and G. Marrucci. The Rheology of Entangled Polymers at Very High Shear Rates. *Europhysics Letters (EPL)*, 21(4):451–456, 1993.

[28] S. Cheng and S.-Q. Wang. Is shear banding a metastable property of well-entangled polymer solutions? *Journal of Rheology*, 56(6):1413–1428, 2012.

[29] K. S. Cho, K. Hyun, K. H. Ahn, and S. J. Lee. A geometrical interpretation of large amplitude oscillatory shear response. *Journal of Rheology*, 49(3):747, 2005.

[30] I. Cohen, B. Davidovitch, A. B. Schofield, M. P. Brenner, and D. A. Weitz. Slip, Yield, and Bands in Colloidal Crystals under Oscillatory Shear. *Physical Review Letters*, 97(21):215502, 2006.

[31] M. W. Collis, A. K. Lele, M. R. Mackley, R. S. Graham, D. J. Groves, A. E. Likhtman, T. M. Nicholson, O. G. Harlen, T. C. B. McLeish, L. R. Hutchings, C. M. Fernyhough, and R. N. Young. Constriction flows of monodisperse linear entangled polymers: Multiscale modeling and flow visualization. *Journal of Rheology*, 49(2):501, 2005.

[32] R. L. Cooke. *Shear Banding in Time-Dependent Flows of Complex Fluids*. PhD thesis, Durham University, `http://etheses.dur.ac.uk/7285/`, 2013.

[33] P. Coussot, J. Raynaud, F. Bertrand, P. Moucheront, J. Guilbaud, H. T. Huynh, S. Jarny, and D. Lesueur. Coexistence of Liquid and Solid Phases in Flowing Soft-Glassy Materials. *Physical Review Letters*, 88(21):218301, 2002.

[34] M. Cromer, G. H. Fredrickson, and L. G. Leal. A study of shear banding in polymer solutions. *Physics of Fluids*, 26(6):063101, 2014.

[35] M. Cromer, M. C. Villet, G. H. Fredrickson, and L. G. Leal. Shear banding in polymer solutions. *Physics of Fluids*, 25(5):051703, 2013.

[36] P. G. de Gennes. Reptation of a polymer chain in the presence of fixed obstacles. *The Journal of Chemical Physics*, 55(2):572–579, 1971.

[37] P. R. de Souza Mendes and R. L. Thompson. A unified approach to model elasto-viscoplastic thixotropic yield-stress materials and apparent yield-stress fluids. *Rheologica Acta*, 52(7):673–694, 2013.

[38] P. R. de Souza Mendes, R. L. Thompson, A. A. Alicke, and R. T. Leite. The quasilinear large-amplitude viscoelastic regime and its significance in the rheological characterization of soft matter. *Journal of Rheology*, 58(2):537–561, 2014.

[39] J. Dealy and K. Wissbrun. Melt rheology and its role in polymer processing, 1990.

[40] B. Debbaut and H. Burhin. Large amplitude oscillatory shear and Fourier-transform rheology for a high-density polyethylene: Experiments and numerical simulation. *Journal of Rheology*, 46(5):1155, 2002.

[41] C. J. Dimitriou, L. Casanellas, T. J. Ober, and G. H. McKinley. Rheo-PIV of a shear-banding wormlike micellar solution under large amplitude oscillatory shear. *Rheologica Acta*, 51(5):395–411, 2012.

[42] C. J. Dimitriou, R. H. Ewoldt, and G. H. McKinley. Describing and prescribing the constitutive response of yield stress fluids using large amplitude oscillatory shear stress (LAOStress). *Journal of Rheology*, 57(1):27, 2013.

[43] T. Divoux, C. Barentin, and S. Manneville. From stress-induced fluidization processes to Herschel-Bulkley behaviour in simple yield stress fluids. *Soft Matter*, 7(18):8409, 2011.

[44] T. Divoux, C. Barentin, and S. Manneville. Stress overshoot in a simple yield stress fluid: An extensive study combining rheology and velocimetry. *Soft Matter*, 7(19):9335, 2011.

[45] T. Divoux, M. A. Fardin, S. Manneville, and S. Lerouge. Shear Banding of Complex Fluids. *Annual Review of Fluid Mechanics*, 48(1):150724171740009, 2015.

[46] T. Divoux, D. Tamarii, C. Barentin, and S. Manneville. Transient Shear Banding in a Simple Yield Stress Fluid. *Physical Review Letters*, 104(20):208301, 2010.

[47] M. Doi and S. F. Edwards. *The Theory of Polymer Dynamics*. Clarendon, Oxford, 1989.

[48] S. F. Edwards. The statistical mechanics of polymerized material. *Proceedings of the Physical Society*, 92(1):9, 1967.

[49] V. Entov and E. Hinch. Effect of a spectrum of relaxation times on the capillary thinning of a filament of elastic liquid. *Journal of Non-Newtonian Fluid Mechanics*, 72(1):31–53, 1997.

[50] P. Erni, P. Fischer, E. J. Windhab, V. Kusnezov, H. Stettin, and J. Luger. Stress- and strain-controlled measurements of interfacial shear viscosity and viscoelasticity at liquid/liquid and gas/liquid interfaces. *Review of Scientific Instruments*, 74(11):4916, 2003.

[51] R. H. Ewoldt. Defining nonlinear rheological material functions for oscillatory shear. *Journal of Rheology*, 57(1):177, 2013.

[52] R. H. Ewoldt, A. E. Hosoi, and G. H. McKinley. New measures for characterizing nonlinear viscoelasticity in large amplitude oscillatory shear. *Journal of Rheology*, 52(6):1427, 2008.

[53] R. H. Ewoldt, A. E. Hosoi, G. H. McKinley, A. Co, G. L. Leal, R. H. Colby, and A. J. Giacomin. An Ontology for Large Amplitude Oscillatory Shear Flow. In *AIP Conference Proceedings*, volume 1027, pages 1135–1137. AIP, 2008.

[54] R. H. Ewoldt and G. H. McKinley. On secondary loops in LAOS via self-intersection of Lissajous-Bowditch curves. *Rheologica Acta*, 49(2):213–219, 2009.

[55] R. H. Ewoldt, P. Winter, J. Maxey, and G. H. McKinley. Large amplitude oscillatory shear of pseudoplastic and elastoviscoplastic materials. *Rheologica Acta*, 49(2):191–212, 2009.

[56] Z. Fahimi, C. P. Broedersz, T. H. S. van Kempen, D. Florea, G. W. M. Peters, and H. M. Wyss. A new approach for calculating the true stress response from large amplitude oscillatory shear (LAOS) measurements using parallel plates. *Rheologica Acta*, 53(1):75–83, 2013.

[57] Y. Fang, G. Wang, N. Tian, X. Wang, X. Zhu, P. Lin, G. Ma, and L. Li. Shear inhomogeneity in poly(ethylene oxide) melts. *Journal of Rheology*, 55(5):939, 2011.

[58] M. A. Fardin, C. Perge, L. Casanellas, T. Hollis, N. Taberlet, J. Ortín, S. Lerouge, and S. Manneville. Flow instabilities in large amplitude oscillatory shear: a cautionary tale. *Rheologica Acta*, 53(12):885–898, 2014.

[59] L. J. Fetters, D. J. Lohse, D. Richter, T. A. Witten, and A. Zirkel. Connection between Polymer Molecular Weight, Density, Chain Dimensions, and Melt Viscoelastic Properties. *Macromolecules*, 27(17):4639–4647, 1994.

[60] S. M. Fielding. Linear Instability of Planar Shear Banded Flow. *Physical Review Letters*, 95(13):134501, 2005.

[61] S. M. Fielding. Complex dynamics of shear banded flows. *Soft Matter*, 3:1262–1279, 2007.

[62] S. M. Fielding. Viscoelastic Taylor-Couette Instability of Shear Banded Flow. *Physical Review Letters*, 104(19):198303, 2010.

[63] S. M. Fielding. Shear banding in soft glassy materials. *Reports on progress in physics. Physical Society (Great Britain)*, 77(10):102601, 2014.

[64] S. M. Fielding. Triggers and signatures of shear banding in steady and time-dependent flows, `http://arxiv.org/abs/1512.04715`. 2015.

[65] S. M. Fielding, R. L. Moorcroft, R. G. Larson, and M. E. Cates. Modeling the relaxation of polymer glasses under shear and elongational loads. *The Journal of chemical physics*, 138(12):12A504, 2013.

[66] S. M. Fielding and P. D. Olmsted. Early Stage Kinetics in a Unified Model of Shear-Induced Demixing and Mechanical Shear Banding Instabilities. *Physical Review Letters*, 90(22):224501, 2003.

[67] S. M. Fielding and P. D. Olmsted. Flow phase diagrams for concentration-coupled shear banding. *The European physical journal. E, Soft matter*, 11(1):65–83, 2003.

[68] S. M. Fielding and P. D. Olmsted. Kinetics of the shear banding instability in startup flows. *Physical Review E*, 68(3):036313, 2003.

[69] S. M. Fielding and P. D. Olmsted. Nonlinear Dynamics of an Interface between Shear Bands. *Physical Review Letters*, 96(10):104502, 2006.

[70] S. Fujii, H. Morikawa, M. Ito, and T. Takahashi. Transient behavior of stress in a wormlike micellar solution under oscillatory shear. *Colloid and Polymer Science*, 2015.

[71] A. Giacomin, R. Bird, L. Johnson, and A. Mix. Large-amplitude oscillatory shear flow from the corotational Maxwell model. *Journal of Non-Newtonian Fluid Mechanics*, 166(19-20):1081–1099, 2011.

[72] T. Gibaud, D. Frelat, and S. Manneville. Heterogeneous yielding dynamics in a colloidal gel. *Soft Matter*, 6(15):3482, 2010.

[73] J. Goveas and P. Olmsted. A minimal model for vorticity and gradient banding in complex fluids. *The European Physical Journal E*, 6(1):79–89, 2001.

[74] R. S. Graham, E. P. Henry, and P. D. Olmsted. Comment on "New Experiments for Improved Theoretical Description of Nonlinear Rheology of Entangled Polymers". *Macromolecules*, 46(24):9849–9854, 2013.

[75] R. S. Graham, A. E. Likhtman, T. C. B. McLeish, and S. T. Milner. Microscopic theory of linear, entangled polymer chains under rapid deformation including chain stretch and convective constraint release. *Journal of Rheology*, 47(5):1171–1200, 2003.

[76] C. Grand, J. Arrault, and M. E. Cates. Slow Transients and Metastability in Wormlike Micelle Rheology. *Journal de Physique II*, 7(8):1071–1086, 1997.

[77] A. K. Gurnon, C. R. Lopez-Barron, A. P. R. Eberle, L. Porcar, and N. J. Wagner. Spatiotemporal stress and structure evolution in dynamically sheared polymer-like micellar solutions. *Soft matter*, 10(16):2889–98, 2014.

[78] A. K. Gurnon and N. J. Wagner. Large amplitude oscillatory shear (LAOS) measurements to obtain constitutive equation model parameters: Giesekus model of banding and nonbanding wormlike micelles. *Journal of Rheology*, 56(2):333, 2012.

[79] D. G. Hassell, T. D. Lord, L. Scelsi, D. H. Klein, D. Auhl, O. G. Harlen, T. C. B. McLeish, and M. R. Mackley. The effect of boundary curvature on the stress response of linear and branched polyethylenes in a contraction-expansion flow. *Rheologica Acta*, 50(7-8):675–689, 2011.

[80] E. J. Hemingway. *Internally and externally driven flows of complex fluids: viscoelastic active matter, flows in porous media and contact line dynamics*. PhD thesis, Durham University, `http://etheses.dur.ac.uk/11310/`, 2015.

[81] V. Herle, P. Fischer, and E. J. Windhab. Stress driven shear bands and the effect of confinement on their structures–a rheological, flow visualization, and Rheo-SALS study. *Langmuir : the ACS journal of surfaces and colloids*, 21(20):9051–7, 2005.

[82] J. Honerkamp and J. Weese. Determination of the relaxation spectrum by a regularization method. *Macromolecules*, 22(11):4372–4377, 1989.

[83] D. M. Hoyle, D. Auhl, O. G. Harlen, V. C. Barroso, M. Wilhelm, and T. C. B. McLeish. Large amplitude oscillatory shear and Fourier transform rheology analysis of branched polymer melts. *Journal of Rheology*, 58(4):969–997, 2014.

[84] D. M. Hoyle, D. W. Auhl, O. G. Harlen, and T. C. B. McLeish. Non-linear step strain of branched polymer melts. In *Journal of Rheology*, volume 53, pages 917–942, 2009.

[85] Y. T. Hu. Steady-state shear banding in entangled polymers? *Journal of Rheology*, 54(6):1307, 2010.

[86] Y. T. Hu and A. Lips. Kinetics and mechanism of shear banding in an entangled micellar solution. *Journal of Rheology*, 49(5):1001, 2005.

[87] Y. T. Hu, C. Palla, and A. Lips. Comparison between shear banding and shear thinning in entangled micellar solutions. *Journal of Rheology*, 52(2):379, 2008.

[88] Y. T. Hu, L. Wilen, A. Philips, and A. Lips. Is the constitutive relation for entangled polymers monotonic? *Journal of Rheology*, 51(2):275–295, 2007.

[89] K. Hyun, S. H. Kim, K. H. Ahn, and S. J. Lee. Large amplitude oscillatory shear as a way to classify the complex fluids. *Journal of Non-Newtonian Fluid Mechanics*, 107(1-3):51–65, 2002.

[90] K. Hyun, M. Wilhelm, C. O. Klein, K. S. Cho, J. G. Nam, K. H. Ahn, S. J. Lee, R. H. Ewoldt, and G. H. McKinley. A review of nonlinear oscillatory shear tests: Analysis and application of large amplitude oscillatory shear (LAOS). *Progress in Polymer Science*, 36(12):1697–1753, 2011.

[91] G. Ianniruberto and G. Marrucci. A simple constitutive equation for entangled polymers with chain stretch. *Journal of Rheology*, 45(6):1305–1318, 2001.

[92] E. A. Jagla. Shear band dynamics from a mesoscopic modeling of plasticity. *Journal of Statistical Mechanics: Theory and Experiment*, 2010(12):P12025, 2010.

[93] A. S. Khair. Large amplitude oscillatory shear of the Giesekus model. *Journal of Rheology*, 60(2):257–266, 2016.

[94] C. Klein, P. Venema, L. Sagis, and E. van der Linden. Rheological discrimination and characterization of carrageenans and starches by Fourier transform-rheology in the non-linear viscous regime. *Journal of Non-Newtonian Fluid Mechanics*, 151(1-3):145–150, 2008.

[95] C. O. Klein, H. W. Spiess, A. Calin, C. Balan, and M. Wilhelm. Separation of the Nonlinear Oscillatory Response into a Superposition of Linear, Strain Hardening, Strain Softening, and Wall Slip Response. *Macromolecules*, 40(12):4250–4259, 2007.

[96] R. G. Larson. Constitutive relationships for polymeric materials with power-law distributions of relaxation times. *Rheologica Acta*, 24:327–334, 1985.

[97] R. G. Larson. Flows of constant stretch history for polymeric materials with power-law distributions of relaxation times. *Rheologica Acta*, 24:443–449, 1985.

[98] R. G. Larson. *Constitutive Equations for Polymer Melts and Solutions*. Butterwirth Publishers, Stoneham, MA, 1988.

[99] R. G. Larson. *The Structure and Rheology of Complex Fluids*. Oxford University Press Inc., New York, 1999.

[100] R. G. Larson, T. Sridhar, L. G. Leal, G. H. McKinley, A. E. Likhtman, and T. C. B. McLeish. Definitions of entanglement spacing and time constants in the tube model. *Journal of Rheology*, 47(3):809–818, 2003.

[101] J. Läuger and H. Stettin. Differences between stress and strain control in the non-linear behavior of complex fluids. *Rheologica Acta*, 49(9):909–930, 2010.

[102] J.-S. Lee, Y.-S. Kim, and K.-W. Song. Transient rheological behavior of natural polysaccharide xanthan gum solutions in start-up shear flow fields: An experimental study using a strain-controlled rheometer. *Korea-Australia Rheology Journal*, 27(3):227–239, 2015.

[103] J. Lefebvre. An outline of the non-linear viscoelastic behaviour of wheat flour dough in shear. *Rheologica Acta*, 45(4):525–538, 2006.

[104] S. Lerouge and J.-F. Berret. Shear-Induced Transitions and Instabilities in Surfactant Wormlike Micelles. In K. Dusek and J.-F. Joanny, editors, *Polymer Characterization*, volume 230 of *Advances in Polymer Science*, pages 1–71. Springer Berlin Heidelberg, 2010.

[105] S. Lerouge, J.-P. Decruppe, and J.-F. Berret. Correlations between rheological and optical properties of a micellar solution under shear banding flow. *Langmuir*, 16(16):6464–6474, 2000.

[106] X. Li, S.-Q. Wang, and X. Wang. Nonlinearity in large amplitude oscillatory shear (LAOS) of different viscoelastic materials. *Journal of Rheology*, 53(5):1255, 2009.

[107] Y. Li, M. Hu, G. B. McKenna, C. J. Dimitriou, G. H. McKinley, R. M. Mick, D. C. Venerus, and L. A. Archer. Flow field visualization of entangled polybutadiene solutions under nonlinear viscoelastic flow conditions. *Journal of Rheology*, 57(5):1411, 2013.

[108] Y. Li and G. B. McKenna. Startup shear of a highly entangled polystyrene solution deep into the nonlinear viscoelastic regime. *Rheologica Acta*, 54(9-10):771–777, 2015.

[109] A. Likhtman, S. Milner, and T. McLeish. Microscopic theory for the fast flow of polymer melts. *Physical review letters*, 85(21):4550–3, 2000.

[110] A. E. Likhtman and R. S. Graham. Simple constitutive equation for linear polymer melts derived from molecular theory: Rolie-Poly equation. *Journal of Non-Newtonian Fluid Mechanics*, 114(1):1–12, 2003.

[111] A. E. Likhtman and T. C. B. McLeish. Quantitative Theory for Linear Dynamics of Linear Entangled Polymers. *Macromolecules*, 35(16):6332–6343, 2002.

[112] J. A. Lissajous. *Mémoire sur l'étude optique des mouvements vibratoires*. 1857.

[113] T. D. Lord, L. Scelsi, D. G. Hassell, M. R. Mackley, J. Embery, D. Auhl, O. G. Harlen, R. Tenchev, P. K. Jimack, and M. A. Walkley. The matching of 3D Rolie-Poly viscoelastic numerical simulations with experimental polymer melt flow within a slit and a cross-slot geometry. *Journal of Rheology*, 54(2):355, 2010.

[114] C.-Y. D. Lu, P. D. Olmsted, and R. C. Ball. Effects of Nonlocal Stress on the Determination of Shear Banding Flow. *Phys. Rev. Lett.*, 84(4):642, 1999.

[115] C.-Y. D. Lu, P. D. Olmsted, and R. C. Ball. Effects of Nonlocal Stress on the Determination of Shear Banding Flow. *Phys. Rev. Lett.*, 84(4):642, 2000.

[116] R. W. Mair and P. T. Callaghan. Observation of shear banding in worm-like micelles by NMR velocity imaging. *Europhysics Letters*, 36(9):719, 1996.

[117] R. W. Mair and P. T. Callaghan. Shear flow of wormlike micelles in pipe and cylindrical couette geometries as studied by nuclear magnetic resonance microscopy. *Journal of Rheology*, 41(4):901–924, 1997.

[118] R. Makhloufi, J. P. Decruppe, A. Aït-Ali, and R. Cressely. Rheo-optical study of worm-like micelles undergoing a shear banding flow. *Europhysics Letters*, 32(3):253, 1995.

[119] S. Manneville. Recent experimental probes of shear banding. *Rheologica Acta*, 47(3):301–318, 2008.

[120] S. Manneville, A. Colin, G. Waton, and F. Schosseler. Wall slip, shear banding, and instability in the flow of a triblock copolymer micellar solution. *Phys. Rev. E*, 75:061502, 2007.

[121] M. L. Manning, E. G. Daub, J. S. Langer, and J. M. Carlson. Rate-dependent shear bands in a shear-transformation-zone model of amorphous solids. *Phys. Rev. E*, 79(1):16110, 2009.

[122] G. Marrucci. Dynamics of entanglements: A nonlinear model consistent with the Cox-Merz rule. *Journal of Non-Newtonian Fluid Mechanics*, 62(2-3):279–289, 1996.

[123] G. Marrucci and N. Grizzuti. The Free Energy Function of the Doi-Edwards Theory: Analysis of the Instabilities in Stress Relaxation. *Journal of Rheology*, 27(5):433, 1983.

[124] G. Marrucci and N. Grizzuti. Fast flows of concentrated polymers - predictions of the tube model on chain stretching. *Gazzetta Chimica Italiana*, 118(3):179–185, 1988.

[125] J. D. Martin and Y. Thomas Hu. Transient and steady-state shear banding in aging soft glassy materials. *Soft Matter*, 8(26):6940, 2012.

[126] Y. Masubuchi. Simulating the flow of entangled polymers. *Annual review of chemical and biomolecular engineering*, 5:11–33, 2014.

[127] T. C. B. McLeish. Tube theory of entangled polymer dynamics. *Advances in Physics*, 51(6):1379–1527, 2002.

[128] D. Mead and L. Leal. The reptation model with segmental stretch. *Rheologica Acta*, 34:339–359, 1995.

[129] D. W. Mead, R. G. Larson, and M. Doi. A molecular theory for fast flows of entangled polymers. *Macromolecules*, 31(22):7895–7914, 1998.

[130] D. Merger and M. Wilhelm. Intrinsic nonlinearity from LAOStrain-experiments on various strain- and stress-controlled rheometers: a quantitative comparison. *Rheologica Acta*, 53(8):621–634, 2014.

[131] S. T. Milner. Dynamical theory of concentration fluctuations in polymer solutions under shear. *Physical Review E*, 48(5):3674–3691, 1993.

[132] S. T. Milner and T. C. B. McLeish. Parameter-Free Theory for Stress Relaxation in Star Polymer Melts. *Macromolecules*, 30(7):2159–2166, 1997.

[133] S. T. Milner, T. C. B. McLeish, and A. E. Likhtman. Microscopic theory of convective constraint release. *Journal of Rheology*, 45(2):539–563, 2001.

[134] R. L. Moorcroft, M. E. Cates, and S. M. Fielding. Age-Dependent Transient Shear Banding in Soft Glasses. *Physical Review Letters*, 106(5):055502, 2011.

[135] R. L. Moorcroft and S. M. Fielding. Criteria for Shear Banding in Time-Dependent Flows of Complex Fluids. *Physical Review Letters*, 110(8):086001, 2013.

[136] R. L. Moorcroft and S. M. Fielding. Shear banding in time-dependent flows of polymers and wormlike micelles. *Journal of Rheology*, 58(1):103, 2014.

[137] T. S. K. Ng, G. H. McKinley, and R. H. Ewoldt. Large amplitude oscillatory shear flow of gluten dough: A model power-law gel. *Journal of Rheology*, 55(3):627, 2011.

[138] P. Nghe, S. M. Fielding, P. Tabeling, and A. Ajdari. Interfacially Driven Instability in the Microchannel Flow of a Shear-Banding Fluid. *Physical Review Letters*, 104(24):248303, 2010.

[139] P. D. Olmsted. Perspectives on shear banding in complex fluids. *Rheologica Acta*, 47(3):283–300, 2008.

[140] G. Ovarlez, S. Rodts, X. Chateau, and P. Coussot. Phenomenology and physical origin of shear localization and shear banding in complex fluids. *Rheologica Acta*, 48:831–844, 2009.

[141] D. S. H. P. J. Schmid. *Stability and Transition in Shear Flows*. Springer, New York, 2001.

[142] D. Pearson, E. Herbolzheimer, N. Grizzuti, and G. Marrucci. Transient behavior of entangled polymers at high shear rates. *Journal of Polymer Science Part B: Polymer Physics*, 29(13):1589–1597, 1991.

[143] W. Philippoff. Vibrational Measurements with Large Amplitudes. *Journal of Rheology*, 10(1):317, 1966.

[144] A. C. Pipkin. Lectures on viscoelastic theory. 1972.

[145] C. Pozrikidis. *Introduction to Theoretical and Computational Fluid Dynamics*. Oxford University Press Inc., New York, 1997.

[146] W. H. Press, S. A. Teukolsky, W. T. Vetterling, and B. P. Flannery. *Numerical Recipes in C*. Cambridge University Press, Cambridge, 1992.

[147] S. A. Prost-Domasky and B. Khomami. A note on start-up and large amplitude oscillatory shear flow of multimode viscoelastic fluids. *Rheologica Acta*, 35(3):211–224, 1996.

[148] O. Radulescu, P. D. Olmsted, and C.-Y. D. Lu. Shear banding in reaction-diffusion models. *Rheologica Acta*, 38:606–613, 1999.

[149] J. Ramirez and A. Likhtman. **R**heology for **E**ntangled **P**olymers: **T**oolkit for **A**nalysis of **T**heory and **E**xperiment. `http://reptate.com/`, 2007.

[150] S. Ravindranath and S.-Q. Wang. Large amplitude oscillatory shear behavior of entangled polymer solutions: Particle tracking velocimetric investigation. *Journal of Rheology*, 52(2):341–358, 2008.

[151] S. Ravindranath and S.-Q. Wang. Steady state measurements in stress plateau region of entangled polymer solutions: Controlled-rate and controlled-stress modes. *Journal of Rheology*, 52(4):957–980, 2008.

[152] S. Ravindranath, S.-Q. Wang, M. Olechnowicz, and R. P. Quirk. Banding in Simple Steady Shear of Entangled Polymer Solutions. *Macromolecules*, 41(7):2663–2670, 2008.

[153] M. J. Reimers and J. M. Dealy. Sliding plate rheometer studies of concentrated polystyrene solutions: Large amplitude oscillatory shear of a very high molecular weight polymer in diethyl phthalate. *Journal of Rheology*, 40(1):167, 1996.

[154] S. Rodts, J. C. Baudez, and P. Coussot. From "discrete" to "continuum" flow in foams. *Europhysics Letters (EPL)*, 69(4):636–642, 2005.

[155] S. A. Rogers. A sequence of physical processes determined and quantified in LAOS: An instantaneous local 2D/3D approach. *Journal of Rheology*, 56(5):1129, 2012.

[156] S. A. Rogers, B. M. Erwin, D. Vlassopoulos, and M. Cloitre. A sequence of physical processes determined and quantified in LAOS: Application to a yield stress fluid. *Journal of Rheology*, 55(2):435, 2011.

[157] S. A. Rogers and M. P. Lettinga. A sequence of physical processes determined and quantified in large-amplitude oscillatory shear (LAOS): Application to theoretical nonlinear models. *Journal of Rheology*, 56(1):1, 2012.

[158] S. A. Rogers, D. Vlassopoulos, and P. Callaghan. Aging, Yielding, and Shear Banding in Soft Colloidal Glasses. *Physical Review Letters*, 100(12):128304, 2008.

[159] C. Roland, L. Archer, P. Mott, J. Sanchez-Reyes, et al. Determining rouse relaxation times from the dynamic modulus of entangled polymers. *Journal of Rheology*, 48(2):395–404, 2004.

[160] J.-B. Salmon, A. Colin, S. Manneville, and F. Molino. Velocity profiles in shear-banding wormlike micelles. *Phys. Rev. Lett.*, 90:228303, 2003.

[161] J.-B. Salmon, S. Manneville, and A. Colin. Shear banding in a lyotropic lamellar phase. I. Time-averaged velocity profiles. *Phys. Rev. E*, 68:051503, 2003.

[162] V. Schmitt, C. M. Marques, and F. Lequeux. Shear-induced phase separation of complex fluids: The role of flow-concentration coupling. *Physical Review E*, 52(4):4009–4015, 1995.

[163] N. Shamim and G. B. McKenna. Mechanical spectral hole burning in polymer solutions: Comparison with large amplitude oscillatory shear fingerprinting. *Journal of Rheology*, 58(1):43, 2014.

[164] S. Skorski and P. D. Olmsted. Loss of solutions in shear banding fluids driven by second normal stress differences. *Journal of Rheology*, 55(6):1219–1246, 2011.

[165] F. Snijkers, R. Pasquino, P. Olmsted, and D. Vlassopoulos. Perspectives on the viscoelasticity and flow behavior of entangled linear and branched polymers. *Journal of Physics: Condensed Matter*, 27(47):473002, 2015.

[166] K. Soo Cho and G. Woo Park. Fixed-point iteration for relaxation spectrum from dynamic mechanical data. *Journal of Rheology*, 57(2):647, 2013.

[167] N. A. Spenley, M. E. Cates, and T. C. B. McLeish. Nonlinear rheology of wormlike micelles. *Phys. Rev. Lett.*, 71:939–942, 1993.

[168] N. A. Spenley, X. F. Yuan, and M. E. Cates. Nonmonotonic Constitutive Laws and the Formation of Shear-Banded Flows. *Journal de Physique II*, 6(4):551–571, 1996.

[169] F. J. Stadler and C. Bailly. A new method for the calculation of continuous relaxation spectra from dynamic-mechanical data. *Rheologica Acta*, 48(1):33–49, 2008.

[170] S. H. Strogatz. *Nonlinear Dynamics and Chaos*. Persues Books Publishing, LLC, 1994.

[171] C. Sui and G. B. McKenna. Instability of entangled polymers in cone and plate rheometry. *Rheologica Acta*, 46(6):877–888, 2007.

[172] P. Tapadia, S. Ravindranath, and S.-Q. Wang. Banding in Entangled Polymer Fluids under Oscillatory Shearing. *Phys. Rev. Lett.*, 96(19):196001, 2006.

[173] P. Tapadia and S.-Q. Wang. Yieldlike Constitutive Transition in Shear Flow of Entangled Polymeric Fluids. *Physical Review Letters*, 91(19):198301, 2003.

[174] P. Tapadia and S.-Q. Wang. Nonlinear Flow Behavior of Entangled Polymer Solutions: Yieldlike Entanglement-Disentanglement Transition. *Macromolecules*, 37(24):9083–9095, 2004.

[175] P. Tapadia and S.-Q. Wang. Direct visualization of continuous simple shear in non-newtonian polymeric fluids. *Phys. Rev. Lett.*, 96:016001, 2006.

[176] T.-T. Tee and J. M. Dealy. Nonlinear Viscoelasticity of Polymer Melts. *Journal of Rheology*, 19(4):595, 1975.

[177] P. J. Turner. Grace, copyright ©. `http://plasma-gate.weizmann.ac.il/Grace/`, 1991-1995.

[178] S.-Q. Wang. Comment on "Nonmonotonic Models are Not Necessary to Obtain Shear Banding Phenomena in Entangled Polymer Solutions". *Phys. Rev. Lett.*, 103(21):219801, 2009.

[179] S.-Q. Wang, G. Liu, S. Cheng, P. E. Boukany, Y. Wang, and X. Li. Letter to the Editor: Sufficiently entangled polymers do show shear strain localization at high enough Weissenberg numbers. *Journal of Rheology*, 58(4):1059–1069, 2014.

[180] S.-Q. Wang, S. Ravindranath, and P. E. Boukany. Homogeneous Shear, Wall Slip, and Shear Banding of Entangled Polymeric Liquids in Simple-Shear Rheometry: A Roadmap of Nonlinear Rheology. *Macromolecules*, 44(2):183–190, 2011.

[181] S.-Q. Wang, S. Ravindranath, P. E. Boukany, M. Olechnowicz, R. P. Quirk, A. Halasa, and J. Mays. Nonquiescent Relaxation in Entangled Polymer Liquids after Step Shear. *Phys. Rev. Lett.*, 97(18):187801, 2006.

[182] M. Wilhelm. Fourier-Transform Rheology. *Macromolecular Materials and Engineering*, 287(2):83–105, 2002.

[183] M. Wilhelm, D. Maring, and H.-W. Spiess. Fourier-transform rheology. *Rheologica Acta*, 37(4):399–405, 1998.

[184] T. Williams, C. Kelley, and many others. Gnuplot 4.4: an interactive plotting program. `http://gnuplot.sourceforge.net/`, 2010.

[185] J. Yerushalmi, S. Katz, and R. Shinnar. The stability of steady shear flows of some viscoelastic fluids. *Chemical Engineering Science*, 25(12):1891–1902, 1970.

[186] X.-F. Yuan. Dynamics of a mechanical interface in shear-banded flow. *Europhysics Letters (EPL)*, 46(4):542–548, 1999.

[187] L. Zhou, L. P. Cook, and G. H. McKinley. Probing shear-banding transitions of the VCM model for entangled wormlike micellar solutions using large amplitude oscillatory shear (LAOS) deformations. *Journal of Non-Newtonian Fluid Mechanics*, 165(21-22):1462–1472, 2010.

[188] L. Zhou, R. H. Ewoldt, L. P. Cook, G. H. McKinley, A. Co, G. L. Leal, R. H. Colby, and A. J. Giacomin. Probing Shear-Banding Transitions of Entangled Liquids Using Large Amplitude Oscillatory Shearing (LAOS) Deformations. In A. Co, L. G. Leal, R. H. Colby, and A. J. Giacmin, editors, *The XV International Congress on Rheology*, volume 1027 of *American Institute of Physics Conference Series*, pages 189–191, Monterey, California, 3-8 August, 2008. AIP.

[189] L. Zhou, G. H. McKinley, and L. P. Cook. Wormlike micellar solutions: III. VCM model predictions in steady and transient shearing flows. *Journal of Non-Newtonian Fluid Mechanics*, 211:70–83, 2014.